Characterisation of the B-RAD radiation survey meter and development of new probes

Francesca Ferrulli

Normandie Université

THÈSE

Pour obtenir le diplôme de doctorat

Spécialité PHYSIQUE

Préparée au sein de l'Université de Caen Normandie

Characterisation of the B-RAD radiation survey meter and development of new probes

Présentée et soutenue par
FRANCESCA FERRULLI

Thèse soutenue le 11/04/2022 devant le jury composé de		
M. FRANCESCO D'ERRICO	Professeur des universités, Universita di Pisa	Rapporteur du jury
M. IMAD LAKTINEH	Professeur des universités, Université Lyon 1 Claude Bernard	Rapporteur du jury
MME MARIE-LAURE GALLIN-MARTEL	Directeur de recherche, Université Grenoble Alpes	Membre du jury
M. MARCO SILARI	Chercheur, CERN	Membre du jury
M. ETIENNE LIENARD	Professeur des universités, Université de Caen Normandie	Président du jury
M. MARC LABALME	Maître de conférences HDR, ENSICAEN	Directeur de thèse

Thèse dirigée par MARC LABALME (Laboratoire de physique corpusculaire (Caen))

UNIVERSITÉ CAEN NORMANDIE

ENSI CAEN
ÉCOLE PUBLIQUE D'INGÉNIEURS
CENTRE DE RECHERCHE

ED 591 PSIME

lpc caen
laboratoire de physique corpusculaire

A nonna Lina
e Vittorio.

Contents

List of Figures

List of Tables

Introduction

The subject of this thesis is the B-RAD radiation survey meter, a new γ-ray monitoring device capable of operating in the presence of strong electromagnetic fields. The B-RAD project started in 2008 when the LHC experiments required a portable device capable of measuring the residual activity around the CERN accelerator areas without turning off the magnetic field. At that time, the most commonly used detectors failed in presence of even weak magnetic fields (below 0.3 T) and/or showed deficiencies already at 0.1 T. The B-RAD was designed and developed by the CERN Radiation Protection (RP) group in collaboration with the Polytechnic of Milan to accomplish this requirement. Nowadays, the B-RAD is an advanced commercial device, marketed by the Italian company ELSE NUCLEAR, for both γ-ray dose rate measurements and γ-ray spectrometry.

The B-RAD consists of a probe connected with a cable to a central unit. The probe contains the sensitive part of the detector: a $LaBr_3$ crystal scintillator coupled with a Silicon Photomultiplier (SiPM) array. The main idea of the B-RAD is that changing the probe, i.e. changing the scintillator, particles different from γ-rays can also be detected. This study was aimed at characterising the B-RAD detector and at developing three additional probes: a probe for neutron dose rate measurements, a probe for fast neutron spectrometry and one for thermal neutron counting.

Chapter 1 provides an introduction to the principles of radiation protection, of radiation instrumentation and an overview of the B-RAD from its conception to the commercial device. Chapter 2 describes the performance tests of the B-RAD commercial versions. Chapter 3 discusses and compares two organic scintillators (a stilbene and an EJ-276 plastic scintillator) proposed for fast neutron dose rate measurements. The work described in Chapter 3 is also described in *F. Ferrulli et al., Characterization of stilbene and EJ-276 scintillators coupled with a large area SiPM array for a fast neutron dose rate detector, Nucl. Instrum. Methods Phys. Res. A 1010 (2021) 165566.* Chapter 4 describes the development of a probe for thermal neutron counting and a probe for fast neutron spectrometry, both based on a Cs_2LiYCl_6:Ce (CLYC) scintillator crystal. Chapter 4 refers to *F. Ferrulli et al., Investigation of CLYC-6 for thermal neutron detection and CLYC-7 for fast neutron spectrometry, Nucl. Instrum. Methods Phys. Res. A,1029 (2022) 166460.* Chapter 5 reports the study of a new neutron/γ discrimination method to be applied with CLYC crystal based on a passive and on-line discrimination method, and discusses its feasibility. This study has been published in *F. Ferrulli et al., Analysis and comparison of the Core-to-Valence Luminescence mechanism in a large CLYC crystal under neutron and γ-ray irradiation through optical filtering selection of the scintillation light, Sens. Actuators A 332 (2021) 113151.* Finally, the results of the thesis and the future steps for the B-RAD development are summarised.

In order to characterise the CLYC crystal, a thermal neutron source for the CERN RP Calibration Laboratory has been designed and built. The details of the design and construction, and the characterisation of the new thermal neutron source, are reported in Appendix A and in *F. Ferrulli et al., A thermal neutron source for the CERN radiation Calibration Laboratory, Appl. Radiat. Isot. 178 (2021) 109977.*

Chapter 1

Radiation protection and instrumentation

This chapter is divided in three sections. Section 1.1 defines the goal of radiation protection and its fundamental quantities. Section 1.2 provides an overview of the radiation monitoring devices available on the market distinguishing between their application. Section 1.3 introduces the B-RAD detector, from its conception to the commercial device, and compares it with some competitors.

1.1 Radiation protection

Protection of personnel working with radiation is essential in any working environment that employs ionizing radiation. The set of rules aimed to achieve the *"protection of people from harmful effects of exposure to ionizing radiation"* is the primary task of radiation protection (International Atomic Energy Agency (IAEA) definition [1]). Ideally, the legal protection limits would be expressed in terms of *physical quantities* (Section 1.1.1), i.e quantities that are directly measurable [2]. However, physical quantities cannot quantify the biological effect of ionizing radiation to human body, so legal limits are expressed in terms of so-called *protection quantities* (Section 1.1.2). The International Commission on Radiological Protection (ICRP) developed the protection quantities to assess and implement the dose limits. To be compliant with dose limits, the so-called *operational quantities* (Section 1.1.3) have also been defined by the International Commission on Radiation Units (ICRU) as conservative estimates of the protection quantities [2].

1.1.1 Physical quantities

- **Fluence**, Φ (m^{-2}) is defined as the ratio between the number of particles $\mathrm{d}N$ crossing an infinitesimal sphere of cross-sectional area $\mathrm{d}a$.

$$\Phi = \frac{dN}{da} \tag{1.1}$$

- **Absorbed dose**, D (Gray, 1 Gy =1 J kg^{-1}) is the average energy $\mathrm{d}\bar{\epsilon}$ delivered by a certain kind of radiation to a volume element of mass dm.

$$D = \frac{d\bar{\epsilon}}{dm} \tag{1.2}$$

- **Linear Energy Transfer,** LET (J m^{-1}, usually expressed in keV $\mu\mathrm{m}^{-1}$) is the average energy $\mathrm{d}\bar{\epsilon}$ lost by a charged particle in electron collisions traversing a distance $\mathrm{d}l$.

$$LET = \frac{d\bar{\epsilon}}{dl} \tag{1.3}$$

1.1.2 Protection quantities

- **Equivalent dose**, H_T (Sievert, 1 Sv = 1 J kg^{-1}) in a tissue or organ T, from radiation R is defined as:

$$H_T = \sum_R w_R D_{R,T} \tag{1.4}$$

  where $D_{R,T}$ is the average absorbed dose and w_R is the radiation weighting factor recommended by the ICRP.

- **Effective dose**, E (Sv).

$$E = \sum_T w_T H_T \tag{1.5}$$

  where w_T and H_T are the weighting factor and the equivalent dose respectively, in the tissues or organs T. E includes the tissues or organs which are considered to be the most sensitive.

1.1.3 Operational quantities

- **Ambient dose equivalent**, $H^*(d)$ (Sv) is defined as the dose equivalent produced by the corresponding expanded and aligned field in the ICRU sphere at depth d (in mm), where $d = 10$ mm is recommanded for penetrating radiation and it is indicated as $H^*(10)$. $H^*(10)$ is the reference quantity for *area monitoring* devices.

- **Personal dose equivalent**, $H_p(d)$ (Sv) is defined as the dose equivalent in standard tissue at a depth d (in mm), below a specified point on the human body, being the specified point usually the position of the individual dosimeter. Normally, $d = 10$ mm is considered for the effective dose, $d = 0.07$ mm is chosen for the dose to the skin, hands and feet. $H_p(10)$ and $H_p(0.07)$ are the reference quantities for *individual monitoring* devices.

1.1.4 Dose conversion coefficients

Conversion coefficients are provided to convert the particle fluence (usually measured by a detector) into protection or operational quantities. Often, radiation protection instrumentations for individual and area monitoring directly provide the operational quantities being the conversion coefficient for effective dose and ambient dose equivalent the most common [2].

1.2 Instrumentation for radiation survey

A radiation survey meter is a hand-held device for radiation detection. The primary function of a survey meter is to measure radiation exposure and/or to detect radioactive contamination in order to guarantee that the radiation levels are always under the legal limits. The second function is monitoring the radiation level, to inform of its possible increasing and to give an alarm if the levels exceed given thresholds [3, 4]. Radiation protection has to deal with different kinds of radiation (usually present together as a mixed radiation field) with different energies and intensities (usually unknown), and different penetrating powers. Therefore, the choice of the survey meter is usually not straightforward since there is no detection system which is able to detect all kinds of radiation.

A brief description of the most common survey meters is here provided, divided according to the particle they are meant to detect (for the sake of simplicity). This is neither an exhaustive list of all the available survey meters nor a complete description of their

working principle, but it is aimed at providing a general overview of the variety of the survey meters present on the market.

1.2.1 X-ray and γ-ray detectors

X-ray and γ-ray detectors are used in several fields such as industry (e.g with radiography or sterilization units), radio-pharmaceuticals, radiation protection, etc. [3]. In general, the survey meters suitable for γ and X-ray measurements are gas-filled detectors, semiconductors such as Cadmium-Zinc-Telluride (CdZnTe) and scintillating crystals such as NaI and CsI.

Gas-filled detectors are divided according to their region of operation in ionisation chambers, proportional counters and Geiger-Müller (GM) counters [5]. The operation region varies with the electric field applied to the detector, as shown in Figure 1.1. Within the regime of the ionization chambers, the electric field is high enough to prevent ion recombination and allow all the primary charges (electron-ion pairs) produced by the direct ionization of the gas to be collected. By increasing the applied voltage, above a certain threshold, the primary electrons start multiplying and the pulse amplitude, for the same energy signal, is amplified. This is the region of operation for proportional counters. Inside this region the gas multiplication is linear, i.e the collected charge is proportional to the original charge. If the applied voltage is further increased some non-linearities arise that characterised the "Limited Proportional Region" (Figure 1.1). The most relevant one is due to the different drift velocity between electrons and positive ions which causes distortions of the electric field inside the detector. Above the "Limited Proportional Region", the operation regime of GM detectors begins. Here the gas multiplication (also called avalanche) proceeds and the proportionality with the original ion pairs is lost. The avalanche is a self-quenched process since it stops when the amount of positive ions produced during the multiplication is able to shield the electric field below the threshold for the gas multiplication.

GM counters are in general preferred in most situations since they are compact and low cost (especially if compared to ionisation chambers), electronically simple and require low maintenance. However, they cannot provide any spectrometry information and they show a long dead time (order of hundreds of microseconds) [5, 6]. Ionisation chambers provide an excellent X and γ-ray ambient dose equivalent response, however they are expensive and require more maintenance than GM detectors. Proportional counters are also widely used, especially when the charge produced by the primary ionizing radiation is too small for adequate operation in ion chambers, e.g. with low energy X-ray radiation [5].

Solid state detectors (semiconductors and scintillators) offer the advantage of being much smaller than the equivalent gas-filled detectors (thanks to their higher densities). Scintillators are widely used in many applications, they offer good sensitivity and spectrometry capability. In certain cases, scintillators also provide radio-isotope identification. They can be made of different scintillating materials, different dimensions (e.g. larger volumes are required for higher sensitivity) and electronic systems. As drawbacks, the scintillator response efficiency is not constant with energy and has to be compensated and their energy resolution is poor compared to semiconductor materials. The latter are commonly used for γ-ray (mostly germanium) and charge particle (mostly silicon) detection and spectrometry. However, because of the small band gap, germanium detectors need to be cooled [5]. This is typically accomplished using a cryogenic liquid such as liquid nitrogen placed in a dewar supporting the detector. Germanium detectors are not hand-held detectors. As an alternative, high Z semiconductors have been developed which can operate at room temperature, essentially based on Cadmium telluride (CdTe) and CdZnTe, mainly for applications in X and γ-ray imaging, astrophysical research, high energy industrial radiography and tomography. Semiconductors are quite sensitive to radiation damage

being crystalline materials. A list of commercial devices for γ-ray detection comparable with the B-RAD (i.e. based on scintillators) is given in Section 1.3.3.

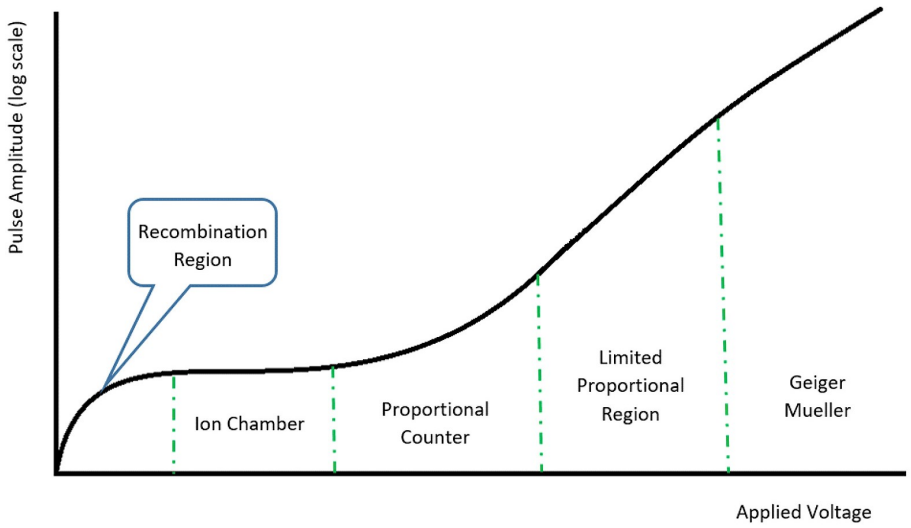

Figure 1.1: The pulse amplitude observed in a gas-filled detector versus the applied voltage for the same amount of energy deposited inside the gas. The different operating regions are also indicated for different applied voltages [6]. The y-axis is in logarithmic scale.

1.2.2 α/β particle detectors

A variety of detectors is present on the market for contamination monitoring, mainly for α/β particle detection, being contamination (external or internal to human body) the main risk of exposure to these particles. Surface contamination is for example important when unsealed radioactive material is being processed or handled. Concerning the detection of α–particles: 1) the probe has to be very close to the surface (α–particles are readily stopped in air), 2) any covering material (grease, oil or paint) on the potentially contaminated surface will attenuate the α–particles or completely stop them, 3) contamination on the probe must be avoided. The most common detector for α–particles is the ZnS scintillator. Different from α–particles, β–particle sources emit over a continuous energy range from 0 up to a maximum energy value which can vary according to the specific radionuclide (e.g. 18 keV for ^{3}H, 2.2 MeV for ^{90}Y). Detectors for β–particles are made up of low atomic number materials in order to avoid/reduce the associated Bremsstrahlung radiation. Usually β–particles are measured with thin end window GM detectors or thin window scintillators of low Z materials [3].

Figure 1.2 shows two commonly used contamination detectors for simultaneous measurements of α and β–particles. They both consist of a thin layer of ZnS(Ag) scintillator for α–particle detection coated on a thin layer of an organic scintillator for β–particle detection. A version of the same detectors exists which is also able of γ-ray detection, by using a thicker plastic scintillator (in the case of the SaphyRAD A-B 170, left plot of Figure 1.2) or an additional GM counter (in the case of the CoMo 170, right plot of Figure 1.2).

Figure 1.2: Two commercial devices for α/β particle detection: the SaphyRAD A-B 170 probe from Bertin Technologies (on the left) and the CoMo 170 from NUVIATech Instruments (on the right).

1.2.3 Neutron detectors

The neutron device mostly used for area monitoring is, since many years, the so-called rem counter. It mainly consists of a thermal neutron detector embedded in a moderator assembly of polyethylene. The construction details of the assembly (e.g. shape, materials, thickness) can vary. The working principle of a rem counter is that its response function reproduces the fluence-to-H*(10) conversion coefficient curve. The response of a traditional rem counter is acceptable for neutron energies up to about 15 MeV, above this energy it considerably underestimates H*(10). The so-called extended neutron rem counters overcome this limitation by inserting a thin layer of high-Z material in the moderator assembly to enhance the response to high energy neutrons, because of secondary neutrons produced by multiplying neutron reactions (e.g. (n, 2n) reaction) in these heavy elements [7, 2]. Figure 1.3 shows two commercial extended rem counters taken as an example.

Figure 1.3: Two commercial neutron rem counters: the FHT 762 Wendi-2 from Thermo Fischer Scientific (on the left) and the Lupin BF3-NP from ELSE NUCLEAR (on the right).

1.3 The B-RAD detector

After having revised the main principles of radiation protection and nuclear instrumentation, this section focuses on the B-RAD detector and its applications. In particular, Section 1.3.1 discusses the reasons that led CERN Radiation Protection (RP) Group, in collaboration with the Polytechnic of Milan, to start the B-RAD project, discussing the B-RAD main concept. Section 1.3.2 summarizes the evolution of the B-RAD since its first conception to the design of the first prototype until the development of an industrialized product. Section 1.3.3 compares the B-RAD with some competitor devices.

1.3.1 Motivation

The B-RAD [8, 9] is a hand-held radiation survey meter specifically designed to work in regions of strong magnetic field (up to 3 T). The B-RAD project started in 2008 from the requirements of the Large Hadron Collider (LHC) experiments [10] for a radiation survey meter able to perform measurements of the residual radioactivity in the experimental halls and in the inner parts of the ATLAS detector [11], while the magnetic field is still on (up to 1 T). Apart from this first specific request, the B-RAD finds various potential applications in several fields at CERN and elsewhere, such as measurements of residual radioactivity on permanent magnets or activated accelerator components, surveys at PET[(1)]/MRI[(2)] scanners and medical accelerators (electron linac), including IGRT[(3)] with MRI-guidance, measurements around cyclotrons for radionuclide production and hadron therapy accelerators. Although the first need was for a simple survey meter, the B-RAD has evolved into an advanced detector for γ-ray dose rate measurements and γ-ray spectrometry.

The B-RAD consists of an active probe connected through a cable with a main unit. The probe includes the detector which consists of a scintillator coupled with a Silicon Photomultiplier (SiPM) array. The control unit houses the battery, the electronics and two displays (one Liquid Crystal Diode (LCD) and one Light Emitting Diode (LED)). Besides the already existing γ-ray probe, the instrument will be provided with additional probes: one for neutron dose rate, one for neutron spectrometry and one for surface contamination measurements.

1.3.2 The evolution of the B-RAD

Tests performed in 2008/2009 on various radiation survey meters revealed that the commercial devices available at that time failed in presence of a magnetic field. In 2010, the CERN RP group signed a collaboration agreement with the Department of Energy of the Polytechnic of Milan (POLIMI) to develop the first prototype of a portable radiation survey meter operating in magnetic fields. The first request was for a device operating up to 1 T with an energy range between 60 keV and 1.3 MeV, suitable for application in accelerators facilities where the average γ-ray energy from residual radioactivity is around 800 keV. The sensitivity range was set between 1 μSv/h and a few mSv/h later extended down to 0.1 μSv/h, i.e. ambient background. Tests performed with the first prototype up to 1 T in the CMS and ATLAS experimental halls confirmed its correct operation. In 2012 a contract extension was signed with the POLIMI and five engineered units were manufactured (with different scintillator materials and/or dimensions and different SiPM configurations) and tested.

The final configuration of the crystal and the SiPM chosen in view of the production of the industrial instrument consisted of:

[(1)] Positron Emission Tomography

[(2)] Magnetic Resonance Imaging

[(3)] Image-Guided Radiation Therapy, i.e. the use of imaging during radiation therapy

- a 4 × 4 SiPM array from SenSL (ArrayC-30035-16P) easily available on the market;
- a 15 Ø × 15 mm^3 cylindrical $LaBr_3$(Ce) crystal which guaranteed a good sensitivity to detect the natural background with dimension well matching the SiPM array.

The $LaBr_3$(Ce) was selected as the scintillating crystal since it satisfied the following specifications:

- Fast decay time (16 ns) for high count rate measurements, essential in radiation protection applications.
- High light yield (63 photons per keV).
- High density (5.06 g/cm^3) for high γ-ray efficiency.
- Low intrinsic radioactivity for operations in low radiation environment [12].

Beside the crystal and the photodetector, the active probe also included an analog signal processing board, a temperature compensation board and a Hall probe for magnetic field measurement. The active probe of the first prototype was enclosed inside a light aluminium box and provided with a handle. The control unit of the first prototype consisted of a plastic box which could be fastened to the operator's waist or carried within a bag. It housed two displays (an LCD display and a LED screen), a USB data interface, a digital board and a rechargeable Pb battery (6 V, 1,200 mA·h). For the final version of the B-RAD, a Li-ion battery with a longer lifetime was adopted. Tests performed up to 1 T revealed that a Li-ion battery properly and safely worked in strong magnetic field regions [12]. Figure 1.4 shows the two main components of the engineered version of the B-RAD prototype.

The first prototype and the five units were extensively tested to check the detector features listed below (described in details in [8]).

- Linearity of its response in the required dose rate range: all units that included the $LaBr_3$ crystal showed a linear response between 1 μSv/h and 1 mSv/h.
- Uniformity of the response inside a magnetic field: the count rate measured for the same configuration, at different values of the magnetic field and in different scenarios (i.e with the probe static or dynamic with respect to the magnetic field) was always constant. Measurements were performed inside a calibrated dipole magnet up to 1 T, in the ATLAS and CMS experimental areas and up to 3 T inside the clinical MRI scanner at the University Hospital in Lausanne (CHUV). A pulling force on the probe was felt starting from 0.3 T, due to the current induced by the field gradient on the metallic components.
- Response efficiency at different energies and energy resolutions: the efficiency at different photon energies from 48 keV up to 1.3 MeV was measured with the first prototype using three γ-ray sources of different energies and eight energies from an X-ray generator. On the basis of the measurements a software algorithm was proposed to compensate for the non-uniform response of the scintillator with the photon energy, successively implemented in the commercial version of the detector. The corresponding energy resolution was 19.2% and 6.8% at 59 keV and 662 keV, for a ^{241}Am and ^{137}Cs source respectively. The 33 keV due to the ^{137}Ba X-ray emission was also detected with an energy resolution of 30.3%, in good agreement with the $(\sqrt{E})^{-1}$ dependence law.

- Temperature dependence: a unit mounting the NaI(Tl) scintillator and a unit mounting the $LaBr_3$(Ce) crystal were placed inside a climate chamber with a ^{137}Cs source at 3 cm of distance and the count rate was measured in the temperature range between -20 °C and 50 °C in steps of 5 °C. The response of the former progressively decreased with the temperature down to about 50% of the initial value, while a variation of 30% was revealed with the latter between the maximum value (at around 0 °C) and the minimum value (at 50 °C). The light yield of $LaBr_3$ showed a lower temperature dependence as compared to the NaI(Tl) crystal.

In 2017 the instrument was patented [9, 8] and CERN has granted the licence to ELSE NUCLEAR [13], which developed a commercial version of the B-RAD.

Figure 1.4: On the left, the active probe of one of the first prototypes of the B-RAD without the front cover to show the $LaBr_3$ crystal; on the right, the control unit.

1.3.3 Comparison between the B-RAD and commercial instrumentation of the same class.

The characteristics and performances of the B-RAD as declared in the datasheet are listed in Table 1.1. Table 1.1 also compares the B-RAD with four commercialized instruments mentioned by the U.S. Department of Homeland security among a list of twenty-three Personal Radiation Detectors (PRDs) and Spectroscopic PRDs [14]. The document was published in 2017 with the aim to provide a list and description of some hand-held personal devices present on the market. Four of these detectors were selected for the comparison because they are suitable to work in magnetic field. Table 1.2 compares the B-RAD with four other devices, not intended to work in magnetic field, but of the same commercial class. Figure 1.5 shows the B-RAD (a), the Identifinder R300 (b) and the Gamma RAE II R (c) listed in Table 1.1, and the LABR-1.5×1.5 detector (d) reported in Table 1.2.

The B-RAD well competes with the other commercial devices and excels for its high sensitivity (90 cps/μSv/h) and optimum energy resolution (3.3%). The B-RAD is an advanced detector that provides several additional features barely available on devices of the same commercial class, such as the algorithm for flattening the energy response, radioisotope identification and the energy calibration which can be updated by the user. The main unit can be carried in a bag whereas the active probe is hand held by the user. It is slightly heavier than other commercial devices (e.g. the Identifinder R300 and RadPasive), but it is compact and well suitable for radiation survey applications.

(a) **(b)**

(c) **(d)**

Figure 1.5: ***(a)*** *The B-RAD detector from ELSE NUCLEAR and three competitors devices:* ***(b)*** *the Identifinder R300 (FLIR Detection),* ***(c)*** *the Gamma RAE II R (Rae System),* ***(d)*** *the LABR-1.5×1.5 (Mirion Technologies).*

Table 1.1: Comparison between the B-RAD and four competing detectors available on the market.

Name	B-RAD [15]	Identifinder R300 [16]	Gamma RAE II R [17]	NetS^2 Smartshield G300 [18]	RadPavise [19]
Company	ELSE NUCLEAR	FLIR Detection	Rae System	Passport System	X-Zlab
Detector type	$LaBr_3$(Ce) with 4×4 SiPM array	γ: three CdZnTe semiconductors γ/n: ^{3}He	CsI with Photodiode (low channels) Energy compensated PIN diode (High channels)	CsI(Tl) with PIN diode readout (for spectroscopy) Bare PIN diode (for low energy and high count rate)	YSO with SiPM
Dose Rate range	0.1 μSv/h–10 mSv/h	≤0.1 μSv/h–10 mSv/h	0.01 μSv/h–6 Sv/h	0.1 μSv/h–60 μSv/h[j] 60 μSv–3 mSv/h[k] 0.1 μSv–3 mSv/h[l]	0.01 μSv/h - 10 Sv/h
Sensitivity	90 cps/μSv/h	47 cps/μSv/h[c] [14] 81 cps/μSv/h[d] [14]	100 cps/μSv/h[h][14] 20 cps/μSv/h[i] [14]	—	98 cps/μSv/h
Spectrometry	Yes	Yes	No	Yes	No
Resolution at 662 keV	3.3%	≤3.5%	—	<7%	—
Energy range	0.03 to 2 MeV	0.03 to 3 MeV	0.06 to 3.0 MeV	0.025 to 3.0 MeV	0.02 to ∼10 MeV
Radionuclide identification	Yes	Yes	—	Yes	No
Weight	2.3kg	≤0.4 kg	0.315 kg	<0.25 kg[m]	0.165 g (without batteries)
Dimensions	16×19×9 cm^3 [a] 18×5 Ø cm[b]	12×7×3 cm^3	12×7×3 cm^3	13×7×3 cm^3 [m]	12×7×3 cm^3
Housing	Aluminium	Aluminium		Rubber case	—
Battery	Packed Li-ion	Li-ion	2 AA alkaline or Nickel-Metal-Hydride	Li-ion	AAA
Autonomy	Up to 12 h	24 h[e] [14]	Up to 500 h	60 h[n]	—
Recharge time	3 h	≤3 h[f] or >5.5 h[g]	—	—	—
Temperature range	0°C to 40°C	-20°C to 50°C	-20°C to 50°C	-20°C to 40°C	0°C to 50°C
Display	1 LCD 1 LED	1 LCD	1 LCD	1 LCD	OLED
Alarm	3 visible LED light	Visible Audio Tactile	Visible LED light Audible buzzer Build in vibration	Visual Audio Vibrator	Visual Audio Vibrator

Table 1.2: Comparison between the B-RAD and other competitors of the same commercial class of the B-RAD.

Name	B-RAD [15]	SAM 950 [20]	LABR-1.5×1.5 [21]	TS215 [22]	RADEAGLE-2LG [23]
Company	ELSE NUCLEAR	Berkeley Nucleonic Corp.	Mirion Technologies	TechnoAP Co., Ltd.	ORTEC
Detector type	$LaBr_3$(Ce) with 4×4 SiPM array	NaI(Tl)/$LaBr_3$/$CeBr_3$ GM tube (for high count rate)	$LaBr_3$(Ce) with PMT	$LaBr_3$(Ce) with PMT	$LaBr_3$(Ce) with PMT GM tube
Dose Rate range	0.1 μSv/h–10 mSv/h	0–100 μSv/h (NaI) 0.1–100 mSv/h (GM)	—	0.001–600 μSv/h	0.01–300 μSv/h up to 1 Sv/h (GM)
Sensitivity	90 cps/μSv/h	—	—	1000 cps/μSv/h	>1600 cps/μSv/h
Spectrometry	Yes	Yes	Yes	Yes	Yes
Resolution at 662 keV	3.3%	NaI: <7% $LaBr_3$: <3% CeB_3: <4%	3%	∼ 3%	≤3%
Energy range	0.03 to 2 MeV	0.02 to 3 MeV	—	0.03 to 3 MeV	0.011 to 3 MeV
Radionuclide identification	Yes	Yes	—	Yes	Yes
Weight	2.3 kg	2.9 kg[o] 4.3 kg[p]	0.43 kg	1.2 kg	2.25 kg
Dimensions	16×19×9 cm^3 [a] 18×5 Ø cm[b]	19×36×21 cm^3	15 cm×6 Ø cm	10×19×4 cm^3 [q] 19 cm×5 Ø cm[r]	25×12×15 cm^3
Housing	Aluminium	—	All metal housing with a magnetic/light shield	—	—
Battery	Packed Li-ion	Li-ion	—	Li-ion	Rechargeable AA Nickel-Metal-Hydride battery pack
Autonomy	Up to 12 h	≥ 8 h	—	∼ 7h	> 8 h
Recharge time	3 h	—	—	—	—
Temperature range	0°C to 40°C	-20°C to 50°C	4°C to 43°C	0°C to 40°C	-20°C to 50°C
Display	1 LCD 1 LED	1 AMOLED	—	1 LCD	1 Transflective Color Thin-Film-Transistor
Alarm	3 visible LED light	Visible Audio	—	(yes)	(yes)

Abbreviations

[a] main unit
[b] probe
[c] in the identification channel
[d] in the dose rate channel
[e] in dose rate mode with dimmed display background and GPS switched off
[f] when using AC
[g] when using USB
[h] Using CsI
[i] Using PIN diode detectors
[j] in spectroscopic mode (full energy range)
[k] in spectroscopic mode (< 200 keV)
[l] in total dose rate mode
[m] with protective rubber overmold
[n] in surveillance mode
[o] Standard NaI(Tl), $LaBr_3$/$CeBr_3$
[p] High sensitivity NaI(Tl)
[q] main unit
[r] probe

Chapter 2

Characterisation of the commercial version of the B-RAD detector

This chapter describes the results of the tests performed to characterise the commercial version of the B-RAD. The aim of this chapter is to demonstrate the applicability of the detector as a survey meter in radiation protection. Additionally, these first tests were useful to provide ELSE NUCLEAR with some feedback to improve the performance of the device.

The first section provides an overview of the B-RAD, showing its software interface and the modes of operation, and explaining its working principle. Section 2.2 shows the results of the tests made on the actual commercial instrument in terms of: uniformity of response with the magnetic field, response linearity with the dose rate, energy range and energy resolution, angular response, internal radioactivity measurement and operational performances. Section 2.3 summarises the results.

2.1 The commercial version of the B-RAD

As mentioned in Chapter 1, in 2017 the instrument was patented [9, 8] and the licence was granted to ELSE NUCLEAR [13] for developing a commercial device. The instrument is equipped with a probe for γ-ray dose rate and γ-ray spectrometry measurements. The probe consists of a cylindrical $LaBr_3$ scintillating crystal with dimensions 15 mm Ø × 15 mm height, coupled to a 4 × 4 Silicon Photomultiplier (SiPM) array by SensL. The use of SiPMs instead of a traditional photomultiplier tube (PMT), along with a proper selection of all electronic components as well as the battery, makes the instrument operation unaffected by magnetic fields. Moreover, the advantage of using a SiPM photodetector instead of a PMT is not restricted to applications with magnetic fields. In fact, it also provides the possibility to have a more compact detector and a lower supply voltage.

In view of using the B-RAD in real operating conditions and in order to be competitive on the market, a big effort was put on the definition of 1) a new plastic case and a light metal electromagnetic shield for the control unit, in order to minimise electromagnetic or induced current effects, to limit the pulling force felt in strong magnetic fields and to reduce the weight of the instrument, 2) on the choice of the battery. Recent strict regulations on the transport of Li-ion batteries in portable devices restricted the choice of commercially available batteries and forced the company to find alternative solutions and design an ad-hoc battery pack.

In July 2018 ELSE NUCLEAR provided us with the first version of the detector. A first set of measurements were performed in order to characterise the detector in terms of dose rate response, response linearity, energy calibration and angular response. An improved version of the B-RAD was delivered to CERN in December 2018, provided with a new customized battery pack. A third and a fourth version were delivered in May 2019 and in December 2019, respectively, in which some electronic issues previously reported had been solved (Figure 2.1). Eventually, in January 2022 ELSE NUCLEAR provided us with the latest version of the B-RAD that is now on the market [15] (Figure 2.2).

Figure 2.1: On the left, the first version of the B-RAD; on the right the fourth version.

Figure 2.2: On the left, the probe of the latest version of the B-RAD; on the right, the control unit of the same version.

2.1.1 Overview of the commercial version

The central unit is tasked with data processing and real-time visualization of parameters and of the measurements results. Figure 2.3 shows the main screen when the B-RAD is switched-on where the main functions are numbered in red.

(1) The first function (*Spectrum Acquisition*) is used to acquire the energy calibrated spectra. This function provides the spectrum in channels, the real and live acquisition times, the integrated number of counts and the integrated dose. The measured

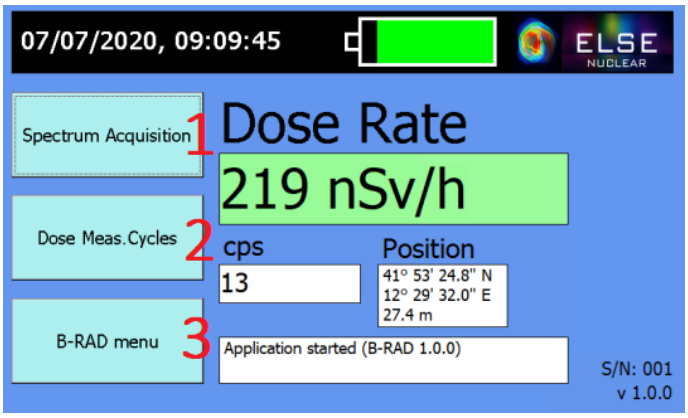

Figure 2.3: Main screen of the B-RAD central unit.

spectrum as well as date and start time of the measurement, the integral dose and the dose rate are automatically saved. All the previous acquired spectra can be load, visualized and through the *Peak search* option the software is able to identify the peaks and give information about the channel, the energy, Full Width at Half Maximum (FWHM) and the corresponding radionuclide.

(2) The second function (*Dose Measurement Cycles*) performs consecutive dose rate acquisition cycles with the possibility to set pauses between measurements. This function allows selecting the number of measurements and the duration of each measurement. At the end of the cycles, the following data are registered:

- Real time
- Live time
- Average dose rate
- Maximum dose rate
- Integral dose

The units of average dose rate, maximum dose rate and integral dose are Sv/h and Sv, respectively, with an automatic adjustment of the scale.

(3) Pressing the *B-RAD menu* bottom the user accesses the following functions.

(3.1) *Energy Calibration.* This function allows the user acquiring a spectrum for energy-channel calibration. After the spectrum acquisition, the user can select the photoelectric peak using two cursors. Once a peak is selected, the software automatically fits the peak with a Gaussian function and calculates the energy resolution (FWHM). A list of peaks can be created (peaks can be deleted or added) and the energy calibration curve is automatically calculated from the data in the saved list. This functionality allows the user to continuously update the energy calibration adding new calibration points or replacing the points previously saved. The detector was delivered by ELSE NUCLEAR already calibrated using four peaks (511 keV and 1274 keV from ^{22}Na and 32 keV and 662 keV from ^{137}Cs).

$$E = -3.213 \times 10^{+1} + 6.044 \times 10^{-1} \times ch. + 2.185 \times 10^{-5} \times ch.^2 \qquad (2.1)$$

where E is the energy in keV and ch the corresponding channel number.

(3.2) *Background Acquisition.* It allows environmental background spectra acquisitions to be performed. The background spectrum acquired via the *Background Acquisition* function can be automatically subtracted by the software to each spectrum acquired via the *Spectrum Acquisition* and *Dose Measurement Cycles* modes.

(3.3) *Settings.* It allows the user to set the following parameters:

- Energy range (only for better visualisation, not applied for dose rate calculation)
- Calibration factor (see below Equation 2.2)
- Dose rate threshold for alarm alerting
- Enable/Disable background subtraction
- Enable/Disable $LaBr_3$ intrinsic spectrum subtraction
- Create, duplicate, edit and delete the isotope library (this function is password-protected). The B-RAD standard library is listed in the manual.

(3.4) *File manager* opens the panel dedicated to file transfer to/from USB drive.

The dose provided by the B-RAD is calculated by software according to Equation 2.2:

$$Dose = \frac{\sum_{ch} (w_{ch} \times E_{ch} \times counts_{ch})}{\sum_{ch} counts_{ch}} \times C_{trigger} \times FC \tag{2.2}$$

in which ch are the energy spectrum channels, w_{ch} is a weighting factor that depends on the efficiency of the crystal as a function of the energy, E_{ch} is the corresponding energy, $counts_{ch}$ are the counts in the corresponding channel, $C_{trigger}$ the actual number of counts detected inside the trigger (i.e. all the signals crossing the threshold), and FC the calibration factor. The weighting factors are set as shown in Table 2.1 based on the measurements described in Chapter 1 (Section 1.3.2) [24] and cannot be freely modified by the user. Because the dose is calculated weighting the number of counts over the energy spectrum (as shown in Equation 2.2), a Pile-Up rejection algorithm is applied in order to avoid distortion of the spectrum itself. $C_{trigger}$ compensates for the number of counts lost during the death time of the detector. Indeed, the live time depends on $C_{trigger}$ according to Equation 2.3:

$$Live\,time = Real\,time \times \frac{\sum_{ch} counts_{ch}}{C_{trigger}} \tag{2.3}$$

where $Real\,time$ is the actual time of the measurement and $counts_{ch}$ and $C_{trigger}$ are defined above.

Table 2.1: Parameters for flattening the energy response. LL and UL are the lower and upper limits of each energy interval, respectively, where the same weighting factor is applied; the corresponding weighting factors are listed in the third column.

LL (keV)	UL (keV)	w_{ch}
0	50	0.66
50	200	0.33
200	300	0.33
300	Inf.	1

Besides the three main buttons listed above, the main screen of the B-RAD also shows the instantaneous dose rate and count rate in counts per seconds (cps), and a battery status indicator. Figure 2.4 shows the five possible battery status indicators.

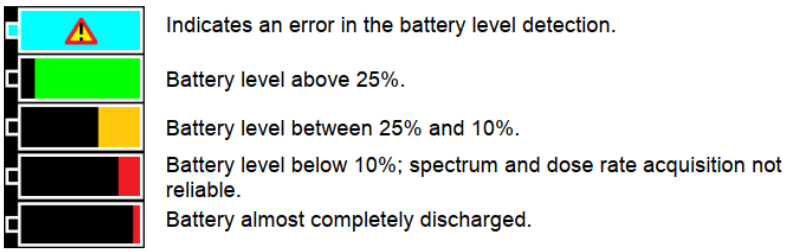

Figure 2.4: The battery status indicators used by the B-RAD.

2.2 Tests of the B-RAD

Once the commercial version of the B-RAD was available, several tests were performed in order to assess the performance of the device according to the required specifications (summarized below). The aim of these measurements was to check the detector's insensitivity to strong magnetic field and to characterise it in terms of dose rate linearity, energy range and angular response. Additionally, we measured the intrinsic radioactivity of the $LaBr_3$ crystal and we performed some operational tests to verify the B-RAD response in a real work environment.

The B-RAD was designed to comply with the following main requirements.

- Portable radiation survey meter for γ-ray dose rate measurements
- Insensitivity to magnetic field up to 1 T (the detectors tested before started to fail after few mT)
- Sensitivity range from 1 μSv/h up to few mSv/h
- Energy range between 60 keV and 1.3 MeV (suitable for accelerator facilities where the average γ-ray energy is 800 keV)

2.2.1 Tests of the B-RAD in a calibrated dipole up to 1.5 T

The measurements were carried out at the Magnetic Measurement Laboratory at CERN inside a calibrated dipole magnet up to 1.5 T [25]. The detector was tested increasing the magnetic field in 0.2 T steps, in three different operating conditions (Figure 2.5):

- The control unit inside the dipole and the probe and the cable outside
- The probe inside the dipole and the control unit and the cable outside
- The probe, the control unit and the cable inside the dipole (for simplicity this configuration is also indicated in this section as "detector" inside the dipole).

A Hall probe was placed inside the dipole to accurately measure the magnetic field. The Hall probe ranges from around 0.35 T to 1.38 T. Beyond these limits measurements with the B-RAD were not performed because the magnetic field inside the dipole cannot be monitored.

For each configuration we performed measurements with a ^{137}Cs source (151.44 kBq on 17/07/2015, about 36 μSv/h in contact) fixed on the probe (as shown in Figure 2.5 on the left). The *Spectrum Acquisition* option was selected in order to acquire the energy spectrum, the count rate and the dose rate. For all measurements we set a time window of 3 minutes.

The objectives of this test were:

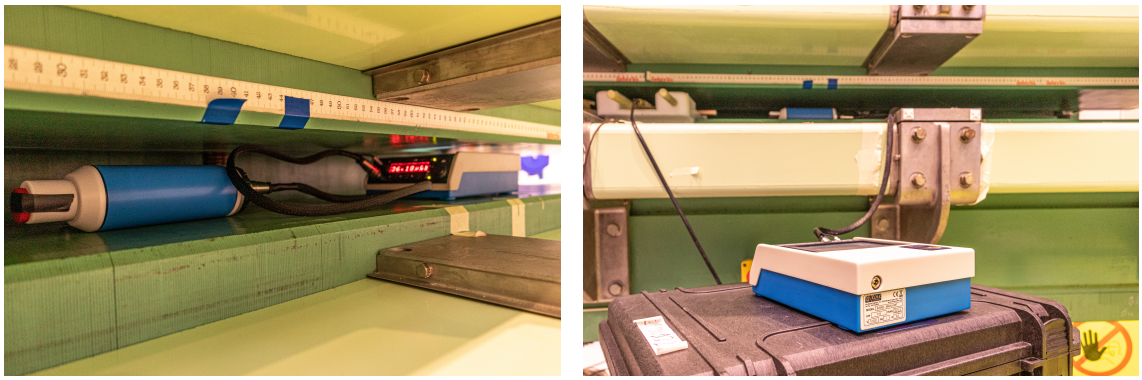

Figure 2.5: Two different working conditions of the B-RAD inside the dipole. On the left, both probe and control unit are inside the dipole magnet and on the right, the probe is inside the dipole while the control unit remains outside.

- To test the lifetime of the new battery
- To test the LED and LCD displays
- To check the mechanical force produced by the magnetic field on the different components of the B-RAD
- To check the effect of the magnetic field on the count rate
- To check the effect of the magnetic field on the spectrometric performance.

The battery was fully recharged before the measurements and lasted during all the measurement cycles (4 hours of operation). Both the LCD[(1)] and the LED[(2)] display worked properly. Starting from 0.4 T, we started to feel a pulling force on the control unit, which became very intense for the highest values of the magnetic field (above 1 T). This is due to the presence of metallic components inside the control unit, such as stainless steel screws and a Faraday cage which isolates the main electronic circuit from the electrostatic field. The mechanical force felt on the probe was always less intense than the one felt on the control unit, but still present for values of the magnetic field above 1 T and when the probe was moved inside the dipole. The mechanical force felt on the control unit above about 1 T was quite strong for a hand-held detector.

An acquisition of the background was performed for 30 minutes both with the detector outside the dipole and with the probe inside the dipole. The measured backgrounds were 92 nSv/h and 66 nSv/h respectively. This difference is expected because of the shielding effect of the magnet when the probe is inside. A measurement was performed at 0 T (i.e. switching the magnet off) for each operating conditions to set a reference. Afterwards, we performed the measurements at different values of the magnetic field and in the different configurations, as explained above.

Figure 2.6 shows the resulting spectra acquired for the three configurations and for the different values of the magnetic field. Figure 2.6 shows that the response of the detector is affected by the magnetic field only when the control unit is inside it. In particular a reduction of the gain of the signal is observed while the magnetic field is increased, with the consequent compression of the energy spectrum and the shift of the ^{137}Cs photoelectric peak toward low energy channels. The variation of the 32 keV peak position is negligble because the gain variation is proportional to the signal amplitude, i.e. to the deposited energy.

[(1)] Liquid Crystal Display
[(2)] Light Emitting Diode

Figure 2.7 shows the position of the ^{137}Cs peak (662 keV) (in terms of channel number) and the corresponding energy resolution (FWHM). The channel and FWHM values correspond to the mean and FWHM values of the Gaussian equation fitting the ^{137}Cs peak of each spectrum. In order to evaluate the uncertainties of each data point, a series of 60 measurements was performed acquiring the spectrum of the same ^{137}Cs source, placed in the same position in respect of the detector and for the same acquisition time (3 minutes). The peak position and the FWHM values of each spectrum were evaluated as described above. A standard deviation of 0.07% and 0.37% of the averaged value were obtained for the peak position and the peak energy resolution, respectively. These uncertainties were applied to the results shown in Figure 2.7. Figure 2.7 shows that the maximum variation of the peak position as compared with the reference value (i.e. at 0 T) is around 6% when only the control unit is inside the dipole at 1.5 T. This effect is negligible when only the probe is inside the dipole. The origin of this particular effect is attributed to an inductance present on the delay line (a 1515-series device from Data Delay Devices [26]. It is a passive delay line designed to shift the input signal by a specific increment of time (100 ns) operating as a special purpose low-pass filter. The energy resolution is not affected by the magnetic field for all the configurations.

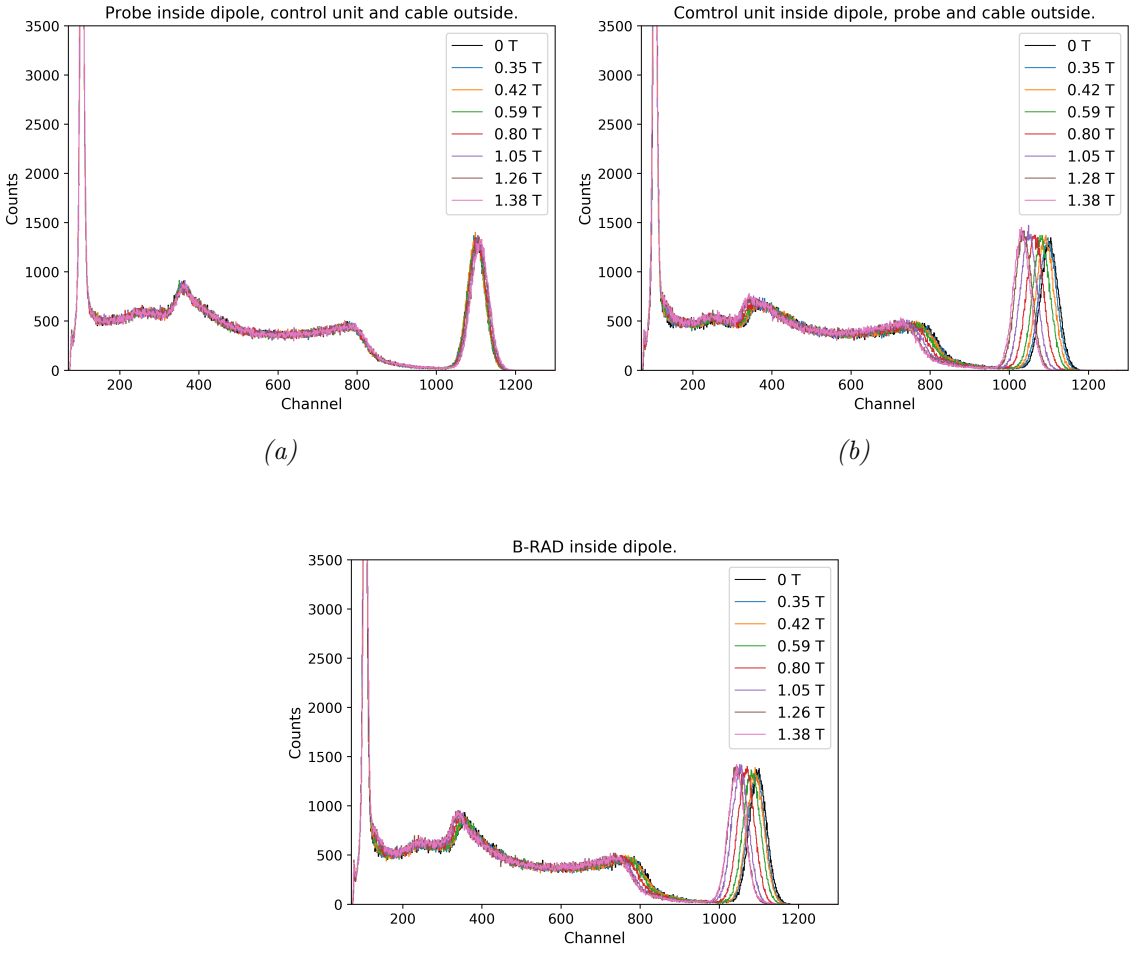

Figure 2.6: The ^{137}Cs spectra acquired with the B-RAD at different values of the magnetic fields and for different configurations: (a) with only the probe, (b) only the control unit and (c) the entire B-RAD inside the dipole.

Figure 2.8 left plot shows the measured count rate (counts per second, cps) for the

three configurations by varying the magnetic field and the reference count rates at 0 T. Figure 2.8 right plot shows the corresponding dose rate values. The statistical uncertainties were calculated. For the dose rate, the statistical uncertainties were obtained by applying the error propagation rules to Equation 2.2, considering the weighting factors, the energy of each channel and the calibration factor as constants. For each configuration the response of the detector in terms of count rate is uniform with the magnetic field. However, the measured cps with only the control unit inside (red data points) is around 5% lower as compared with the blue and black configurations (the probe and the unit + probe inside the dipole). This result is independent of the magnetic field, since the count rate measured with only the control unit inside the dipole is consistent with the reference count rate measured in the same configuration. This reduction is most likely due to the increasing of the backscattered component when the probe is inside the dipole. This hypothesis is currently being investigated by FLUKA Monte Carlo simulations[3]. As shown in Figure 2.5, because of the small air gap between the two poles of the dipole (8 cm), the probe is unavoidably close to the walls of the dipole.

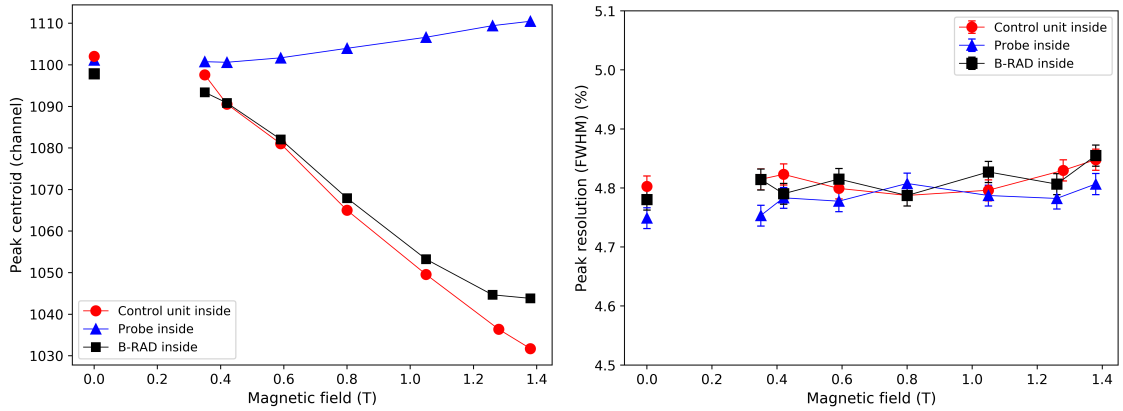

Figure 2.7: Position (left plot) and resolution (right plot) of the ^{137}Cs peak measured with the B-RAD for three different working conditions at different values of the magnetic field and without the magnetic field. Error bars not shown are smaller than the data points.

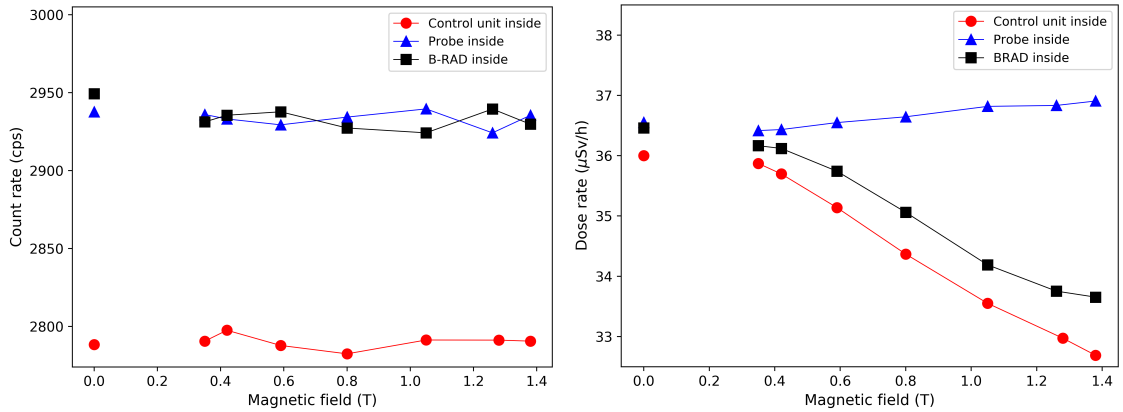

Figure 2.8: Count rate (left plot) and dose rate (right plot) measured with the ^{137}Cs source for three different working conditions at different values of the magnetic field and without the magnetic field. Error bars are smaller than the data points.

While the count rate can be assumed independent of the magnetic field, Figure 2.8

[3]The results were not yet available at the time of submitting the thesis.

right plot shows that the corresponding dose rate varies similar to the variation of the position of the ^{137}Cs peak. This variation comes from the algorithm used by the software to calculate the dose rate (Equation 2.2), which weights the detected counts over the energy spectrum. However, the variation is almost negligible below around 0.5 T and it is less than 10% at 1.5 T. From the operational point of view, this variation is acceptable for radiation protection purposes. Otherwise a software compensating algorithm might be introduced by the company. In this case a Hall probe, able to accurately measure the magnetic field, must be implemented on the device.

A further test was performed to check whether moving the probe during the measurement inside the dipole affects the count rate or the spectrometric performance. The same test was repeated with the control unit. The measurements were performed at three different values of the magnetic field: 0.35 T (the minimum measurable field), at 0.8 T and at 1.38 T (the maximum measurable field). The spectra and the dose rate measured in dynamic conditions both with the probe and with the control unit were always consistent with the spectra and the dose rate measured for the same configuration and the same magnetic field in static condition. It can be asserted that the movement of the detector inside the magnetic field does not affect the result of the measurement.

A final test was performed to check if a dependence on the B-RAD response with the magnetic field exists because of the cable. Both the probe and the cable were placed inside the dipole, whereas the control unit was kept outside, where the stray field was about 30% of the field inside (Figure 2.9). The variation of the dose rate measured with the cable inside and outside was negligible. A slightly variation on the position of the main peak was observed which is attributed to the magnetic field present on the control unit. This test confirms that the only component of the B-RAD affected by the magnetic field is the control unit. This effect is under investigation by the company in order to be solved in the future versions of the detector, e.g. via a software compensation algorithm.

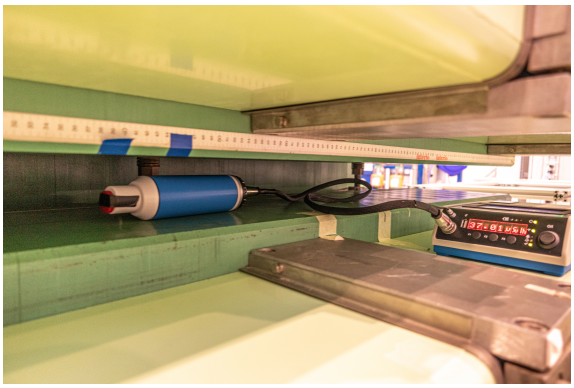

Figure 2.9: The B-RAD measuring the ^{137}Cs source with the probe and the cable inside the dipole and the control unit outside.

2.2.2 Test of the B-RAD at ISOLDE facility inside a magnetic field up to 2.5 T

The on-line isotope mass separator ISOLDE (Isotope Separator On Line DEvice) [27] is a facility dedicated to the production of a large variety of radioactive ion beams (over 1,300 isotopes of more than 70 elements) for many different experiments. The facility is located at the Proton-Synchrotron Booster (PSB) at CERN since 1992.

Measurements were performed inside the ISOLDE Solenoidal Spectrometer (ISS) [28]. The ISS is a fixed experimental set-up of the HIE-ISOLDE (High Energy and Intensity) project, an upgrade that aims to increase the facility's energy and intensity. Figure 2.10

shows a 3D view of HIE-ISOLDE linac and of the three experimental stations (Miniball, ISS and Scattering Chamber). The ISS has been developed for precision studies of inelastic scattering and transfer reactions induced by radioactive ion beams from the HIE-ISOLDE. It consists of the 4T former-MRI solenoid, a silicon sensor array and the SpecMAT, a project for placing an active gas target inside the solenoid. During normal operation a thin plastic foil target containing hydrogen nuclei is placed close to the centre of the solenoid and bombarded by accelerated radioactive nuclei from HIE-ISOLDE. The emitted reaction products are bent by the magnetic field until they reach the position-sensitive silicon detector and their energy is measured.

The measurements with the B-RAD were performed inside the solenoid in August 2019 during the preparation for a new ISS detector's installation. The solenoid used for this project is an OR66 ex-MRI (Figure 2.11) magnet that was previously used for medical imaging research at the University of Queensland's Centre for Advanced Imaging in Brisbane, Australia. Its purchase was jointly funded by the STFC and the University of Liverpool and it was transported to CERN in early 2016. Figure 2.12 shows the ISS field strength at 2.47 T on the solenoid axis ($r < 20$ mm) along the beam direction; $z = 0$ mm on the horizontal axis corresponds to the middle of the solenoid. The magnetic field slightly deviates around $z = \pm 700$ mm according to the values of the radius (always below 20 mm) as shown on the same plot. Inside the whole solenoid ($r < 300$ mm from the axis) the field is still very homogenous.

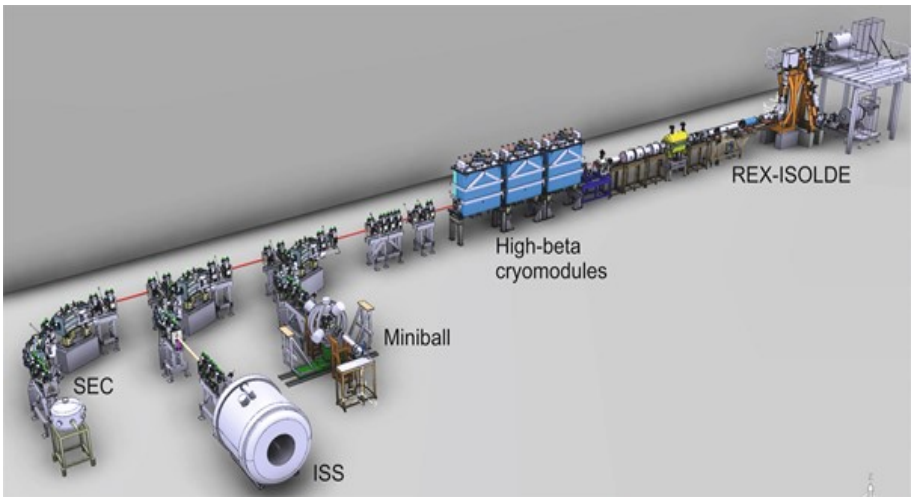

Figure 2.10: 3D view of the HIE-ISOLDE linac and of the three experimental stations (Miniball, ISS and Scattering Chamber).

The measurements were carried out in three steps:

(1) Ramping-up the current of the solenoid and the consequent induced magnetic field. The current was ramped up from 0 to 269.4 A (corresponding to 2.5 T) at a rate of 2 A/min, which means that the magnetic field takes around 2-2.5 hours to reach its maximum value. It was not possible to stop the ramping at intermediate values

(2) At constant field, the magnetic field was kept constant at its maximum value (2.5 T)

(3) Ramping-down the current; the ramping-down occurs with the same procedures and rate of the ramping up

Measurements were performed simulating two different working conditions of the B-RAD: the probe inside the field and the control unit outside (during the ramping-up and at 2.5 T field) and the entire B-RAD inside the solenoid (during the ramping-down). Because of a

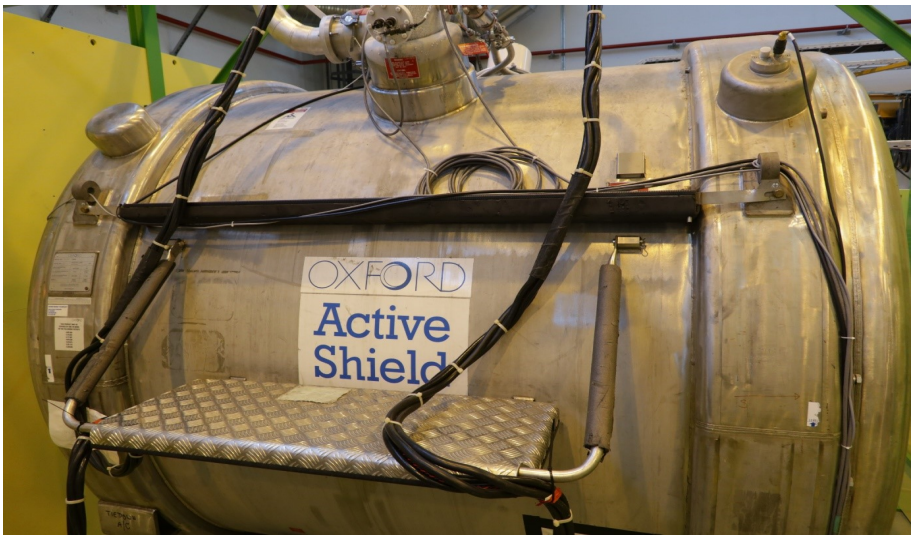

Figure 2.11: The solenoid of the ISOLDE Solenoidal Spectrometer (ISS).

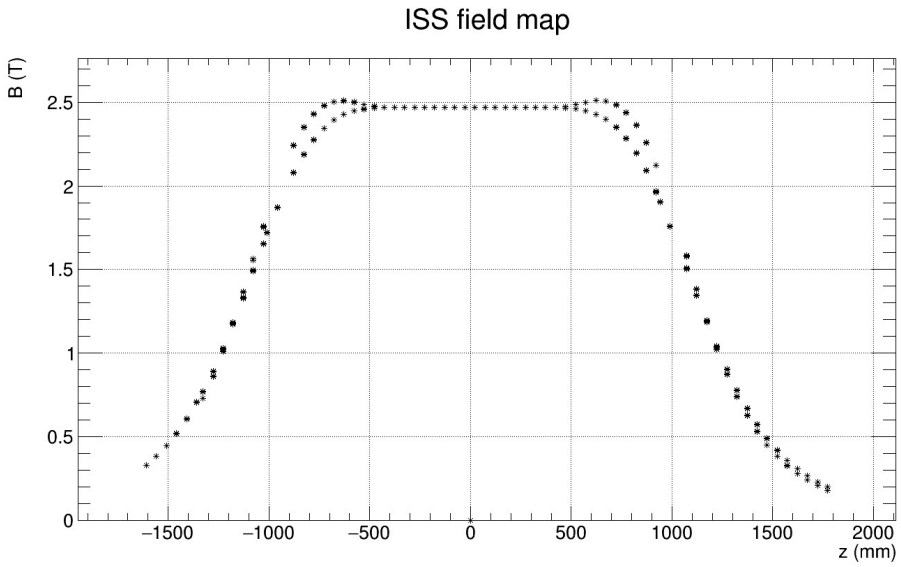

Figure 2.12: Plot of the ISS field strength on the solenoid centre axis and for r equal to 20 mm along the beam direction [29].

restriction to do multiple ramps due to the liquid He consumption, it was not possible to perform measurements with the control unit inside and the probe outside. Ramping the solenoid up and down consumes about 5% of the liquid He volume at once and the liquid He content should be at least 40% of the maximum filling level to allow safe operation [29].

The B-RAD was fixed with cable ties to a tripod which made possible to place the detector not further than 50 cm away from the middle of the solenoid, in the beam direction, where the magnetic field is still uniform (see Figure 2.12). Figure 2.13 shows the B-RAD fixed on the tripod in the first configuration, the control unit outside (on the left) and the probe inside (on the right).

A ^{137}Cs γ source ($\sim$ 36 μSv/h at contact) was fixed to the probe; before ramping-up the magnetic field, the B-RAD was set in order to measure both the dose rate and the spectrum in time intervals of one minute continuously and automatically during all the ramping-up. A time window of one minute guarantees a good statistics (high number

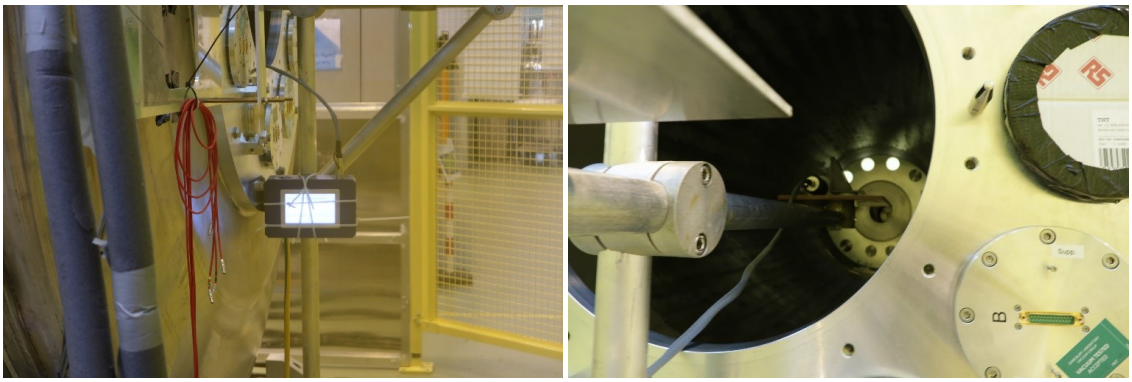

Figure 2.13: The experimental setup with the control unit outside the magnet (on the left) and the probe inside (on the right).

of counts) and it is short enough to consider the magnetic field constant. The same setup was used during the ramping down. Figure 2.14 shows the measured dose rate from 0 to 2.5 T at step of 0.1 T for the two configurations, the horizontal line is the dose rate measured outside the magnetic field. When only the probe was inside the solenoid, the response of the detector was always uniform for all values of the magnetic field, with deviation between the reference and the measured values of around 3%. When the whole B-RAD was inside, the count rates slightly decreased between 0.1 T and 0.5 T, afterward it stabilised around a value 15% lower than the reference value. The reason of this decreasing is associated to the dependence of the dose rate with the energy spectrum and the variation of the latter when the control unit is inside a magnetic field (as explained in Section 2.2.1 for the measurements in the dipole and below for these measurements). However, a direct comparison with the measurements performed in the dipole cannot be performed because of two main reasons: 1) the measurements in ISOLDE were performed with the previous version of the B-RAD which implemented a different algorithm for the dose rate calculation, 2) the position of the B-RAD (of the control unit in particular) in respect of the magnetic field lines was different. Figure 2.15 shows the spectra acquired at three different values of the magnetic field for the two configurations.

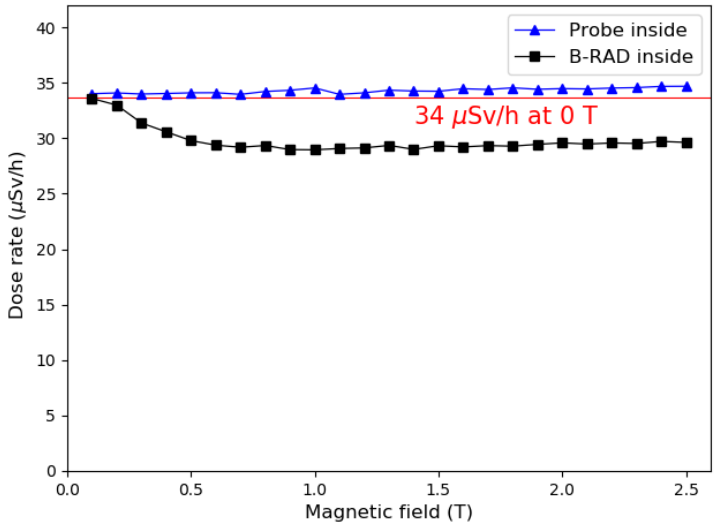

Figure 2.14: Dose rate measured with the B-RAD for two different working conditions: only the probe inside (in blue) and the entire detector inside the solenoid (in black). The horizontal line shows the reference dose rate value measured outside the magnetic field.

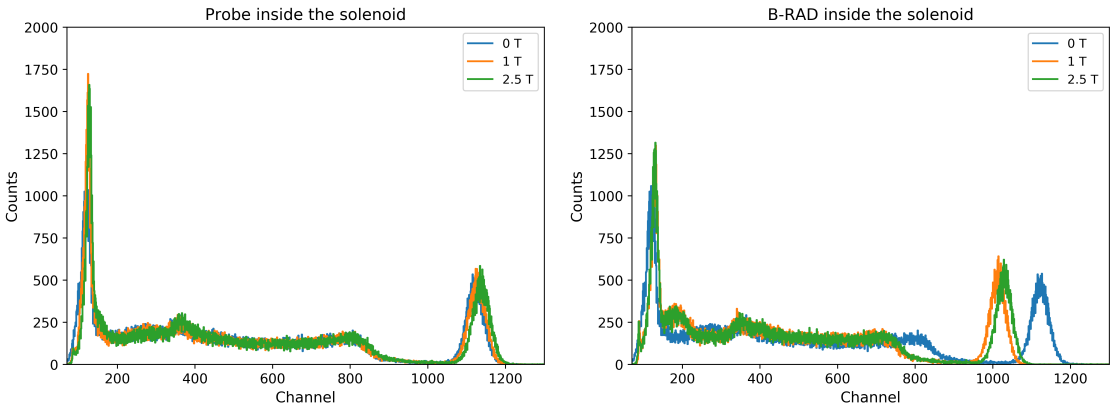

Figure 2.15: The ^{137}Cs spectra acquired with the B-RAD with only the probe inside the magnetic field (left plot) and with the whole B-RAD inside (right plot) for three different values of the magnetic field.

As mentioned above and as expected by the previous measurements (Section 2.2.1), the spectrum shifts towards lower energy values when the control unit is inside the magnetic field. In that case no effect was visible when only the probe was inside. However, Figure 2.15 shows a slight shift also in the latter configuration, which is probably due to the fact that we were not able to place the control unit far from the solenoid when the probe was inside (because of the limited length of the cable and the necessity to place the probe as close as possible to the middle of the solenoid), so that the control unit was exposed to the stray magnetic field.

A Hall sensor is integrated into the B-RAD probe inside the printed circuit board (PCB) placed in the active probe to measure and provide the user with the intensity of the magnetic field. This probe is made of a single coil and therefore measures correctly only when the B-field is perpendicular to the coil plane. During the measurements described in Section 2.2.1 we were not able to calibrate the Hall sensor, since the B-RAD probe can only be placed in the dipole gap as shown in Figure 2.5 left, and in this configuration the Hall probe is parallel to the B-field lines. During the measurements performed in ISOLDE instead, the probe was placed perpendicularly respect to the magnetic field lines and its calibration was feasible.

The non-calibrated value measured by the Hall probe was read on the screen of the B-RAD each five minutes during all the measurement cycle (both during the ramping-up and the ramping-down). In Figure 2.16 the arbitrary value measured by the Hall probe is plotted against the magnetic field. The response of the probe is very linear up to 1 T, above which the value read on the screen was always around 210. This saturation effect was checked both during the ramping-up and the ramping-down.

During these tests, the B-RAD and its main components (the battery and the two displays) worked properly inside the magnetic field. The count rate measured up to 2.5 T deviated from the reference value (measured at 0 T) by less than 15%. The control unit was slightly affected by the magnetic field since the acquired spectrum slightly shifted toward lower energy values (proportionally to the magnetic field intensity) when it was placed inside the field. This can probably due to the effect of the field on the electronic components. The measurements showed that the radio-isotope identification algorithm may fail because of this effect, however it did not affect the measured dose rate.

The B-RAD is also equipped with a Hall probe to indicate the value of the magnetic field in which the B-RAD is operating. The Hall probe was calibrated with the magnetic field intensity, however it saturated at around 1 T. This saturation effect can be accepted taking into account that it is reached at quite intense magnetic fields. Beyond this value

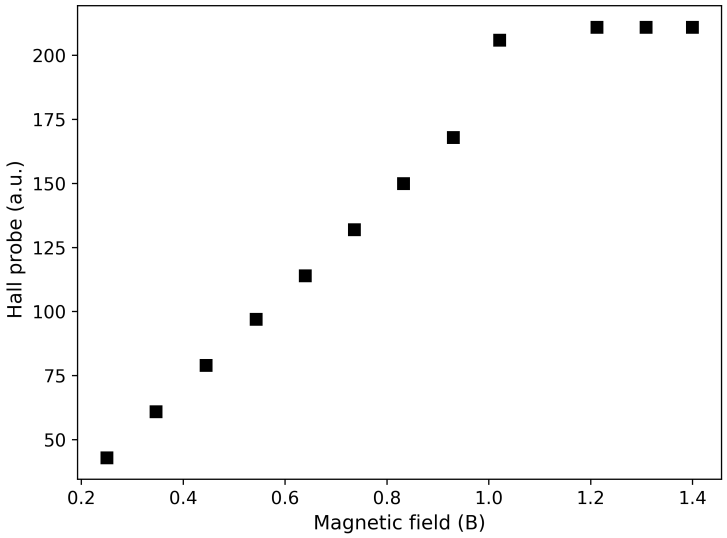

Figure 2.16: Plot of the magnetic field measured by the Hall probe (in arbitrary units) as a function of the actual value of the magnetic field from 0.25 to 1.5 T.

it can be sufficient to just inform the operator that the magnetic field intensity is higher than 1 T. This specific Hall probe is made of a single coil so that its reading strongly depends on its position with respect to the field lines. As a future objective the probe should be replaced by a tri-coil one able to measure the magnetic field irrespective of its orientation and a new calibration should be performed in this case.

2.2.3 Measurements at the CERN RP Calibration Laboratory

The B-RAD was tested at the RP Calibration Laboratory [30, 31] in order to check the linearity of its response as a function of dose rate, the dose rate working range and to check the calibration factor set in the B-RAD by the company.

The measurements were performed using a ^{137}Cs source. The activity and the distance of the source were varied in order to obtain different reference dose rate values in the range between 450 nSv/h (the lowest achievable dose rate at the Calibration Laboratory) and 10 mSv/h. The *Dose Measurement Cycles* mode was selected by setting 16 measurements of 30 seconds for each irradiation position. Because the B-RAD cannot be remotely controlled, we needed to start the acquisition before the source was moved to its exposure position. For each position, measurements made before the source was in its exposure position were discarded. For measurements below 10 μSv/h, the background was acquired at the same irradiation position as the measurements, and properly subtracted to the measured dose rate. Above 10 μSv/h the background was negligible.

Figure 2.17 shows the response of the B-RAD (in terms of dose rate) as a function of the reference dose rate and the results of the linear fitting performed on the acquired data. Table 2.2 reports the irradiation settings of each measurement and the corresponding dose rate measured by the B-RAD. It also compares the reference and the measured dose rate.

The response is very linear from 1 μSv/h to 2 mSv/h. An overestimation of the dose rate is observed below 1 μSv/h, where a major uncertainty of the reference dose rate should also be considered. For higher dose rates the detector starts to deviate from the linearity as shown in Table 2.2 and saturation effects arise. An excellent match between the reference and the measured dose rate is observed between around 1 μSv/h and 400 μSv/h (difference less than 5%). In the 800 nSv/h - 1 mSv/h range, the percentage difference is within the acceptable uncertainty in radiation protection applications (around 10%

of variation). Beyond this range, the variation is not negligible but still acceptable in radiation protection (around 20%).

As shown in Table 2.2 the B-RAD, also in the linear range, slightly underestimates the reference dose rate. This might be due to a non perfect evaluation of the calibration coefficient set in the B-RAD software. However, the latter can be modified in the future after a proper calibration of the device.

For a complete analysis, the response of the detector to different energy γ-ray sources should be measured in the future. Because sources different from ^{137}Cs are not available at the CERN Calibration Laboratory, we did not perform this analysis.

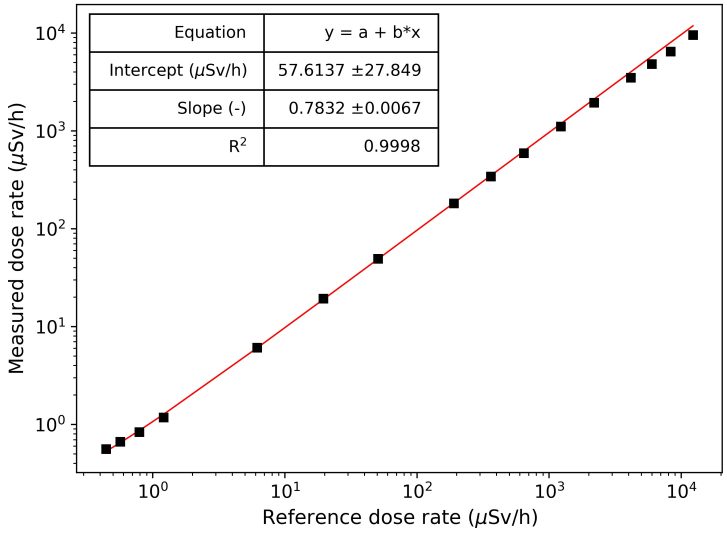

Figure 2.17: Response of the commercial version of the B-RAD as a function of dose rate; the error bars are smaller than the data points. The red line represents the linear fit; the fit parameters are shown in the plot.

Table 2.2: Irradiation settings at the RP Calibration Laboratory and results.

Activity	Distance (cm)	Reference dose rate (μSv/h)	Measured dose rate (μSv/h)	(Reference - Measured)/ Reference dose rate
300 MBq	580	0.44	0.56	-27%
300 MBq	540	0.57	0.67	-18%
300 MBq	480	0.79	0.83	-6%
300 MBq	400	1.2	1.18	2%
300 MBq	180	6.1	6.12	0.4%
300 MBq	100	19.54	19.37	0.8%
3 GBq	200	50.70	49.39	3%
30 GBq	330	189.84	182.01	4%
30 GBq	240	361.78	342.40	5%
30 GBq	180	642.96	594.56	8%
30 GBq	230	1227.6	1131.17	9%
300 GBq	330	2184.0	1948.92	11%
300 GBq	240	4153.2	3498.43	16%
300 GBq	200	5988.0	4840.07	19%
300 GBq	170	8299.2	6471.50	22%
300 GBq	140	12264.0	9568.29	22%

2.2.4 Test of the energy range and energy resolution of the B-RAD

The energy spectra of three different γ-ray sources (^{137}Am, ^{137}Cs, ^{60}Co) were acquired in order to check the energy range and the energy resolution (FWHM) of the B-RAD, as shown in Figure 2.18. The energy range of the B-RAD, initially set from 60 keV, was later extended down to 30 keV. Indeed, the 33 keV X-ray following the ^{137}Cs decay was clearly detected. As reported in Figure 2.18 the energy resolution is less than 5% at 662 keV.

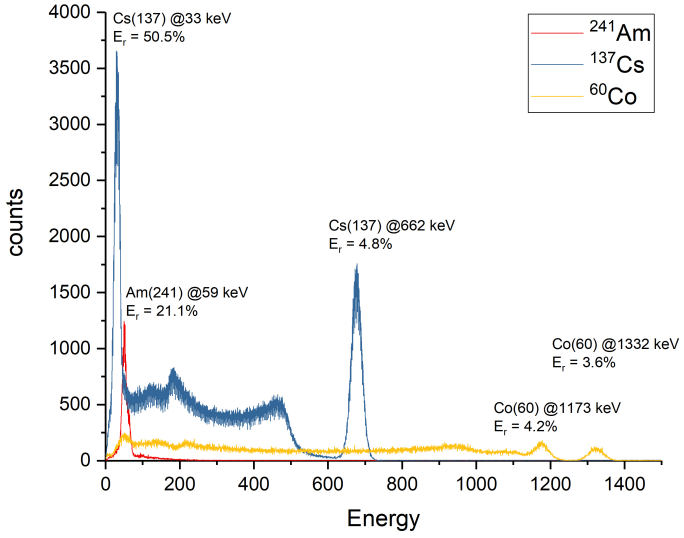

Figure 2.18: The energy calibrated spectra of three different γ-ray sources acquired with the B-RAD and the corresponding energy resolution.

2.2.5 The angular response

The focus of these measurements was to evaluate the angular response of the B-RAD. Measurements were performed at twelve different angles between the crystal and a ^{137}Cs source: 0°, -30°, -60°, - 90°, - 120°, - 150°, +30°, +60°, +90°, +120°, +150°, +180°, where 0° corresponds to the probe axis parallel to the source field lines. The probe was placed on a rotating table software-controlled and rotated in respect of the source direction. The signs + and - correspond to clockwise and anti-clockwise rotations, respectively. The source-to-detector distance was kept constant at 250 cm and the detector exposed to a 3 GBq source (32 μSv/h).

The measurements were carried out using the *Dose Measurement Cycles* mode following the same experimental procedure described in Section 2.2.3. The results are reported in Table 2.3 and shown in Figure 2.19. A 5% uncertainty must be considered to take into account both the statistical and the experimental uncertainties, the latter mainly associated with the positioning of the detector. The response of the B-RAD is very symmetric in respect of its axis (0°) and the measured dose rate is almost uniform in the -120°–+120° angular range, with a total variation between the minimum and maximum dose rate of around 3%. However, beyond this range the response of the B-RAD clearly drops by 66% when the probe is at 180°. This variation is most probably due to the scattering of γ-rays on the probe itself. Besides the crystal, the probe consists of a cylindrical casing and a handle which may interfere with the measurement.

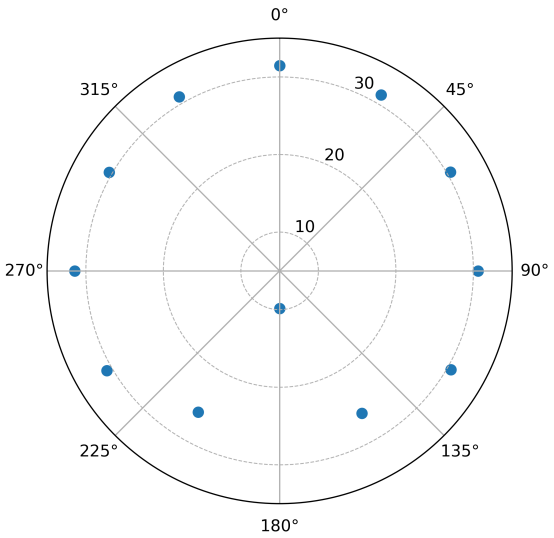

Figure 2.19: Polar plot of the dose rate measured by the B-RAD as a function of the angle between the source and the detector. The dose rate is represented on the radius of the plot, in (μSv/h).

Table 2.3: Results (dose rate) of the instrument response at different angles of the detector from the source direction.

Angle	Dose rate (μSv/h)
0°	31.46
-30°	30.91
+30°	31.19
-60°	30.40
+60	30.46
-90°	31.42
+90°	30.60
-120°	30.75
+120°	30.50
-150°	26.02
+150°	26.21
+180°	9.84

2.2.6 The $LaBr_3$ internal radioactivity

The intrinsic radioactivity of the $LaBr_3$ crystal is well known and deeply studied [32, 33, 34]. The new software version installed in the detector provides the possibility to enable/disable the subtraction of the $LaBr_3$ intrinsic spectrum from a measurement. To activate this option, the $LaBr_3$ intrinsic spectrum was measured and saved in the setting of the B-RAD.

The internal radioactivity of the $LaBr_3$ scintillator comes from the presence of the ^{138}La isotope ($T_{1/2} = 1.5\times10^{11}$ years) in the crystal. Figure 2.20 shows the ^{138}La decay chain. The most probable decay is the electron capture (EC) to the first excited level of ^{138}Ba followed by the emission of a 1435.8 keV γ-ray and by the emission of the 32 keV X-ray of ^{138}Ba. The second decay channel is the β^-–decay to the excited state of the ^{138}Ce and the consequent emission of a 788.7 keV γ-ray.

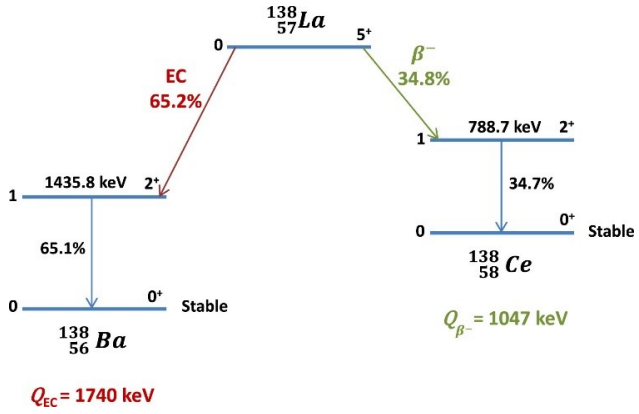

Figure 2.20: Decay scheme of ^{138}La [34].

In order to measure the intrinsic radioactivity of the crystal, the B-RAD was placed inside a lead shielded chamber as shown in Figure 2.21. The dose rate inside the shield was measured with an Automess 6150AD6 [35] detector equipped with a 6150 ADb [36] probe (AD6+ADb). The detector was placed inside the chamber with a camera pointing on the display to record the data and the dose rate was measured for 10 minutes. Fig-

ure 2.22 shows the dose rate recorded every 2 seconds. The average measured dose rate was 20 nSv/h.

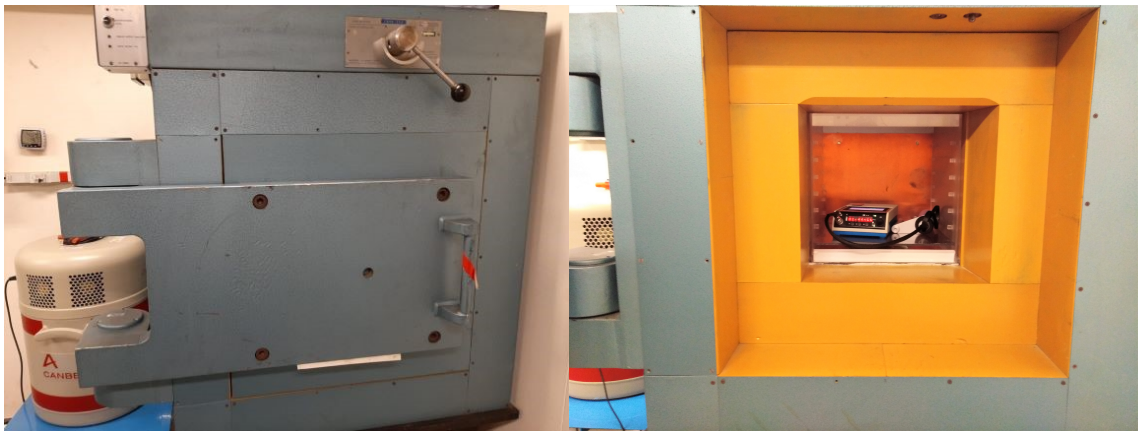

Figure 2.21: The shielded chamber on the left and the B-RAD inside it on the right.

A measurement of 6 hours was performed with the B-RAD. Because of the battery consumption it was not possible to perform a longer measurement (the battery lifetime is 8-10 hours). Figure 2.23 shows the measured energy spectrum, calibrated according to the equation saved in the B-RAD software (Equation 2.1). The peak at around 1450 keV is due to the 1435.8 keV γ-ray of ^{138}Ba in coincidence with the 32 keV X-ray (when the X-ray is detected) following the ^{138}La electron capture; the broad spectrum between 750 keV and 1000 keV comes from the β^- decay of ^{138}La (789 keV of the γ-ray plus the energy of the $\beta-$ particle). The portion of the spectrum below 750 keV is γ-ray background from the^{238}U and the ^{232}Th decay chain. Above 2000 keV the $LaBr_3$ spectrum exhibits the α-peaks of the ^{277}Ac decay chain, due to the ^{277}Ac contamination which is unavoidable because of the similar chemical composition of Ac with La [33, 37]. The measured dose rate was 57 nSv/h. Taking into account the background measured in the shielded chamber, the dose rate due to the intrinsic radioactivity of the $LaBr_3$ is about 37 nSv/h.

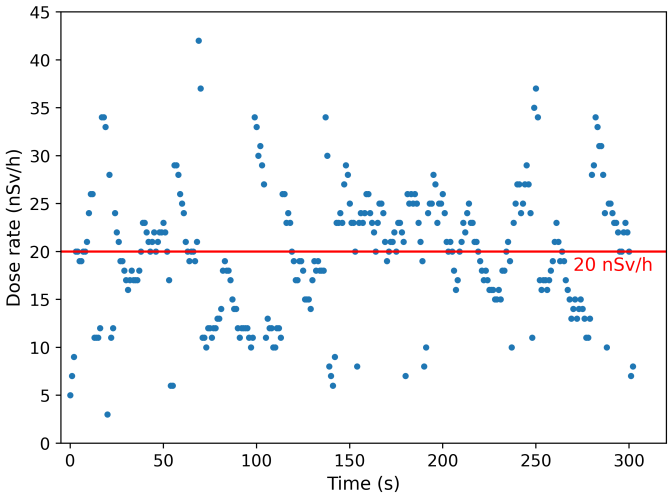

Figure 2.22: The instantaneous dose rate measured by the Automess AD6+AD-b detector inside the shield every 2 seconds; the red line is the average value.

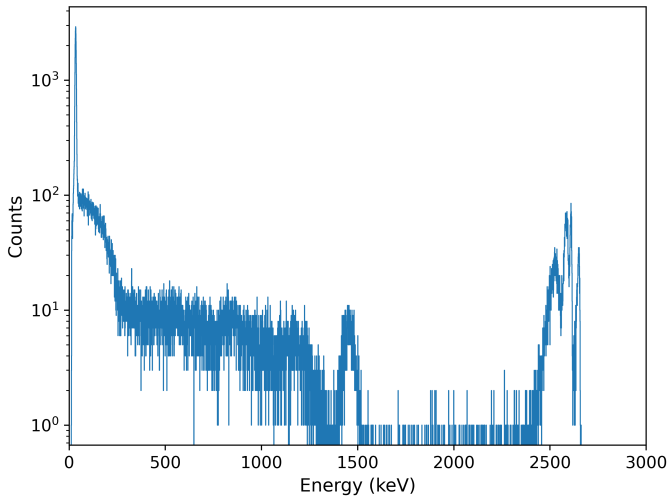

Figure 2.23: The energy calibrated spectrum of the $LaBr_3$ crystal acquired inside a shielded chamber.

2.2.7 Operational tests

The RP Radioactive Waste (RW) section requested the use of the B-RAD to measure the residual radioactivity of more than 500 permanent magnets mounted on ion pumps from the former Large Electron-Positron (LEP) collider [38, 39, 40], currently stored at CERN in view of their radiological clearance and elimination [41]. Because of the residual magnetic field the other commonly used detectors failed. This request pushed us to test the operational performance of the B-RAD. We used the B-RAD to measure the residual radioactivity of twenty of these magnets (Section 2.2.7.1). Moreover, we evaluated the potential reactivity of the B-RAD to detect a radioactive source, placed at an unknown location within a controlled configuration at the RP- Special Project (SP) laboratory (Section 2.2.7.2). Finally, we checked the stability of the B-RAD response, monitoring the measured dose rate and the energy calibration over a period of one month (Section 2.2.7.3).

2.2.7.1 Measurement of the residual radioactivity of the permanent magnets

The twenty selected magnets were placed on the floor at more than one meter apart from each other (Figure 2.24). Before starting the measurements, the background was measured for 20 minutes; the resulting value was 92 nSv/h. Thereafter each magnet was measured at four different points (two on the top and two on the bottom) and a further measurement was performed by scanning the inner part of each magnet, as shown in Figure 2.25. All measurements were performed at contact. Fifty percent of the measured magnets are thus classified as slightly radioactive (TFA, *très faiblement radioactif* in French) as the measured dose rate was 30 nSv/h above the background level. The other magnets were classified as non radioactive. The B-RAD is under consideration for routine use for the free-release of about 500 permanent magnets stored in ISR7.

2.2.7.2 Assessment of the B-RAD capability to detect a radioactive source

Two different tests were performed to better understand the responsiveness of the B-RAD in actual working conditions [42]. These tests did not follow rigorous procedures since they were aimed at providing qualitative information about the performances of the detector.

(1) A ^{137}Cs source (151.44 kBq on 17/7/2015) was hidden in 20 m^2 room (Figure 2.26, classified as controlled area, and the time employed with the B-RAD to find it was

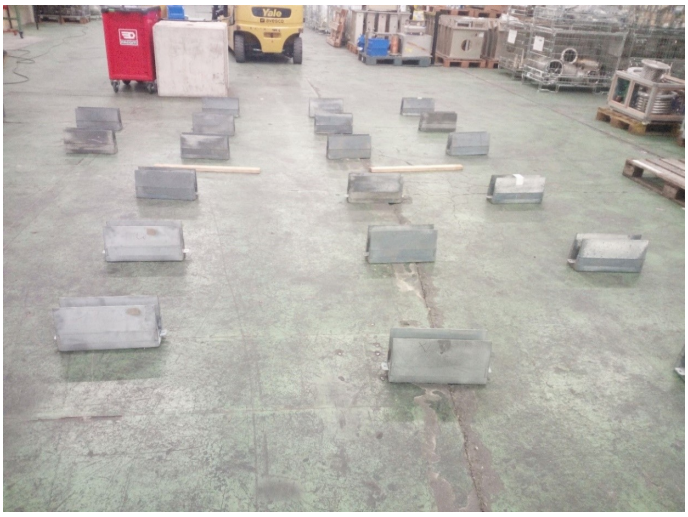

Figure 2.24: The twenty permanent magnets measured with the B-RAD at ISR7.

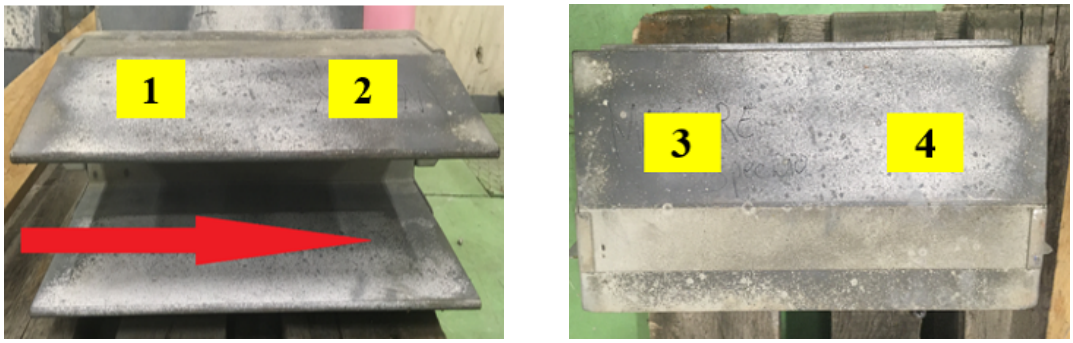

Figure 2.25: Top (on the left) and bottom (on the right) view of a magnet; the four measurement points and the scan direction are specified.

determined

(2) The same ^{137}Cs source was placed on a table and the B-RAD was hand-held, the operator walking nearby the source (see trajectory in Figure 2.27) at different speeds in order to find the maximum speed at which the source is detected

The first test was performed two times; in both cases, when the B-RAD was getting close to the source the measured dose rate was around four times the background level and despite the large surface of the room compared to the size of the source and the amount of material stored, the operator managed to localize the source in less than 10 minutes. The second test was performed approaching the source until a distance of around 30 cm (150 nSv/h at 30 cm). The maximum speed at which the source could be detected was around 2 m/s; while walking faster no relevant variations from background were visualized on the display. On the other hand, when the probe got very close to the source (almost in contact), the B-RAD always detected it.

The detector generally showed a good reactivity in presence of a radioactive source (^{137}Cs with an activity of 151.44 kBq) at around 30 cm distance, the visualized dose rate rapidly increased above the background level, however it did not reach a constant value because the dose rate is calculated every second and the value displayed is continuously updated. According to the specific application, the operator can select a longer acquisition time to get a more accurate value of the dose rate.

Figure 2.26: RP-SP laboratory in building 24 where the ^{137}Cs source was hidden for the localisation test with the B-RAD.

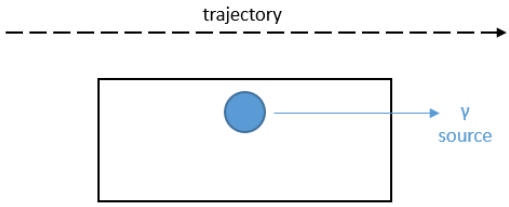

Figure 2.27: Position of the γ-ray source with respect to the B-RAD during the test 2: the source was placed on a table while the B-RAD was moved along the shown trajectory.

2.2.7.3 Test of the stability of the B-RAD's response and energy calibration

In order to check the stability in time of the latest version of the B-RAD, ten measurements were performed over one month under exactly the same conditions and at the same time testing the energy calibration stability. The measurements were performed with three γ-ray sources, placing them (in turn) in contact with the probe in the same position, as shown in Figure 2.28 (the sources have the same geometry). The employed sources are: ^{137}Cs (151.44 kBq on 17/7/2015), ^{60}Co (39.51 kBq on 25/01/2017) and ^{241}Am (39.52 kBq on 17/7/2015).

Measurements were performed in the RP-SP laboratory following the procedure described below:

(1) Battery of the B-RAD completely charged

(2) Acquisition of the background for 1 hour with the $LaBr_3$ subtraction option enabled

(3) Measurement with the source without background subtraction (no automatic subtraction of the background via the software was performed)

(4) Calculation of the net dose rate for each source. The net dose rate was calculated as the difference between the dose rate with the source and the dose rate of

the background (the subtraction of the LaBr3 intrinsic spectrum is included in the background)

(5) Evaluation of the position and of the FWHM of each photopeak. The peak position and the FWHM were automatically calculated by the B-RAD software and accessed through the *Peak Search* option

All the measurements were performed with the *Spectrum Acquisition* option. Table 2.4 summarises the results. The empty fields in Table 2.4 refer to measurements affected by experimental error and therefore discarded from the analysis: changing the source surface in contact with the probe, the dose rate differs by around 30% for ^{137}Cs and by around 90% for ^{241}Am. This effect is not present with the ^{60}Co source, probably because of different reasons, e.g. the much higher energy of the γ-rays, the thickness of the source shielding or the shielding that surrounds the crystal.

Figure 2.28: Measurement of a ^{137}Cs source's contact dose rate with the B-RAD. The source is placed in contact with the probe (red circle).

From data in Table 2.4, the averaged dose rates and their absolute uncertainties were calculated. The measured dose rate is 31.38 $\pm$ 0.07 μSv/h for the ^{137}Cs source, 30.99 $\pm$ 0.09 μSv/h for the ^{60}Co source and 1.34 $\pm$ 0.04 μSv/h for the ^{241}Am. The positions of the ^{137}Cs and ^{60}Co photopeaks are almost constant during the measurement period; a variation 0.6% and 0.3% for ^{137}Cs and ^{60}Co (both peaks) was revealed. A major variation of 20% was observed with ^{241}Am, probably due to the lower count rate and statistics in terms of γ-rays emitted by the crystal because of the lower energy of the source (close to the noise).

We can conclude that the response of the B-RAD in terms of dose rate is quite stable. For the same setup, a variation of around 1% was calculated when the B-RAD measures quite high dose rates (30 μSv/h) while the variation was around 9% for much lower values (close to the background). The energy calibration was checked by monitoring the position of the photopeak for different γ-ray sources; no relevant variations were detected except for a low activity and low energy ^{241}Am source.

2.3 Conclusions

Several tests were performed on the industrialized version of the B-RAD with the aim to characterise the device and to check whether it satisfies the initial specifications. These

tests were also useful to provide the company with feedbacks which led to the improvement of the detector. The B-RAD properly works up to 2.5 T, however a pulling force was felt starting from 0.4 T, especially on the control unit, which becomes quite strong when the magnetic field is further increased. The response of the B-RAD in terms of count rate was always uniform in different working conditions for the detector (the control unit and the probe inside the magnetic field, only the probe and only the control unit inside the magnetic field). A particular effect is observed when the control unit is exposed to a magnetic field which consists in the shifting of the energy spectrum. For a ^{137}Cs source, the photoelectric peak shifts by 6% at 1.5 T in regard to 0 T towards lower energy channels. As a consequence the measured dose rate reduces when the magnetic field increases. This reduction is negligible up to around 0.5 T and is always lower than 10% up to 1.5 T. This uncertainty can be accepted in many applications in radiation protection or can be software compensated in the future versions of the detector.

The linearity of the B-RAD response with the dose rate was measured from 450 nSv/h up to 10 mSv/h and it started to deviate from linearity around 2 mSv/h. The nominal sensitivity range of the B-RAD, provided by the company, extends from 0.1 μSv/h up to 10 mSv/h. The B-RAD showed a wide energy range (30 keV–1.5 MeV) with different γ-ray sources and a very good energy resolution (less than 5% at 662 keV). Its response showed a negligible angular dependence between -120° and +120°. Eventually, the intrinsic spectrum of the $LaBr_3$ crystal was measured (around 40 nSv/h) and saved on the detector setup for automatic subtraction.

Operational tests performed on the B-RAD showed a good capability of the device to detect the presence of an unknown γ-ray source at an unidentified location and a fast response as soon as the device approached the source. The B-RAD also showed a stable response over a tested period of one month, a variation of only 1% of the dose rate was measured with the same source in the same identical configuration (^{137}Cs and ^{60}Co). A higher variation (around 9%) was measured only with low energy and low activity γ-ray source essentially due to the lower statistics (^{241}Am). Finally, the B-RAD was considered to measure the residual radioactivity of more than 500 permanent magnets mounted on the ion pumps from the former LEP collider in view of their radiological clearance and elimination since all the other common devices failed. The B-RAD was employed on twenty randomly selected magnets and it allowed to classify 50% of them as radioactive.

Table 2.4: Summary of the stability test. For each day of measurement and for each source, the table reports the acquisition time (in seconds), the net dose rate (in μSv/h), the peak position (channel) and the energy resolution (FWHM).

.

	Source	Acquisition time (s)	Net dose rate (μSv/h)	Peak position (channel)	Energy resolution (%)
Day 1 14/02/2020	Background	3600	0.069		
	^{137}Cs	252	31.31	1078	5.9%
	^{60}Co	350	30.91	1784	5.6%
				2001	4.71%
	^{241}Am	957	-	206	41.5%
Day 2 19/02/2020	Background	3600	0.070		
	^{137}Cs	177	31.38	1081	5.9%
	^{60}Co	287	31.44	1789	5.5%
				2008	4.8%
	^{241}Am	757	1.31	197	33.2%
Day 3 21/02/2020	Background	3600	0.070		
	^{137}Cs	124	-	1078	5.8%
	^{60}Co	287	31.20	1788	5.7%
				2005	4.6%
	^{241}Am	757	1.45	213	27.6%
Day 4 25/02/2020	Background	3600	0.069		
	^{137}Cs	176	31.72	1075	5.8%
	^{60}Co	381	31.26	1786	5.5%
				2002	4.7%
	^{241}Am	1163	1.44	231	29.4%
Day 5 25/02/2020	Background	3600	0.068		
	^{137}Cs	158	31.38	1078	5.9%
	^{60}Co	314	30.94	1786	5.6%
				2003	4.6%
	^{241}Am	1950	-	232	33.2%
Day 6 28/02/2020	Background	3600	0.069		
	^{137}Cs	165	-	1078	5.8%
	^{60}Co	318	30.69	1784	5.4%
				2001	4.7%
	^{241}Am	1261	-	210	40.1%
Day 7 2/03/2020	Background	3600	0.069		
	^{137}Cs	136	31.09	1079	6.0%
	^{60}Co	350	30.82	1785	5.6%
				2001	4.7%
	^{241}Am	2404	1.21	186	37.4%
Day 8 2/03/2020	Background	3600	0.071		
	^{137}Cs	147	31.24	1079	6.0%
	^{60}Co	358	31.23	1788	5.7%
				2007	4.8%
	^{241}Am	2837	1.23	189	35.7%
Day 9 2/03/2020	Background	3600	0.069		
	^{137}Cs	135	31.54	1079	6.0%
	^{60}Co	308	30.72	1787	5.5%
				2003	4.8%
	^{241}Am	5820	1.31	196	33.3%
Day 10 2/03/2020	Background	3600	0.071		
	^{137}Cs	125	31.36	1077	5.9%
	^{60}Co	322	30.65	1787	5.6%
				2005	4.5%
	^{241}Am	3567	1.42	209	28.8%

Chapter 3

Characterisation of stilbene and EJ-276 as probes for fast neutron dose rate measurements

In this chapter, a stilbene and an EJ-276 (plastic) organic scintillator are considered in view of their application in the B-RAD detector, as an additional probe for fast neutron dose rate measurements. Section 3.1 indroduces the organic scintillators. In particular it discusses the neutron kinematics and the neutron spectrum in organic materials (Section 3.1.1), the γ-ray interaction in organic scintillators and the emerging energy spectrum (Section 3.1.3) and the difference in the time profile of signals produced by the interaction with different kinds of particles (Section 3.1.4). Section 3.2 explains the Pulse Shape Discrimination (PSD), a method for particle discrimination commonly used in organic scintillators. In this work the PSD is considered for neutron/γ-ray (n/γ) discrimination.

Sections 3.3 and 3.4 are dedicated to the performance tests of the two selected scintillators. Section 3.3 describes the experimental setup. Section 3.4 addresses the energy calibration and energy resolution, the n/γ discrimination via the PSD, the count rate linearity, the neutron detection efficiency, a Pile-Up Rejection (PUR) algorithm developed for application in high-intensity and mixed radiation fields and the temperature dependence. Finally, Section 3.5 summarises the results.

3.1 Introduction to organic scintillators

Organic scintillators are widely used in particle detection. They are often preferred to inorganic crystals since their fabrication is easier, they have short decay times and lower cost. Moreover, the capability to perform particle discrimination [5] makes them suitable for particle detection since it allows γ-ray background elimination. As neutron detectors, organic scintillators have been investigated for several applications such as fission neutron detection [43], fast neutron imaging [44], neutron spectrometry (with unfolding) [45] and as an alternative to ^{3}He counters in non-proliferation application, homeland security and fusion research [46, 47].

3.1.1 Kinematics of neutron elastic scattering

Neutron detection in organic scintillators is based on elastic scattering of neutrons by light ions. Hydrogen is probably the most common choice as target nucleus and the recoil nuclei that result from neutron scattering on ordinary hydrogen are recoil protons. Because of the high hydrogen content in organic materials, successful applications have been reported using crystals such as anthracene or stilbene, liquid scintillators and plastic scintillators.

For incoming neutrons with non-relativistic energy, the recoil nucleus kinetic energy in the laboratory reference system as a function of the scattering angle in the centre-of-mass system is given by the following formula [5]:

$$E_R = \frac{2A}{(1+A)^2}(1 - cos\Theta)E_n \tag{3.1}$$

in which E_R is the recoil nucleus kinetic energy, E_n the incoming neutron kinetic energy, A the target mass number and Θ the scattering angle in the centre-of-mass coordinate system. The relationship between the scattering angle in the laboratory and centre-of-mass system is given by Equation 3.2. Using Equation 3.2 to convert Equation 3.1 in the laboratory coordinate system (target at rest), the relationship between the energy of the incoming neutron and the recoil nucleus results in Equation 3.3 [5]:

$$cos\theta = \sqrt{\frac{1 - cos\Theta}{2}} \tag{3.2}$$

$$E_R = \frac{4A}{(1+A)^2}(cos^2\theta)E_n \tag{3.3}$$

where θ is the angle between the direction of the recoil nucleus and the direction of the incident neutron, in the laboratory frame. The recoil energy is a function of the scattering angle: it is maximum when $\theta = 0°$ and it is minimum when $\theta = 90°$, that means the recoil is emitted perpendicular to the incoming neutron direction. It can be noticed that for hydrogen (A=1) the maximum energy that can be transferred in an elastic reaction is equal to the total neutron energy. This makes hydrogen the best candidate for slowing down neutrons in general, because, in principle, all of the neutron energy can be transferred to the target in a single reaction. Moreover, the cross section for neutron elastic scattering from hydrogen is quite large and its energy dependence is accurately known. For carbon (A= 12), which together with hydrogen is the second constituent of an organic scintillator, the maximum energy that can be transferred to an ion in a single elastic scattering is around 28% of the incoming neutron energy.

3.1.2 The emerging neutron spectrum

The emerging spectrum after neutron irradiation in organic scintillators is determined by the energy distribution of recoil nuclei after neutron scattering. The probability distribution of the recoil nucleus energy can be calculated by the following formula [5]:

$$p(E_R) = \frac{(1+A)^2}{A}\frac{\sigma(\Theta)}{\sigma_s}\frac{\pi}{E_n} \tag{3.4}$$

where σ_s is the total scattering cross-section integrated over the solid angle and $\sigma(\Theta)$ the differential scattering cross section in the centre-of-mass system. A very important simplification applies when the target nucleus is hydrogen: the scattering process is almost isotropic in the centre-of-mass coordinate system, then $\sigma(\Theta)$ does not change with Θ and is equal to a constant $\sigma_s/4\pi$. The expected proton recoil energy distribution is therefore a simple rectangular distribution between zero and the full neutron energy.

Organic scintillators also contain carbon ions in significant quantities. However, scattering of neutrons on carbon rarely provides observable light pulses since the scintillation efficiency decreases for high dE/dx particles and the average energy of carbon recoils is quite low. The amplitude of light pulses often fall below the discrimination level of the counting system. Only at energies greater than 8–9 MeV, two neutron reactions on carbon ions become competitive: $^{12}C(n,\alpha)$ and $^{12}C(n,n')$ with a threshold energy of 6.17 MeV and 7.98 MeV, respectively.

Moreover, additional effects affect the spectrum of the deposited energy inside the scintillator [5]:

1. Wall effect
   If the dimensions of the scintillator are small with respect to the mean free path of recoil nuclei, they escape from the detector and part of their energy is not deposited. The effect on the spectrum is to shift events from high pulse heights to lower amplitudes.

2. Multiple scattering on hydrogen
   For large volume detectors it is possible for neutrons to scatter more than once from hydrogen nuclei. If these events occur within a very short period of time as compared with the pulse shaping time, a single pulse is detected. The total effect is to enhance the number of counts at high energy.

3. Scattering from carbon
   Even if elastic scattering from carbon ions usually does not produce detectable events, the scattered neutron may still undergo a hydrogen scattering with a lower initial energy (between 72% and 100% of its initial energy).

4. Detector resolution
   The detector response will always tend to broaden from the ideal rectangular spectrum because of the intrinsic energy resolution, which depends on the number of photoelectrons emitted per deposited energy, and of the noise due to all the effects related to the collection of the visible light and to the electronic system.

It is important to say that the first three effects account for the energy deposition inside the scintillator, but the spectrum emerging from scintillators is also affected by the non-linearity between the light output yield and the energy.

3.1.3 γ-ray interaction in organic scintillators and Compton edge evaluation

Organic scintillators are made of low Z materials and have low density. Therefore, their interaction with γ-rays mainly occurs through Compton scattering [5]. Because of the lack of the photoelectric peak, the Compton edge has to be assumed as reference point for the energy calibration. However, one of the major obstacles is to accurately set its position over the acquired spectrum [48, 49, 50].

Compton scattering involves a photon and a loosely bound-shell orbital electron of an atom. The impinging photon transfers a portion of its energy to the electron, while it is deflected trough an angle θ with respect to its initial direction with less energy than its initial one. Because the photon energy greatly exceeds the energy of the electron, as a first approximation the electron can be treated as a free particle. Applying the energy and momentum conservation, the relationship between the kinetic energy before and after the collision is given by Equation 3.5.

$$h\nu' = \frac{h\nu}{1 + \frac{h\nu'}{m_e c^2}(1 - cos\theta)} \tag{3.5}$$

where $h\nu$ is the initial energy of the photon, $h\nu'$ is the energy of the scattered photon, $m_e c^2$ the rest mass energy of the electron (0.511 MeV) and θ the scattering angle in the laboratory frame.

Scintillating materials measure the energy of the recoil electron. This is equal to the difference between the initial energy of the photon ($h\nu$) and the energy of the scattered

photon ($h\nu'$). Because in normal conditions Compton scattering occurs inside a detector at all scattering angles, the energy of the recoil electrons is distributed as a continuum along two extreme cases (which can be derived from Equation 3.5):

- $\theta \cong 0°$. The energy of the scattered photon is almost equal to its initial energy and the Compton electron has a very low energy.
- $\theta = 180°$. The impinging photon is back scattered. The Compton electron emerges in the forward direction with the maximum energy that can be transferred to an electron trough a single Compton interaction.

The Compton scattering occurs for all angles according to the Klein-Nishina distribution (not isotropically distributed), i.e. the energy spectrum ranges from $\theta = 0°$ up to $\theta = 180°$, when the maximum energy is transferred through a single Compton interaction, and the theoretical shape is not a rectangle. This energy can be simply derived from Equation 3.5 as follows:

$$E_{e^-} = h\nu - h\nu'(\theta = 180^o) = \frac{2(h\nu)^2}{2h\nu + m_e c^2} \tag{3.6}$$

where E_{e^-} is the kinetic energy of the emitted electron, $h\nu$ and $h\nu'$ the energy of the impinging and emitted photons, respectively. Equation 3.5 assumes that electrons are initially unbound. The electron binding energy has a particular effect on the shape of the Compton spectrum: at fixed angle, the energy of the scattered photon broadens according to a certain energy distribution (while Equation 3.5 predicts a specific value). This is the reason why at the Compton edge the shape of the spectrum drops with a slope rather than vertically. However, in actual detectors, these effects are usually masked by the finite energy resolution of the detector, which is the main reason for the spread of the spectrum [5].

3.1.4 The time profile

The scintillation process in organic scintillators depends on their molecular energy level structure. For the majority of organic scintillators, it is based on a π-electron structure, as illustrated in Figure 3.1. When a charged particle passes nearby, it transfers its kinetic energy to the scintillator molecule exciting it. This energy transfer is represented in Figure 3.1 by the *Absorption* arrow. This excitation process is almost instantaneous, i.e. it happens in a negligible period of time, and it is usually followed by a de-excitation process to the initial state, called *Fluorescence* or *Prompt emission*. As shown in Figure 3.1 a competitive de-excitation mechanism might occur called *Inter-system crossing* which consists in the transition of some excited singlet states into an excited triplet state (where the energy levels of the singlet and triplet state are indicated in Figure 3.1). The latter de-excites according to its own life-time which is usually larger than the fluorescence, being few nanoseconds a typical value for the fluorescence, while the life-time of the triplet state can be of the order of milliseconds. This slower process is called *Phosphorescence* or also *Delayed emission*. A third non-direct mechanisms exists, which is called *Delayed fluorescence*. It involves two molecules in a long-lived state (such as the triplet state), close to each other and interacting. From this bimolecular interaction, one molecule can lead to the ground state and the other to the S_1 state with the consequent de-excitation, entirely similar to the fluorescence emission. This mechanism is dependent on the density of the triplet states, i.e. on the ionization density of the incident particle. Particles with higher Linear Energy Transfer (LET) (i.e. higher ionization density) promote the delayed fluorescence and the corresponding scintillation light is characterised by a slower time profile. The PSD method, described in the following section, is based on this principle.

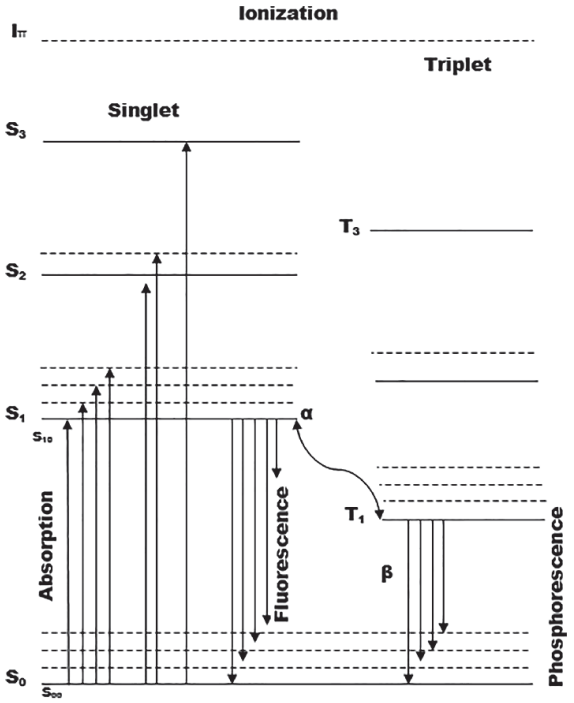

Figure 3.1: Electron energy structure of a single molecule of an organic scintillator [51].

3.2 The Pulse Shape Discrimination method

The PSD exploits the different time profile produced in scintillators by different kinds of particle due to their different LET (as explained in the previous section). Several PSD methods exist mainly divided in two types: analogue, i.e., based on a specific electronic circuitry [5], and digital, i.e., by sampling the output pulse and by applying a dedicated algorithm. A second distinction can be done between methods that measure the rise time of the output pulse (only analogue) and methods that integrate the signal over two different time windows also called Charge Integration methods (analogue and digital) [5].

In this work the PSD was always performed using a digital method and by applying the Charge Integration algorithm. According to the Charge Integration method, the PSD parameter is calculated for each signal as follows:

$$PSD = \frac{Q_{long} - Q_{short}}{Q_{long}} \tag{3.7}$$

where Q_{short} and Q_{long} are the integrals of the signal (i.e. the charge) calculated over two different integration times (t_{short} and t_{long} respectively), as shown in Figure 3.2.

The PSD distribution of each particle is described by a Gaussian-like equation in the 1D PSD histogram plot and a Figure of Merit (FOM) can be defined to quantify the goodness of the PSD. For the n/γ discrimination, the FOM is defined according to Equation 3.8.

$$FOM = \frac{x_n - x_\gamma}{FWHM_n + FWHM_\gamma} \tag{3.8}$$

where x_n and x_γ are the mean values of the Gaussian fitting equations of the neutron and γ-ray distributions respectively, and $FWHM_n$ and $FWHM_\gamma$ the corresponding Full Width at Half Maximum (FWHM).

As a general rule, a good discrimination is performed, i.e. no overlapping exists between the two Gaussian distributions, if Equation 3.9 is met.

$$(x_n - x_\gamma) > 3 \times (\sigma_n + \sigma_\gamma) \tag{3.9}$$

where σ_n and σ_γ are the standard deviations of the neutron and γ-ray distributions. Considering $FWHM = 2.36 \times \sigma$ and Equation 3.8, Equation 3.9 can be written as FOM > 1.27.

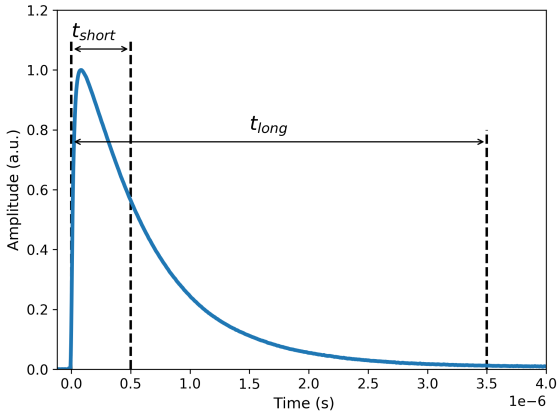

Figure 3.2: An example of a pulse with the integration time windows t_{short} and t_{long} selected for the PSD analysis.

3.3 Detectors and experimental setup

The stilbene and the EJ-276 are organic scintillators characterised by a similar chemical composition, low density (close to 1 g cm^{-3}) and short scintillation decay times (less than 500 ns). Table 3.1 summarizes and compares the main properties of the two scintillators used in this work according to the datasheets or the literature (when data from the datasheet were missing). The quenching factor for recoil protons is also reported in view of their application as fast neutron detectors.

As shown in Figure 3.3 and reported in Table 3.1, the stilbene was already provided by the manufacturer with an aluminium housing and an external reflector. On the other hand, the EJ-276 was purchased from the company in a bare state and a Teflon tape was used to cover the external surface of the scintillator. Due to the isotropic nature of the light emission, an external reflector (such as an aluminium foil or Teflon tape) is needed to prevent light escaping from the scintillator, especially for lower light yield scintillator (as the EJ 276).

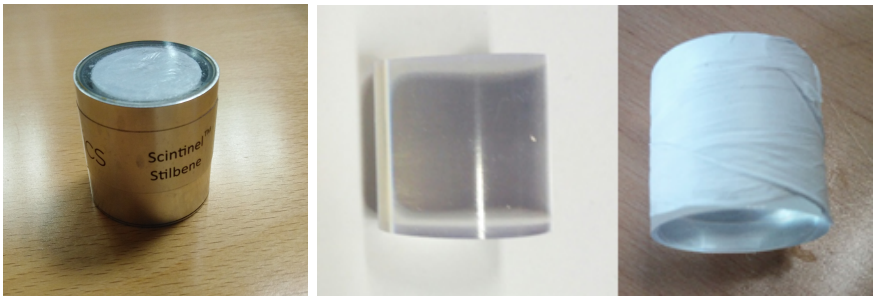

Figure 3.3: On the left, the stilbene scintillator; on the right, the EJ-276 as provided by the manufacturer and the same scintillator wrapped in Teflon tape.

Table 3.1: Comparison of the main properties of the stilbene and EJ-276 scintillators.

	Stilbene	EJ-276
Manufacturer	Inrad Optics	Eljen Technology
Type of scintillator	Organic crystal	Organic plastic
Shape and dimensions	1–inch right cylinder	1–inch right cylinder
Chemical composition	$C_{14}H_{12}$ [52]	4.546×10^{22} H atoms cm^{-3} 4.906×10^{22} C atoms cm^{-3} [53]
Density	1.15 g cm^{-3} [52]	1.096 g cm^{-3} [53]
Housing and external reflector	Yes (wrapped in a PTFE)	No (wrapped in Teflon tape)
Peak scintillation wavelength	390 nm [52]	425 nm [53]
Scintillation light yield	14,000 ph. MeV^{-1} [52]	8,600 ph. MeV^{-1} [53]
Decay constants [ns]	4, 35, 332 [54]	13, 35, 270 (γ) 13,59,460 (n) [53]
Recoil proton quenching factor[(1)] (proton recoil energy)	0.1–0.17 [55] (300 keV–3MeV)	0.08–0.3 [56] [(2)] (300 keV–3MeV)

The scintillators were coupled with an 8 × 8 SiPM Array J-30035-64P from SensL [57] using the Rhodorsil Pate 7 optical grease [58] and placed inside a light-tight box. A specifically designed board, called Blueboard (Figure 3.4), was used for bias voltage supplying and signal acquisition. A bias voltage of +28.5 V, corresponding to 4 V of overvoltage, was supplied to the common cathode of the SiPM array. The Photon Detection Efficiency (PDE) for the selected overvoltage is around 40% for the stilbene and 43% for the EJ-276 [57]. The summed anode signal was acquired for signal analysis.

The Blueboard was designed by the Radiation Protection (RP) Special Project (SP) section at CERN for application with scintillators and large area SiPM arrays. The schematic is described in details in [59]. The Blueboard has several advantages, the main ones are listed below:

- The bias voltage is provided by the A7525DU SiPM Power Module from Nuclear Instrument [60] (see Figure 3.4), a compact module powered by 5 V with a USB cable and connected to a laptop.
- It allows output signal processing with four different output channels (indicated in Figure 3.4) corresponding to different stages of the signal processing.
- It includes a temperature sensor and a dedicated circuitry which, together with the Power Module, can correct the bias voltage with temperature variation, i.e. a temperature compensation system.
- It is very compact and it can replace the external voltage supply meter.

The first output, which corresponds to the summed anode signal (standard output), was acquired during the measurements by placing a jumper between the first and the second stage (as numbered in Figure 3.4). The other outputs corresponding to an amplification circuit, an RC circuit and a Gaussian shaper, were not used in this work, as well as the temperature compensation.

[(1)]The quenching factor is defined as E_{vis}/E_r where E_{vis} is the energy in electron equivalent measured with the scintillator after γ-ray calibration and E_r the energy of the recoil proton emitted by the neutron reaction.

[(2)]Data have been extrapolated from the light yield data relative to 477 keVee.

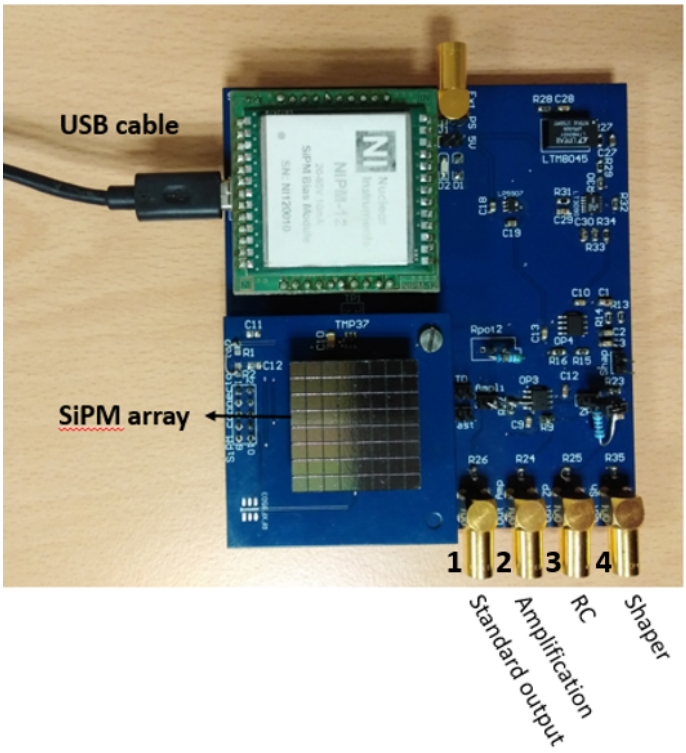

Figure 3.4: The customized board (called Blueboard) developed by the RP-SP group at CERN. The Nuclear Instruments Power Module and the four different outputs of the Blueboard are also shown.

3.4 Characterisation of the stilbene and EJ-276

The scintillators were coupled with the 64 pixel SiPM array from SensL and the output signal was acquired with the Blueboard. The summed anode signal was sent to a CAEN DT5720 digitizer (12 bit, 250 Ms/s) and the digitizer threshold was set at 100 keVee for the stilbene and 250 keVee for the EJ-276. The energy thresholds were obtained calibrating the detectors with a ^{137}Cs and a ^{22}Na γ-ray source. Both the Power Module and the digitizer were controlled by a laptop with the corresponding interface software (called Zeus and DPP-PSD respectively). The scintillators were characterised in terms of the energy calibration and energy resolution, the n/γ discrimination via the PSD, the count rate linearity, the neutron detection efficiency and temperature dependence. A Pile-Up Rejection (PUR) algorithm was developed for application in high-intensity and mixed radiation fields and tested. Only the measurements described in Section 3.4.4 were carried out sending the output signal to a Teledyne LeCroy Waverunner 8104 Oscilloscope (1 GHz, 20 Gs/s) with a 50 Ω termination (instead of the digitizer) because it allows for a higher sampling frequency and more flexibility of parameter setting. Around 30,000 signals were saved for each measurement and analysed offline with a Python code [61].

Figure 3.5 shows the experimental setup with the CAEN digitizer. The acquisition board and the scintillator are inside the light-tight box.

3.4.1 Energy calibration and energy resolution

Three different γ-ray sources were used to perform the energy calibration: ^{22}Na (36.09 kBq), ^{137}Cs (151.44 kBq) and ^{60}Co (39.51 kBq). Table 3.2 reports the energy values of the photon emissions and their equivalent Compton edge as calculated by Equation 3.6. In this study, the energy calibration was performed according to two methods, as described

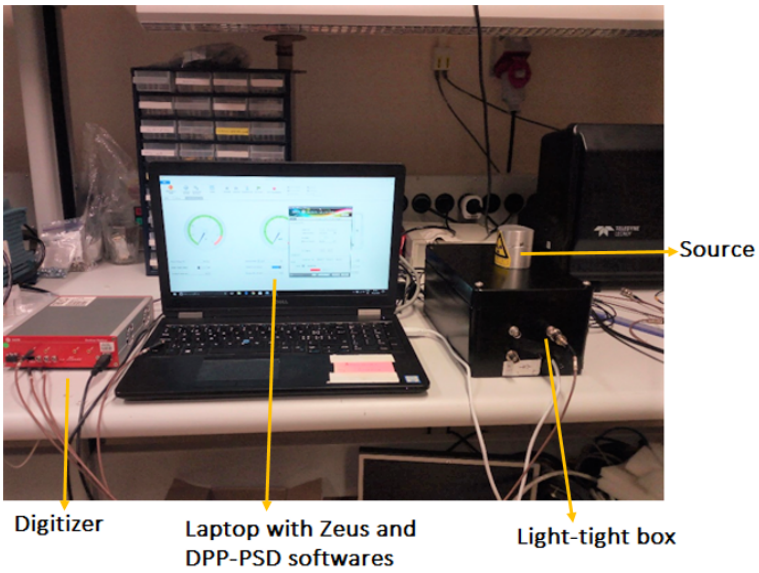

Figure 3.5: The experimental setup used for the characterisation of the stilbene and EJ-276. The scintillator and the readout board are inside the light-tight box.

below.

Table 3.2: Photon energy (E_γ) and equivalent Compton edge energy (E_{CE}) for three different γ-ray sources: ^{22}Na, ^{137}Cs and ^{60}Co.

Source	E_γ (keV)	E_{CE} (keV)
^{22}Na	511	340
	1275	1062
^{137}Cs	662	477
^{60}Co	1173	963
	1332	1118

3.4.1.1 First method: Gaussian fitting

In the first method, each Compton edge was fitted using a Gaussian function. However, the position of the Compton edge on the fitting function is not well defined as it depends on the scintillators and on the electronic setup. Various prescriptions were given by Dietze and Klein [48] for different scintillator sizes and resolutions and for different source energies. Beghian et al. [62] suggested 66%, Honecker and Grässler [63] 70% of the maximum of the measured energy spectrum in the Compton edge region. Three different cases were considered in this work: the Compton edge was assigned to the channels corresponding to the 90%, 70% and 50% of the maximum beyond the peak.

Figure 3.6 shows the ^{137}Cs spectrum acquired with the stilbene scintillator and the Gaussian fit in red, Figure 3.7 shows the linear fit for the stilbene and plastic scintillators and the energy corresponding to each calibration point when the position of the Compton edge is set to 50%. Because of the poorer energy resolution of the EJ-276, the two Compton edges of ^{60}Co were not well distinguishable in the experimental spectrum. For this reason, a single fit was performed and a single calibration point was obtained considering the position of the mean energy of the two Compton edges (i.e. 1041 keV) [64]. Table 3.3

reports the linear fitting equations and the corresponding R^2 values for the three different positions of the Compton edge, for both detectors.

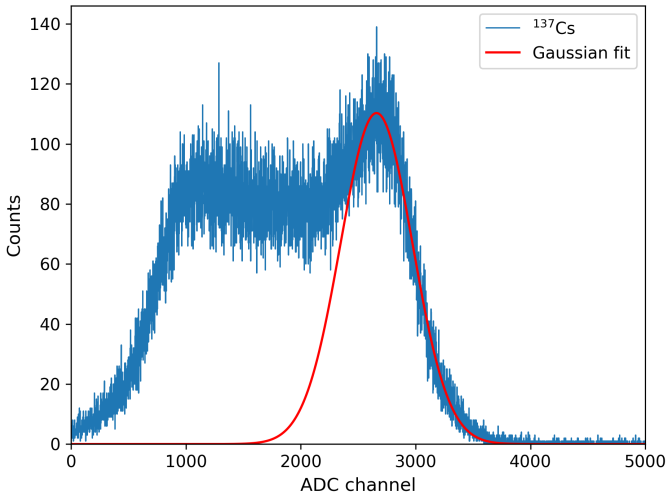

Figure 3.6: The ^{137}Cs spectrum acquired with the stilbene scintillator coupled with the 8×8 SiPM array. The Compton continuum spectrum is visible, the red line is the Gaussian fit of the Compton edge.

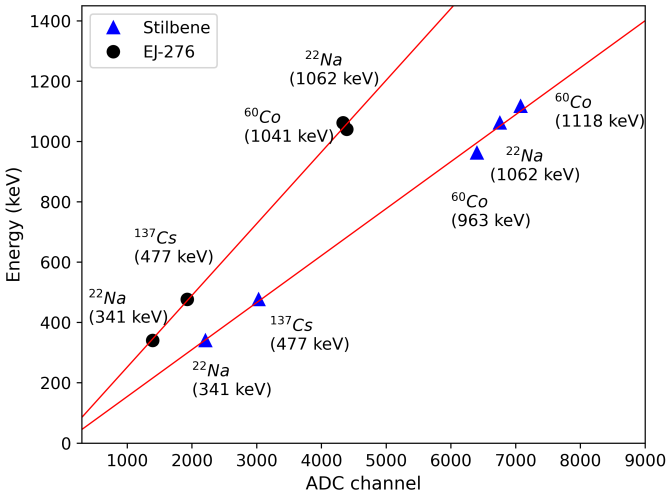

Figure 3.7: Compton edge positions of ^{137}Cs, ^{60}Co and ^{22}Na sources in the stilbene and EJ-276 scintillators and the linear fit to the data points (red solid line).

This first method was mainly used to check the linearity of the scintillators' response with the energy and to reveal any differences in the energy resolution of the two scintillators. Both scintillators show a good linearity for all the three cases (i.e. 50%, 70% and 90%) as shown by the obtained R^2 values. By comparing the slopes of the energy calibration equations of the stilbene and EJ-276, for the three cases (Table 3.3), the slope obtained with the EJ-276 is always more than 50% greater than the slope calculated for the stilbene. This is expected because of the different light yield of the two scintillators, however their difference is slightly overestimated by this method (14,000 ph. Mev^{-1} versus 8,600 ph. Mev^{-1}, see Table 3.1). The small intercepts of the energy calibration equations is also expected since it is due to the non-linearity of organic scintillators at low energies (below 100 keV) [49, 65]. However, this is a poor method of calibration since it assumes *a priori* the exact position of the Compton edge and, above all, it sets for different energy

Table 3.3: Energy calibration equations for the stilbene and the EJ-276 obtained with a Gaussian fit of the Compton edge. E is the energy in keV and ch. the corresponding channel number; the R^2 of the linear regression is also reported.

		Equation	R^2
Stilbene	50%	$E(keV) = (0.156 \pm 0.004) \times ch. + (-1.232 \pm 27.025)$	0.9985
	70%	$E(keV) = (0.158 \pm 0.004) \times ch. + (10.887 \pm 23.754)$	0.9988
	90%	$E(keV) = (0.161 \pm 0.004) \times ch. + (25.792 \pm 21.534)$	0.9990
EJ-276	50%	$E(keV) = (0.237 \pm 0.007) \times ch. + (14.354 \pm 22.232)$	0.9992
	70%	$E(keV) = (0.244 \pm 0.012) \times ch. + (25.504 \pm 38.062)$	0.9976
	90%	$E(keV) = (0.251 \pm 0.019) \times ch. + (41.244 \pm 57.768)$	0.9943

values, the same relative position of the Compton edge (respect to the maximum of the acquired spectrum).

3.4.1.2 Second method: Monte Carlo simulation

In the second method, the theoretical spectra of ^{137}Cs, ^{60}Co and ^{22}Na in the stilbene and EJ-276 scintillators were calculated using the FLUKA Monte Carlo code version 4 [66, 67, 68]. A Gaussian Energy Broadening (GEB) was applied to the simulated spectra to take into account the finite energy resolution of the detectors. The broadened spectrum is obtained by sampling, per each energy bin of the simulated spectrum, N energy values from a Gaussian distribution, where N is the number of counts in the selected energy bin. The Gaussian distribution is centred in E, where E is a random value of the energy sampled from E_i and E_{i+1}, where i is the energy bin of the selected bin, and its σ is proportional to $\sqrt{E}$. The energy resolution is defined as $R_E = FWHM/E$.

The broadened spectrum was normalized to the maximum of the experimental Compton distribution and its x-axis (in energy scale) was linearly scaled in order to match the experimental spectrum (in ADC channels). Both the scaling factor and the R_E values were varied to find the broadened spectrum, which best fitted the experimental one (through least square minimization) in the Compton edge area. Figure 3.8 shows, in the top, the three spectra (experimental, simulated and broadened) of ^{137}Cs and ^{60}Co for the stilbene, and, in the bottom, the plots of the residuals between the experimental and broadened spectra, in the selected energy range. Figure 3.9 shows the same results for the EJ-276.

The position of the Compton edge of ^{137}Cs (477 keV) for the stilbene and EJ-276 was found at 92% and 90% of the position of the maximum, respectively (which correspond to 74% and 73% of the peak height). As for the first method, with the EJ-276 the two Compton edges of ^{60}Co were not well distinguishable and a single fit was performed considering 1041 keV as the calibration point. From the plots of the residuals, the Compton edges are well fitted in the selected energy ranges, i.e., in the Compton edge range. The fitting region was in fact restricted to the Compton edge range since the photon backscattering and the source geometry, which affect the spectrum shape below the Compton edge, were not taken into account. Figure 3.10 shows the calibration points and the linear fits for both scintillators. Table 3.4 reports the linear fitting equations and the corresponding R^2.

As the first method, the second method shows that the response of both scintillators with energy is linear (the R^2 values of the linear fitting equations are close to one) in the selected energy range. The different slopes of the energy calibration equations for the two scintillators are coherent with their different light yields and a small intercept is also obtained. This attests to the use of the first method for qualitative and comparative

analysis. On the other hand, the first method does not allow for quantitative analysis. For the second method, the different slopes of the two scintillators better agrees with the different light yield (for the EJ-276 the slope is 40% higher than stilbene) and the energy resolution is 15% and 20% for the stilbene and the EJ-276 respectively. For comparison, the energy resolution of the first method was calculated as the ratio between the FWHM and the mean value of the Gaussian equation fitting the Compton edge of the ^{137}Cs spectrum (477 keV), when the Compton edge is selected at 90% of the height peak, for the stilbene, and at 50% for the EJ-276. These two cases were selected as the case which best match the energy calibration equation obtained with the second method (which is taken as reference), for each scintillator. The corresponding energy resolutions at 477 keV for the first method (Gaussian fitting) are 30% and 36% for stilbene and EJ-276 respectively, significantly worse than the values obtained with the second method (Monte Carlo Simulation).

The calculation of the energy calibration and the energy resolution in organic scintillators is not unique as explained in [64]. The first method is based on fitting the Compton edge of the experimental spectra with a Gaussian equation. It allows comparing the different performances of the two selected scintillators, however it is not able to correctly determine the actual position of the Compton edge, i.e. the resulting energy calibration equation and energy resolution is not reliable. This method is rejected and a second method is proposed to be implemented in the B-RAD. It consists in fitting the experimental spectra with the ideal spectra calculated by MC simulation and later applying a GEB, to take into account the finite energy resolution of the detector. With this method, the energy resolution for the stilbene and the EJ-276 scintillators at 477 keV is 15% and 20% respectively. Both scintillators show a relatively poor energy resolution which is expected because of the low light yield (especially if compared with inorganic scintillators). However, a poor energy resolution and a few percent variation due to the uncertainty of its calculation are acceptable for the scope of this study since the two detectors were considered for use as dose rate survey meters.

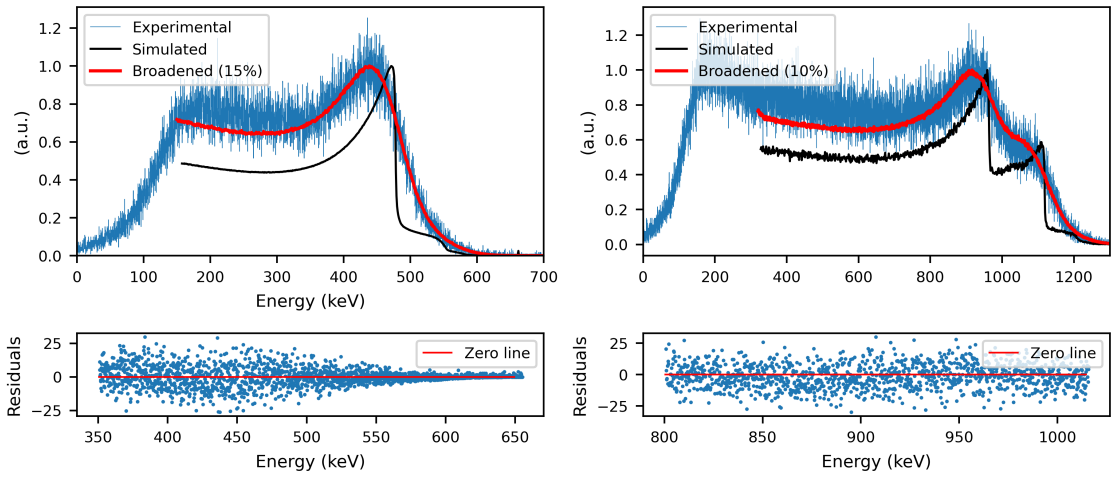

Figure 3.8: Comparison of the normalized spectrum of a ^{137}Cs source (on the left) and of a ^{60}Co source (on the right) measured with the stilbene scintillator (blue line), the FLUKA simulated spectrum (black line) and the result of the GEB of the simulated spectrum which best fits the experimental data (red line). On the bottom, the plots of the residuals between the experimental and broadened spectra.

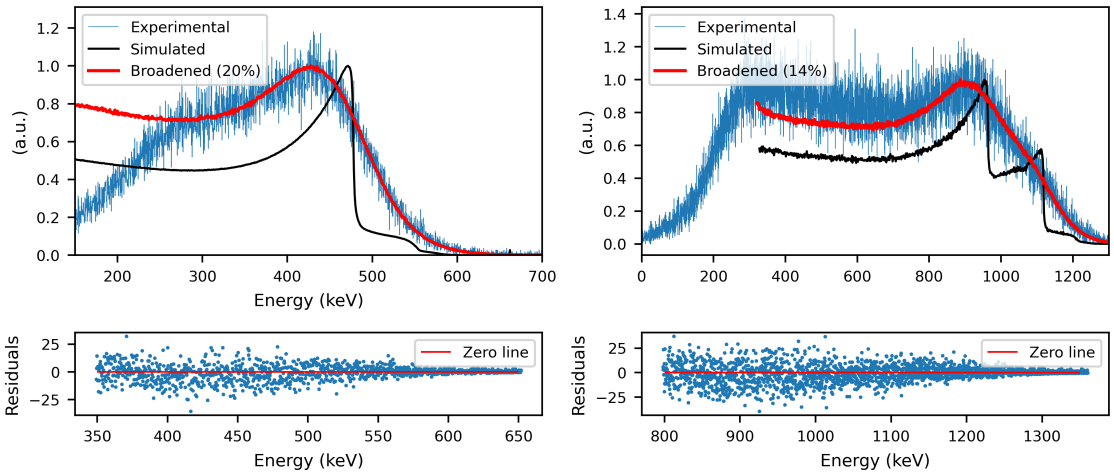

Figure 3.9: Comparison of the normalized spectrum of a ^{137}Cs source (on the left) and of a ^{60}Co source (on the right) measured with the EJ-276 scintillator (blue line), the FLUKA simulated spectrum (black line) and the result of the GEB of the simulated spectrum which best fits the experimental data (red line). On the bottom, the plots of the residuals between the experimental and broadened spectra.

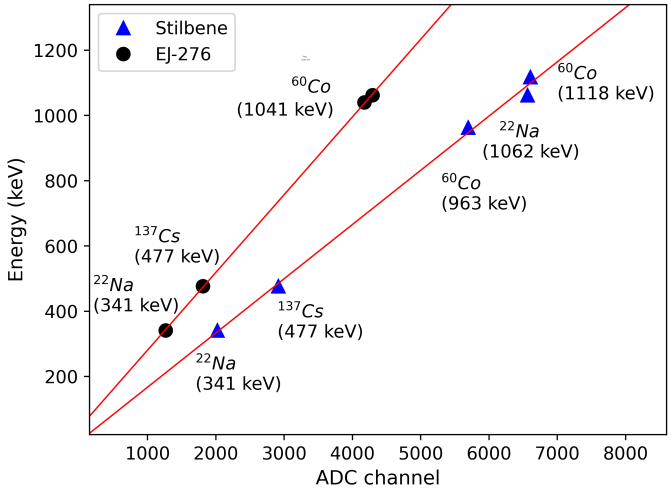

Figure 3.10: Compton edge positions of ^{137}Cs, ^{60}Co and ^{22}Na sources for the stilbene and EJ-276 scintillators. The red lines show the linear fits to the data points.

Table 3.4: The energy calibration equation for the stilbene and the EJ-276 using the Monte Carlo simulation for the evaluation of the actual position of the Compton edge. E is the energy in keV and ch. the corresponding channel. The R^2 of the linear regression is also reported.

	Equation	R^2
Stilbene	$E(keV) = (0.166 \pm 0.005) \times ch. + (0.952 \pm 27.426)$	0.998
EJ-276	$E(keV) = (0.238 \pm 0.002) \times ch. + (42.440 \pm 5.507)$	0.999

3.4.2 Pulse Shape Discrimination

The capability to discard γ-ray signals is a priority of a neutron detector since a γ-ray background is always present with neutron fields. Organic scintillators are sensitive both

to neutron and γ-ray radiation, however they are capable of n/γ discrimination via PSD methods (see Section 3.1.4). The PSD capability of the stilbene and EJ-276 scintillators is studied using the Charge Integration method discussed in Section 3.2.

Each scintillator was irradiated with Am-Be source neutrons using the experimental setup described in Section 3.3. The PSD analysis was performed with the DPP-PSD software provided with the CAEN digitizer which calculated the PSD of each detected signal using Equation 3.7 and allows an on-line visualization of the PSD versus Q_{long} (as defined in Equation 3.7) plot. Different measurements were performed by changing the integration times t_{short} and t_{long}. For each measurement, the PSD values were collected, plotted into a histogram and the histogram plot fitted using a sum of two Gaussian equations. The corresponding FOM was calculated as defined by Equation 3.8. The maximum FOM was found setting t_{short} and t_{long} to 300 ns and 1.5 μs for the stilbene and to 300 ns and 1.3 μs for the EJ-276. The corresponding FOM was 1.54 $\pm$ 0.03 for the stilbene and 0.90 $\pm$ 0.01 for the EJ-276, setting the energy threshold to 100 keVee and to 250 keVee respectively.

Figures 3.11 and 3.12 show the PSD histogram plot and the 2D histogram plot of the PSD versus energy obtained with the stilbene and the EJ-276 respectively, for the corresponding t_{short} and t_{long} which maximise the FOM. The two different distributions unveiled from the histogram plot (Figures 3.11 and 3.12, left) correspond to γ-ray and neutron events and are associated to two different regions in the 2D plot (on the right). In the 2D PSD plot, the red box identifies the γ-ray pulses and the blue box the neutrons. In the 1D PSD histogram plots the corresponding fitting equations are also shown.

The γ-ray distribution on the 1D histogram plots of the PSD (Figures 3.11 and 3.12, left) deviates from a Gaussian-like distribution, because of a long tail at the left of the centroid. This tail was present also changing the integration time windows and it was attributed to the quantization error of the digitizer for low amplitude signals [69]. The digitizer is indeed based on an ADC (analogue-to-digital converter) which works as following: it receives as input an analogue voltage signal (continuous signal); it samples and quantizes the input signal with a constant sampling time step (the sampling frequency); it sends as output a series of binary numbers representing the original input signal. In general, the ADC is always affected by some non-linearities, such as intrinsic non-linearities of the electronic circuitry, clock jitter (i.e. deviation of the clock signals respect to their ideal values) and quantization error. The latter is considered in this case since it increases with decreasing the signal pulse height [69]. The reader is referred to [69, 70] for a deep study of the dependence between the digitizer parameters and the PSD performances. Neverthless, Flaska et al. recommand the use of a 12-bit, 250 MHz digitizer (such as the one used in this study) for good PSD results, however when excellent performances are required, higher resolution or higher sampling frequency digitizers must be chosen (in [70] the FOM increases of $\sim$50% when a 14-bit digitizer is used in place of a 12-bit).

A further observation can be made from the PSD analysis. The neutron distributions on the 2D plots (Figures 3.11 and 3.12, right) tend to move toward lower PSD values with the increasing energy. This effect was already detected by other authors with different organic scintillators [70, 71]. It is due to the dependence of the PSD with energy for neutrons in organic scintillators. Indeed, at higher energies the number of delta electrons emitted with the recoil protons (emitted after elastic neutron scattering, see Section 3.1.1) increases. As a consequence the portion of the initial energy deposited directly by protons reduces and the resulting signal is faster, being protons particles with higher dE/dx than electrons (see Section 3.1.4).

Comparing the two scintillators, the stilbene clearly shows a better n/γ discrimination respect to the EJ-276, confirmed by the higher FOM (1.54 versus 0.90) obtained with a lower energy threshold (100 keVee versus 250 keVee). This difference is mainly attributed to the different light yield between the two scintillators (14,000 ph. MeV^{-1} versus

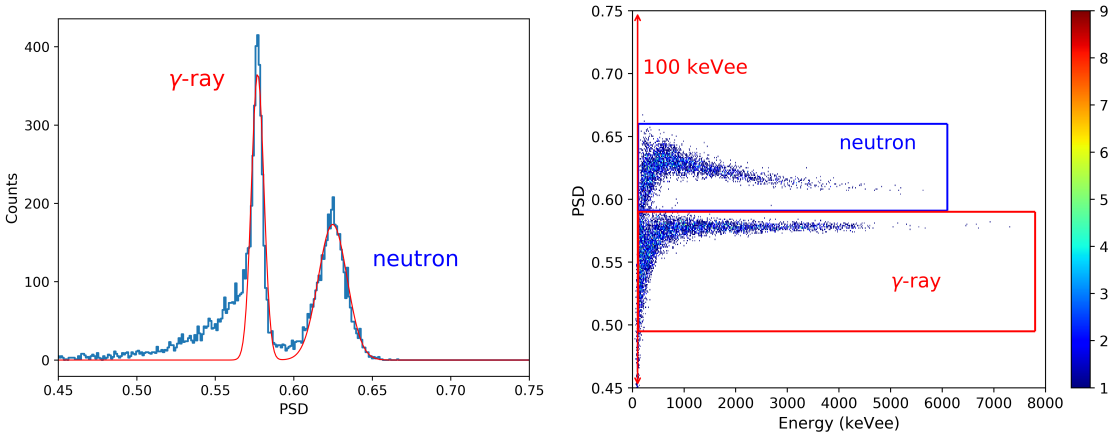

Figure 3.11: On the left, the PSD histogram plot calculated for the stilbene and an Am-Be neutron source, and the fitting equation to the neutron and γ-ray events; on the right, the 2D PSD histogram plot where the γ-rays and neutrons are identified by the two regions highlighted by a red and a blue box.

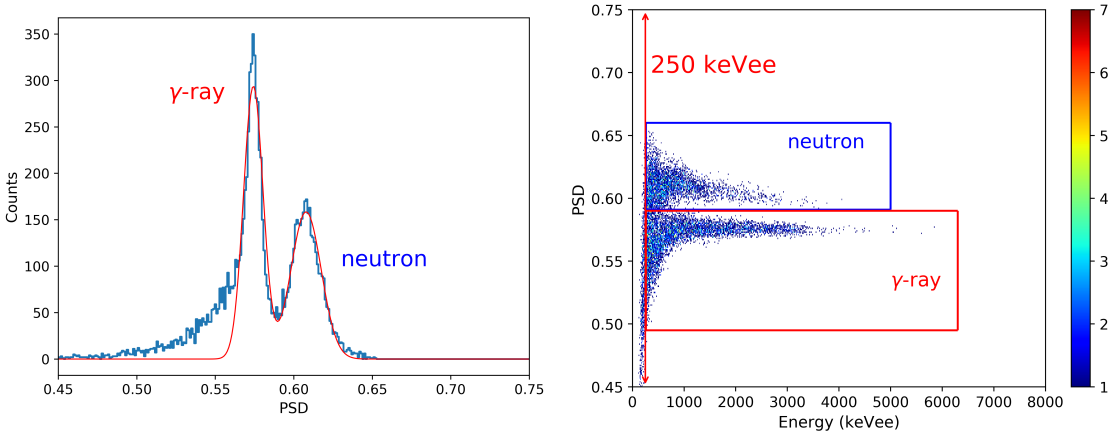

Figure 3.12: On the left, the PSD histogram plot calculated for the EJ-276 and an Am-Be neutron source, and the fitting equation to the neutron and γ-ray events; on the right, the 2D PSD histogram plot where the γ-rays and neutrons are identified by the two regions highlighted by a red and a blue box.

8,600 ph. MeV^{-1}). For small amplitude signals, the PSD Gaussian distribution is wider and the region of overlapping between the neutron and γ-ray distributions increases. On the other hand, the different FOM values is only partially due to the small difference in the scintillators' decay times. In fact, the stilbene and EJ-276 have comparable de-excitation decay times (see Table 3.1), as confirmed by the small difference between the time windows obtained in correspondence of their maximum FOM and by Figure 3.13. Figure 3.13 compares the normalised standard pulses for both scintillators, where the standard pulse was calculated by averaging the measured neutron and γ-ray signals separately (discriminated via the PSD analysis).

For the EJ-276, a higher FOM value can be obtained by increasing the energy threshold or by increasing the bias voltage. The former removes from the analysis the low amplitude signals where the PSD distributions spread the most, the latter results in a linear increase of the SiPM gain. In the former case, a higher energy threshold of $\sim$ 800 keVee had to be set to reach a sufficient discrimination (FOM $>$ 1.27) (see Figure 3.14). In the latter case, a trade-off exists, since the dark current increases with the overvoltage more than

linearly. The 28.5 V value of bias voltage was experimentally determined as the optimum voltage for the detection efficiency in [59]. For this reason, different values of overvoltage were not considered in this work.

Table 3.5 finally compares the FOM calculated in this work with one derived in other studies. The source, the energy range[(3)] and the employed photodetector for each study is also reported. The FOM found in this work is within the range of values found in the literature. The deviation from the best FOM can be explained by the different energy threshold and/or by the use of a different photodetector.

The better PSD capability, with a lower energy threshold, shown by the stilbene makes it more suitable for the B-RAD detector. However, the worse performance of the EJ-276 is mainly attributed to its lower light yield. Better results can be obtained for example with an amplification circuitry, avoiding increasing the energy threshold (and as a consequence reducing the detection efficiency) or increasing the overvoltage (which might lead to noise increase as well).

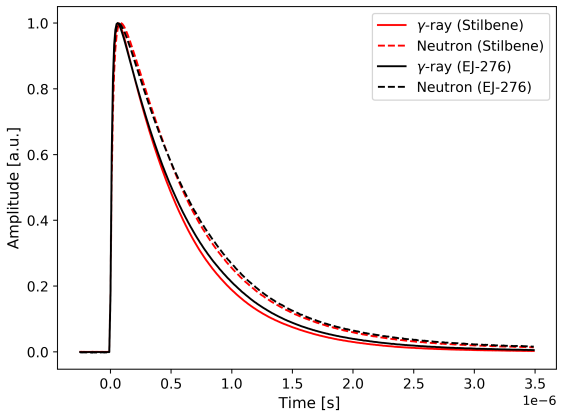

Figure 3.13: The neutron and the γ-ray standard pulses calculated with the stilbene and the EJ-276.

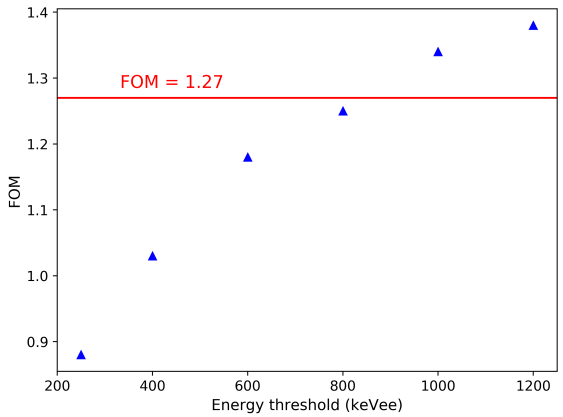

Figure 3.14: The FOM calculated with the EJ-276 for different energy thresholds.

3.4.3 Count rate linearity

For an ideal detector, the count rate increases linearly with the dose rate. In reality, the count rate linearly increases up to a limit where the count rate starts to saturate because

[(3)] In this study the FOM was obtained by analysing all the signal above the threshold. An alternative method is to calculate the FOM by considering only the signals within a narrow energy range.

Table 3.5: Comparison between the FOM calculated in this work and literature data. The size of the scintillator, the photodetector and the source are specified. The energy cut-off or the energy range selected for the PSD calculation are given in brackets.

	This work	Steinberger et al. [72]	Taggart et al. [73]	Grodzika-Kobylka et al. [74]
Dimensions	Ø1 inch × 1 inch cylinder	6 mm × 6 mm × 50 mm	6 mm × 6 mm × 6 mm	Ø1 inch × 1 inch cylinder
Photodetector	64 pixels J-Series SiPM array	SensL C-Series SiPM	J-series SiPM (single pixel)	R6233-100 Hamamatsu PMT
Source	AmBe	^{252}Cf	Am-Be	PuBe
FOM Stilbene	1.54 (100 keVee)	1.17 (100–200 keVee)	—	1.74 (100 keVee)
FOM EJ-276	0.90 (250 keVee)	—	2.39 (500–600 keVee)	1.09 (100 keVee)

of pile-up events. In fact, by increasing the source intensity, the probability to have two (or more) events during the same acquisition time increases (pile-up) and two (or more) events are counted by the detector as a single events [5]. The count rate of the stilbene and EJ-276 as a function of the dose rate was measured both with a γ-ray source and a neutron source. The effect of the pile-up on the PSD analysis was also studied when the detectors are exposed to a mixed n/γ radiation field, which represents a more realistic scenario. Pile-up effect leads to a degradation of the PSD performances and a reduction of the FOM, since a pile-up signal either falls in the wrong particle distribution or does not fall in any of the two distributions that the PSD analysis individuates [5].

It is worth mentioning that pile up related effects are mainly affected by the electronic read-out system (i.e. the 64 pixel array) and by the selected PSD parameters. The results presented in this work are thus mainly aimed at comparing the two scintillators for their application in the B-RAD detector. However, they can also be used for comparison with similar detectors, especially because of the lack in the literature of data measured with similar photodetectors (large SiPM array).

The scintillators were exposed to different photon dose rates from 1 μSv/h to 15 mSv/h using a ^{137}Cs source at the Calibration Laboratory of the Radiation Protection group at CERN [30, 31]. Figure 3.15 shows the resulting count rate as a function of the dose rate and of the source particle frequency (expressed as the rate of the source particle fluence in cm^{-2} s^{-1}). The linear fitting equations calculated outside the count rate saturation region are also shown (for a better visualization the plot in Figure 3.15 starts from 300 μSv/h). For both detectors, count rate saturation effects start at around 1 mSv/h (i.e. around 10^6 cm^{-2} s^{-1} source particle frequency) which corresponds to around $3 - 4 \times 10^4$ counts per seconds (cps).

The measurements were repeated with an Am-Be neutron source at dose rates between 5 μSv/h and 1.5 mSv/h, which is the maximum available dose rate at the Calibration Laboratory. The neutron count rate was derived from the PSD analysis after rejecting the γ-ray events. Figure 3.16 shows the results: the left y-axis is the measured count rate, while the right y-axis represents the count rate corresponding to neutron events only, calculated after the PSD. As can be seen, the response is linear over the entire range since the maximum particle frequency is below the saturation limit for both detectors. The maximum count rate measured with the Am-Be source is of the order of 10^3 cps for both detectors. The total source particle frequency is actually unknown because the γ-ray field emitted by the Am-Be source is not characterised. However, the maximum count rate

measured by both detectors is quite lower than the count rate saturation value found with the photon source.

The pile-up depends only on the frequency of the particle interacting inside the crystal (which is proportional to the lower x-axis of Figures 3.15 and 3.16). The dose rate instead also depends on the radiation weighting factor w_R, i.e. on the type of particle. According to the ICRP Report 92 [75], the recommended w_R for photons is 1, while for neutrons it varies with energy. Between 2 MeV–20 MeV, i.e. at the energy range of the Am-Be spectrum main peak, the recommended w_R for neutrons is 20. For this reason at the same dose rate (around 1 mSv/h), with ^{137}Cs the detectors start to saturate, whereas with Am-Be their response is still linear.

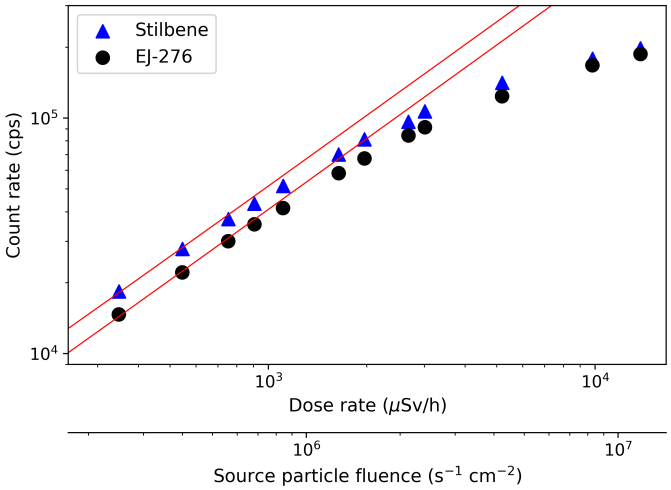

Figure 3.15: Count rate versus dose rate (top x-axis) and source particle fluence rate (bottom x-axis) measured with the stilbene (blue triangles) and the EJ-276 (black dots) scintillators when exposed to photons from a ^{137}Cs source before the count rate saturation region. The red line represents the linear fits calculated outside the count rate saturation region to the data points. The error bars are smaller than the data points.

The variation of the PSD with increasing pile-up was studied by means of the 2D PSD histogram plot. Each detector was first irradiated with the Am-Be source alone at the maximum available dose rate, i.e around 1.5 mSv/h. Afterward, the detectors were exposed simultaneously to the ^{137}Cs and Am-Be sources. The neutron source activity and the source to detector distance were kept constant to maintain the neutron dose rate at 1.5 mSv/h, whereas the photon dose rate was progressively increased by increasing the source activity. Five ^{137} Cs sources are available at the Calibration Laboratory with activity of 300 MBq, 3 GBq, 30 GBq, 300 GBq and 3 TBq. Because of the lack of information of the γ-ray component of the Am-Be source, the total frequency of the source particles is unknown and the following results are presented as a function of the count rate measured by the detectors. Figures 3.17, 3.18 and 3.19 compare the 2D histogram of the PSD versus energy measured with the stilbene with the Am-Be source alone, adding the 30 GBq ^{137}Cs source and adding the 300 GBq ^{137}Cs source, respectively. The source configuration is also indicated in the corresponding figure. The count rate measured for the three configurations was around 1×10^3 cps, 5×10^3 cps and 4×10^4 cps, respectively. With 30 GBq ^{137}Cs (Figure 3.18) many pile-up events are detected in the energy range of the ^{137}Cs source, which become dominant with 300 GBq ^{137}Cs. The same behaviour is observed with the EJ-276 starting at 3.5×10^3 cps. Figures 3.18 and 3.19 clearly show that the signals affected by pile-up are spread along the entire PSD range leading to a bad discrimination and to a completely wrong estimation of the dose rate if the energy

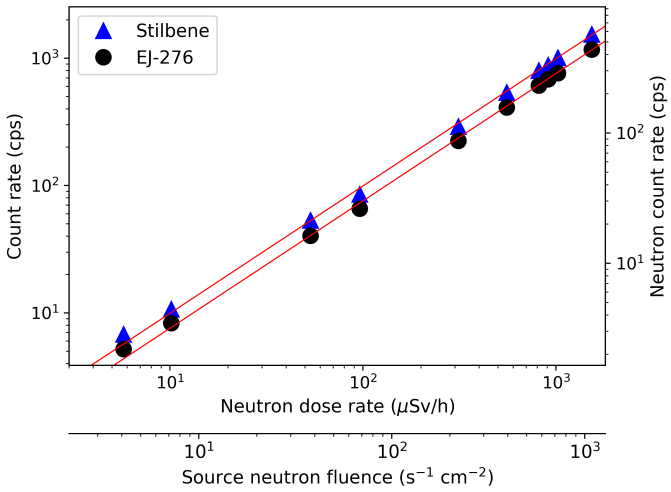

Figure 3.16: On the left y-axis, count rate versus dose rate (top x-axis) and source neutron fluence rate (bottom x-axis) measured with the stilbene (blue triangles) and the EJ-276 (black dots) scintillator when exposed to an Am-Be neutron source. On the right y-axis, the neutron count rate calculated after the PSD analysis for the same measurements. The red lines represent the linear fits to the data points. The error bars are smaller than the data points.

threshold is not modified.

The PSD was also monitored by calculating the FOM while keeping constant the energy threshold of each detector. Figure 3.20 shows the results: the full symbols refer to the measurements with the Am-Be source alone, the open symbols to the Am-Be + ^{137}Cs sources. The FOM is expressed as a function of the total count rate. The dashed lines represent the limit of the working region of the two detectors, at which a less accurate PSD can still be performed (the variation between the maximum and the minimum value is about 5%). They correspond to 5×10^3 cps for the stilbene and to 3.5×10^3 cps for the EJ-276, i.e. when the 30 GBq ^{137}Cs source is used in combination with the Am-Be source. Above 10^4 cps a zero value was arbitrary assigned to the FOM since the discrimination was not feasible. Increasing the energy threshold, a correct discrimination can be restored for example, as can be seen in Figure 3.18, where the discrimination is still feasible if the energy threshold is set above 1.5 MeVee.

The measurements performed at the Calibration Laboratory show that the maximum count rate sustained by both detectors is of the order of 10^4 cps corresponding to about 10^6 cm^{-2} s^{-1} source particle frequency (when the detectors are exposed to ^{137}Cs). With an Am-Be source this leads to a working range up to more than 1 mSv/h neutron dose rate, which is acceptable for a portable neutron dose rate meter. However the unavoidable and usually not quantifiable γ-ray background could pose a problem: when exposed to a mixed n/γ radiation field (1.5 mSv/h neutron dose rate, 60 μSv/h photon dose rate) the FOM of both scintillators drastically drops. As stated before, the count rate range in our detectors is mainly limited by the high capacitance of the employed photodetector. For this reason, it can be extended simply by using a fast PMT in place of the large area SiPM array. This option was not considered since the B-RAD is designed to work in high magnetic field regions and a PMT cannot be employed. A Pile-Up Rejection (PUR) algorithm was instead tested as discussed in the following section.

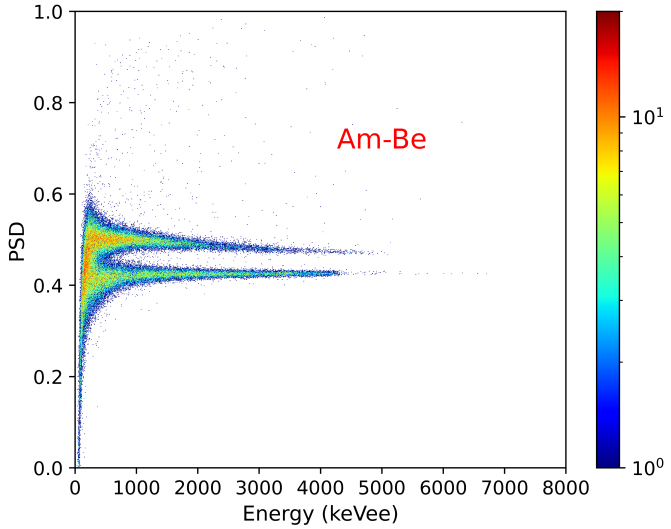

Figure 3.17: 2D histogram plot of the PSD for the stilbene when irradiated with an Am-Be neutron source at 1.5 mSv/h (around 1,000 cps).

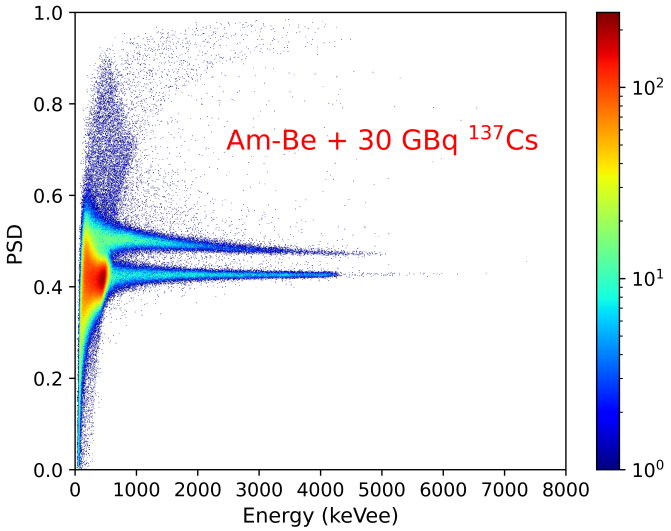

Figure 3.18: 2D histogram plot of the PSD for the stilbene when irradiated with an Am-Be neutron source at 1.5 mSv/h and a ^{137}Cs photon source at 60 µSv/h (around 5,000 cps).

3.4.4 Pile-up rejection

A PUR algorithm was developed to improve the PSD analysis and increase the count rate linearity of the two detectors. The PUR algorithm was defined similarly to the fractional double-pulse technique described in [46, 47]: a pulse is classified as double if consecutive samples (points of the digitalized pulse) exceed a certain fraction of the pulse height in the tail region. The algorithm was tested for a single combination of the parameters (time windows and threshold) since the results were sufficiently good and proved the possibility to apply the proposed PUR. However, for its application in the B RAD, these parameters must be optimised.

The time windows were selected by a qualitative analysis, i.e. by observing the neutron and photon standard pulses (see Figure 3.21). For both scintillators, the tail region was selected starting from 1 μs (indicated by the dashed black vertical line in Figure 3.21) and the total recorded length was set at 4 μs. The threshold (represented by the horizontal

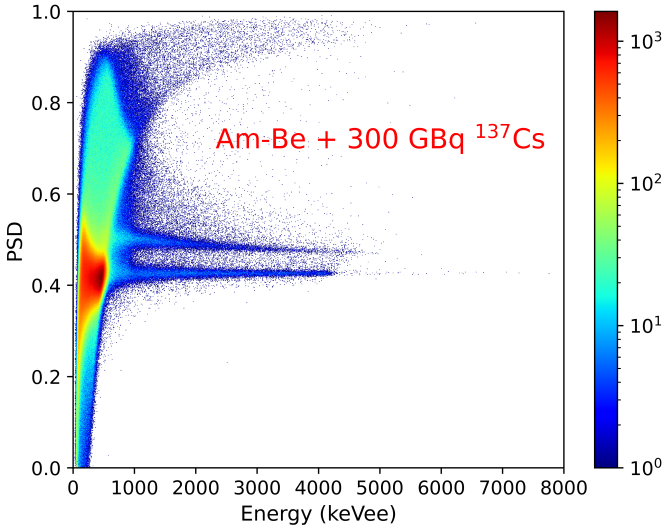

Figure 3.19: 2D histogram plot of the PSD for the stilbene when irradiated with an Am-Be neutron source at 1.5 mSv/h and a ^{137}Cs photon source at 650 µSv/h (around 40,000 cps).

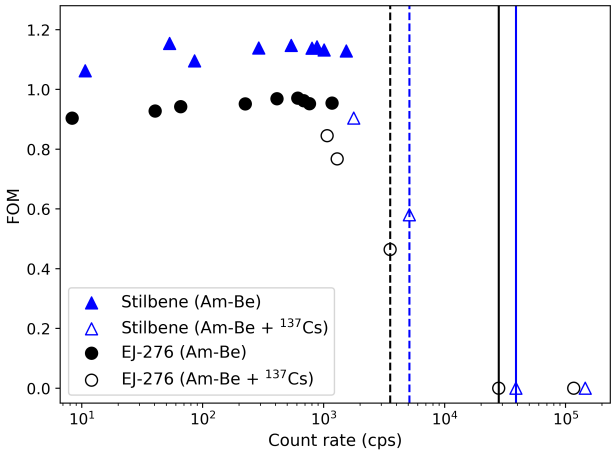

Figure 3.20: FOM as a function of count rate for two source configurations. The full symbols are the FOM calculated with the stilbene (blue triangles) and the EJ-276 (black dots) irradiated with an Am-Be source at different dose rates. The open symbols are the FOM calculated with the stilbene (blue triangles) and the EJ-276 (black dots) irradiated with an Am-Be source at a constant dose rate (1.3 mSv/h) and with a ^{137}Cs source at variable dose rate. The dashed vertical lines represent the limit for the stilbene (blue dashed line) and the EJ-276 (black dashed line) when the PSD is still feasible; the continuous lines represent the limit for the stilbene (blue line) and the EJ-276 (black line) at which the discrimination can no longer be performed.

line in Figure 3.21) was selected as the fraction of the γ-ray pulse amplitude at 1 μs with respect to the pulse height. The number of samples was chosen to exceed the time interval between the dashed black and dashed-dotted red vertical lines in Figure 3.21. The latter was selected as the point where the neutron pulse crosses the threshold. Following this approach, the threshold was set at 19% and 21% of the pulse height, for the stilbene and the EJ-276, respectively. The sampling frequency was set to 250 MHz for both scintillators.

At first, the PUR was applied after irradiating the detectors with a ^{137}Cs source in the 1 μSv/h–15 mSv/h dose rate range. Figures 3.22 and 3.23 show the 2D histogram plots acquired with the stilbene before and after applying the PUR at 1 mSv/h and at

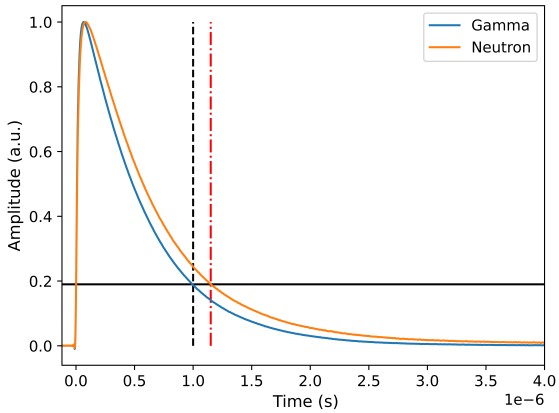

Figure 3.21: The neutron and γ-ray standard pulses in stilbene. The horizontal line represents the amplitude threshold selected for the PUR, the vertical lines the minimum time intervals that the signal amplitude must exceed, in the tail region, to be discarded by the PUR.

10 mSv/h, respectively. One should note that γ-ray events are expected in the bottom region of the plot, delimited in Figures 3.22 by the continuous red line. Figure 3.22 (left) shows as γ-ray events are erroneously classified as neutron events because of pile-up, while Figure 3.22 (right) demonstrates that the PUR is able to correctly remove them.

In analogy to [46], the erroneous classification ratio (ER) was calculated as the ratio between the signals detected in the neutron region over the total detected pulses, before and after the PUR. The results are plotted in Figure 3.24 for the stilbene (on the left) and the EJ-276 (on the right). After the PUR, for both detectors the curves of ER decreases by a factor of 10 in regard to the same curves obtained before the PUR, also at high dose rates. The two curves of ER after the PUR seem to saturate above 1 mSv/h, while the curves of ER before the PUR are linear up to 10 mSv/h. This is probably due to the spreading of the pile-up events along the entire PSD range, i.e., also in the γ-ray region (below the continuous red line in Figures 3.22 and 3.23). A corrected ER factor (ER_{cor}) was defined as the ratio between the signals detected in the neutron region over the signals detected in the region delimited by the γ-ray distribution, confined in Figures 3.22 and 3.23 by the continuous and dashed red lines. The ER_{cor} is also plotted in Figure 3.24 (red crosses). The ER_{cor} is linear up to 10 mSv/h for both detectors. Above this value it starts to saturate for the EJ-276 probably because pile-up events are also detected inside the γ-ray region, which cannot be discriminated by the PUR. However, the PUR is still able to well discard false events in the neutron region, as shown in Figure 3.23.

The PUR was also tested in a mixed n-γ field from an Am-Be source, at around 1.5 mSv/h, and from a ^{137}Cs source, at 5 μSv/h and 60 μSv/h. Figures 3.25 and 3.26 show the PSD plot before and after the PUR for the stilbene. The green lines were calculated from the PSD plot (Q_{long} vs Q_{short}) acquired with the Am-Be source alone as the lines which enclose the region of the neutron signals.

The PSD is dominated by the ^{137}Cs signals, especially with the 60 μSv/h ^{137}Cs source, however the Am-Be source is still detected below the ^{137}Cs distribution. The tails of the neutron and γ-ray distributions can be identified. After applying the PUR, the pile up signals are correctly rejected. In fact, more than 95% of the signals above the neutron region are always discarded. With 5 μSv/h ^{137}Cs source, less than 5% of the signals inside the neutron region are erroneously rejected. With 60 μSv/h source (and at higher dose rate) the number of detected neutrons (among 30,000 signals) was too low to evaluate the efficiency of the PUR. This is due to the dead time of our acquisition system, mainly

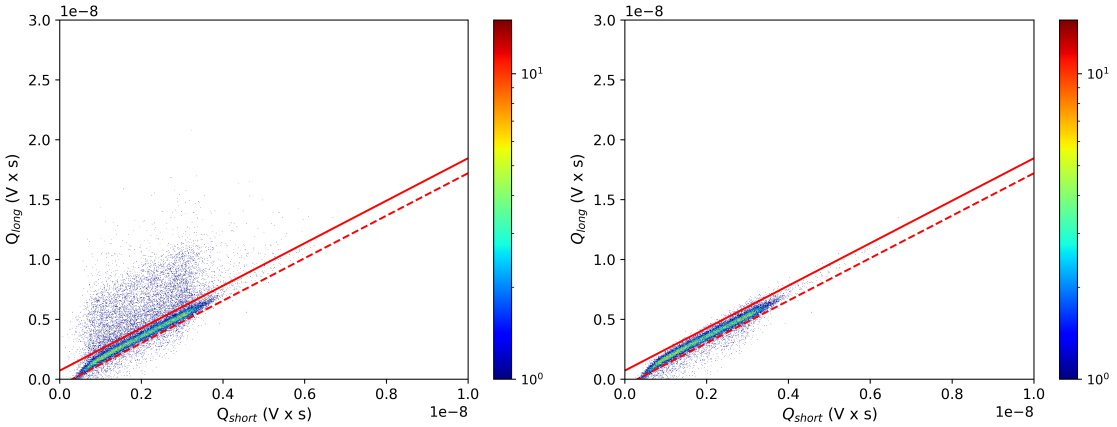

Figure 3.22: The Q_{long} vs Q_{short} 2D histogram plot of the stilbene irradiated with a ^{137}Cs source at 1 mSv/h before (left) and after (right) applying the PUR algorithm. The two red lines delimit the γ-ray region.

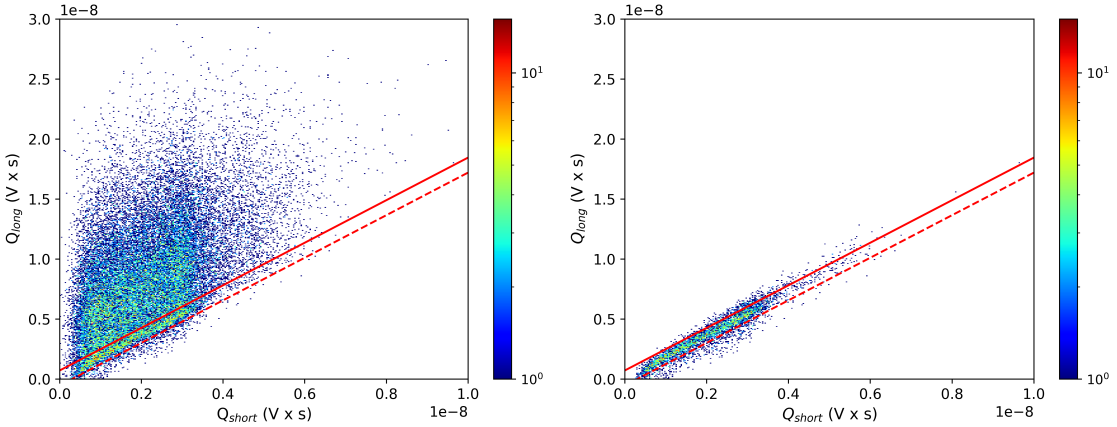

Figure 3.23: The Q_{long} vs Q_{short} 2D histogram plot of the stilbene irradiated with a ^{137}Cs source at 10 mSv/h before (left) and after (right) applying the PUR algorithm. The two red lines delimit the γ-ray region.

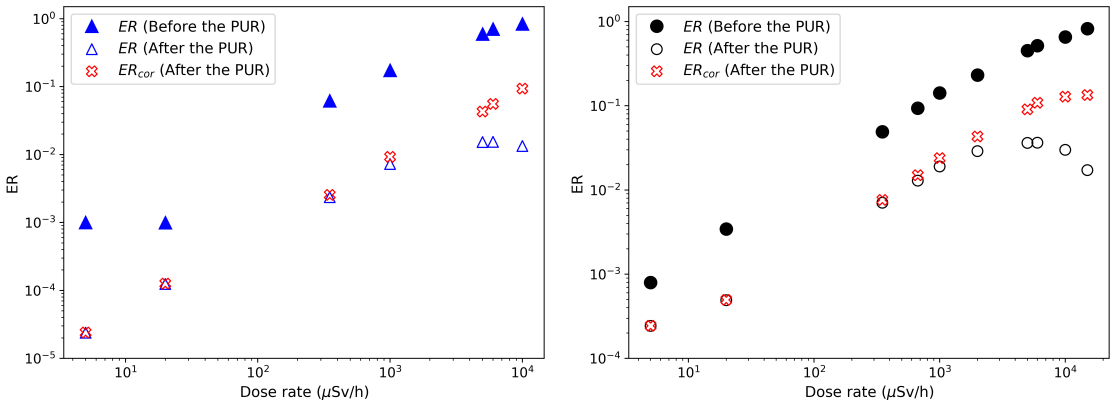

Figure 3.24: The ER and the ER_{cor} for the stilbene (left) and EJ-276 (right) irradiated with a ^{137}Cs at different dose rate values, before and after applying the PUR algorithm.

induced by the oscilloscope used instead of the digitizer, combined with the relatively high γ-ray sensitivity of organic scintillators. Nonetheless, Figure 3.26 shows that neutrons from

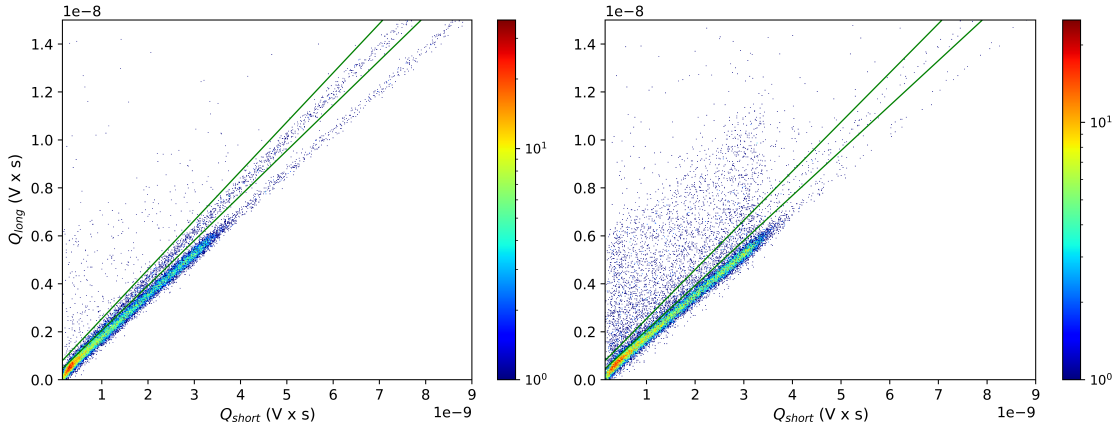

Figure 3.25: The Q_{long} vs Q_{short} 2D histogram plot for the stilbene irradiated with an Am-Be source (at 1.5 mSv/h) and a ^{137}Cs source (at 5 µSv/h on the left and at 60 µSv/h on the right), before applying the PUR algorithm. The green lines delimit the detected neutron signals.

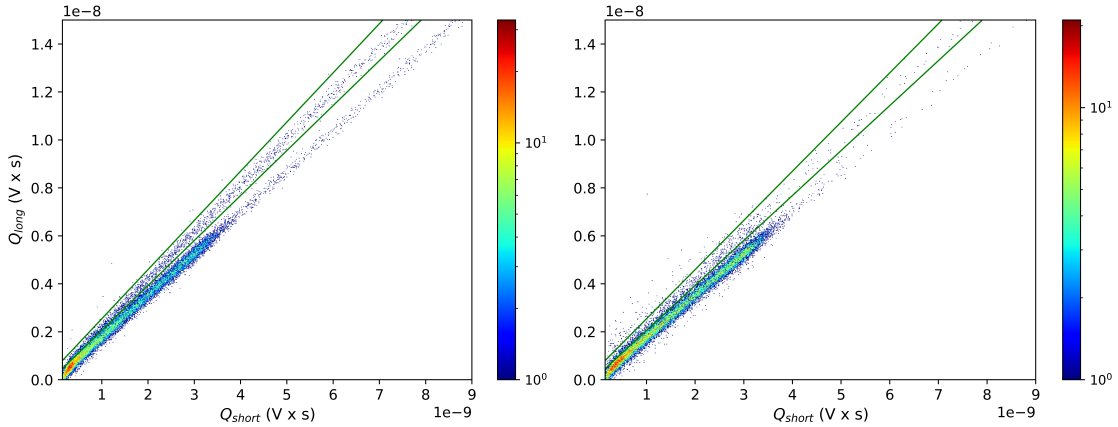

Figure 3.26: The Q_{long} vs Q_{short} 2D histogram plot for the stilbene irradiated with an Am-Be source (at 1.5 mSv/h) and a ^{137}Cs source (at 5 µSv/h on the left and at 60 µSv/h on the right), after applying the PUR algorithm. The green lines delimit the detected neutron signals.

the Am-Be source are still detectable after the PUR, in spite of the low n/γ ratio.

Due to the long time profile of the detectors (discussed above) and the non-negligible sensitivity of organic scintillators to γ-rays, a pile-up rejection algorithm is necessary in many applications for the B-RAD. The PUR proposed in this work is promising: with ^{137}Cs, the pile-up events were correctly discarded up to more than 10 mSv/h, above the upper limit of the dose rate range for common portable survey meters (few mSv/h). With the Am-Be neutron source the PUR discards pile-up events at the expense of the neutron detection efficiency, but without rejecting all neutron signals. However, for the latter case, only a qualitative analysis was possible because of the low number of detected Am-Be particles.

3.4.5 Neutron detection efficiency

After characterising the detectors in terms of n/γ discrimination capability and dose rate working range, the neutron detection efficiency must be evaluated. However, in organic scintillators the calculation of the neutron detection efficiency is not an easy task for

two main reasons: 1) the pulse height spectrum in organic scintillators has a continuum shape (see Section 3.1.2), and hence the calculated efficiencies are hugely affected by the threshold (all the counts below the threshold are not counted); 2) the emerging neutron spectra in organic scintillators depends on the spectrum of the specific source neutron. However a comparative analysis between the stilbene and EJ-276 can be performed.

The neutron detection efficiency was calculated as the average of the intrinsic neutron efficiencies (ϵ_i) measured in the linear range between 5 μSv/h and 1.5 mSv/h (see Figure 3.15), where ϵ_i is defined as follows [76]:

$$\epsilon_i = \frac{R_{det}}{A \times \Omega} \tag{3.10}$$

where R_{det} is the detector count rate, A the source activity in terms of neutrons per s and Ω the solid angle subtended by the detector from the source. The intrinsic detection efficiency can be expressed in terms of percent by multiplying ϵ_i by 4π. Two Am-Be sources of 100 GBq and 888 GBq were used for the measurement, corresponding to 6.40×10^6 neutrons per second and to 5.03×10^7 neutrons per second, respectively, as provided by the manufacturer. The different ratio between the nominal activity (in Bq) and the neutron fluence for the two sources might be due to a different composition of the source components since the Am/Be ratio of both sources is unknown. This difference might also origin from a different geometry between the two sources which might lead to a different amount of material surrounding the source in its irradiation position.

The obtained neutron detection efficiencies are 12% for the stilbene and 9% for the plastic, which correspond to 2.0 counts per nSv and 1.4 counts per nSv, respectively. The values in counts per dose were calculated taking into account the dose per fluence coefficient of the Am-Be (391 pSv cm^2) reported by the ISO 8529-1:2001 [77]. If the same energy threshold is applied to both scintillators equal to 250 keVee, the calculated efficiency of the two detectors is comparable: 1.4 counts per nSv for the EJ-276 and 1.7 counts per nSv for the stilbene.

3.4.6 Temperature dependence

Finally the temperature dependence of both detectors is discussed. For scintillator and SiPM based detectors the variation of the detector response with temperature is usually a crucial point since it depends on two independent effects: the variation of the scintillator light yield and the variation of the SiPM gain. The latter is a well-known effect which consists of the increase of the breakdown voltage with temperature. This effect is due to the decreasing of the potential barrier between the p-n junction, and the corresponding gain reduction. The net effect of the SiPM to the detector system can be translate as an increasing of the detection threshold [78]. The gain variation can be estimated by the data provided by the manufacturer. According to [57], the breakdown voltage increases with temperature at a rate of 21.5 mV °C^{-1} and the gain linearly decreases.

The rate of variation of the breakdown voltage with temperature was also measured and compared with the datasheet [57]. The SiPM array was coupled to the ArrayJ-BOB3-64-V1PO breakout board, a commercial readout board provided by SensL specifically developed for easy testing and readout of ArrayJ products (Figure 3.27). The board and the SiPM array were placed in a climate chamber inside a light-tight box. The temperature of the SiPM was measured by a thermocouple placed close to it, because of the different thermal inertia of the box and the climate chamber. The temperature of the chamber was varied from -10°C to 40°C and measurements were carried out at 10°C steps. At each temperature, a varying bias voltage from 1 V to 30 V was supplied to the SiPM by a Keithley 2450 source meter [79], placed outside the chamber. The bias voltage was varied every 2 s with a 1 V step well before the breakdown and 0.1 V on the proximity and above.

The higher sampling frequency in the former case, ensures the accuracy of the breakdown voltage calculation. The current across the SiPM was measured by the same source meter using the Keithley Kickstart software for automatic acquisition. The breakdown voltage at each temperature was obtained as *"the voltage intercept of a straight line fit to a plot of* $\sqrt{I}$ *vs. V, where V is the overvoltage."* [57]. Figure 3.28 shows the $\sqrt{I}$ *versus* V plot measures at 20°C with the linear fit in the region above the breakdown voltage.

Figure 3.29 shows the values of the breakdown voltage measured at each temperature and the linear fit to the data points. The resulting fitting equation is shown in Figure 3.29. The calculated gradient is 21.7 ± 0.6 mV/°C in perfect agreement with the value reported from the datasheet.

Figure 3.27: The SiPM Array J-30035-64P and the ArrayJ-BOB3-64-V1PO breakout board used to measure the variation of the breakdown voltage with temperature.

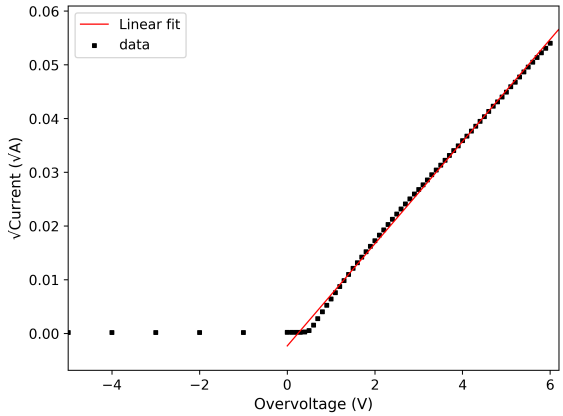

Figure 3.28: The square root of the current versus the overvoltage measured with the J-30035-64P SiPM array at 20°C and the linear fit to the data points above the breakdown voltage.

The temperature dependence of the stilbene and EJ-276 detectors was measured by placing the detector inside the light-tight box, in the climate chamber. The temperature

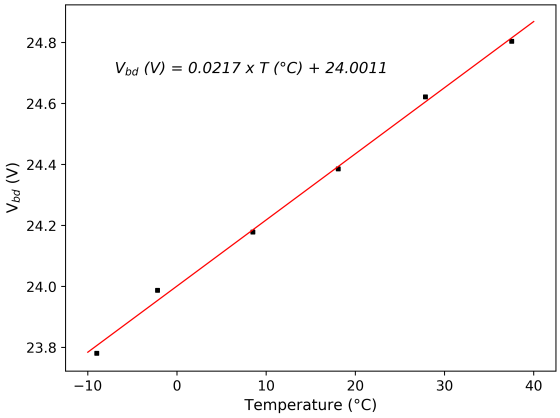

Figure 3.29: The breakdown voltage versus temperature measured with the J-30035-64P SiPM array and the linear fit to the data points.

of the chamber was varied from -10°C to +40°C at a rate of 10°C h^{-1} (according to the manufacturer [52]) and the temperature of the SiPM was measured by a thermocouple as in the previous measurements. Measurements were performed in 10°C steps with a ^{137}Cs and an Am-Be source independently. The combined effect of the light yield variation and of the SiPM, was evaluated by measuring the variation of the Compton edge position (in the ^{137}Cs spectrum), calculated as described in Section 3.4.1. The Compton edge variation due to the SiPM contribution was assumed proportional to the gain variation. Finally, the contribution of each scintillator was obtained from the comparison of the measured and calculated variation of the Compton edge position, since the former is ascribed to the SiPM + scintillator system, while the latter is attributed to the SiPM only.

Figure 3.30 compares the variation of the measured and calculated Compton edge position for both detectors. The x-axis is the temperature measured by the probe close to the SiPM. For the stilbene, below ∼20°C the measured Compton edge position linearly decreases with temperature with a slope of -18.7 ± 0.4 channel °C^{-1} versus a variation of -12.7 channel °C^{-1} due to the SiPM only, i.e. the light yield of the stilbene decreases inducing a faster variation of the Compton edge position. Above 20°C the stilbene light output increases and partially compensates the SiPM effect. Similarly, for the EJ-276, the Compton edge position decreases below 20°C (see Figure 3.30). Nonetheless, the difference between the measured and calculated curves is smaller: -10.5 ± 0.6 channel °C^{-1} versus -7.6 channel °C^{-1} respectively. Above 20°C, the temperature dependence is mainly attributed to the SiPM. This is partially in agreement with [80], where the variation of the Compton edge position measured by a PMT with a plastic scintillator is almost flat in the temperature range -30°C –20°C. However, in [80] the exact composition of the plastic scintillator is not specified. The total percent variation of the Compton edge position is around 25% for both detectors.

The variation of the PSD capability was also investigated with the Am-Be source by observing both the variation of the PSD distribution, and of the FOM. Figure 3.31 shows the PSD distribution at different temperatures for the stilbene and the EJ-276, and Figure 3.32 compares the variation of their FOM. In Figure 3.31, the left and right Gaussian distributions (on both plots) are associated to γ-rays and neutrons respectively. In both detectors, up to 20°C, the shape of the PSD distribution remains unchanged but, as expected, the number of counts decreases with temperature because of the increasing breakdown voltage. For the stilbene, at 30°C and 40°C, the neutron distribution shifts to the right and the right tail of the γ-ray distribution increases. The intensity of the fast decay appears to decrease with temperature in favour of the slow component. This effect

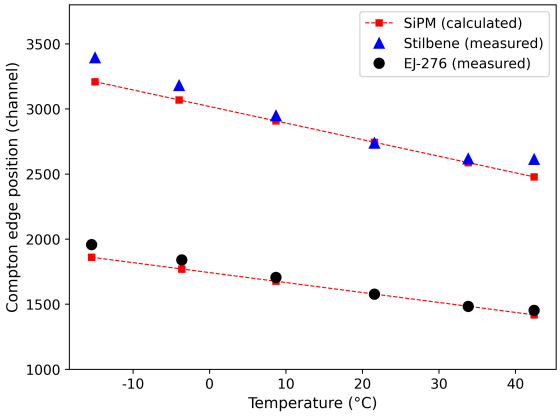

Figure 3.30: Variation with temperature of the Compton edge position of a ^{137}Cs source for the stilbene and EJ-276. The x-axis is the temperature measured by a thermocouple close to the SiPM array while the temperature chamber was varied between -10°C and +40°C. The error bars are smaller than the data points.

is generally possible since the temperature can affect different scintillation mechanisms in different ways. For the EJ-276, the PSD distribution above 20°C shows an opposite trend as compared to the stilbene. The peaks of the two Gaussian equations slightly move to the left and in addition, some signals are detected in the region between the two distributions. At higher temperatures, the lower light yield of the EJ-276 combined with the higher breakdown voltage of the SiPM has a large impact on the PSD analysis. A greater number of signals is in fact detected just above the digitizer threshold and it is well known that for low amplitude signals the discrimination is not clear. To overcome this limit and for a better comprehension, a higher bias voltage can be set in the EJ-276 detector. For both scintillators the temperature increase induces a broadening of the neutron and γ-ray distributions in the PSD plot resulting in the decrease of the FOM (see Figure 3.32).

The variation with temperature of the light yield in organic scintillators has not been quantified yet. Baker et al. [81] reported a weak decreasing trend of the stilbene light yield with increasing temperature between -90–70°C, partially in agreement with this work. In [81] the stilbene was irradiated both with a γ-ray source and a neutron source. A study was performed with an anthracene crystal (comparable to the stilbene) only for a 6°C temperature range (22–28°C) and only for γ-ray detection [82]. In this study, a slightly linear decreases of the light output was measured of less than 10%. In [80], the temperature dependence of the stilbene is deeply investigated between -30°C and 60°C and the pulse shapes at different temperature are also reported. The pulse shape seems to be constant in the aforementioned range. However, the discussion is lacking and a more accurate study is necessary (e.g. fitting of the average signals). On the other hand, the light yield of plastic scintillators was considered temperature independent [83] until recent studies have demonstrated some dependence [84, 85]. In [85], a small or almost null temperature dependence was measured for some plastic scintillators according to the substrate material.

Figure 3.33 shows the variation of the neutron counts with temperature (15 minutes of acquisition time). The variation of the neutron counts with temperature is around 10% for both detectors, which is still acceptable for applications in radiation protection. The measured neutron counts with the stilbene has a minimum at 10°C, while the EJ-276 is almost flat up to 20°C and shows a decreasing trend above that temperature. This variability makes the temperature correction not an easy task. Further investigation such

as measurements with a PMT and a pulse shape analysis should be performed.

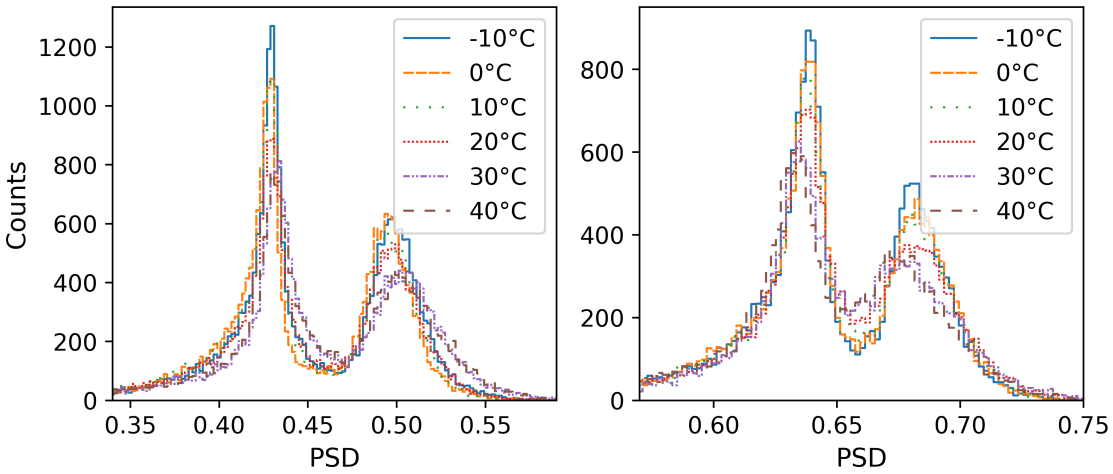

Figure 3.31: Variation of the PSD distribution measured with an Am-Be source with the stilbene (left) and EJ-276 (right) while the temperature varied between -10°C and +40°C.

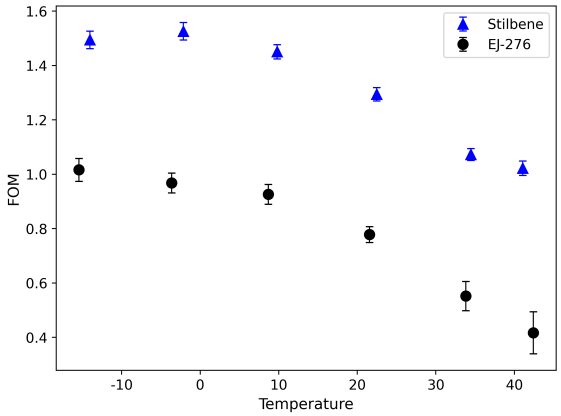

Figure 3.32: Variation with temperature of the FOM measured with an Am-Be source for the stilbene and EJ-276. The x-axis is the temperature measured by a thermocouple close to the SiPM array, while the temperature in the chamber varied between -10°C and +40°C.

3.5 Conclusions

The performance of a stilbene and an EJ-276 plastic scintillator coupled to an 8 × 8 SiPM array J-30035-64P from SensL were evaluated and compared, in view of their potential application in the B RAD portable survey meter for fast neutron detection. The reported results show that the energy resolution with a ^{137}Cs source is 15% for the stilbene and 20% for the plastic. Due to the low atomic number of organic scintillators, their energy resolution is poor however they were not considered for spectrometry applications.

For the considered application, two important parameters are the capability to discriminate and reject the γ-ray component from the neutron one and the neutron detection efficiency. The stilbene shows a better n/γ discrimination capability via the PSD with respect to the EJ-276: a FOM of 1.54 is achieved with the minimum threshold, while a threshold of about 800 keV had to be set to reach a sufficient discrimination with the

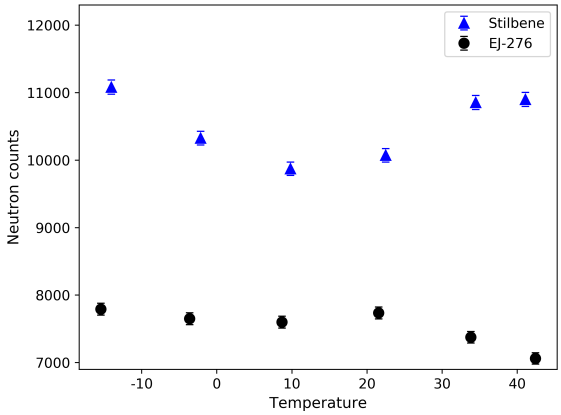

Figure 3.33: Variation with temperature of the measured neutron counts (15 minutes of acquisition time) with an Am-Be source for the stilbene and EJ-276. The x-axis is the temperature measured by a thermocouple close to the SiPM array while the temperature in the chamber varied between -10˚C and +40˚C.

plastic (FOM $>$ 1.27). The neutron detection efficiencies are 12% for the stilbene and 9% for the plastic (2.0 nSv per counts and 1.4 nSv per counts, respectively).

The response of both stilbene and plastic starts to deviate from linearity at 1 mSv/h photon dose rate, whereas the PSD is stable up to 1.5 mSv/h neutron dose rate. However, the presence of a usually unknown γ-ray background together with the neutron field could limit the detector working range. When exposed to a mixed n/γ radiation field, the FOM of both scintillators drastically drops above 3–4$\times 10^3$ cps.

Below this limit, a Pile-Up Rejection algorithm can reduce the detection of false neutron events by one order of magnitude without affecting the neutron detection efficiency. Above this limit, the PUR algorithm can correctly remove pile-up events at the expense of the latter. The two scintillators show similar performance in terms of temperature variation in the range -10°C to +40°C. The variation of the measured Compton edge position is around 25%, while the variation of the neutron count rate is around 10%. This variation can be accepted in certain applications in radiation protection.

The work presented in this chapter was presented to the ELSE NUCLEAR company who will proceed in the development of an actual probe for fast neutron dose rate measurements.

Chapter 4

Investigation of CLYC-6 for thermal neutron detection and CLYC-7 for fast neutron spectrometry

This chapter identifies two additional neutron probes for the B-RAD, both based on Cs_2LiYCl_6:Ce (CLYC) crystal. CLYC is an inorganic scintillator available with either natural abundance of ^{6}Li and ^{7}Li (7.6% and 92.4% respectively) or enriched in ^{6}Li or ^{7}Li (respectively called in this work CLYC-6 and CLYC-7). The former is suitable for thermal neutron detection, the latter is commonly used for fast neutron measurements. In this chapter, a CLYC-6 and a CLYC-7 crystal were studied as a thermal neutron detector and as a fast neutron spectrometer respectively, in view of their possible integration in the novel B-RAD radiation survey meter.

The original project of the B-RAD did not include a probe for thermal neutron detection, since the greatest contribution to the total ambient dose equivalent is usually provided by fast neutrons (e.g. at high energy accelerators). However, the availability of a CLYC-6 crystal together with the increasing request on the market for a thermal neutron detector, as an alternative to the commonly used ^{3}He proportional counter, led us to investigate CLYC-6 as an additional probe for the B-RAD.

This chapter is divided as follows. Section 4.1 provides the basis for understanding the scintillation mechanism in inorganic scintillators such as CLYC. Section 4.2 summarises the CLYC main properties and the main neutron reactions involved in CLYC-6 and CLYC-7. Section 4.3 reports the details of the experimental setups and the methods used for the data analysis. Sections 4.4 and 4.5 discuss the CLYC-6 and CLYC-7 performances respectively. Section 4.6 reports the results in view of their application in the B-RAD.

4.1 Scintillation mechanism in inorganic crystals

The scintillation mechanism in inorganic scintillators depends on the energy band structure of the crystal lattice. An example is shown in Figure 4.1. Electrons in the so-called valence band are bound to the crystal, whilst electrons in the conduction band are free to migrate. When a charged particle crosses the crystal depositing its kinetic energy, the electrons in the valence band can excite to the conduction band, however any energy levels in between the valence and the conduction band is forbidden. When the electrons de-excited from the conduction to the valence band a photon is emitted with the same energy of the band gap. Two main reasons prevent their detection: 1) this process is inefficient since the

emission band almost overlaps the absorption band of the crystal, i.e. most of the emitted photons do not escape from the crystal; 2) the typical band gaps correspond to energy above the visible range. For this reason impurities are added into inorganic scintillators, usually called activators, which form the so-called recombination or luminescence centres.

In doped crystal the scintillation process usually occur as follows.

(1) The charged particle deposits its kinetic energy inside the crystal along its track.

(2) Electrons in the valence band absorbe this energy and excite to the conduction band, leaving the corresponding holes in the valence band.

(3) Holes rapidly drift to the activator centres and ionize them.

(4) Electrons in the conduction band travel throughout the crystal until they reach an ionized activator centre.

(5) Electrons drop in the activator site creating with the holes a neutral configuration with its own energy level structure lying within the forbidden energy gap (see Figure 4.1).

(6) If the activator centre is in an excited state, it de-excites to its ground state with the emission of scintillation light. The light emitted by the activator sites is in the visible range and is not absorbed by the crystal.

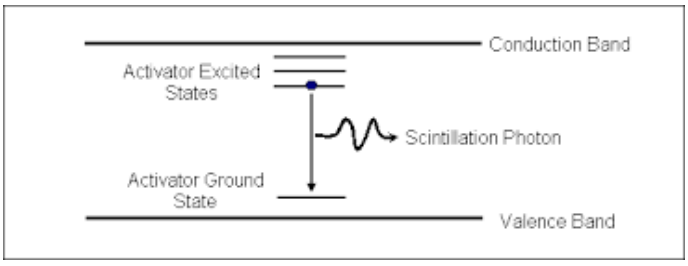

Figure 4.1: Energy band structure of a doped crystal scintillator [5].

The scintillation mechanism described above is simplified. In reality different scintillation mechanisms might be present in the same crystal also coming from the crystal itself (also called host luminescence). Another possibility is that the produced electron and hole travel together inside the crystal in a loosely bound configuration called exciton, instead of independently, and de-excites when it reaches an activator site. In general, the light emitted by a scintillator after an event of energy deposition can come from the de-excitation of different exciting states, each one characterised by its own characteristic decay time. As a result, the pulse coming from a scintillator usually shows both fast and slow components. Since the proportion between the slow and the fast components depends on the ionization density of the primary radiation, particle discrimination via the PSD method is usually possible also in inorganic crystals, as in CLYC. Additional effects affect the final de-excitation time of each scintillation mechanism, such as the temperature dependence.

Otherwise, competitive processes can also be present, such as afterglow and radiationless transitions (i.e. quenching effects) [5]. The latter lead to some non-linearities, which are, nevertheless, less important than in organic scintillators. Quenching effects are promoted by particles with high ionization density, i.e. the light yield differs with the type of particle crossing the scintillators per unit energy. This difference is quantified by the quenching factor as deeper described in Section 4.4.2 and Section 4.5.2 for CLYC-6 and CLYC-7. respectively.

4.2 Neutron detection in CLYC-6 and CLYC-7 crystal

CLYC is a promising inorganic scintillator from the elpasolite family. It is characterised by high density (3.3 g cm^{-3}), high Z_{eff} (54), light yield linearity down to low energies (the light yield variation is 1.6% from 662 keV down to 14.4 keV) and good energy resolution ($< 5\%$ at 662 keV according to the datasheet) [86]. It can detect both γ-ray and neutron radiation with excellent neutron/γ-ray (n/γ) discrimination capability by the Pulse Shape Discrimination (PSD) technique (FOM > 2 according to the literature data) [87].

In CLYC-6, thermal neutrons are detected via the ^{6}Li(n,t)α reaction on ^{6}Li [88]. The (n,t) reaction is characterised by a relatively large Q-value of 4.78 MeV and a high cross section (940 b at 25 meV, see Figure 4.2 left plot). Moreover, the pulse height spectrum acquired by a lithium-based scintillator shows a single peak in correspondence of the thermal neutron reaction since the ^{6}Li neutron reaction goes exclusively on the ground state of its reaction products [5].

CLYC-7 is used for fast neutron measurements via the ^{35}Cl(n,p)^{35}S and ^{35}Cl(n,α)^{32}P reactions [89] below $\sim$ 20 MeV, with ^{35}S and ^{32}P in the ground or excited states. The Q-value of the (n,p) and (n,α) is 615 keV and 937 keV respectively. The right plot of Figure 4.2 shows the (n,p) and (n,α) cross sections on ^{35}Cl below 14 MeV. Below 5 MeV the ^{35}Cl(n,p)^{35}S is dominant. The energy threshold for the (n,α) reaction and for the (n,p) reactions to the excited states of ^{35}S is around 2 MeV. Between 5 MeV and 18 MeV, the cross section of the (n,p) and (n,α) reactions to the ground and to the excited states of the ^{35}S and ^{32}P respectively, are comparable and the different reactions cannot be distinguished [89]. Above $\sim$ 20 MeV the (n,t) and (n,d) reactions become also comparable. These reactions are not considered in this work because outside the energy range of interest for the B-RAD.

CLYC-7 was recently investigated [90, 91, 92] as a fast neutron spectrometer without unfolding below about 10 MeV, since the energy deposited by the emitted proton and α-particle is linearly proportional to the kinetic energy of the impinging neutron. In [89], the response of CLYC-7 to mono-energetic neutrons showed promising results as a spectrometer, since the energy peak coming from the ^{35}Cl(n,p)^{35}S reaction was still detected up to 8 MeV. However, above 2.5 MeV a second peak due to the (n,α) reaction is present [89] at lower energies because of the lower quenching factor for the (n,α) reaction in regard to the (n,p) reaction. Above 5.5 MeV, the spectrum degenerates in a continuum. Figure 4.3 shows the neutron spectra acquired by D'Olympia et al. [89] irradiating a CLYC-7 crystal with different mono-energetic neutron sources. Therefore, as already underlined in [93], fast neutron spectrometry with CLYC-7 in presence of a continuum spectrum is quite difficult already above 2.5 MeV since neutrons with the same energy undergo competing nuclear reactions and the univocal correlation between the initial neutron energy and the energy deposited by the emitted particle is lost.

On the other side, CLYC-6 cannot be employed as a spectrometer because the acquired neutron spectrum is usually dominated by a narrow peak due to the ^{6}Li(n,t)α reaction from thermal neutrons [5, 93, 92]. However, its large cross section makes it suitable for thermal neutron detection.

4.3 CLYC scintillators and experimental set-up

Both CLYC-6 and CLYC-7 crystals used in this work, were grown by Radiation Monitoring Device Inc. (RMD) [95]. The former (serial number 730-3D1, April 2020) is a parallelepiped with dimensions of 18×18×5 mm^3, enriched in ^{6}Li to >95%. The latter (serial number 039-2, September 2017) is a 1–inch right cylinder enriched in ^{7}Li to >99%. Both crystals were wrapped with a reflective inner coating and encapsulated in an

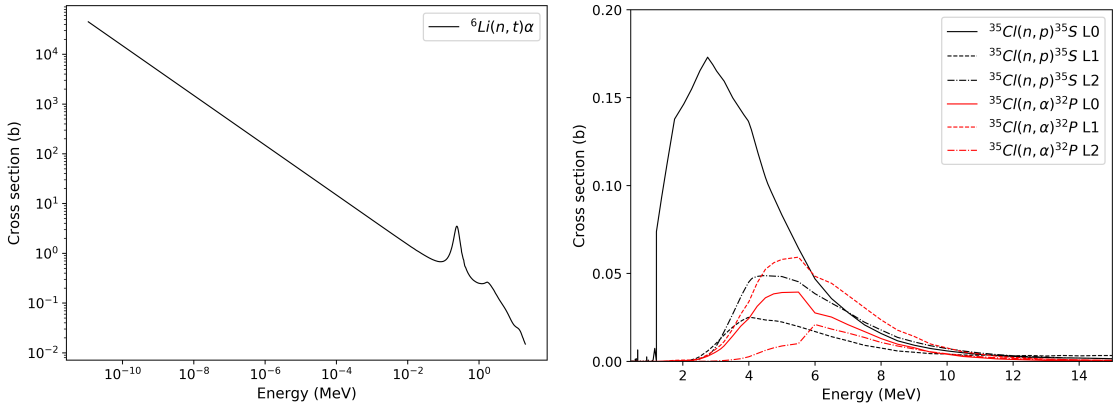

Figure 4.2: On the left, the (n,t) reaction cross section on ^6Li. On the right, the (n,p) and (n,α) reaction cross sections on ^{35}Cl, where L0 stands for the ground state and L1 and L2 for the first and second excited states. Data are taken from the ENDF/B VIII.0 library [94].

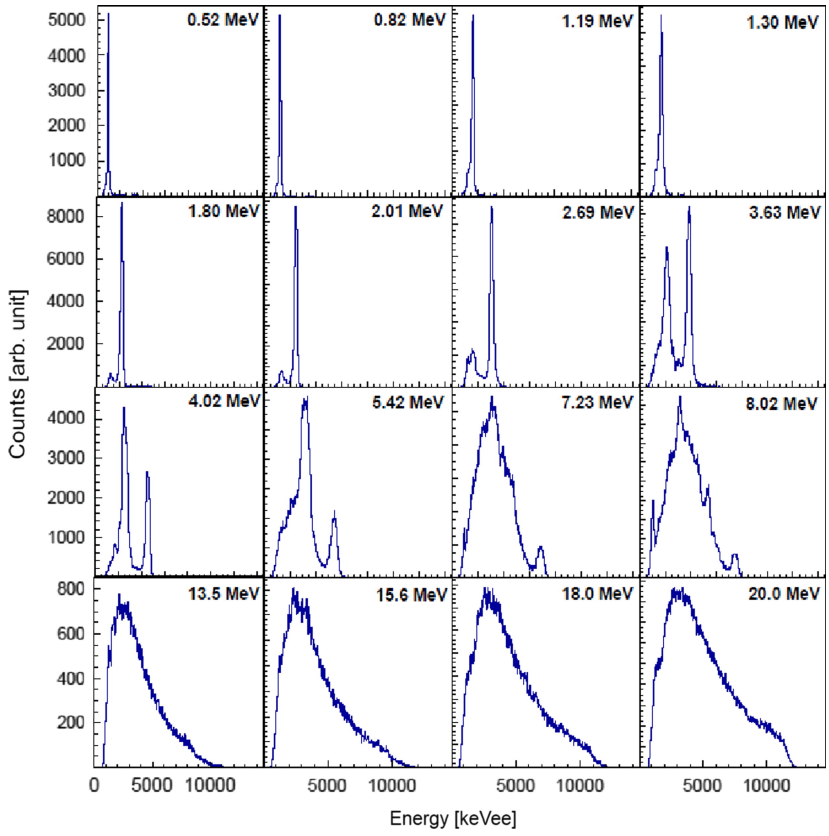

Figure 4.3: Calibrated neutron spectra acquired by D'Olympia et al. with CLYC-7 irradiated by mono-energetic neutron sources, as indicated in each plot [89].

aluminium casing (Figure 4.4) because CLYC is hygroscopic.

Each crystal was coupled with a R6231-100 Superbialkali Hamamatsu PMT [96] operating at +1100 V with optical grease, and placed inside a light–tight box. The output signal was directly sent to a 1 GHz, up to 2.5 Gs/s, 12 bit HDO6104 Teledyne Lecroy Oscilloscope, by a 50 Ω termination. The sampling frequency in this work was set to 250 Ms/s. Each signal was saved and offline analysed with a Python code [61]. For the measurement of the neutron detection efficiency a CAEN DT5720 digitizer (12 bit, 250 Ms/s) was used

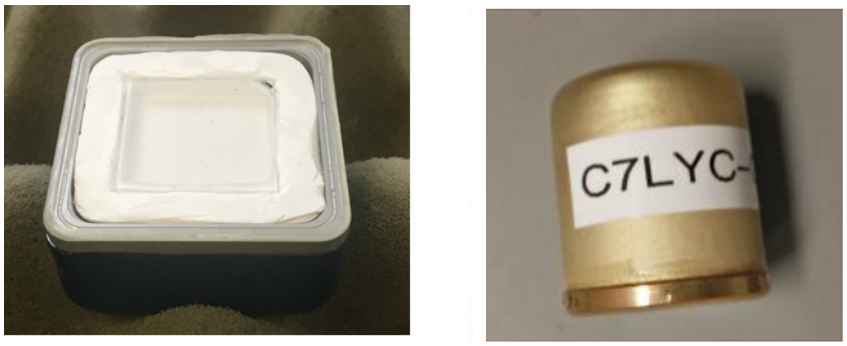

Figure 4.4: CLYC-6 (on the left) and CLYC-7 (on the right) crystals with their own packages.

in place of the oscilloscope, because it allows faster signal processing and is provided with the DPP-PSD software for on-line PSD analysis (which was used instead of the Python analysis).

Before each measurement, the experimental set-up was energy calibrated with γ-ray sources of different energies (^{137}Cs and either ^{60}Co or ^{22}Na). The charge spectrum of each γ-ray source was acquired by calculating the charge of each signal as the pulse integral over the selected acquisition time. The charge to energy equation was calculated by linear fitting of the data points corresponding to each photoelectric peak. The energy resolution of CLYC under γ-ray irradiation has been already investigated by many authors and it was not studied in this work. However, by way of example, Figure 4.5 shows the energy calibrated spectra of different γ-ray sources in CLYC-6 (on the left) and CLYC-7 (on the right).

A Thermo Scientific MP 320 Deuterium-Deuterium (D-D) generator [97] emitting 2.5 MeV neutrons was used for the measurements of the n/γ discrimination, energy resolution and quenching factor. The neutron energy resolution of CLYC-7 was not calculated because of a sudden degradation of the crystal, which only concerns the measurements with the D-D generator (Sections 4.5.1 and 4.5.2). The neutron detection efficiency of CLYC-6 was measured with the thermal neutron field available at the Calibration Laboratory (Cal Lab) of CERN Radiation Protection group, whose design and construction is described in details in Appendix A. The study of CLYC-7 as a fast neutron spectrometer was also performed by irradiating the crystal with neutrons from both an Am-Be source and a ^{252}Cf source. The measurements with the Am-Be and ^{252}Cf sources were performed before the worsening of the crystal performance.

In order to discriminate neutron from γ-ray events, the PSD analysis was performed by means of the Charge Integration Method, as described in the previous chapter. The n/γ PSD was performed by always setting the time windows t_{prompt} and t_{delay} to 70 ns and 2 μs respectively, unless otherwise specified in the corresponding section. The values of t_{prompt} and t_{delay} were selected as the time windows that optimise the FOM [59].

4.4 Measurements with CLYC-6

This section discusses the n/γ discrimination capability, the energy resolution and the quenching factor of the ^{6}Li(n,t)α reaction in CLYC-6. The measurements described in Sections 4.4.1 and 4.4.2 were performed with the mono-energetic neutron beam from the D-D generator, while the neutron detection efficiency was evaluated at the CERN Cal Lab.

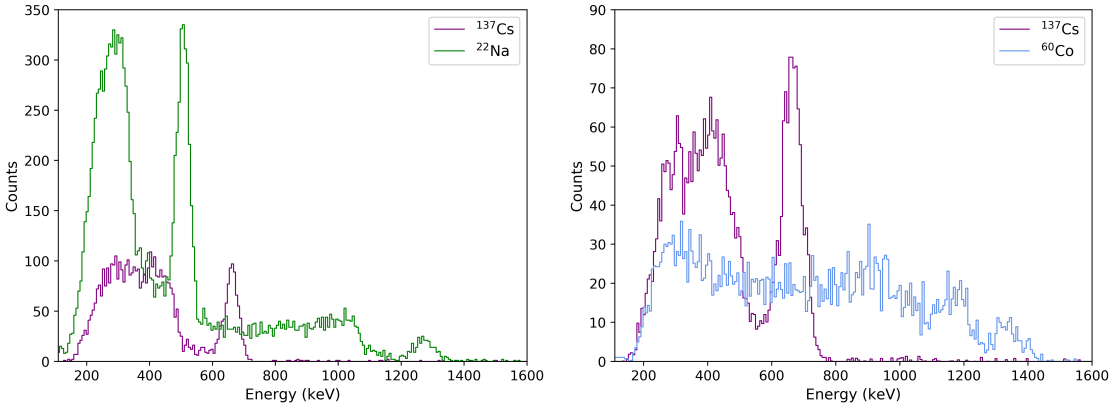

Figure 4.5: On the left, the ^{137}Cs and ^{22}Na energy calibrated spectra acquired with CLYC-6. On the right, the ^{137}Cs and ^{60}Co energy calibrated spectra acquired with CLYC-7.

4.4.1 n/γ discrimination capability

The n/γ discrimination capability of CLYC-6 was evaluated via the PSD method. Figure 4.6 shows the 1D and 2D histogram plots of the PSD and PSD versus energy acquired with CLYC-6 and the D-D generator. The calculated FOM is 2.20 (for 100 keVee energy threshold), which confirms the excellent n/γ discrimination capability of the crystal. The 2D PSD plot clearly shows the separation between the neutron events (on top of the plot) and the γ-ray events (on the bottom) with no overlap between the two distributions. The neutron distribution is dominated by a blob at around 3 MeVee corresponding to the ^{6}Li(n,t)α reaction from thermal neutrons [91, 93, 98] which corresponds to a single narrow energy peak in the neutron spectrum (see Figure 4.7) as discussed in the next section.

4.4.2 Neutron spectrum, quenching factor of the ^{6}Li(n,t)α reaction and energy resolution measured with a D-D generator

From the PSD analysis the neutron events were selected and plotted in terms of counts versus energy, after the energy calibration. Figure 4.7 shows the resulting neutron spectrum acquired with the D-D generator. The main peak is attributed to the thermal neutron absorption on ^{6}Li [88]. The detected peak was fitted using a Gaussian fitting equation and the corresponding Gaussian fit is shown in Figure 4.7. The detection of a single peak allows the calculation of the quenching factor for the ^{6}Li(n,t)α thermal neutron reaction.

The quenching factor q_F is defined as:

$$q_F = \frac{E_{eq.}}{E_N + Q} \tag{4.1}$$

where $E_{eq.}$ is the energy in equivalent electron-volt (eVee) of the reaction, E_N the energy in electron-volt of the impinging neutron and Q the Q-value of the reaction in electron-volt. In this case, E_N is negligible (i.e., thermal energy) and the Q-value is 4.78 MeV. $E_{eq.}$ was calculated as the centroid of the Gaussian fit of the peak in the neutron spectrum (Figure 4.7), i.e., 3.1 MeV. The resulting q_F is 0.6484 $\pm$ 0.0004 consistently with [99] which reports a value of 0.7 for the ^{6}Li(n,t)α reaction.

Thermal neutrons are probably produced by the scattering of the 2.5 MeV source neutrons with the surroundings. The 2.5 MeV source neutrons can also directly interact with CLYC-6 via the ^{6}Li(n,t)α reaction. These events should appear on the right-end side of the thermal peak [91], however due to the difference between the thermal and fast neutron cross sections (940 b at 25 meV versus 0.17 b at 2.5 MeV), the thermal peak is dominant. Neutrons of 2.5 MeV are also detected via the ^{35}Cl(n,p)^{35}S reaction (the

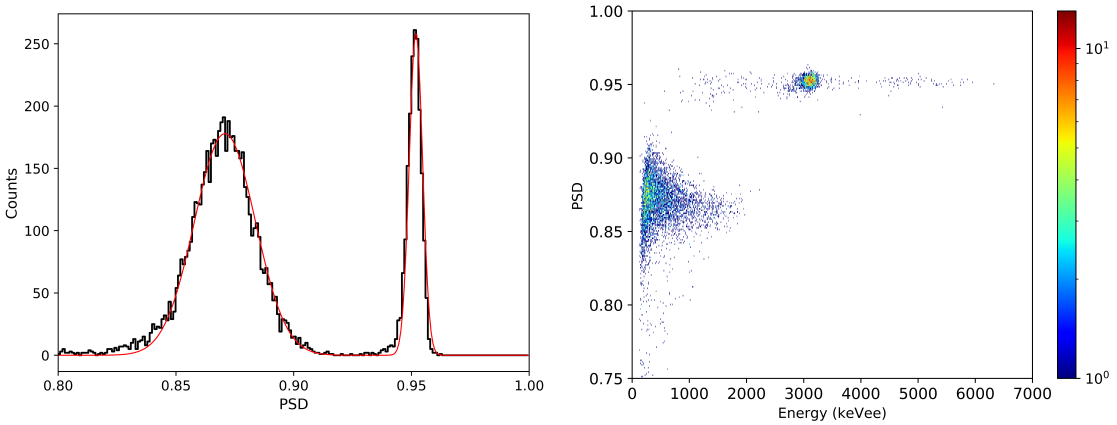

Figure 4.6: Left: the 1D PSD histogram plot acquired with CLYC-6 irradiated with 2.5 MeV neutrons from a D-D generator. The red line is the Gaussian fit to the γ-ray (left peak) and neutron (right peak) distributions. Right: the 2D PSD plot for the same measurement.

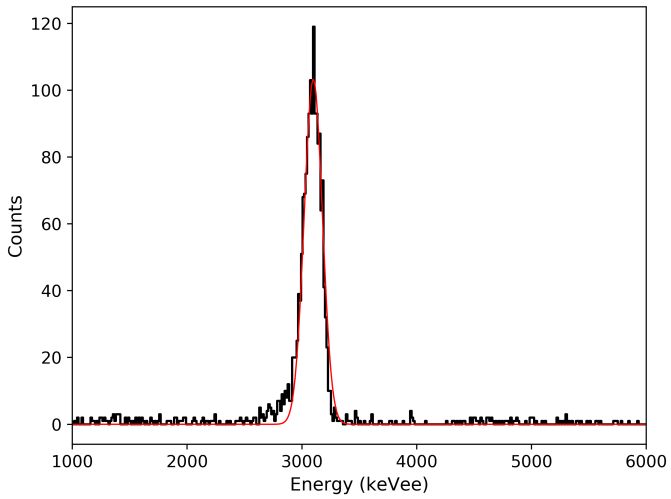

Figure 4.7: The neutron spectrum acquired with CLYC-6 irradiated with 2.5 MeV neutrons from a D-D generator. The red line is the Gaussian fit to the peak corresponding to the $^{6}Li(n,t)\alpha$ reaction.

cross section for 2.5 MeV neutrons is 0.19 b) as a single energy peak at 2.5 MeV + the Q-value of the reaction, multiplied by the proton quenching factor equal to 0.9 (defined by Equation 4.1 and calculated in Section 4.5.2), i.e. at 2.8 MeV. The corresponding peak should appear at the left of the thermal neutron peak and can be the origin of the small bump visible just below the thermal peak [91, 92].

The energy resolution was calculated as the ratio between the corresponding Full Width at Half Maximum (FWHM) and the mean value of the peak. The thermal neutron energy resolution is 6%. As expected CLYC-6 shows a good energy resolution, coherently with its relatively high light yield. Nevertheless, CLYC-6 was investigated as a thermal neutron counter and the most important parameter is the thermal neutron efficiency, which is discussed in Section 4.4.3.

4.4.3 Neutron detection efficiency

The measurements of the neutron detection efficiency of CLYC-6 were carried out at the CERN Cal Lab employing the so-called "cylinder" configuration (see Appendix A) of the thermal neutron source, i.e. a tailored cut polyethylene cylinder was placed around the Am-Be source of the Cal Lab to moderate the fast neutrons emitted by the source and produce a thermal neutron field. The crystal was aligned with the source with two orthogonal lasers. Thirteen measurements were performed by placing the crystal at different distances from the source (from 30 cm to 200 cm) and irradiating the crystal at each position for five minutes. The neutron count rate was obtained after the PSD analysis, performed by the digitizer by means of the DPP-PSD software. Only the neutron signals under the thermal neutron peak (2.5–3.5 MeV [100]) were selected. Figure 4.8 shows the 2D PSD histogram plot measured at 80 cm of distance from the source (taken as example). The neutron signals selected for the efficiency calculation are delimited in Figure 4.8 by the green box.

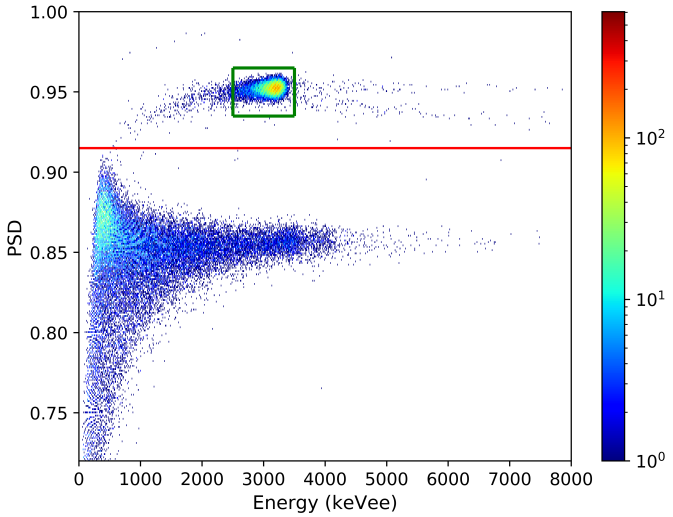

Figure 4.8: The 2D PSD histogram plot acquired with CLYC-6 irradiated with a thermal neutron source at 80 cm from the source. The red line divides the signals due to neutron events (above the red line) and γ-ray events (below the red line). The green box delimits the neutron signals under the thermal neutron peak (2.5–3.5 MeV).

For comparison, the neutron count rates at the same irradiation positions were measured with a Centronic SP9/152/Kr ^{3}He proportional counter, filled with a gas mixture of ^{3}He at 2.33 kPa (2.3 atm) and Kr at 1.22 kPa (1.2 atm). The counter was supplied with +820 V and the output signal processed by an ORTEC 142IH preamplifier, an ORTEC 570 amplifier (assembled in a portable NIM crate) and an Amptek Pocket Multi-Channel Analyser 8000D. Thermal neutrons are detected via the ^{3}He(n,p)^{3}H reaction, characterised by a cross-section of 5330 b at 2.5 meV and a Q-value of 764 keV. The neutron count rate was measured integrating the spectrum of the recoils acquired by the multi-channel analyser above a proper energy threshold. The threshold was set in order to cut the electronic noise and γ-ray events. The same proportional counter was used for the characterisation of the thermal neutron source described in Appendix A. The acquired spectrum and the selected threshold are shown in Figure 4.9 for 80 cm source-to-detector distance.

The resulting count rates were divided by the volume of the corresponding detector: 1.62 cm^3 for CLYC-6, 17 cm^3 for the ^{3}He counter. Figure 4.10 shows the count rate per unit volume obtained with both detectors at each irradiation position. The neutron detection efficiency per unit volume of the studied CLYC-6 crystal is higher than that of

the employed ^{3}He proportional counter, that is about 60% smaller than CLYC-6. This is in agreement with Glodo et al. [101] who measured a higher neutron detection efficiency per unit volume of a thin CLYC-6 crystal respect to a 10 atm ^{3}He tube (9 cm^{3} volume). The former has the same thickness of CLYC-6 used in this work (0.5 cm). CLYC-6 is thus a perfect candidate to replace ^{3}He counter in thermal neutron detection. However, it is important to mention that the results reported by Glodo et al. also show that the geometry and the dimensions of CLYC-6 affect the neutron detection efficiency. In fact, the relationship between CLYC-6 and the ^{3}He counter is reversed for thicker CLYC-6 crystals (the count rate per unit volume of ^{3}He is higher), indicating that the majority of the thermal neutron reactions on ^{6}Li occur in the first centimetre of the crystal.

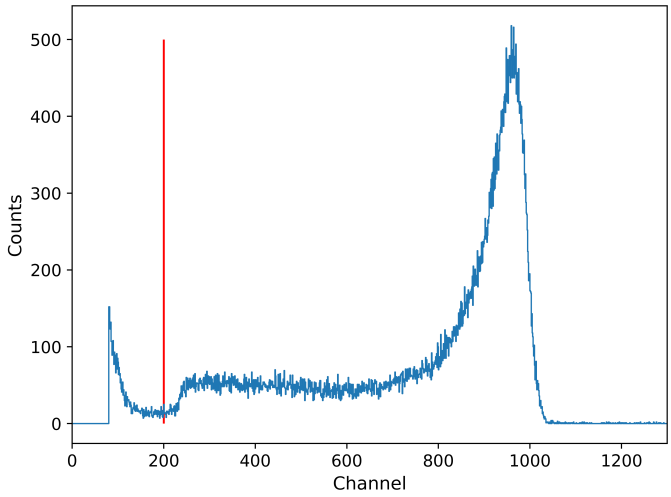

Figure 4.9: The spectrum acquired with the ^{3}He proportional counter at 80 cm from the source. The red line shows the selected threshold.

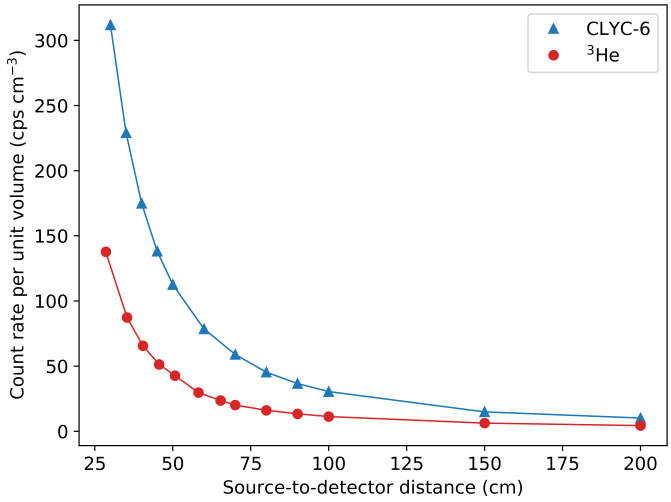

Figure 4.10: The count rate per unit volume obtained with CLYC-6 and the ^{3}He counter for different irradiation positions.

4.5 Measurements with CLYC-7

This section analysis CLYC-7 in terms of the n/γ discrimination and provides the quenching factor of the ^{35}Cl(n,p)^{35}S measured with the same D-D generator. The fast neutron spectrometric capability of CLYC-7 was investigated with the continuum neutron spectra from Am-Be and ^{252}Cf sources. A proton/α-particle (p/α) discrimination via the PSD method is also proposed, by exploiting the different Linear Energy Transfer (LET) of protons and α-particles. A preliminary analysis was made with Am-Be (section 4.5.3) and ^{252}Cf (Section 4.5.4) sources. The proposed p/α discrimination and its feasibility are discussed in Section 4.5.5.

4.5.1 n/γ discrimination capability

The PSD analysis was performed on the signals acquired with CLYC-7 irradiated with the D-D generator. The resulting 1D and 2D histogram plots of the PSD and PSD versus energy are shown in Figures 4.11. The Gaussian fits of the neutron and γ-ray distributions are also plotted in Figure 4.11. The corresponding FOM is 2.04, confirming excellent n/γ discrimination. It also proves that the degradation mentioned in Section 4.3 did not affect the n/γ discrimination performances, it appeared instead as reduction of the scintillation light emitted by CLYC-7 and the consequent worsening of the energy resolution. The FOM for CLYC-7 is slightly lower than for CLYC-6 in agreement with [100], where a FOM of 2.5 and 2.8 is reported for CLYC-7 and CLYC-6 respectively, setting the energy threshold to 500 keVee.

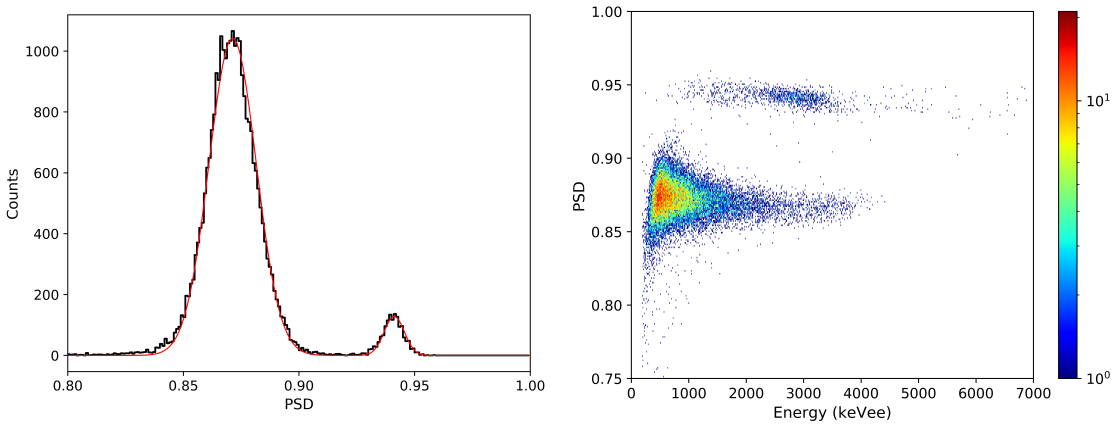

Figure 4.11: Left: the 1D PSD histogram plot acquired with CLYC-7 irradiated with 2.5 MeV neutrons from a D-D generator. The red line is the Gaussian fit to the γ-ray (left peak) and neutron (right peak) distributions. Right: the 2D PSD plot for the same measurement.

4.5.2 Quenching factor of the ^{35}Cl(n,p)^{35}S and ^{35}Cl(n,α)^{32}P reactions

Figure 4.12 shows the neutron spectrum acquired with CLYC-7 irradiated with 2.5 MeV neutrons from the D-D generator. The main peak at 2.83 MeVee is attributed to the (n,p) reaction on ^{35}Cl, while the smaller peak at around 1.7 MeVee to the (n,α) reaction [93] and the (n,p) reaction to the excited states of ^{35}S. Some counts in this energy range can also derive from scattered neutron background.

The quenching factor for the ^{35}Cl(n,p) reaction was calculated using Equation 4.1, where $E_{eq.}$ is the centroid of the Gaussian fit to the 2.83 MeVee peak shown in Figure 4.12,

$E_N = 2.5$ MeV and $Q = 0.615$ MeV. A value of 0.91 was found, in perfect agreement with literature data (from 0.85 to 0.92 in [93], 0.9 in [99]).

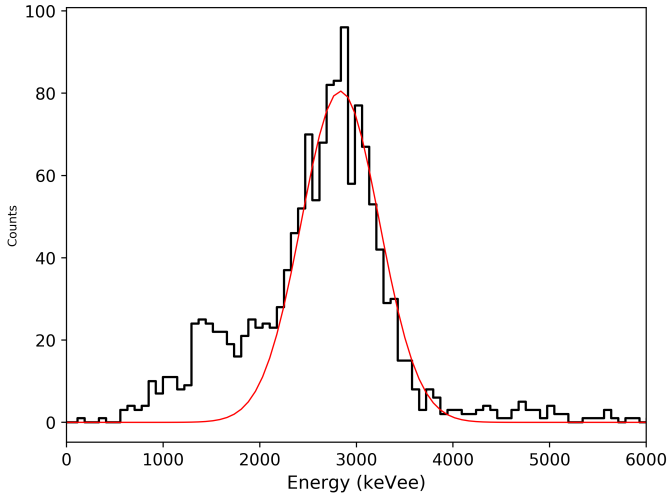

Figure 4.12: The neutron spectrum acquired with CLYC-7 irradiated with 2.5 MeV neutrons from a D-D generator. The red line is the Gaussian fit to the peak at 2.83 MeVee corresponding to the $^{35}Cl(n,p)^{35}S$ reaction.

4.5.3 p/α discrimination for the Am-Be neutron spectrum

As discussed in Section 4.2, fast neutron spectrometry with CLYC-7, without unfolding, is already difficult starting from 2.5 MeV mainly because of the presence of both the (n,p) and (n,α) reaction. A p/α discrimination would allow improving the performance of CLYC-7 as a fast neutron spectrometer up to higher energies. The p/α discrimination proposed in this work is based on the PSD method as described in this section.

CLYC-7 was irradiated with Am-Be source neutrons. The n/γ PSD analysis was first performed as in the previous measurements to discard the γ-ray events. Figure 4.13 shows the 2D histogram plot of the PSD versus energy where the red line delimits the neutron and γ-ray regions in the PSD space. The distance between x_γ and the red line is larger than $3\sigma_\gamma$, where x_γ and σ_γ are the centroid and the standard deviation of the Gaussian equation fitting the γ-ray distribution. Few signals were detected in between the neutron and γ-ray distributions. Because of the uncertainty associated to these signals, they were discarded from the analysis. It is worth mentioning that these signals are 7% of the total neutron signals and are spread over about 5 MeV. Their effect on the resulting neutron spectrum is negligible (the neutron spectrum with these signals differs by less than 1% compared with the spectrum without).

The γ-ray events were discarded, and the PSD analysis was repeated on the selected neutron signals by varying t_{prompt} from 10 ns to 1.5 μs while t_{delay} was kept constant at 2 μs. Figure 4.14 shows the 2D histogram plots of the PSD versus energy for the different values of t_{prompt}, as indicated in each plot. The width of the binning and the scale of the x-axis are the same for all plots, while the y scale changes to better visualise the region of interest of each plot. For larger t_{prompt} values (bottom plots) the neutron signals follow a unique distribution. By decreasing the value of t_{prompt}, below 100 ns, a second distribution arises that deviates from the main distribution. This trend indicates that the signals differ in the first part of their time profile. Variations on the first part of the signals become indeed negligible for larger values of t_{prompt}, when t_{prompt} is almost equal to t_{delay}.

Furthermore, this second distribution appears at higher PSD values, which means that it is composed of slightly slower signals. For this reason, we associated this distribution to

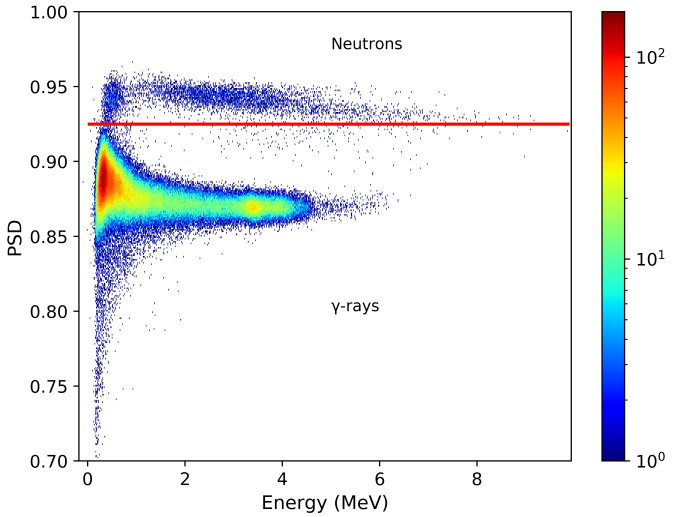

Figure 4.13: 2D histogram plot of the PSD versus energy for CLYC-7 irradiated with Am-Be source neutrons.

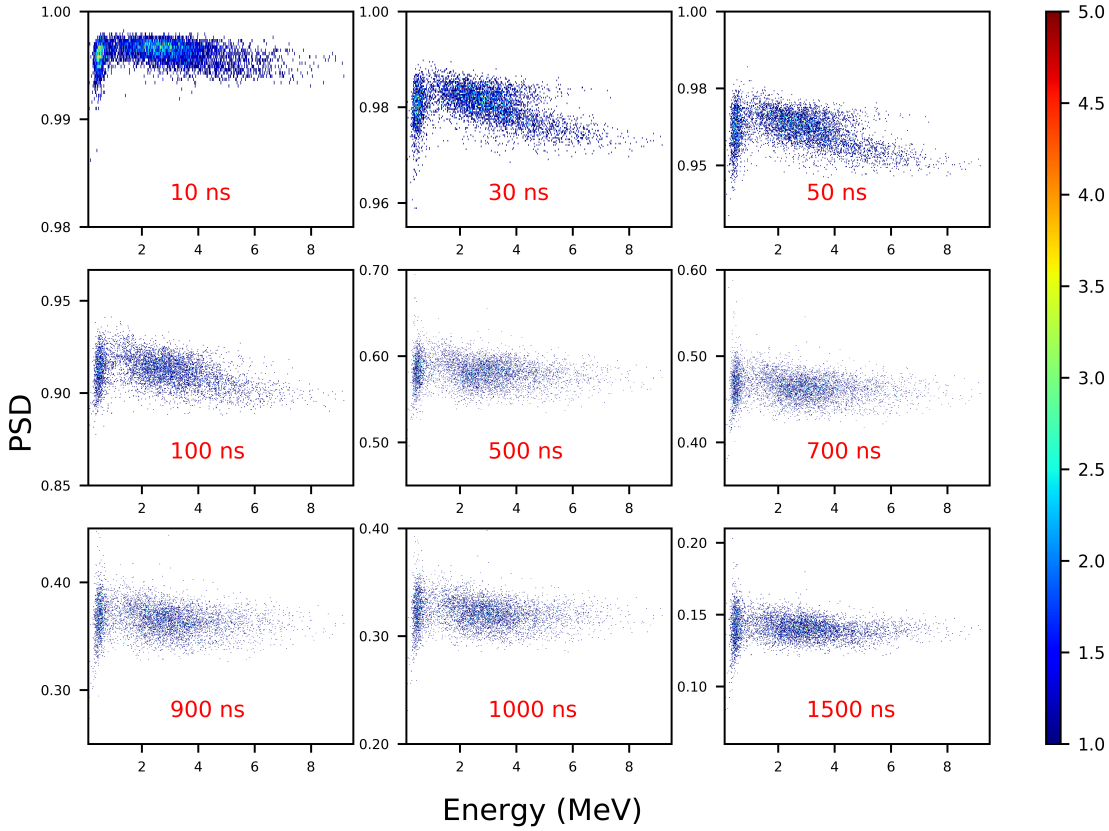

Figure 4.14: 2D histogram plots of the PSD versus energy for CLYC-7 of the neutron signals from an Am-Be source at different t_{prompt}. The value of t_{prompt} is indicated in each plot, whilst t_{delay} is constant (2 μs).

α-particle events: α-particles are higher LET particles (i.e., slower signal) as compared to protons. The α-particle distribution should appear starting from about 2 MeV. Below this value, its cross section is negligible compared with the (n,p) cross section (less than 1%). However, due to the small difference of their signal profiles, the two distributions overlap

between 2 MeV and up to around 4 MeV. Only above this energy two distributions can be identified.

For each value of t_{prompt}, the PSD values corresponding to the neutron signals were plotted into a histogram, selecting only the signal with E > 4 MeV. For t_{prompt} equal to 30 ns and 50 ns only, two Gaussian-like distributions appear which were fitted using a Gaussian equation, and the FOM calculated as follows:

$$FOM = \frac{x_\alpha - x_p}{FWHM_\alpha + FWHM_p} \tag{4.2}$$

where x_α and x_p are the peak centroids of the α-particle and proton Gaussian distributions and $FWHM_\alpha$ and $FWHM_p$ the corresponding FWHM. The maximum calculated FOM was 0.77 ± 0.04 for 50 ns which was thus selected for the p/α discrimination. Figure 4.15 compares the PSD histogram plot obtained for t_{prompt} = 500 ns (on the left) and t_{prompt} = 50 ns. The Gaussian fittings on the latter plot are also shown. The separation between the proton and the α-particle distributions is not good (in fact a FOM < 1.25 implies that $x_\alpha - x_p < 3(\sigma_\alpha + \sigma_p)$), however two distributions have been detected, while it was not possible for other t_{prompt} values (such as for t_{prompt} = 500 ns, as shown in Figure 4.15).

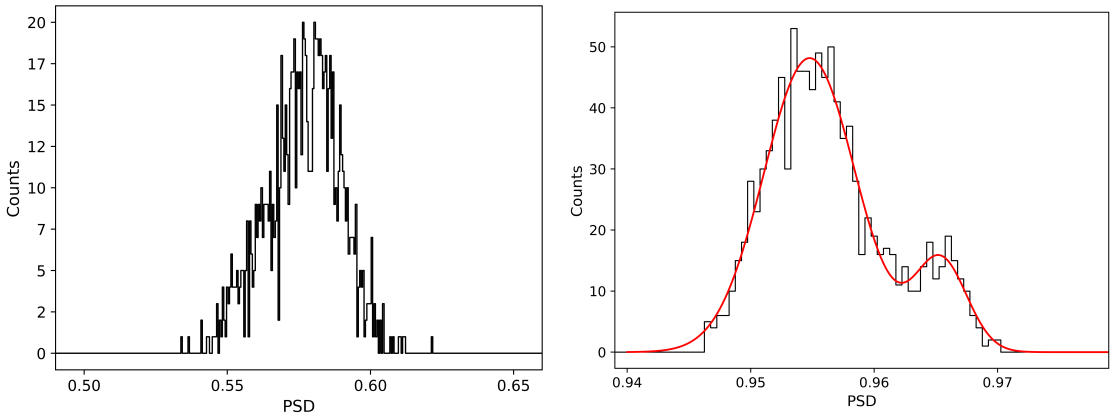

Figure 4.15: The 1D histogram plot of the PSD for CLYC-7 for neutron signals at t_{prompt} = 500 ns (on the left) and t_{prompt} = 50 ns (on the right). The right plot also shows the Gaussian fit to the selected proton and α particle distributions.

A PSD cut-off value equal to 0.9622 was defined, below which the pulses were classified as produced by protons and above which by α-particles, excluding from the α-particles all the signals detected as a blob below 1.5 MeV which spread over a wider PSD range (0.95–0.98). The latter are instead classified as protons since the (n,α) cross section is negligible below 1.5 MeV (0.10977 b the (n,p) cross section versus 0.0005 b the (n,α) cross section at 1.5 MeV [94]). According to this criterion, the pulses from protons and α-particles were collected separately and plotted into a histogram. The spectra so calculated correspond to the spectra of the energy deposited by protons and α-particles respectively, as a function of $E_{eq.}$. We will refer to them as $S_p(E_{eq.})$ and $S_\alpha(E_{eq.})$.

Inverting Equation 4.1, the corresponding neutron spectra can be calculated as follows:

$$E_N = (E_{eq.}/q_F) - Q \tag{4.3}$$

The neutron energy spectra, labelled as $S_p(E_N)$ and $S_\alpha(E_N)$, were calculated applying equation 4.3 to $S_p(E_{eq.})$ and $S_\alpha(E_{eq.})$, assuming q_F equal to 0.9 for protons (see Section 4.5.2) and to 0.5 for α-particles as provided in [99]. The Q-value is 615 keV for the (n,p) reaction and 938 keV for the (n,α) reaction. Figure 4.16 shows $S_p(E_{eq.})$ and $S_p(E_N)$, Figure 4.17 $S_\alpha(E_N)$ and $S_\alpha(E_N)$.

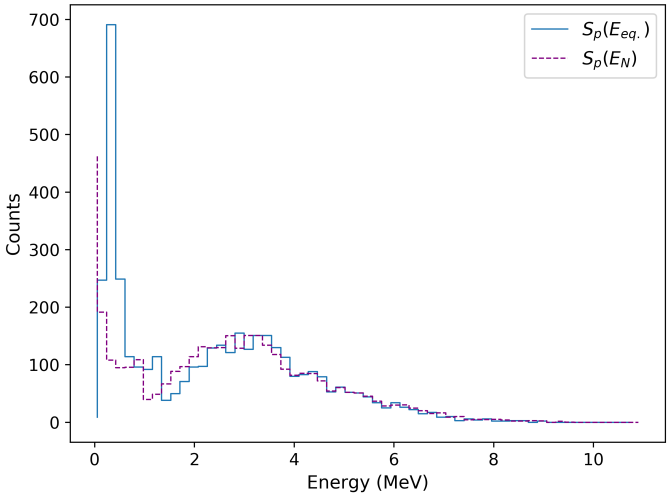

Figure 4.16: The spectrum of the energy deposited by protons in CLYC-7 (continuous blue line) and the related spectrum of the incoming neutrons (dotted purple line), calculated taking into account the quenching factor (0.9) and the Q-value of the reaction (615 keV).

The total spectrum of the incoming neutrons was calculated as the sum of $S_p(E_N)$ and $S_\alpha(E_N)$ and is compared with the ISO spectrum [77] and with the spectrum calculated without the p/α discrimination in Figure 4.18. The three spectra have been normalised to their maximum (discarding the energy bins below 500 keV). Figure 4.18 also shows the percentage difference ($d_\%$) between the Am-Be ISO spectrum and the spectrum with and without the p/α discrimination. $d_\%$ is defined as:

$$d_\% = \frac{|y_{ISO,i} - y_i|}{y_{ISO,i}} \times 100 \tag{4.4}$$

where $y_{ISO,i}$ is the intensity of the normalised Am-Be ISO spectrum in the i-th bin and y_i the normalised counts of the experimental spectrum for the same bin. The average $d_\%$ for E $>$ 500 keV (i.e. for fast neutron energies) is 46% with the p/α discrimination and 68% without the p/α discrimination.

The results obtained with the p/α discrimination for the Am-Be source irradiation case are promising. After the p/α discrimination the measured Am-Be spectrum better match the corresponding ISO spectrum: the percent difference between the experimental and the ISO spectrum, averaged over the spectrum energies, improves by 20% when the p/α discrimination is applied. Between 2–5 MeV the spectrum with the p/α discrimination is always closer to the corresponding ISO spectrum than the spectrum without discrimination. The bad match between the reference and the experimental spectrum below 2 MeV is due to the uncertainty associated with the p/α discrimination since, in this region, many proton and α-particle pulses overlap. A high peak at low energy is also visible, which can be due to either the scattered neutron component [88] or the resonance peaks of the (n,p) cross section below 1 MeV [98] as shown in Figure 4.19. Also above 5 MeV the difference between ISO and experimental spectra increases, probably because of the drop of the (n,p) cross section at 5 MeV and the increasing importance of different reaction channels (see Figure 4.2).

4.5.4 p/α discrimination for the ^{252}Cf neutron spectrum

CLYC-7 was irradiated with ^{252}Cf source neutrons and the procedure described in Section 4.5.3 was applied to the acquired data. For this case only, t_{delay} were set to 1.5 μs (because

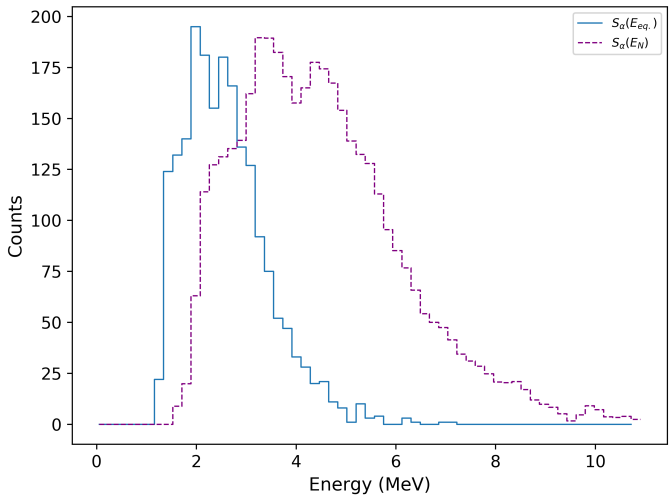

Figure 4.17: The spectrum of the energy deposited by α particles in CLYC-7 (continuous blue line) and the related spectrum of the incoming neutrons (dotted purple line), calculated taking into account the quenching factor (0.5) and the Q-value of the reaction (938 keV).

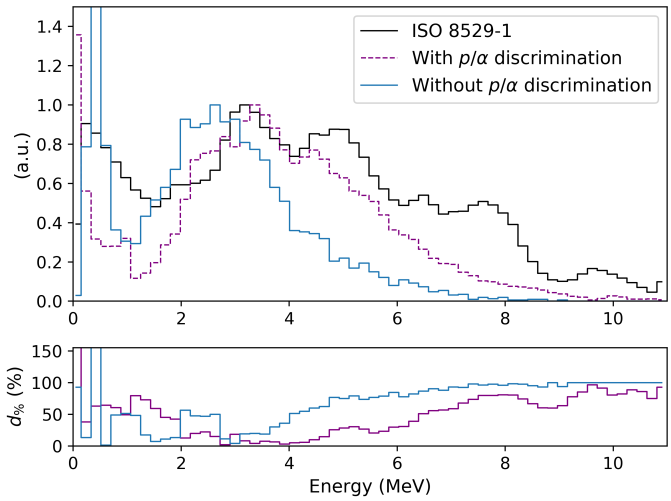

Figure 4.18: Top: comparison between the Am-Be ISO spectrum (continuous black line) and the neutron spectrum measured with CLYC-7, without discrimination of neutron signals (continuous blue line) and with the p/α discrimination (dotted purple line). Bottom: percent variation between the Am-Be ISO spectrum and the spectrum obtained with (continuous purple line) and without (continuous blue line) p/α discrimination.

the recording time of the signals was set to 1.5 μs) while t_{prompt} was kept at 70 ns for the n/γ discrimination and at 50 ns for the p/α discrimination. Figure 4.20 compares the ISO spectrum [77] and the experimental spectrum before and after the analysis proposed in this work. The resulting $d\%$ parameters for E > 500 keV were 61% and 77% with and without the p/α discrimination respectively.

As well as for the Am-Be source, the spectrum obtain after the p/α discrimination with the ^{252}Cf spectrum better matches the corresponding ISO spectra. The percent difference improves by more than 15%. Except at 13 MeV for two bins, above 3 MeV, $d_{\%}$ with the p/α discrimination (represented by the purple line on the bottom plot of Figure 4.20) is always smaller than $d_{\%}$ obtained without the p/α discrimination (blue line of the same plot). Below 2 MeV the p/α discrimination does not show any improvements because of

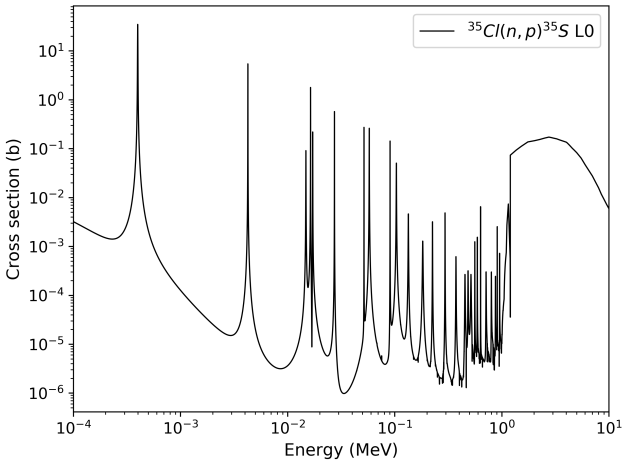

Figure 4.19: Zoom of the total cross section of the (n,p) and (n,α) reactions on ^{35}Cl, in the region of interest. Below 1 MeV several resonance peaks are visible [94].

the overlapping between the proton and α-particle distributions in this energy region. The low energy peak detected with the Am-Be source is not revealed because of the lack of thermal neutrons in the ^{252}Cf spectrum.

The ^{252}Cf neutron spectrum has a more pronounced low energy component as compared to the Am-Be spectrum and, as a consequence, the shape of the experimental spectrum without the p/α discrimination already matches quite well the peak of the ISO spectrum between 2 MeV and 3 MeV [90]. However, the tail of the spectrum is not well reproduced, whilst the p/α discrimination partially restores the correct shape above 3 MeV.

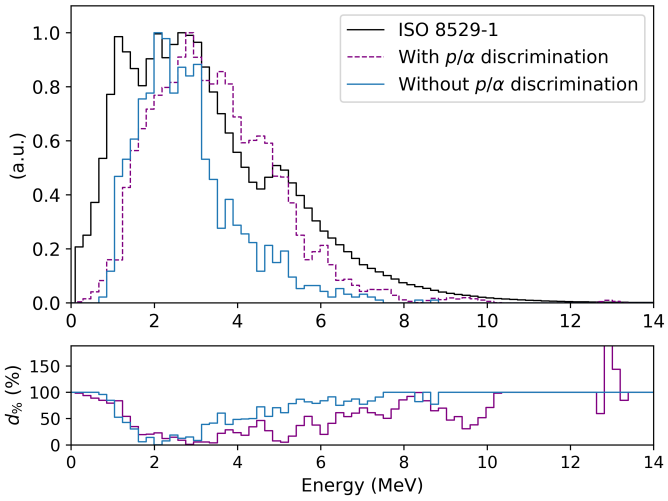

Figure 4.20: Top: comparison between the ^{252}Cf ISO spectrum (continuous black line) and the neutron spectrum measured with CLYC-7, without discrimination of neutron signals (continuous blue line) and with the p/α discrimination (dotted purple line). Bottom: the percentage variation between the ^{252}Cf ISO spectrum and the spectrum obtained with (continuous purple line) and without (continuous blue line) the p/α discrimination.

4.5.5 Discussion on the p/α discrimination

In order to better investigate the correctness of the p/α discrimination, a pulse shape analysis of the signals identified as neutrons was performed. It also helped to quantify the difference in terms of time profile between the signals defined as either protons or α-particles by the p/α discrimination proposed in this work. Only the signals acquired with CLYC-7 irradiated with the Am-Be source were considered and the standard pulse of protons and α-particles was calculated as follows. All signals were aligned and the PSD was calculated as described in Section 4.3 (t_{prompt} = 70 ns and t_{delay} = 2 μs). The γ-ray signals, i.e. the signals below the red line in Figure 4.13, were discarded and the p/α discrimination was applied to the remaining signals as described in Section 4.5.3 (t_{prompt} = 50 ns and t_{delay} = 2 μs). Only the events with E > 4 MeV were selected, where the recognised proton and α-particle distributions do not overlap (see Figure 4.14, case t_{prompt} = 50 ns). The pulses recognised as protons were averaged and normalised to obtain the proton standard pulse. The same calculation was performed to obtain the α-particle standard pulse. Figure 4.21 shows the results.

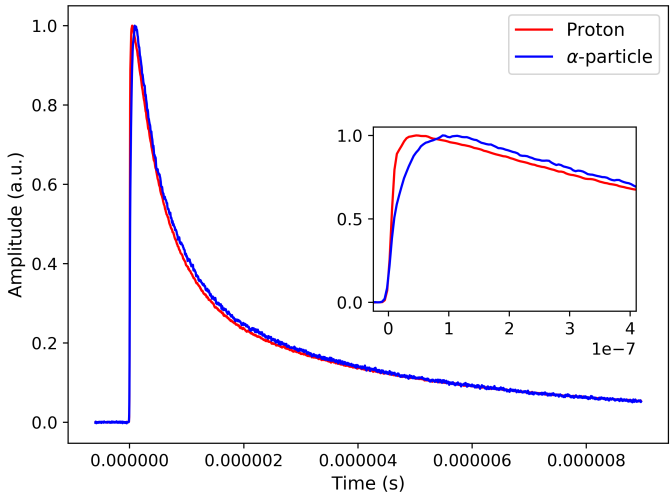

Figure 4.21: The proton and α-particle standard pulses obtained with the proposed p/α discrimination, in CLYC-7 irradiated with Am-Be source neutrons.

The pulse shape analysis demonstrates the correctness of the method since the signals ascribed to protons are faster than the signals ascribed to α-particles, i.e. the PSD is able to distinguish even small differences in the time profile if the proper time windows are selected. This was also demonstrated for higher neutron energies (up to 60.5 MeV) in [102]. For the case considered in this work, the proton and α-particle's standard pulses differ the most in the first 100 ns of the signal, during their rise time. The rise time of the proton and α-particle standard pulses is 16 ns and 48 ns respectively. The tails of the two signals are slightly different up to around 4 μs. However, the corresponding fall times are more comparable, 5.4 μs for protons and 5.5 μs for α–particles.

The p/α discrimination via the PSD method is in principle possible. In fact, with the properly selected time windows, different kinds of particles are collected in different distributions in the PSD plot. Giaz et al [88] also detected two different distributions irradiating CLYC-7 with 14.1 MeV neutrons. The two distributions were also attributed to different LET particles, i.e., protons and α-particles. However, Giaz et al. did not exploit this difference to improve the CLYC spectroscopic capability. A similar analysis was instead proposed by Dolympia et al [89] with a 7.23 MeV mono-energetic neutron beam. However, a continuous neutron spectrum, as used in this work, represents a more realistic scenario.

Despite the p/α discrimination performed in this study improves the performance of CLYC-7 as a spectrometer, the method is still not rigorous since the overlapping region between the proton and α-particle is dominant and the selection of the discrimination parameter is affected by high uncertainty. A second limitation exists which cannot be overcome: the contribution to the neutron spectrum of the (n,p) and (n,α) reactions leaving the ^{35}S and ^{32}P in their excited states. These reactions contribute to the neutron spectrum also below 8 MeV, depositing per event less energy compared with the corresponding reaction leaving the ^{35}S and ^{32}P to the ground states. However, protons emitted by the (n,p) (ground state) reactions cannot be distinguished by protons emitted after the (n,p) (excited state) reactions. The same is valid for α-particles. In general, the analysis can be improved for example with the use of a faster photodetector, a specific electronic readout or a more sensitive PSD analysis.

4.6 Conclusions

CLYC-6 (enriched in ^{6}Li to $> 95\%$) and a CLYC-7 (enriched in ^{7}Li to $> 99\%$) crystals were studied as thermal neutron detector and as fast neutron spectrometer respectively for the B-RAD detector. Both crystals show excellent n/γ discrimination capability evaluated by the PSD method (FOM > 2).

As neutron counter, the thermal neutron detection efficiency of CLYC-6 was measured relative to that of a ^{3}He proportional counter. For the thermal neutron field available at Cal Lab and for the same irradiation position, CLYC-6 shows a 60% higher efficiency per unit volume. CLYC-6 represents an appealing alternative to the ^{3}He counter, especially because of the diminishing stockpile of ^{3}He gas [101].

The neutron spectrometry capability of CLYC-7 was investigated irradiating the crystal with the continuum neutron spectra from Am-Be and ^{252}Cf sources. A p/α discrimination was carried out by the PSD method, to distinguish between the protons and α-particles produced by the two main reactions occurring in the crystal below 10 MeV. After p/α discrimination the experimental neutron spectra better match the corresponding ISO spectra above 2 MeV. The best match was found between 2 MeV and 4 MeV, where the difference with the ISO spectrum is below 30%. Below 2 MeV, the overlapping of proton and α-particle pulses is not negligible, whilst above 5 MeV different reaction channels become comparable with the aforementioned ones. In spite of some limitations and the non perfect match between the experimental and the predicted spectra, the application of CLYC-7 as a portable fast-neutron spectrometer for the B-RAD detector is still attractive. A small, lightweight, single detector, instead of the commonly used Bonner Sphere Spectrometer, represents a great advantage especially in some applications in radiation protection where some uncertainty is acceptable.

As a conclusion, CLYC-7 is a suitable candidate for a probe for fast neutron spectrometry for B-RAD below ~ 5 MeV and, simultaneously, as a stationary environmental detector to monitor both the γ-ray (with the current probe) and the neutron dose rates. CLYC-6 can instead be used for neutron count rate and measurement of neutron ambient dose equivalent if embedded in a moderator (typically polyethylene) to increase the thermal neutron component of the neutron field.

Chapter 5

Investigation of a new n/γ discrimination technique with CLYC-7 through optical filtering selection of the scintillation light

In the context of the study of the B-RAD's neutron probe, the CLYC-7 crystal was selected and studied as a fast neutron spectrometer. In this chapter, a new n/γ discrimination method specifically thought for CLYC-7 is proposed and discussed.

The standard way to perform n/γ discrimination with scintillators is the Pulse Shape Discrimination (PSD) technique. However, the PSD has some unavoidable drawbacks: long computing time (especially when off-line analysis is required), digitalization errors for low amplitude signals (when digital algorithms are used), limitations in terms of count rates and detected false positives [103]. In order to overcome these difficulties with the PSD the Polytechnic of Milan, in collaboration with the Department of Materials Science of the University of Milano - Bicocca (DMS-UNIMIB), proposed a novel approach: exploiting the difference in the emission spectra of two different scintillators, a passive and on-line discrimination is feasible [104].

A similar idea may in principle be applied to the CLYC scintillator: when irradiated by γ radiation, the light emission spectrum of the crystal shows the characteristic doublet peak of its activator (Ce^{3+}), between 340-500 nm, and a second peak at around 300 nm. The latter is due to an intrinsic scintillation mechanism called core-to-valence luminescence (CVL) and in principle vanishes when the same crystal is irradiated by neutrons only. The details of the scintillation mechanisms in CLYC are described in Section 5.1.

Relying on this hypothesis, we proposed to couple the scintillator with two different photodetectors: one of them directly coupled with the crystal, the second one with an optical filter placed in-between crystal and photodetector. The filter is chosen in such a way that only the light in the CVL wavelength range (due to γ radiation) reaches the photodetector, to eventually discriminate which particle interacts in the crystal through an anti-coincidence electronic setup. The CVL behaviour when the crystal is excited by neutrons and γ-ray was therefore investigated, correlating the time response to the scintillation wavelength spectrum.

The analysis was carried out following two different methods: 1) by measuring the X-ray and γ-ray excited radio-luminescence (RL) spectra at different photon energies (Section 5.2), and 2) by performing a pulse shape analysis of the signal produced by the interaction of γ-rays and neutrons, using both a photomultiplier tube (PMT) (Section 5.3) and a Time Correlated Single Photon Counting (TCSPC) technique [105, 106] (Section 5.4). All measurements were repeated with and without an optical filter in between the crystal

and the sensor. This allowed investigating the effect on the CVL scintillation mechanism due to different impinging particles. Section 5.6 discusses the feasibility of the proposed method and its applicability to the B-RAD detector.

5.1 Scintillation mechanism in CLYC

The CLYC scintillator is a Ce^{3+}-doped crystal from the elpasolite family. For Ce^{3+} elpasolite crystals, up to four scintillation mechanisms contribute to the overall emission [59, 107, 108]:

(1) The CVL (also called cross-luminescence or Auger free luminescence) is an ultrafast mechanism where an electron from the core band is excited into the conduction band. The consequent hole produced in the core band recombines with an electron of the valence band. Since the valence band is filled with electrons, the recombination probability is large resulting in a fast process [109]. The CVL is a competitive radiative de-excitation process with a decay time faster than that of the other three scintillation mechanisms present in CLYC [110, 111]. In CLYC, the CVL has a decay time of the order of 1–5 ns and is characterized by the emission of photons in between the deep-Ultraviolet (UV) and Near Ultraviolet (NUV) region (225–330 nm) [59, 107].

(2) The direct electron-hole capture (also called fast mechanism) consists in a free electron excited by the ionizing radiation from the valence band to the conduction band. The consequent free electron/hole pair, created along the track of the original particle, is directly captured by the Ce^{3+}. It is characterised by a decay time of the order of 50 ns.

(3) The binary electron-hole recombination (or intermediate mechanism) occurs when, instead of being directly captured by Ce^{3+}, the hole is trapped between two anions (Cl^- in the case of the CLYC) to form the so-called V_k complex [108]. The V_k centre can move from one site to an adjacent site by thermal activation and can be trapped by a Ce^{3+} centre to form Ce^{4+} or Ce^{3+}-V_k complex. Eventually, the free electron excited by the primary radiation into the conduction band, is trapped by the centre leading to the excitation of Ce^{3+} followed by photon emission (radiative recombination). Alternatively, it is also possible that the electron is first trapped by the Ce^{3+} and the V_k centre diffuses toward it. This mechanism is thus related to the Ce^{3+} de-excitation and is characterized by a decay time of the order 500 ns.

(4) The slowest mechanism is related to the host luminescence, with the formation of the so called self trapped excitons (STEs), i.e. a V_k centre which traps the free electron from the conduction band, before reaching the Ce^{3+} centre. The STE is a luminescence defect in itself and is characterized by a decay time of several microseconds [108, 107]. The STEs can also de-excite on Ce^{3+}, hence in the range 350–450 nm, but the decay constant is still governed by the STE migration dynamics, with a half life of a few microseconds [108].

Figure 5.1 shows a schematic of the energy levels of each scintillation mechanism (plots (c), (d) and (e) were taken from [108]). Plot (a) shows the CVL, plot (b) the fast Ce^{3+} emission, usually ascribed to γ-ray irradiation only. Plot (c) shows the intermediate mechanism, i.e. the V_k centre transferring its energy to the Ce^{3+}. The STE is represented both as a luminescence centre itself (plot (d)) and when it transfers its energy to the Ce^{3+} (plot (e)). Table 5.1 summarises the four mechanisms and reports the wavelength region and the characteristic decay time of each scintillation mechanism.

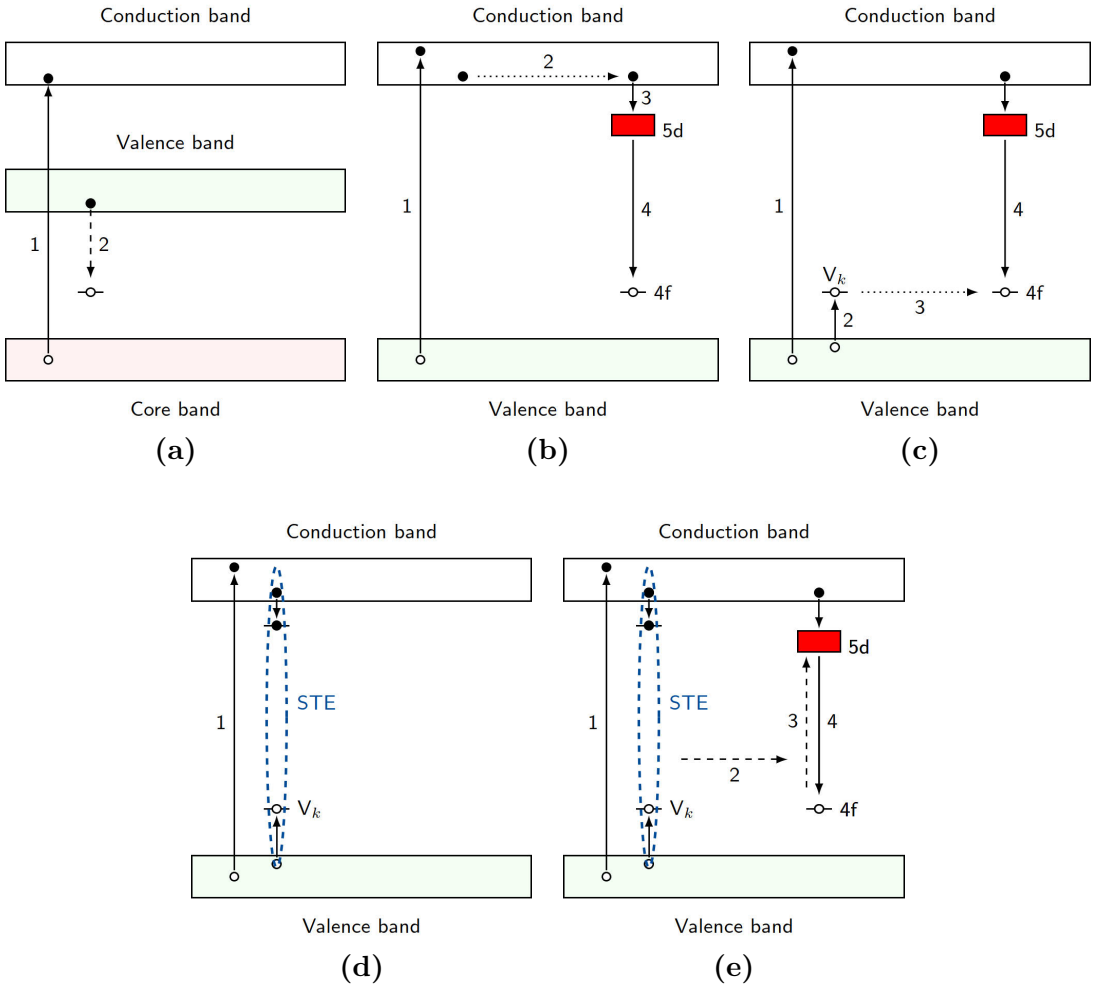

Figure 5.1: Scintillation mechanisms in CLYC [108]. ***(a)*** *Excitation of an electron from the core band to the conduction band and subsequent formation of a hole (1); the hole in the core band then recombines with a valence electron (2) causing the emission of the CVL light.* ***(b)*** *Excitation of an electron from the valence to the conduction band (1); the electron then migrates (2), reaching a Ce^{3+} recombination site (3), with the subsequent radiative de-excitation (4).* ***(c)*** *Excitation of an electron from the valence to the conduction band (1) leaving a hole in the valence band; the hole is then trapped in a positive V_k centre, forming a Cl^{2-} molecular complex (2). This defect thermally migrates (3) to a Ce^{3+} centre forming a Ce^{4+} or a Ce^{3+} + V_k complex. Eventually, the new centre recombines with an electron from the conduction band (4).* ***(d)*** *Excitation of an electron from the valence to the conduction band and formation of a V_k complex (1); a free electron is then trapped forming a STE complex, which can recombine radiatively* ***(e)*** *After the formation of the STE (1), this complex thermally migrates to a Ce^{3+} centre (2). The STE can de-excites transferring its energy to a Ce^{3+} centre (3), which subsequently recombines (4).*

5.2 Radioluminescence measurements

The measurements described in this section were aimed at studying the scintillation light emitted by CLYC in the wavelength domain. A radio-luminescence (RL) spectrum is the scintillation light distribution in wavelength (or frequency or energy) [112], when the crystal is excited by ionizing radiation. Two sets of measurements were carried out: the first was performed at DMS-UNIMIB using a home-made apparatus consisting of an X-ray

Table 5.1: The four scintillation mechanisms present in CLYC crystal and the corresponding wavelength region and decay time.

Scintillation mechanism	Wavelength	Decay time
CVL	between UV and NUV region (225–330 nm)	1–5 ns
Fast	Ce^{3+} emission region (340–500 nm)	$\sim$ 50 ns
Intermediate	Ce^{3+} emission region (340–500 nm)	$\sim$ 500 ns
STE	host luminescence (250-500 nm)	order μs
	Ce^{3+} emission region (340–500 nm)	order μs

tube operating at 20 kV, the second set was performed at the Polytechnic of Milan with a portable spectrometer and irradiating the crystal with X-rays in the energy range between 17–200 keV and a ^{137}Cs source. The latter measurement was performed with and without the optical filter.

5.2.1 Radioluminescence measurement setup

The homemade apparatus at University of Milano - Bicocca (Figure 5.2) is composed by a Philips 2274 X-ray tube with a tungsten target operating between 10 kV and 32 kV: the electrons are emitted from the cathode through thermionic effect and subsequently accelerated and collected to the anode. X-rays are produced by Bremsstrahlung and the resulting spectrum is a continuum. The emitted photons emerge from the X-ray tube through a beryllium window. The tube and the crystal are held in a vacuum chamber, in order to avoid ionization of air and its consequent UV emission. The light emitted by the crystal is collected and focused on the entrance slit of a Czerny-Turner monochromator (Jobin-Yvon Triax 180) by two off-axis parabolic mirrors. The main part of the monochromator is the grating; it has the function of diffusing the light at different angles according to the wavelength. Three different gratings are available at DMS-UNIMIB with different dispersion and resolution. Eventually, the emitted light is detected by a liquid nitrogen cooled CCD (Jobin-Yvon Spectrum One 3000) made up of 1024 pixels, coupled to the monochromator [113]. For these experiments, an entrance slit width of 0.25 mm and a 100 grooves/mm grating operating in the 200–1400 nm range were chosen.

The second set of measurements employed a portable Back-thinned CCD Array Spectrometer Prime X (B&W TEK) [114]. A portable device was used for the irradiations performed at the calibration laboratory of the Polytechnic of Milan. X-ray fields were produced via a high-stability Seifert ISOVOLT 320/10 X-ray generator (maximum voltage 300 kV). The tube provides the complete ISO 4037 standard X-ray series radiation qualities [115]. In particular, the quasi-monoenergetic Narrow series (N-series) were employed. The N-series radiation qualities are recommended for the study of the energy dependence of the response of dosimeters [115]. γ-ray fields were produced by a certified 370 GBq ^{137}Cs isotopic source. The scintillation light emitted by the crystal was sent to the spectrometer through an optical fiber cable. The fibre and the crystal were coupled using a black cone and a tailored 3D printed assembly to optimize the light collection and reduce the light losses. The spectrometer was controlled via a laptop. The filter employed is an Asahi Spectra XUV0325 Shortpass Optical filter (Ø 25 mm, wavelength cut-off 325 nm) [116]. Its transmittance was measured with an Agilent Varian Cary 50 spectrophotometer ranging from 190 nm to 1100 nm.

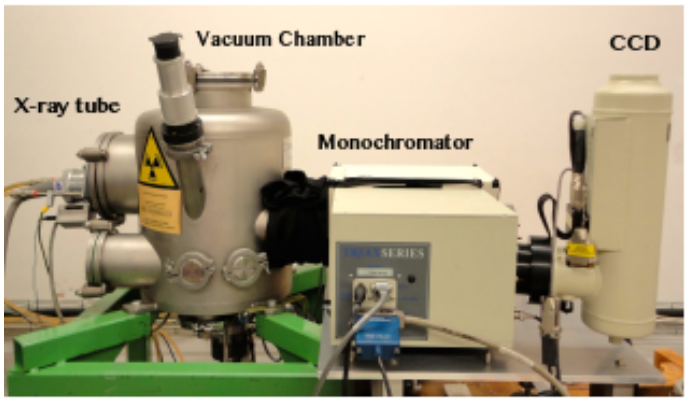

Figure 5.2: Home-made apparatus for RL measurements [113].

5.2.2 Radioluminescence measurement results

Figure 5.3 shows the results of the RL characterization of the crystal performed at the University of Milano - Bicocca. The X-ray tube was operated at 20 kV and 20 mA and for an acquisition time of 25 s. Data were recorded and corrected as follows:

- background subtraction: a flat background of around 1000 counts was subtracted for each channel (the background was calculated as the averaged counts below ∼200 nm);
- normalization to unit time (second);
- correction for the spectral response of the detection system, calculated as explained below.

The apparatus was first calibrated by a Xenon lamp coupled with a monochromator to produce an excitation source at each specific wavelength. Each one of the 1024 CCD channels was associated to its corresponding wavelength and data interpolated to obtain the wavelength-channel conversion equation. The spectral response of the system was later calculated by means of two calibrated lamps, in the UV (200–400 nm range) and in the visible region (250–2400 nm range), respectively. The spectral response curve was calculated as the ratio between the experimental curve and the theoretical one; the former was calculated by acquiring the RL spectra of the two lamps, the latter by interpolating the data supplied by the manufacturer. The spectral response represents the efficiency of the system as a wavelength function; when a RL spectrum is acquired, the raw data has to be weighted over the spectral response of the corresponding system.

Figure 5.3 shows the resulting CLYC RL spectrum. It presents the characteristic doublet peak due to the Ce^{3+} emission in the 340–500 nm range, peaked at 375 nm and 395 nm. A band is also revealed at around 300 nm, which is usually attributed to the CVL scintillation mechanism [110, 117]. The relative intensity of the CVL mechanism with respect to the total scintillation light was quantified as the ratio of the area under the CVL portion of the spectrum (between 260 nm and 330 nm) over the area under the entire emission spectrum (between 260 nm and 500 nm). The CVL contribution is about 5% of the total signal. Figure 5.3 also shows the measured filter transmittance. It can be observed that the filter is selective to the CVL emission and completely cuts the Ce^{3+} emission region.

Figures 5.4 and 5.5 show the results obtained at the Polytechnic of Milan. Figure 5.4 shows the emission spectra resulting after an acquisition time of 2 minutes irradiating the crystal with the ^{137}Cs source, with and without the shortpass filter in between the CLYC and the optical fibre cable. Figure 5.5 shows the RL spectra obtained irradiating the crystal

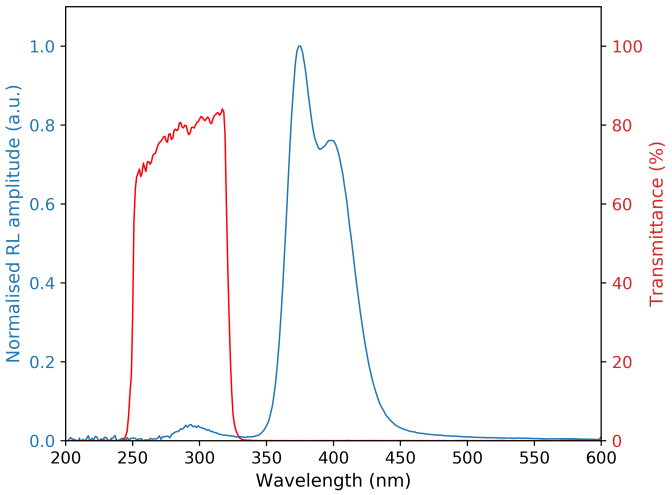

Figure 5.3: Left y-axis: RL emission spectrum in CLYC irradiated with the X-ray tube operated at 20 kV. Right y-axis: measured transmittance of the Asahi Shortpass filter.

at different X-ray energies and with ^{137}Cs photons. The operational conditions (irradiation geometry and X-ray tube current), for the spectra in Figure 5.5, were set in order to acquire sufficiently intense spectra with the lowest integration time (45–60 seconds). A long acquisition time, especially if combined with high dose rate, results in very noisy spectra (characterized by intense spikes in various channels). Moreover, it was noticed that high current values of the X-ray tube significantly increases the background even with the optical fibre alone (without the scintillator). Considering these problematic, the analysis was performed selecting the cleanest and more intense spectra and performing an accurate background subtraction in addition to the background subtraction applied during each measurement.

The spectra are background corrected and normalized to their maximum. The background was calculated as the average value of counts in the 800–900 nm region. The spectra do not provide quantitative information since they are not corrected for the spectral response of the detector, because the response of the CCD was not characterized below 350 nm. Below this value there are no quantitative information. However, a comparison in relative terms is still valid since the experimental setup was the same for all irradiations performed at the Polytechnic.

RL measurements under neutron irradiation were undertaken using an 888 GBq Am-Be neutron source at CERN. The employed readout setup was the same as the one used at the Polytechnic of Milan. A 5 cm thick lead slab was interposed between the neutron source and the crystal to suppress the γ-ray background. In spite of the relatively high activity of the source, the low ^{35}Cl capture cross section and the low sensitivity of the portable spectrometer prevented the detection of any signal above the instrument noise.

The measurement demonstrates the proper selectivity of the filter in cutting the Ce^{3+}-related emission (Figure 5.4). The curves shown in Figure 5.5 do not reveal any dependence of the CVL mechanism on the energy of the incident photons, even though some authors working on the CLYC characterization agree that the CVL mechanism is energy dependent. If a dependence of the CVL on energy in the tested 17–662 keV range exists, the shape of the scintillation spectrum must vary as a function of the photon energy. This plays in favour of the application of this method: if a dependence exists, methods based on the CVL suppression for neutron identification might return wrong results, i.e. low-energy photon-induced events could be misinterpreted as neutron-induced ones. This should be particularly critical in the case of a system using an optical-based discrimination readout.

On the other side, RL measurement confirms that the light emitted in the near UV region is only a portion (about 5%) of the total light emitted by CLYC, which means that the signal to detect after the filter (in the final configuration) might be difficult to detect.

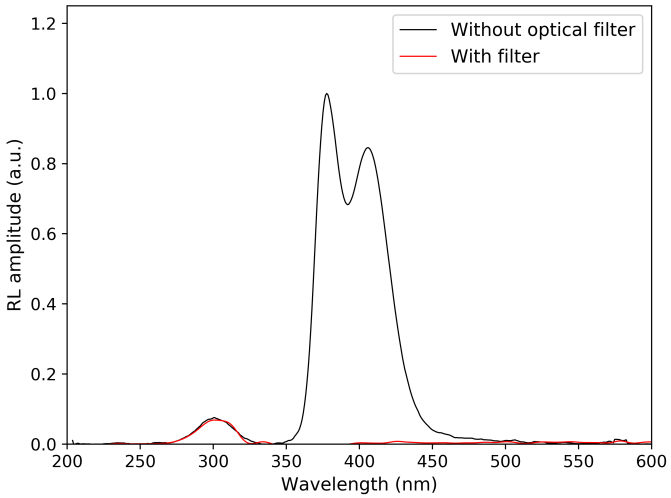

Figure 5.4: RL emission spectrum in CLYC irradiated with the ^{137}Cs source, measured with and without the Asahi Shortpass filter between the crystal and the optical fiber.

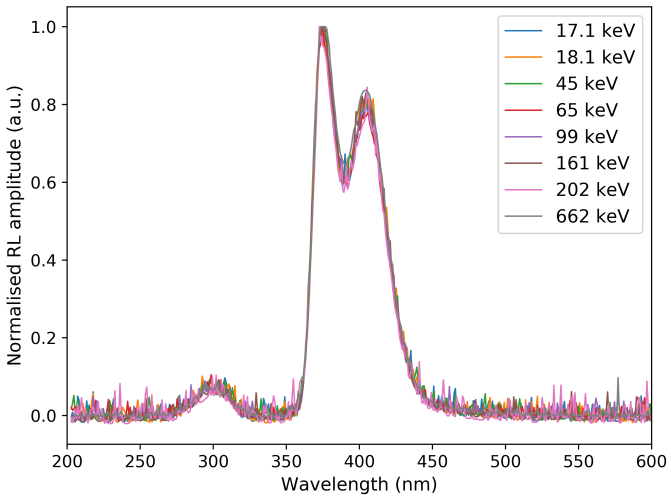

Figure 5.5: Normalized RL emission spectra of CLYC irradiated with X-rays of different energies (mean values between 17.1 keV and 202 keV) and with the ^{137}Cs source (662 keV).

5.3 Pulse shape analysis with the ultra-fast PMT

This section discusses the different scintillation mechanisms in CLYC from the point of view of their characteristic de-excitation times via the pulse shape analysis. Four experiments were performed with CLYC coupled with an ultra-fast PMT and the optical filter: ^{137}Cs irradiation in bare configuration (i.e. CLYC facing the PMT), ^{137}Cs irradiation in filtered configuration (i.e. with the optical filter placed between CLYC and PMT), Am-Be irradiation in bare configuration and Am-Be irradiation in filtered configuration. The corresponding γ-ray and neutron standard pulses were calculated to obtain the time information. Before carrying out the measurements herein described, the transmittance

curve of the optical grease employed in this measurements (Section 5.3.2) was measured (Section 5.3.1).

5.3.1 Measurement of the optical grease transmittance curve

The transmittance of the Rhodorsil Pate 7 optical grease [58] was measured with the aim to check its transmittance in the CVL region. The grease transmittance was measured by means of the PerkinElmer LAMBDA 650 UV/VIS Spectrometer [118]. The spectrometer is provided with two radiation sources, a deuterium lamp and a halogen lamp, to cover the wavelength range 190–900 nm. The light from the source passes through a first optical system consisting of several mirrors, two monochromators, two gratings and one chopper. During this step, the beam is dispersed into its spectral components and according to the rotational position of the grating a portion of this spectrum is selected (i.e. specific values of wavelengths). The grating rotation scans the entire wavelength range from 900 nm to 190 nm, in 2 nm steps. The rotation of the chopper splits the beam into two beams: the reference beam and the sampling beam. The sample is placed in the sampling beam's trajectory, while the reference beam does not cross it. Both beams are collimated through a second optical system (consisting of mirrors), toward a PMT operating in the UV/VIS range which measures the amount of light of the two beams. The transmittance of the sample is calculated by comparing the reference and the sampling beams. A simplified schematic of the optical system is shown in Figure 5.6.

The optical grease was applied as a small and uniform layer between two small plates of quartz, which was placed in the sample reference position. The measurement revealed that the transmittance of the optical grease is almost constant at 90% between 400–800 nm, it decreases down to 70% from 400 nm to 200 nm and it drops down to 30% below 200 nm (see Figure 5.7). The considered grease is thus suitable for measuring light emitted also in the CVL range. Despite of the reduction of its transmittance, 70% is acceptable.

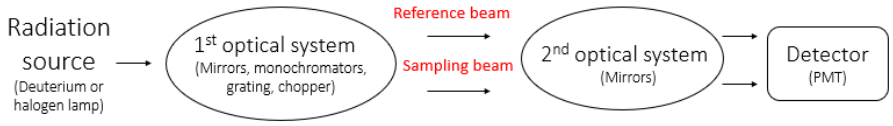

Figure 5.6: Simplified schematic of the LAMBDA 650 optical system.

5.3.2 Setup with the ultra-fast PMT

The Hamamatsu H6610 Bialkali PMT [119] was selected, on the suggestion of the manufacturing company (Radiation Monitoring Devices), for two main reasons: its time response and its spectral response. According to the datasheet, at 25°C the PMT is characterised by a rise time of 0.7 ns and by a transit time spread of 0.16 ns. Since the detected pulse is the result of the convolution between the time response of the scintillator and the PMT, the response of the PMT can be neglected if the PMT response is faster than the characteristic decay times we are interested in.

Besides being characterised by a very short decay time (order of ns), the CVL mechanism is observed in the UV wavelength range (250-350 nm). As shown in Figure 5.8, the quantum efficiency of the H6610 PMT (the dash line referring to H6610) is almost flat from 200 nm up to ∼430 nm, around its maximum value (about 20 %) and slowly decreases at lower wavelengths down to 160 nm, characteristic cut-off wavelengths of its window material (silica glass) [119].

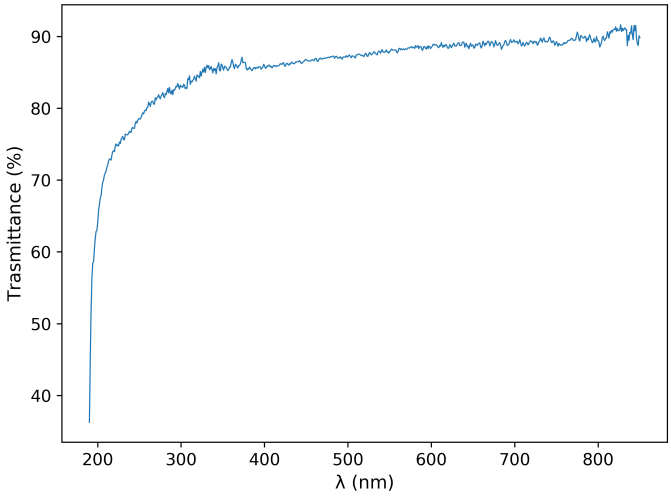

Figure 5.7: Measured transmittance curve of a thin layer of Rhodorsil Pate 7 optical grease in between two quartz plates.

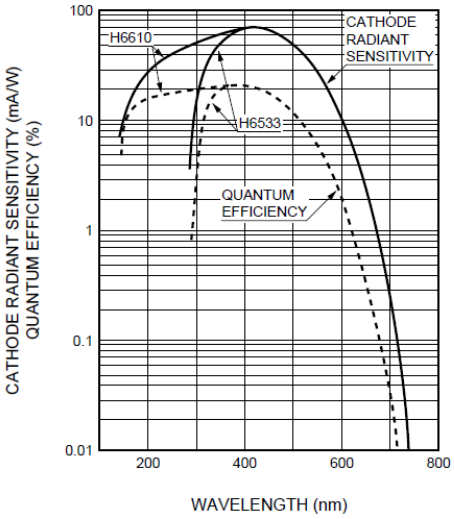

Figure 5.8: Quantum efficiency and Cathode Radiant Sensitivity (mA/W) of the H6610 Hamamatsu PMT [119].

Without the filter, CLYC was coupled with the H6610 PMT through the Rhodorsil Pate 7 optical grease; the effective area of the PMT photocathode (20 mm diameter) was completely covered by the crystal surface whose diameter is 25.4 mm. A negative high voltage of 2500 V was supplied to the PMT, as recommended by the datasheet, whereas the output was directly connected to the Teledyne LeCroy Waverunner 8104 Oscilloscope (1 GHz, 20 GS/s) with a 50 Ω termination. The PMT and the crystal were placed inside a light-tight and thermally regulated chamber kept at constant temperature of 18°C. With the filter, the latter was interposed between the PMT photocathode and the CLYC and a thin layer of the optical grease was applied on both the filter surfaces.

5.3.3 Results with the ultra-fast PMT

In the case of the γ-ray irradiation (i.e. with ^{137}Cs), all pulses were analysed by aligning, normalizing and averaging the data under the ^{137}Cs photopeak at 662 keV, thus obtaining the so-called standard pulse. In the case of Am-Be irradiation, particle discrimination was first performed by the Pulse Shape Discrimination (PSD) using the charge integration

method.

Figure 5.9 shows the PSD histogram plot and the 2D histogram plot of the PSD versus the total charge in the case of unfiltered Am-Be irradiation. The acquired signals were then classified in the PSD space, and only those belonging to the neutron region of the PSD space (blue box in the right plot of Figure 5.9) were used for the decay time analysis. The neutron region was defined by the signals with a PSD value within $x_n \pm \sigma_n$, i.e. between 0.082 and 0.113, in order to cut the signals in the tails of the Gaussian distribution. For the sake of completeness, also the signals classified in the PSD space as photons (red box in the right plot of Figure 5.9) were averaged and the corresponding standard pulse was calculated for the decay time analysis.

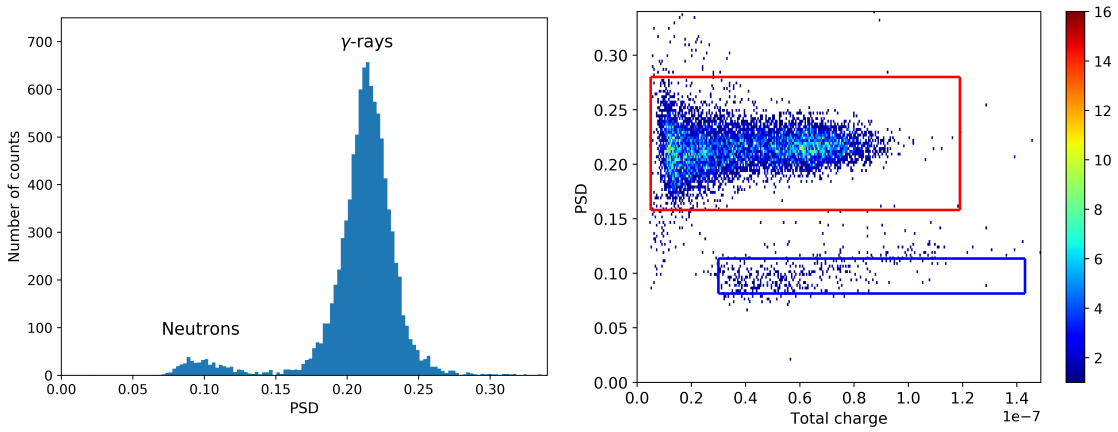

Figure 5.9: On the left, the PSD histogram plot calculated for the Am-Be neutron source; on the right, the 2D PSD histogram plot where γ-rays and neutrons are identified by the two regions enclosed in a red and a blue box, respectively.

As mentioned above, measurements were performed for both the bare and the filtered configuration. However, the filtered results had to be discarded, because the filter did not significantly modify the recorded signals in the case of both γ-ray and neutron irradiations. This result is in contrast with the previous RL measurements, where it was observed that only the emission related to the CVL region was transmitted by the optical filter, and thus an appreciable distortion of the signal was expected. Moreover, the signal amplitude did not vary significantly. Therefore, the filtered results were rejected because of experimental errors. Two possible explanations are: 1) a problem in the measurement setup, i.e. inaccurate coupling between crystal and filter, or 2) effects of the optical grease and/or direct coupling between crystal and filter. The second hypothesis is related to the fact that the dichroic filter used is slightly sensitive to both the impinging photon direction and the refractive index of the medium it is in contact with. The filter transmittance was measured in air (Figure 5.3), while during the measurements with the PMT the filter was in between the PMT and CLYC and its surfaces were covered by the optical grease.

The obtained decay curves of the standard pulses were fitted using a sum of four, for γ-rays, and three, for neutrons, exponential decays, according to the following equation:

$$y(t) = \sum_i A_i e^{-t/\tau_i} \tag{5.1}$$

where A_i is the amplitude of each exponential and τ_i the decay time.

Figures 5.10, 5.11 and 5.12 show the standard pulses with the fit and the plot of the residuals calculated as the difference between the experimental and the model predictions. In all cases the fit is satisfactory, with $R^2 \sim 1$; the model does not systematically underestimate/overestimate the experimental data. The results of the fits are summarized in

Table 5.2. For each pulse, the table reports the time constants τ_i and the relative intensity of the associated scintillation mechanism in relation to the total signal. The relative intensities were calculated as the percent contribution of the single scintillation mechanism to the total signal. A total uncertainty of 10 % was estimated for these measurements. The uncertainty of the calculated decay time is mainly affected by the number of the averaged signals, the signal alignment and the region selected as neutrons or photons in the 2D PSD histogram plot, whereas the uncertainty on the fitting procedure is negligible.

For comparison Table 5.3 reports the characteristic decay times obtained by other authors for γ-rays and neutrons. Table 5.4 compares the rise and transit time and the lower wavelength of the spectral response for the PMT used in this work and the PMTs employed by the authors cited in Table 5.3.

Table 5.2: The decay times (τ) and the relative intensity (Int) of the CLYC scintillation mechanisms calculated for the standard pulses produced by γ-rays and neutrons. Measurements performed with the Hamamatsu H6610 PMT.

	CVL		Fast Ce^{3+}		V_k		STE		
Particle (source)	τ_1 (ns)	Int (%)	τ_2 (ns)	Int (%)	τ_3 (ns)	Int (%)	τ_4 (ns)	Int (%)	R^2
γ-rays (^{137}Cs)	2.7 ± 0.3	1.10	45 ± 5	3.26	781 ± 78	20.68	6325 ± 633	74.96	0.988
γ-rays (Am-Be)	2.5 ± 0.2	1.49	43 ± 4	3.70	747 ± 75	21.11	5806 ± 581	73.70	0.997
Neutrons (Am-Be)	1.7 ± 0.2	0.22	—	—	824 ± 82	25.57	6140 ± 614	74.21	0.993

Table 5.3: The decay times (τ) of the CLYC scintillation mechanisms induced by γ-rays and neutrons from the literature.

		CVL	Fast Ce^{3+}	V_k	STE
Budden et al. [111]	γ-rays	3 ns	72 ns	415 ns	3.47 μs
	Neutrons	—	—	393 ns	3.18 μs
D'Olympia et al. [87]	γ-rays	48 ns	280 ns	730 ns	5.24 μs
	Neutrons	—	440 ns	1.17 μs	6.31 μs
Wen et al. [120] *	γ-rays	96–24 ps	47–54 ns	651–690 ns	4.96–5.15 μs
	Neutrons	—	—	624 μs	4.57 μs

* For γ-rays, the decay times were calculated for different energy depositions in the energy range 190–1010 keV.

The results presented in this work for the γ-ray irradiation are coherent with the literature data. Four mechanisms were observed with the following decay times: CVL 1–5 ns, direct capture $\sim$ 50 ns, binary recombination mediated by V_k $\sim$ 700 ns and STE $\sim$ 5 µs. For the neutron irradiation, these results are only in partial agreement with the literature, since the present results show that an ultra-fast scintillation mechanism is also present with neutrons, which was attributed to the CVL. The faster decay time of the CVL with neutrons might be due to the statistical uncertainty of the standard pulse. On the contrary, literature data agree on the quenching effects of high LET particles, such

Table 5.4: The main properties of the PMT employed in this work and by other authors for the calculation of the scintillation decay times in CLYC.

	PMT	Rise time	Electron Transit Time	Transit Time Spread	Wavelength cut-off
This work	Hamamatsu H6610	0.7 ns	10 ns	0.16 ns	~150 nm
Budden et al.	Hamamatsu R11625	1.3 ns	5.8 ns	0.27 ns	300 nm
D'Olympia et al., Wen et al.	Hamamatsu R6231-100	8.5 ns	48 ns	6.9 ns	300 nm

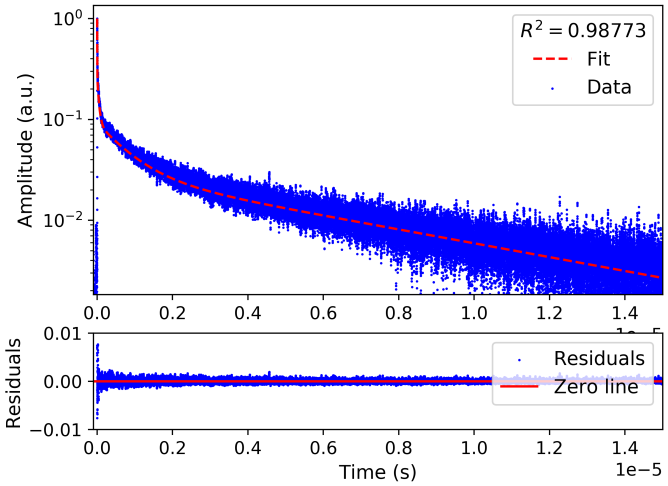

Figure 5.10: Top: the standard pulse and the fit of the photon signals for the ^{137}Cs source irradiation. Bottom: the plot of the residuals.

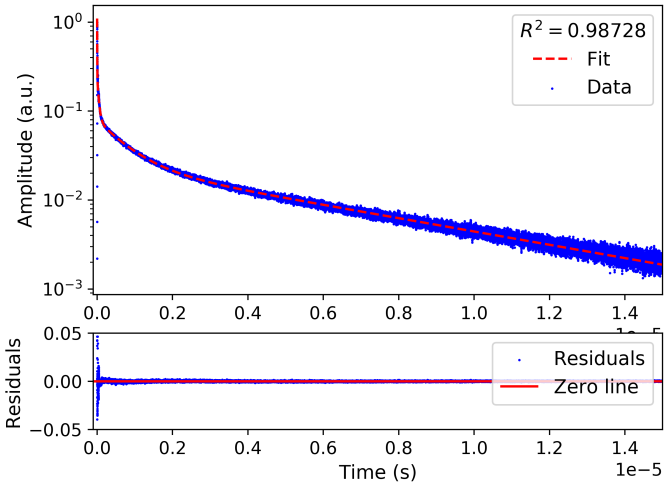

Figure 5.11: Top: the standard pulse and the fit of the photon signals for the Am-Be source irradiation. Bottom: the plot of the residuals.

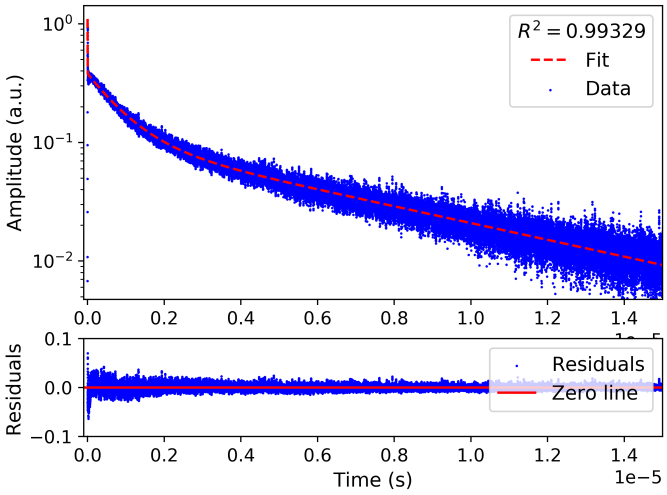

Figure 5.12: Top: the standard pulse and the fit of the neutron signals from the Am-Be source irradiation. Bottom: the plot of the residuals.

as the reaction products from neutron reactions, on the CVL. The LET of an α-particle produced by a neutron from an Am–Be source in CLYC is around 150 keV/μm while it is 15 keV/μm for a proton, i.e. 30 and 3 times higher, respectively, than 5 keV/μm, i.e. the maximum LET studied in Section 5.2.2.

According to the present results, the CVL is only partially quenched by neutrons, while the fast decay is completely quenched. In fact, the neutron standard pulse is better fitted by a 3-exponential function rather than a 4-exponential one. The relative importance of the CVL drops from 1.1% with a 4-exponential function in the case of γ-ray irradiation, down to 0.22% with a 3-exponential function in the case of neutron irradiation. This result is not in complete disagreement with literature data. Firstly, the CVL is actually quenched by high LET particles, while the low intensity of the residual CVL might not be observed if the employed setup is not sensitive enough. In the present experiment, the flat spectral response and fast rise time of the Hamamatsu H6610 PMT together with the fast oscilloscope allowed distinguishing between the two contributions (CVL and fast Ce^{3+}) even in the case of a strong CVL quenching. However, Figure 5.12 clearly shows a fast peak also for the neutron pulse.

As concerns the application of this method to the B-RAD, the presence of the CVL under neutron irradiation prevents its implementation, since all the signals would be rejected. However, the n/γ discrimination could be still envisaged if the pulses produced by neutrons via the CVL only are always smaller than the pulses produced by γ-rays through the CVL only. In this case, with a proper energy threshold, the signals produced by neutrons due to the CVL cannot be detected. This can be clarified by the neutron excited RL spectrum, which can give quantitative information of the light emitted by neutrons in the CVL region. As stated before, with our own setup this measurement did not provide any information. Further investigation are necessary.

5.4 Pulse shape analysis with the Time Correlated Single Photo Counting (TCSPC)

As in the previous section, the measurements here described reveal the characteristic decay times of the crystal using a different method: the Time Correlated Single Photon Counting (TCSP). The TCSPC technique is specifically aimed for precise time measurements of inorganic scintillators [105, 106]. The working principle of the TCSPC technique and the specific setup employed in this work are described in Section 5.4.1, while the results are discussed in Section 5.4.2. As explained in Section 5.4.1, this TCSP setup can only provide the decay times under γ-ray irradiation. However, it is possible to establish a correlation between the PMT and the TCSP by means of the results obtained with the γ-ray source and validate the former method which gives information also under neutron excitation. This is discussed in Section 5.5.

5.4.1 TCSPC setup

A ^{22}Na β^+ source was interposed between the CLYC and a fast detection system called start detector. The start detector is composed of a 2 mm $\times$ 2 mm $\times$ 5 mm LSO:Ce crystal coupled to an Hamamatsu Photonics K.K. (HPK) S13360-3050 Silicon Photomultiplier (SiPM) with a Meltmount thermoplastic, connected to a NINO readout board [121]. On the other side, CLYC faced a Vacuum Ultraviolet single–photon avalanche diode (VUV–SPAD) from Fondazione Bruno Kessler, called stop detector ([122]). A SPAD is a photodiode operating in Geiger mode as an on-off switch triggered by a photon arriving on its surface. A SiPM is actually a dense array of independent SPADs, whose function is to count the number of photons reaching the SiPM surface [123]. In the hereby described setup, the CLYC and the stop detector (the VUV–SPAD) were not optically coupled [124].

The TCSPC technique works as follows (Figure 5.13). When one of the two annihilation γ-rays emitted in coincidence by the source is detected in the start detector, the time measurement starts. If the second γ-ray interacts with the crystal facing the stop detector, the scintillation produces several visible photons following its characteristic decay time statistics. The time measurement stops when the first scintillation photon reaches the stop detector. Saving a large number of events and plotting them on a histogram, the decay time of the scintillator is reconstructed in terms of number of counts versus emission time [105, 106].

The measurement was performed with and without the filter. In the former case, the filter was interposed between the CLYC and the stop detector, at a distance of a few centimetres from both. Because of the smaller dimensions of the stop detector (a few tens of μm^2) compared to the surface of the filter (Ø 25 mm), it is reasonable to assume that the light reaching the photodetector was correctly filtered.

5.4.2 Results with the TCSPC setup

Figure 5.14 shows the results of the TCSPC measurement: the left plot shows the unfiltered configuration, the right plot the filtered one. The points in the histogram are the time measurements with a bin width of 60 ps. The green line is the moving average of the data, the red line is the fit to the data. The plot of the residuals of each pulse is also shown. Table 5.5 reports the decay times τ_d, with their statistical uncertainties and their relative intensity on the total signal. A 0.5 % uncertainty on the calculation of the decay times is due to the TCSPC setup [105], which is negligible with respect to the fitting uncertainty. Thus, the latter is reported in Table 5.5.

The decay constants estimated with the TCSPC setup without the filter match reasonably well the decay times measured with the PMT and are consistent with literature

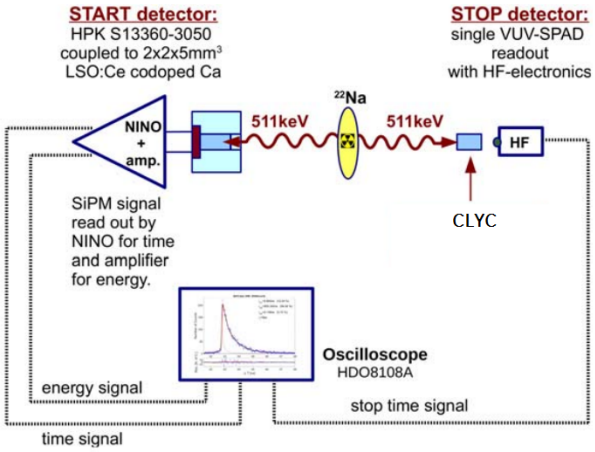

Figure 5.13: The TCSPC setup with the CLYC crystal [27].

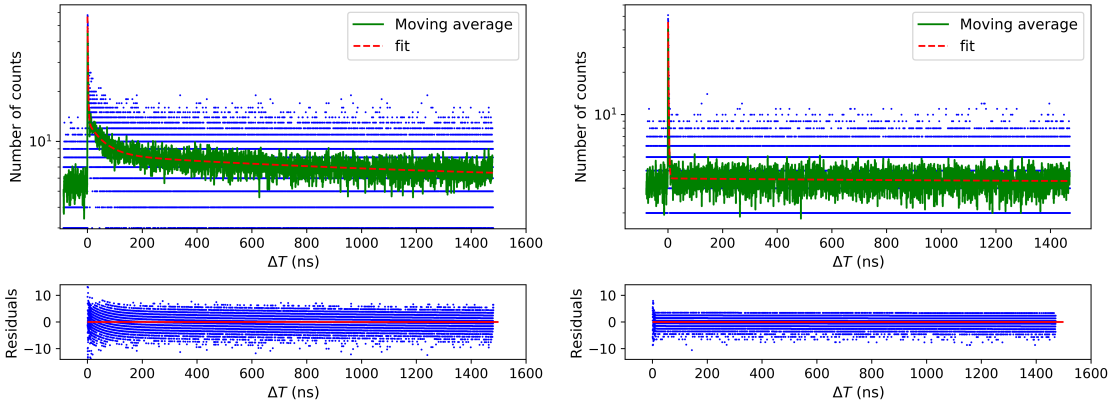

Figure 5.14: The result of the TCSPC measurement of the CLYC response without the filter (on the left) and with the filter (on the right). The points are the measured data, the green line is the moving average and the red line is the fit. The bottom plots show the corresponding residuals.

Table 5.5: The decay times (τ) and the relative intensity (Int) of the CLYC scintillation mechanisms estimated through the TCSPC technique in both bare and filtered configurations.

Setup	CVL		Fast Ce^{3+}		V_k		χ^2
	τ_1 (ns)	Int (%)	τ_2 (ns)	Int (%)	τ_3 (ns)	Int (%)	
Unfiltered	1.90 ± 0.07	2.06	57 ± 4	6.53	1379 ± 67	91.41	1.002
Filtered	1.67 ± 0.04	18.58	—	—	1639 ± 482	81.42	0.997

data, taking into account the different recorded length [111, 120]. In the filtered configuration the fast emission is dominated by the CVL mechanism, while the Ce^{3+} emission around 50 ns is not detected, so it appears that optical filtration is in line with the RL measurements.

The TCSPC setup is optimized for the estimation of the fastest decay mechanisms of the analysed scintillator. In particular, its 60 ps discretization and the possibility to introduce the impulse response function of the measurement system in the fit allow pre-

cisely estimating extremely fast decay constants [106]. Conversely, the 1500 ns integration window does not permit distinguishing between the two slowest scintillation mechanisms, which are merged in a single V_k + STE component.

The results with the TCSPC setup play in favour for the application of the method to the B-RAD. The measurements confirm the presence of the CVL component under γ-ray excitation, i.e. γ-ray events can be rejected by the anti-coincidence system.

5.5 Discussion

The different experiments here reported observe the same scintillation process from different perspectives, i.e. in the time and wavelength domains. The RL filtered versus unfiltered results can be qualitatively compared to the TCSPC filtered versus unfiltered results, respectively. In both cases, the optical filter was placed at a certain distance between the crystal and the sensor, without any optical coupling. The RL measurement results showed that no signal was collected at wavelengths longer than the filter cut-off. In the TCSPC experiments, the decay constant of the fast mechanism, which is confined within 350–450 nm wavelength range, completely disappeared.

The merged V_k + STE component becomes appreciably slower with the optical filtration, thus suggesting that also the intermediate component, which is again confined in the Ce^{3+}-related region, was blocked by the filter. Literature data and the RL measurement (Figure 5.3) endorse this hypothesis. Thus, the retention of the slower component in the filtered signal can be ascribed to the STE de-excitation since its emission spectrum spans from 240 nm up to 460 nm [107, 108, 125], even though in large doped crystals the STEs mainly de-excite on Ce^{3+}, as discussed in Section 5.2. Therefore, most of the signal belonging to the lower wavelength region appears to be dominated by STE de-excitation instead of CVL (at least $> 80\%$ relative importance; the exact value can be obtained with integration windows at least ≤ 15 μs). However, the number of counts of the filtered signal in the tail region is around the background level and its estimation is affected by a major uncertainty. For this reason, the relative intensities of the decay mechanisms in the deep-UV–NUV region cannot be precisely evaluated.

The TCSPC and fast PMT results can be quantitatively compared. The H6610 PMT is particularly fast: its rise and transit times are of the order of tenths of ns. However, considering the 1–5 ns decay constant of the CVL, the PMT response function is expected to perturb the estimation of the decay constant. On the contrary, the 1500 ns integration window allowed distinguishing between the intermediate and the slow components. Therefore, the two measurements allow estimating different quantities in the bare configuration under γ-ray irradiation, but a correspondence should first be established. To assess the correspondence between the two measurements, one can integrate the fast PMT measurement in the bare configuration under photon irradiation for 1500 ns and compare it to the corresponding TCSPC result. The fit has to be done with the same 3-exponential function of the TCSPC experiment. Table 5.6 summarizes the obtained fit coefficients with their statistical uncertainty and their relative intensities.

The two fits are quantitatively super-imposable. The main difference is a 45% discrepancy on the CVL decay constant, which is slower in the case of the fast PMT measurement. The result was expected since the PMT response time is comparable to the CVL decay constant. However, the relative intensity is the same for the PMT and TCSPC measurements. Hence, the four decay coefficients estimated with the fast PMT measurement (see Table 5.2) can be considered sufficiently accurate for estimating the effects of the neutron quenching on the CLYC scintillation mechanisms. Therefore, the conclusions drawn in Section 5.3.3 are further validated, i.e. with neutrons the fast mechanism is fully quenched, while the CVL is strongly, but only partially, quenched.

Table 5.6: Decay constants (τ) and relative intensities (Int) of the CLYC scintillation mechanisms measured with the TCSPC technique compared to the Hamamatsu H6610 PMT results. In both cases the integration time was 1500 ns.

Setup	CVL		Fast Ce^{3+}		V_k	
	τ_1 (ns)	Int (%)	τ_2 (ns)	Int (%)	τ_3 (ns)	Int (%)
TCSPC	1.90 ± 0.07	2.06	57 ± 4	6.53	1379 ± 67	91.41
PMT	2,80 ± 0.03	2.04	49± 5	6.46	1394 ± 139	91.50

It is worth mentioning that the quenching of the CVL by heavy ions is still under study, especially for relatively new crystals such as CLYC. Most of the authors agree with ascribing this effect to the high excitation density promoted by heavy ions [87, 126, 127], however its origin is not completely clear. For example, according to Kirm et al., [126], the quenching of the CVL is due to the higher probability, with increasing LET, of recombination between the electrons of the conduction band with the holes of the core band. This recombination competes with the CVL. Nevertheless, in [127] an ultra-fast scintillation mechanism (< 1 ns), ascribed to the CVL, was actually measured in a BaF_2 crystal after heavy ion irradiation. Further investigations are required, in particular in the light of performing n/γ discrimination using the emission-wavelength information.

5.6 Conclusions

The proposed n/γ discrimination based on the optical filtration of CLYC-7 scintillation light is a completely new and promising method for the B-RAD. It would allow avoiding the time and battery consuming PSD method due to the continuous digitalizing of the signal. Furthermore, the traditional PSD method is usually affected by count rate limitations (dead time increasing) and false positives.

The different experiments performed using CLYC-7 and the Asahi optical filter were aimed at verifying its feasibility, but also allowed precisely characterizing the material scintillation process. The wavelength-resolved RL results obtained with different photon energies verified that there is no energy-dependence of the CLYC emission in the range 17–662 keV, i.e. X-ray and γ-ray stimulations do not significantly distort the CLYC scintillation process. This result plays in favour to its application on the B-RAD. However, the CVL component is only 5% of the total scintillation and it could be below the lower detectable limit of the photodetector.

On the other hand, the fast PMT measurements revealed that a residual CVL signal is observed also under neutron excitation. Moreover, the filtered versus unfiltered TCSPC experiments suggested that in the 250–330 nm region both the CVL and the host luminescence are present, with a predominant contribution due to the STE de-excitation. However, the relative intensity of these two mechanisms cannot be precisely estimated because of the uncertainty affecting the STE estimation and the short integration window of the TCSPC experiment. The RL spectrum of CLYC-7 under neutron irradiation can quantify the contribution of the CVL respect to other scintillation mechanisms. At the time being, this method cannot be applied to the B-RAD since further tests have to be performed.

Conclusions

The commercial version of the B-RAD radiation survey meter by ELSE NUCLEAR was fully characterised. The response of the device was tested both in terms of γ-ray dose rate and γ-ray spectrometry in magnetic fields from 0.2 T up to 2.5 T, with a ^{137}Cs source. The measurements were performed in different configurations of the detector (probe+unit, only probe, only the main unit inside the magnetic field) simulating different working scenarios. All the components of the B-RAD work properly even in high magnetic fields, especially the LCD and LED displays and the battery that showed in the previous versions some deficiencies. The case of the B-RAD has been optimise to minimise the pulling force acting on the mechanical components, however an intense force is still felt on the main unit above 0.5 T, increasingly strong with the magnetic field. The response in terms of count rate was very uniform up to 2.5 T for all the configurations. However, a variation of the energy spectrum is present when the unit is inside the magnetic field that leads to a variation of the measured dose rate. This variation is negligible up to 0.5 T and is of the order of 10% at 1.5 T. From the operational point of view, these results are acceptable in radiation protection.

Tests performed at CERN confirmed the good linearity with the dose rate in the 1 μSv/h–2 mSv/h range (variation in respect of the reference dose rate of less than 10%), the wide energy range (30 keV–2 MeV) and the very good energy resolution (less than 5% at 662 keV). The B-RAD response is almost not affected by the direction of the detector in respect of the source direction, except when the source is behind the probe (at 180°$\pm$30°). For these angles, the measured dose rate drops by 70% in respect of the nominal value. The B-RAD is also a stable device, with a fast response time. It was already tested to measure the residual activity of twenty permanent magnets stored at CERN allowing 50% of them to be classified as radioactive. The other devices in use at CERN failed because of the presence of the magnetic field.

The current B-RAD has by far met the original requirements, i.e. a radiation survey meter for residual activity measurements in magnetic field regions. It is a developed device for γ-ray spectrometry and dose rate measurement, with a wide energy and dose rate working range. It provides a flattening algorithm to compensate the variation of the scintillation efficiency with the energy, a temperature compensation system and nuclide identification. Up to now, the B-RAD is only provided with a probe for γ-ray detection, but additional probes, for particles different form γ-rays, are under investigation.

In this context, two organic scintillators were studied and compared in view of their application to the B-RAD as a probe for fast neutron dose rate. One–inch right cylindrical stilbene and EJ-276 (plastic) scintillators were coupled with a large area SiPM array (8×8 pixels) and characterised in terms of: energy calibration and resolution with γ-ray sources, neutron/γ-ray (n/γ) discrimination via the Pulse Shape Discrimination (PSD), linearity with the dose rate, temperature dependence and neutron detection efficiency. The energy calibration was performed with three different γ-ray sources taking the Compton edges as calibration points. The Compton edge of each spectrum was obtained by comparing the experimental spectrum with the spectrum calculated, for the same source, with a Monte Carlo simulation and applying a Gaussian Energy Broadening. The calibration curves

of both scintillators are very linear except for low energy values (below 100 keV) where non-linearities in organic scintillators arise. The calibration curves confirm the better light yield of the stilbene in respect of the EJ-276 (14,000 photons per MeV versus 8,600 photons per MeV) and the better energy resolution (15% versus 20% at 477 keV). The stilbene shows better n/γ discrimination performances with a FOM of 1.54 versus 0.90 obtained with the plastic. This results plays in favour of the use of the stilbene since n/γ discrimination is essential for any neutron detector. The response in terms of count rate of both scintillators is linear with the source dose rate up to around 3-4 $\times 10^3$ detected counts per second, which corresponds to around 1 mSv/h from a ^{137}Cs source and more than 1.5 mSv/h with an Am-Be source. The saturation limit was not reached in the latter case even with the highest activity Am-Be source available. For a portable detector these limits can be accepted, however a Pile-Up-Rejection (PUR) algorithm, as the one proposed in this work, can improve the linearity up to 10 mSv/h for ^{137}Cs. With the Am-Be source the PUR correctly removed false events at the expenses, however, of the neutron detection efficiency. A PUR rejection must be considered for use of the detector with high intensity source. However, a quantitative analysis of the reduction of the neutron detection efficiency when the PUR is applied was not carried out, but must be performed in the future. The neutron detection efficiency obtained with an Am-Be source is 12% for the stilbene and 9% for the EJ-276, mainly because of the lower energy threshold settable with the former. The two detectors show a variation of around 25% of their light yield in the -10 °C–40 °C temperature range, whilst the neutron count varies in the same temperature range of around 10%, which is acceptable for many application in radiation protection.

Two additional probes were studied based on CLYC crystals: a probe for thermal neutron detection (CLYC-6 based) and a probe for fast neutron spectrometry (CLYC-7 based). Both CLYC-6 and CLYC-7 crystals have an excellent n/γ discrimination capability (FOM > 2) and a very good energy resolution (thanks to the high light yield of inorganic crystal). The former represents an appealing alternative to the bare ^{3}He proportional counter, currently in use in homeland and national security, medicine, industry. However ^{3}He is in short supply on the market and alternatives have been investigated. In this work, a thin CLYC-6 scintillator showed a better thermal neutron detection per unit volume than a traditional spherical ^{3}He counter (more than 60%). It is easy to transport and it can be easily embedded in PE materials to enhance the thermal neutron response.

The use of CLYC-7 as a fast neutron spectrometer is also attractive. It allows fast neutron spectrometry using a single and relatively small detector (a 1–inch right cylinder scintillator was used in this study) avoiding the heavy Bonner Sphere Spectrometry system, which also requires the unfolding procedure. However, fast neutron spectrometry with CLYC-7, without unfolding, is in principle limited up to 2.5 MeV, since, below this energy, neutrons are detected only via the (n,p) nuclear reaction. Above this energy, the (n,α) reaction is also present. In this work a proton/α-particle discrimination technique is proposed and tested with the continuous neutron spectra from an Am-Be and a ^{252}Cf source. The method improves the spectrometry performance of the crystal especially between 2 MeV and 5-6 MeV. The method did not provide a perfect match between the experimental and the reference spectrum, but it is able to well predict the position of the main peak for both tested neutron sources. In many application, e.g. around medical accelerator facilities, where the neutron energies are always below a few MeV this results are interesting. At the time being, the company is working on the implementation of the probe for fast neutron dose rate and spectrometry on the current commercial version.

Although the PSD method is a well-known and effective way to discriminate different particles, some limitations exists, such as long computing time, false positives (usually minimised by increasing the energy threshold), which increase especially with high intensity sources. A passive and on-line method, as the one proposed in this thesis, is sometimes

preferred. This new method is applicable with CLYC and is based on two assertions: in CLYC, a scintillation mechanism only excited by γ-rays exists; this scintillation mechanism emits in a different wavelength range in respect of the other scintillation mechanisms. According to the literature these requirements are met in large CLYC crystals with the CVL scintillation mechanism. However CLYC is a relatively new crystal and studies on its scintillation processes are still ongoing. A quantitative analysis of the quenching effect on the CVL with different particles is still lacking in the literature. We thus performed a study of the scintillation light emitted by CLYC with an interest on the CVL both from the wavelength and the time point of view. It results that the CVL intensity does not change with the X and γ-ray excitation in the range 17 keV–662 keV. The CVL is actually quenched by neutrons, however a residual of the CVL was detected also under neutron excitation. The first result shows that the light emitted by the CVL after a γ-ray interaction can actually produce a detectable signal capable of rejecting γ-ray events. The second result implies that all the neutron events would be rejected, and the method cannot be employed. However, the method is still feasible if the quenching effect on the CVL due to neutrons is strong enough to produce a signal which is always rejected by the energy threshold. Further analysis are necessary, in particular the neutron excited radioluminescence spectrum which can provide quantitative information on the CVL emitted after neutron excitation. This innovative method is promising, but is not ready for its application on the B-RAD.

Nowadays, the B-RAD is available on the market and two units have been purchased by CERN for current use in radiological clearance projects. At CERN, there is also an interest in the B-RAD to perform residual activity measurements of materials that have to be transported internally. Besides its use at CERN, the B-RAD can find several applications in medical fields, industry, radiological waste.

Appendix A

A thermal neutron source for CERN Radiation Calibration Laboratory

A.1 Introduction

Appendix A presents the design, construction and experimental characterisation of a thermal neutron source for CERN radiation Calibration Laboratory (CalLab). It consists of a neutron thermalization assembly, to be used with the existing Am-Be source irradiator and specifically designed to maximise the thermal neutron fluence. The design and the characterisation were carried out via Monte Carlo (MC) simulations, benchmarked with the measurements performed with a bare ^{3}He counter.

Section A.2 introduces the CERN CalLab and other thermal neutron facilities taken as reference. Section A.3 discusses the MC simulations performed to determine the optimum geometry and dimensions of the assembly. Based on these results, the moderator assembly was designed and built (section A.4). Thereafter, measurements with a bare ^{3}He proportional counter were performed to benchmark the MC predictions (section A.5). Additional MC simulations were then performed to characterise the new thermal neutron facility in terms of intensity and uniformity of the thermal neutron fluence and neutron energy spectrum. Simulations were also carried out enclosing the irradiation position within a cadmium shell, which can be used to discard the fast neutron contribution through a difference method. The details of the simulations are discussed in section A.6. Section A.7 compares the results presented in this work with the reference facilities. Section A.8 summarises the results.

A.2 Overview of thermal neutron facilities

The CalLab is a state-of-the-art radiation calibration facility. It is provided with a small room housing a 11.8 TBq (in August 2014) ^{60}Co source mainly used for studies of radiation damage to electronics, and a main calibration hall (13 m $\times$ 13 m $\times$ 13 m in size) housing four Am-Be neutron sources, six γ-ray sources, two β sources and an X-ray generator [31, 128, 30]. The main hall is used for a variety of metrology and dosimetry applications, from the calibration of personal dosimeters, handheld survey meters and monitors installed in the accelerator tunnels and experimental areas, to characterization of novel detectors.

A thermal neutron source usually consists of one or more fast neutron sources surrounded by moderating material, graphite and polyethylene (PE) being the most common. Table A.1 reports the main characteristics of five different thermal neutron facilities

in the world. Thermal neutron facilities employing graphite usually consist of very large moderating assemblies. An example is the facility at PTB in Braunschweig, Germany (see Table A.1). Bedogni et al. [129, 130] proposed a new design, based on a cavity with PE walls, which embodies the radionuclide source, the irradiation volume and, between them, a shadow PE sphere or bar. The main concept is that neutrons reach the irradiation location only after several scattering reactions.

For the CERN CalLab we proposed a thermal neutron assembly consisting of a small moderator to be placed around the source and a reflector box facing it. At the CalLab the neutron source is indeed stored at the bottom of the room and is raised to its irradiation position inside a cylindrical aluminium guide by a pneumatic system (Figure A.1). The fast neutron source cannot be surrounded by PE walls and the thermal neutron fluence is instead increased by the scattering reactions of thermal neutrons on the reflector's walls, which encloses the detector under test and delimits the irradiation region. It is also possible to use the moderator only, i.e. without the reflector box. For this reason, this second option is also discussed in the following sections.

Table A.1: Comparison of the main properties of six worldwide thermal neutron facilities.

Facility	Source	Moderator material	Moderator geometry	Size	Thermal neutron fluence rate ($E_n < 0.5$ eV)	
SIGMA (France)	6 Am-Be sources	graphite	single block	150 × 150 × 150 cm^3	1,513 cm^{-2} s^{-1}	[131]
PTB (Germany)	16 Am-Be sources	graphite	single block	150 × 150 × 180 cm^3	80 cm^{-2} s^{-1}	[132]
FANT (Spain)	Am-Be source	polyethylene	Parallelepiped-like irradiation cavity	90 × 70 × 70 cm^3	1000 cm^{-2} s^{-1}	[133]
			shadow cylinder	10 cm ⌀ × 20 cm		
ETHERNES (Italy)	Am-Be source	polyethylene	Parallelepiped-like irradiation cavity	63 × 45 × 45 cm^3	from 550 to 800 cm^{-2} s^{-1}	[129]
			shadow sphere	20 cm ⌀		
HOTNES (Italy)	Am-B source	polyethylene	Cylinder-like irradiation cavity	30 cm ⌀ × 70 cm	from 700 to 1,000 cm^{-2} s^{-1}	[130]
			shadow cylinder	10 cm ⌀ × 20 cm		

A.3 Moderator assembly optimisation

This section is divided in three parts: the first describes the simulation geometry and the primary beam particles; the second part describes how the neutron fluence has been scored; the last one shows the results and point out the best geometry.

The MC simulations were performed with version 4.0 of the FLUKA code [66, 67, 68]. During all the simulations described in Appendix A, the input card DEFAULT was set to the option PRECISIOn, which ensures the fully analogue absorption for low-energy neutrons and neutron transport down to 1×10^{-14} GeV [68].

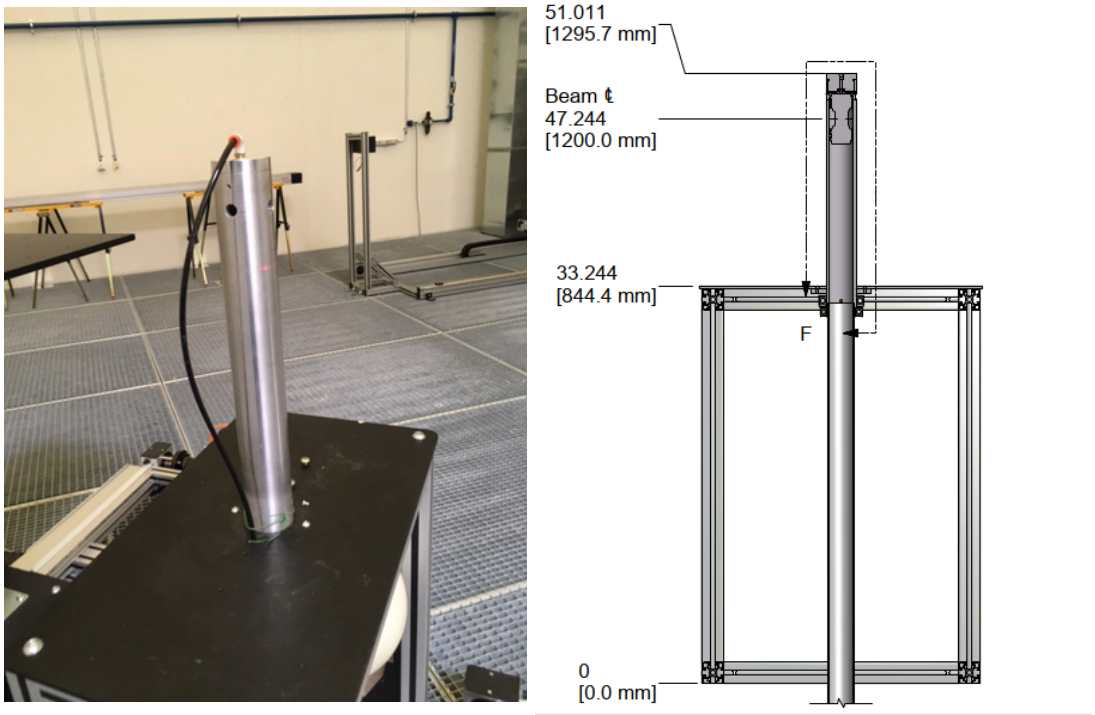

Figure A.1: On the left: the aluminium guide housing the Am-Be source in its irradiation position at the Callab; the red spot corresponds to the irradiation position. On the right: a 2D view of the same; the not specified units of measure are in inch, the zero level corresponds to the grid floor, while the beam label to the height of the irradiation position.

A.3.1 Simulation geometry and source beam particles

The FLUKA geometry reproduced the main calibration hall, 13 ×13 × 13 m^3 in size, with 80 cm thick concrete walls and 40 cm concrete roof [30]. To minimise the scattered neutron component, the floor consists of a metal grid located at half-height of the room, i.e., 6.5 m from the bottom. For the simulations, the metal grid was approximated by a 0.62 cm thick stainless-steel layer having the same density as the actual grid. This approximation does not affect the simulation results of neither the neutron spectrum nor the values of ambient dose equivalent, H*(10) [30].

This guide was simulated as a hollow aluminium cylinder running from the bottom of the hall to 130 cm height above the floor. The ISO 8529-1 Am-Be spectrum [10] was used to model the source term, as shown in Figure A.2. The other sources of the CalLab were not simulated since their influence to the thermal neutron fluence can be neglected.

Source moderator

The moderator was simulated centred at the source irradiation position. PE was chosen as moderating material and two different geometries were investigated, spherical and cylindrical. For the former, five simulations were performed for sphere radii of 9 cm, 10 cm, 11 cm, 12 cm and 15 cm. For the latter, a cylinder was defined with the axis coincident with the axis of the aluminium guide: four simulations were carried out for 8 cm, 9 cm, 10 cm and 11 cm radii. The height of the cylinder was adjusted in order to have, for each radius, the same PE thickness on top and on the side. On the top part of both geometries, a cylindrical hole 0.33 cm in radius was included in the moderator, above the aluminium guide, to accommodate the cable connected to the pneumatic system described in section A.4.1. A thin air gap (0.01 cm) was included between the guide and the moderator. Fig-

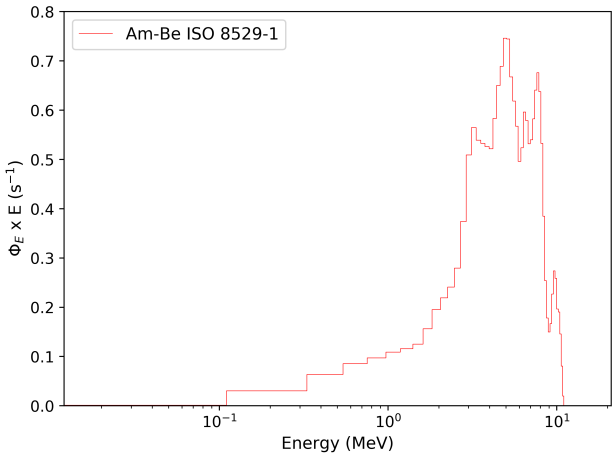

Figure A.2: The Am-Be ISO spectrum.

ure A.3 compares the two geometries. The PE was defined as a C_2H_4 compound with a density of 0.94 g cm^3. The cross section of H in the C_2O compound (at 296 K) was assigned to hydrogen by the LOW-MAT card.

Reflector box

For the moderator that maximises the thermal neutron fluence, the simulations were repeated adding a PE slab behind the region where the thermal fluence is scored. The slab thickness was optimised performing three simulations with thickness of 3 cm, 6 cm and 9 cm. Afterwards five slabs of the selected thickness (see section A.3.3) were placed around the scoring region (three on the sides, one on the top and one on the bottom) in the shape of a box leaving open the side facing the source.

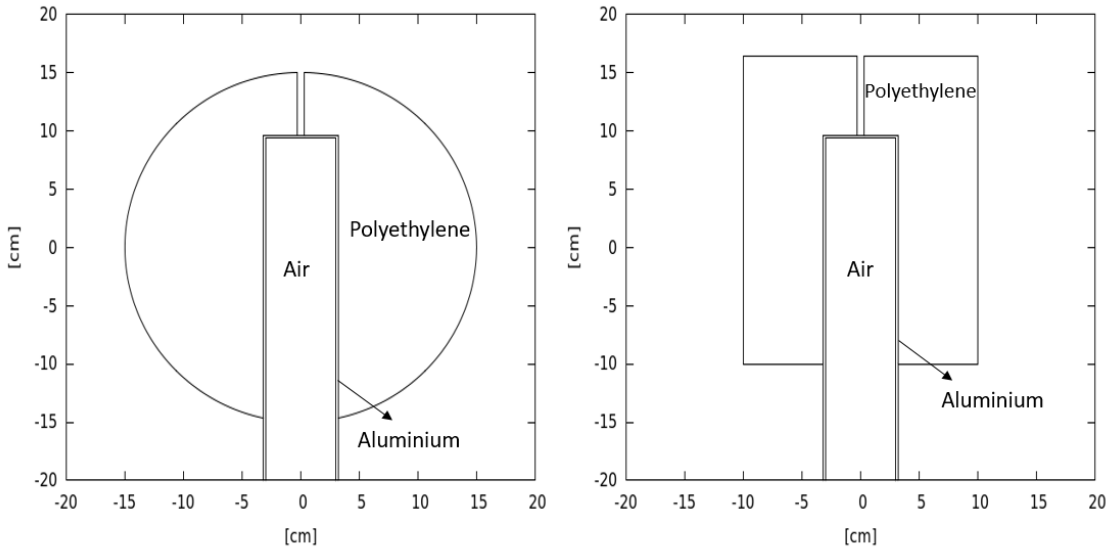

Figure A.3: Cross-sectional view of the FLUKA geometry of the moderator: spherical on the left, cylindrical on the right.

A.3.2 Scoring

The neutron fluence was scored using the USRTRACK card which defines a volume detector and estimates the track-length fluence on the selected region [68]. The USRTRACK detector was defined in a 10 cm diameter sphere of air placed at 10 cm from the external surface of the moderator and at the same height of the source with respect to the floor.

A.3.3 Results and discussion

Source moderator

Figure A.4 shows the lethargy plot of the neutron fluence over the entire energy range and of the thermal region only, for the nine geometries (five spherical and four cylindrical). The spectra are labelled according to geometry (sphere or cylinder) and radius. Table A.2 lists, for each configuration, the thermal neutron fluence normalized per source neutron, in the range 0 to 500 meV. For both geometries, an optimum moderator thickness exists, below which the thermal fluence decreases because the PE is not thick enough to thermalize the source neutrons, and above which it decreases because of self-absorption of thermal neutrons in the PE. This is evident with the 15 cm sphere, for which also the fast neutron peak visibly reduces. The maximum thermal neutron fluence is obtained with a cylindrical moderator of 9 cm radius. The cylinder better thermalises the Am-Be spectrum than the sphere: the neutron fluence with the 9 cm cylinder is 1.7 times higher than the maximum neutron fluence obtained with the 10 cm radius sphere.

Reflector box

Figure A.5 shows the variation of the thermal neutron fluence with the rear PE slab of varying thickness. The fluence increases up to a slab thickness of 6 cm. Figure A.6 compares the neutron fluence obtained with only the PE cylinder, with the cylinder and the 6 cm PE slab, and with the cylinder and the PE box with 6 cm think walls. The corresponding values of the thermal fluence are reported in Table A.3. The thermal component, with respect to the cylindrical moderator alone, increases by a factor of 1.5 and 8.2 with the slab and the box, respectively. The fast neutron component remains approximately constant as shown in figure A.6. The ratio between the thermal and the fast neutron fluence increases from 0.21 with only the cylinder to 1.43 with the cylinder and the box.

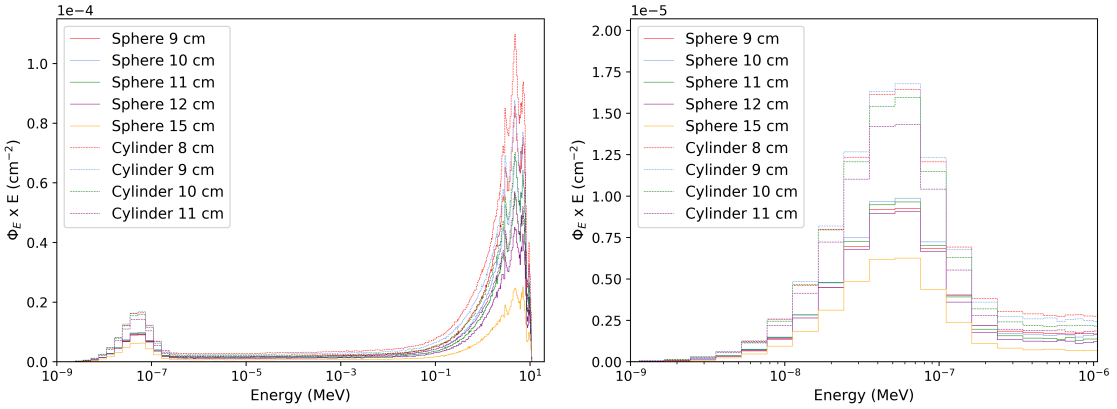

Figure A.4: Neutron fluence spectra calculated by FLUKA with each of the nine moderators (left), and a zoom of the same plot in the thermal energy range (right).

Table A.2: Thermal neutron fluence per source neutron calculated with FLUKA for the different geometries and radii of the moderator.

Geometry	Radius	Thermal neutron fluence (cm^{-2}) per source neutron
Sphere	9 cm	$1.97\times10^{-5} \pm 5.23\times10^{-8}$
Sphere	10 cm	$2.07\times10^{-5} \pm 4.92\times10^{-8}$
Sphere	11 cm	$2.01\times10^{-5} \pm 5.33\times10^{-8}$
Sphere	12 cm	$1.88\times10^{-5} \pm 5.64\times10^{-8}$
Sphere	15 cm	$1.28\times10^{-5} \pm 3.99\times10^{-8}$
Cylinder	8 cm	$3.47\times10^{-5} \pm 6.54\times10^{-8}$
Cylinder	9 cm	$3.50\times10^{-5} \pm 7.36\times10^{-8}$
Cylinder	10 cm	$3.29\times10^{-5} \pm 6.55\times10^{-8}$
Cylinder	11 cm	$2.97\times10^{-5} \pm 6.67\times10^{-8}$

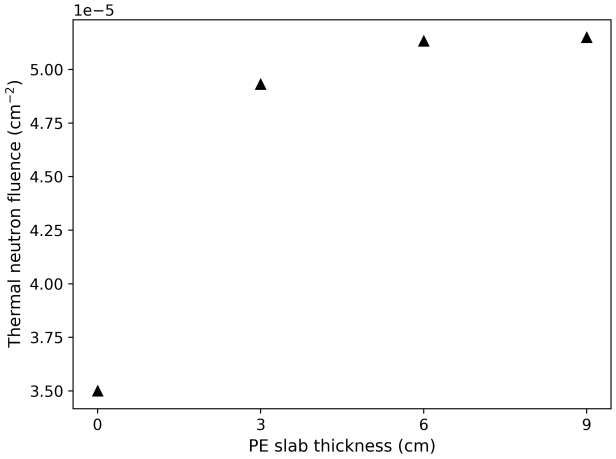

Figure A.5: Thermal neutron fluence as a function of thickness of the PE slab placed behind the scoring region. The uncertainties on the data points are smaller than the size of the symbols.

Table A.3: Thermal neutron fluence per source neutron, obtained with the cylinder (9 cm radius), the cylinder and the 6 cm PE slab at the back of the scoring region, the cylinder and the PE box (6 cm thick walls) surrounding the scoring region.

Source moderator	Entry assembly	Thermal neutron fluence (cm^{-2}) per source neutron
Cylinder 9 cm	-	$3.50\times10^{-5} \pm 7.36\times10^{-8}$
Cylinder 9 cm	6 cm PE back slab	$5.13\times10^{-5} \pm 8.44\times10^{-8}$
Cylinder 9 cm	PE box	$2.88\times10^{-4} \pm 2.31\times10^{-8}$

A.4 Design and construction of the moderator assembly

This section describes the design and the building of the moderator and box. Moreover, it discuss the construction of an ad-hoc extension plate built to place the PE box as close to the neutron source as possible.

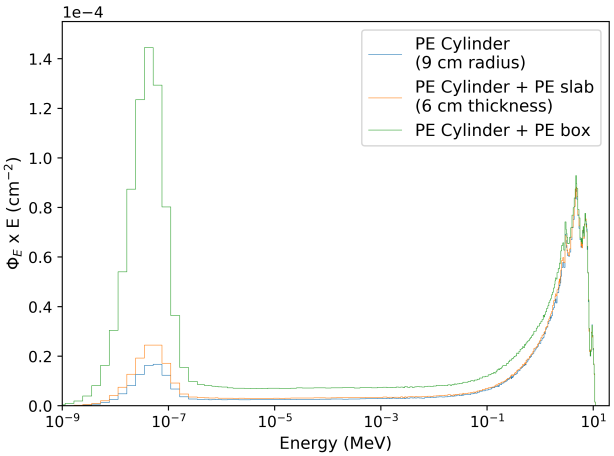

Figure A.6: Neutron fluence spectra obtained with the PE cylindrical moderator (9 cm radius), the cylinder and the 6 cm PE slab at the back of the scoring region, the cylinder and the PE box surrounding the scoring region.

A.4.1 Design of PE moderator and PE box

A 1-meter-long rod of Ultra High Molecular Weight PE (0.93 g cm^{-3}) was tailored cut to obtain a cylinder with a diameter of 18 cm and 25.5 cm height, with a central hole of 19.7 cm height and 6.46 cm diameter, slightly larger than the aluminium guide. The PE cylinder (5.5 kg in weight) slides over the neutron source guide and leans on it, without any additional support. The aluminium guide is connected through a cable, plugged on its top, to a pneumatic system whose goal is to "suck" the neutron source in its irradiation position. For this reason, a hole of 0.66 cm diameter was drilled on top of the cylinder to house the cable. Each of the five walls of the PE box consists of two 2.5 cm thick PE slabs (according to the thickness ready available) providing a 30 cm × 30 cm × 30 cm irradiation volume. The total weight of the box is around 20 kg.

A.4.2 Design for the extension plate

The extension plate consists of an aluminium slab 100 cm long, 50 cm wide and 0.5 cm thick, with drilled holes to bolt it to the support table that is part of the irradiation system. A 3D printed support was built to correctly place the ^{3}He proportional counter used to characterise the field at the centre of the PE box. Figure A.7 shows the complete moderator assembly.

A.5 Experimental measurements benchmarking the Monte Carlo predictions

This section describes the experimental setup of the measurements performed with a bare ^{3}He proportional counter. As also discussed in this section, the experimental setup was reproduced in FLUKA and the corresponding expected counts were calculated. The experimental and simulation results are shown and compared.

A.5.1 Experimental setup

The measurements were performed with a Centronic SP9/152/Kr ^{3}He proportional counter. The counter was supplied with +820 V and the output signal processed by an ORTEC 142IH preamplifier, an ORTEC 570 amplifier (assembled in a portable NIM crate) and an

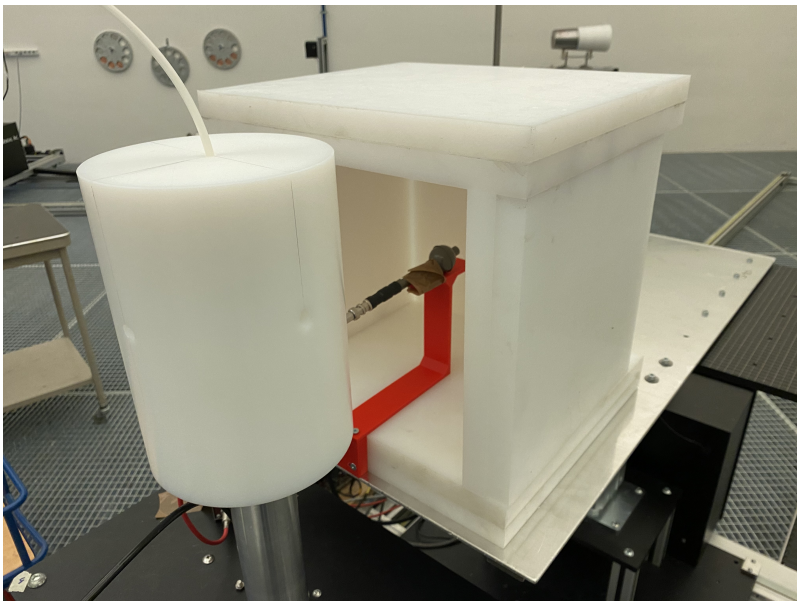

Figure A.7: The thermal source assembly with the PE cylinder placed on top of the source guide and the irradiation box placed on the aluminium plate bolted to the support table. The ^{3}He proportional counter, used for the experimental characterisation of the field, is shown on a custom-made support at the centre of the box.

Amptek Pocket Multi-Channel Analyser 8000D. The multi-channel analyser was used to acquire the spectrum of the recoils in the ^{3}He gas, with a threshold set to cut the electronic noise and signals from γ-ray events. The neutron counts were obtained integrating the spectrum above this threshold. The centre of the detector was aligned to the source by two orthogonal lasers. Eight measurements were performed changing the source-to-detector distance from 30 cm to 70 cm, first with the moderating cylinder alone and afterwards with the cylinder and the box (in the following we identify these two configurations as "cylinder" and "cylinder + box"). In the "cylinder + box" configuration, the ^{3}He counter was placed at the centre of the box. The measurements were performed with two of the four Am-Be neutron sources available. For the "cylinder", the measurements were performed with the 888 GBq (in January 2015) source, emission rate of 5.03×10^{7} neutrons per second, for the "cylinder + box" with the 100 GBq (in January 2015) source, 6.40×10^{6} neutrons per second. All results were normalised to the source activity.

A.5.2 Monte Carlo simulations

The sensitive volume of the proportional counter was modelled as a sphere of 1.6 cm radius with a 0.5 mm thick aluminium wall, filled with a gas mixture of ^{3}He at 2.33 kPa (2.3 atm) and Kr at 1.22 kPa (1.2 atm). The stem was simulated as a hollow aluminium cylinder filled with air as in [134]. Simulations were performed placing the centre of the ^{3}He volume at the same distances from the source as in the experimental set-up. The number of events per primary particle were scored by the DETECT card assigned to the sensitive volume of the counter. Figure A.8 shows a 3D view of the geometry in the "cylinder + box" configuration with the ^{3}He counter at the centre of the box. The extension plate and the plastic support of the ^{3}He counter were also included in the simulations.

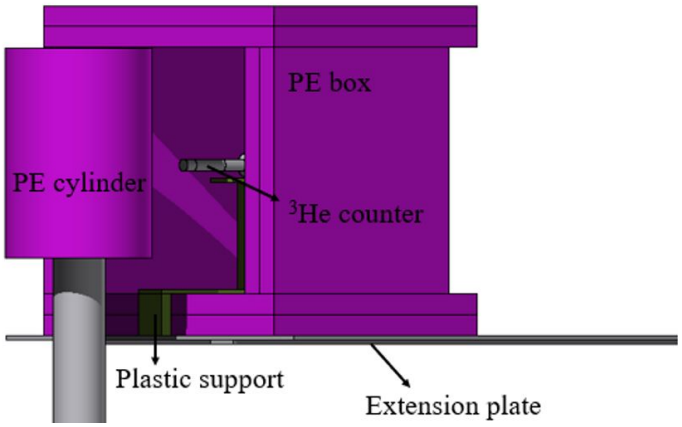

Figure A.8: 3D view of the FLUKA geometry in the "cylinder + box" configuration, with the 3He counter at the centre of the box.

A.5.3 Results and discussion

Figures A.9 compare, for the two configurations, the measured ^{3}He count rate and the count rate predicted by FLUKA at the eight irradiation positions. The measured count rate with the "cylinder + box" is always eight times larger than the one measured with the "cylinder". For both the "cylinder" and "cylinder + box" configurations, measurements and simulations are in very good agreement, with differences below 10%. Having confirmed that the Monte Carlo simulations accurately predict the experimental field, additional simulations were performed to provide a complete characterisation of the field, as discussed in the next section. Figures A.10 shows the spectra of the recoils in the ^{3}He gas acquired in the "cylinder" and "cylinder + box" configuration, respectively. The spectra are labelled according to the corresponding source-to-detector distance. The threshold set to calculate the integral neutron counts is shown by a vertical red line. The spectra reproduced the energy deposition events of the protons emitted by the ^{3}He(n,p) promoted by the thermal neutrons. The main peak collects the full energy deposition events and it corresponds to 764 keV, i.e. the reaction $Q - value$. The continuum below the main peak is due to the wall-effect and its relevance depends on the detector parameters (e.g. pressure, supplied voltage), as described in detail in [5].

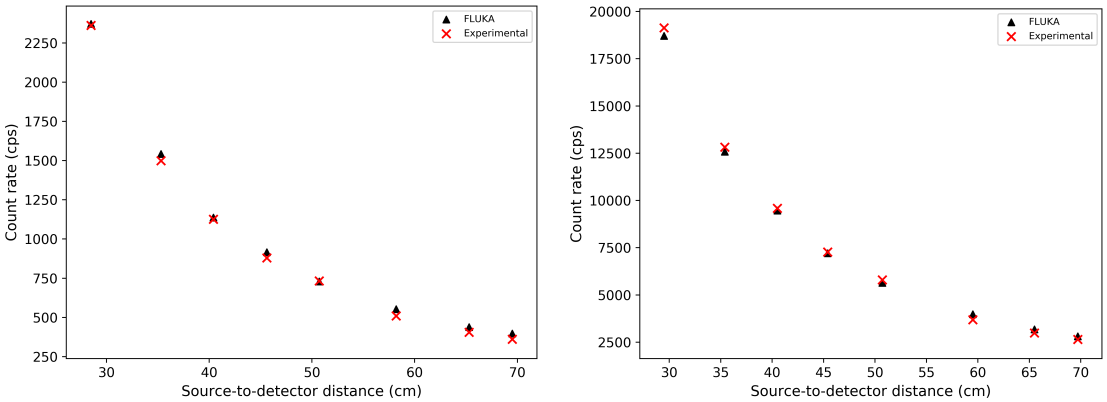

Figure A.9: Comparison between the count rate measured by the ^{3}He proportional counter and the count rate predicted by the FLUKA simulations at the eight irradiation positions for the "cylinder" (on the left) and "cylinder + box" (on the right)configuration. The uncertainties on the data points are smaller than the size of the symbols.

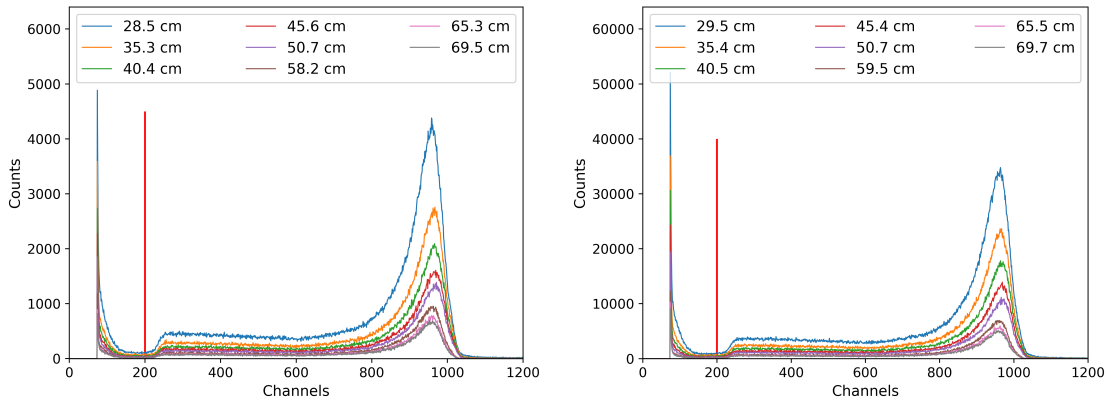

Figure A.10: The recoil spectra acquired with the ^{3}He proportional counter in the"cylinder" (on the left) and "cylinder + box" (on the right) configuration. The red vertical line represents the threshold set for the calculation of the integral neutron counts.

A.6 Thermal neutron source characterisation

The thermal neutron source was finally characterised with FLUKA. In particular, the neutron fluence was calculated at 30 cm from the source, i.e. the closest experimental source-to-detector distance, discriminating the thermal neutron contribution from the epithermal and fast one. The spatial distribution of the thermal neutron field was also evaluated with the USRBIN detector. The USRBIN card defines indeed a so-called binning detector, which scores the spatial distribution of the requested quantity (the fluence in this case) over a regular spatial binning which is independent from the simulation geometry [68]. Eventually, we checked with FLUKA the possibility to calculate the thermal neutron fluence with a difference method.

A.6.1 Neutron fluence calculation

The neutron fluence was calculated with the USRTRACK card by assigning the scoring region consisted of a 3.2 cm diameter sphere of air (the same volume as the ^{3}He counter). Both the "cylinder" and the "cylinder + box" were investigated and, for completeness, the neutron fluence was also scored with the bare Am-Be source. Table A.4 reports, for all configurations, the calculated neutron fluence for the 888 GBq and 100 GBq sources, at 30 cm from the source. The neutron fluence is given in three broad energy ranges: thermal ($<$ 500 meV), intermediate (500 meV – 100 keV) and fast ($>$ 100 keV). Both the measurements described in section A.5 and the simulations confirm that with the "cylinder + box" set-up the thermal neutron fluence is around eight times higher than with the "cylinder" only. Nevertheless, the cylinder alone already provides a quite intense thermal neutron fluence. The results with the bare source are also reported. The increase of the thermal neutron component in the "cylinder + box" configuration is also evident from figure A.11, which also shows that the epithermal and fast components are almost constant as expected.

A.6.2 Spatial distribution

For the "cylinder + box" case, the thermal neutron fluence was scored inside the box on a regular spatial binning with 1 cm spatial resolution. For the "cylinder" configuration the thermal neutron fluence was scored, with the same procedure, in the area surrounding the source (±50 cm from the source). Figure A.12 shows the 2D maps of the thermal

Table A.4: Neutron fluence at 30 cm distance from the 888 GBq and 100 GBq Am-Be sources calculated by FLUKA.

Source configuration	Neutron energy	888 GBq ($cm^{-2} \times s^{-1}$)	100 GBq ($cm^{-2} \times s^{-1}$)
Bare source	Thermal (< 500 meV)	-	-
	Intermediate (500 meV - 100 keV)	$5.53\times10^{4} \pm 6.46\times10^{2}$	$7.04\times10^{3} \pm 8.23\times10^{1}$
	Fast (>100 keV)	$3.75\times10^{6} \pm 5.42\times10^{3}$	$4.77\times10^{5} \pm 6.89\times10^{2}$
Cylinder	Thermal (< 500 meV)	$7.43\times10^{2} \pm 5.85$	$9.46\times10^{1} \pm 0.74$
	Intermediate (500 meV - 100 keV)	$7.86\times10^{2} \pm 6.09$	$1.00\times10^{2} \pm 0.76$
	Fast (>100 keV)	$2.99\times10^{3} \pm 1.59\times10^{1}$	$3.81\times10^{2} \pm 1.51$
Cylinder + box	Thermal (< 500 meV)	$5.75\times10^{3}3 \pm 1.59\times10^{1}$	$7.32\times10^{2} \pm 2.03$
	Intermediate (500 meV - 100 keV)	$1.86\times10^{3} \pm 9.27$	$2.37\times10^{2} \pm 1.18$
	Fast (>100 keV)	$3.39\times10^{3} \pm 1.26\times10^{1}$	$4.31\times10^{2} \pm 1.61$

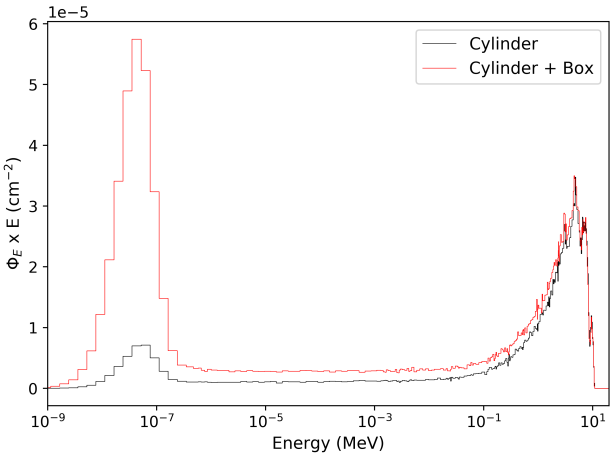

Figure A.11: Neutron fluence spectra per Am-Be source neutron obtained with the "cylinder" and the "cylinder + box" configurations at 30 cm from the source.

neutron fluence (0-500 meV) calculated for the 888 GBq source inside the box, along the three axes parallel to the box walls. Figures A.12 (a,b) are the maps along the planes x = 0 cm and y = 0 cm respectively, which pass via the centre of the box. Figures A.12 (c,d) are the maps along the planes z = 14 cm and z = 30 cm, as indicated in Figure A.12 (b). The thermal neutron fluence inside the box is rather uniform from the plane z = 20 cm (i.e., at 5 cm from the entrance of the box) up to z = 45 cm (the bottom of the box). In the region between z = 15 cm and z = 20 cm, the fluence is not constant with a maximum around 7×10^{3} $cm^{-2}s^{-1}$ in correspondence of the position facing the source, while it is around 5.5×10^{3} $cm^{-2}s^{-1}$ in the rest of the box.

The region near the source, i.e., at the entrance of the box, shows a larger variation of the thermal fluence, as expected. In [130], the fluence varies by about 30% in the irradiation position closest to the source, while beyond 6 cm distance it becomes very homogenous (variation around 1%). In our case, the fluence variation is 25% near the box entrance (z = 14 cm plane) and 4% at the nominal irradiation position (z = 30 cm plane).

Figure A.13 shows the 2D maps of the thermal neutron fluence for the "cylinder" configuration within 50 cm distance from the source. Figure A.14 plots the corresponding 1D projection along the z axis at source height. As expected, the thermal fluence decreases as d^{-2}, where d is the source-to-detector distance. The largest variation occurs in the

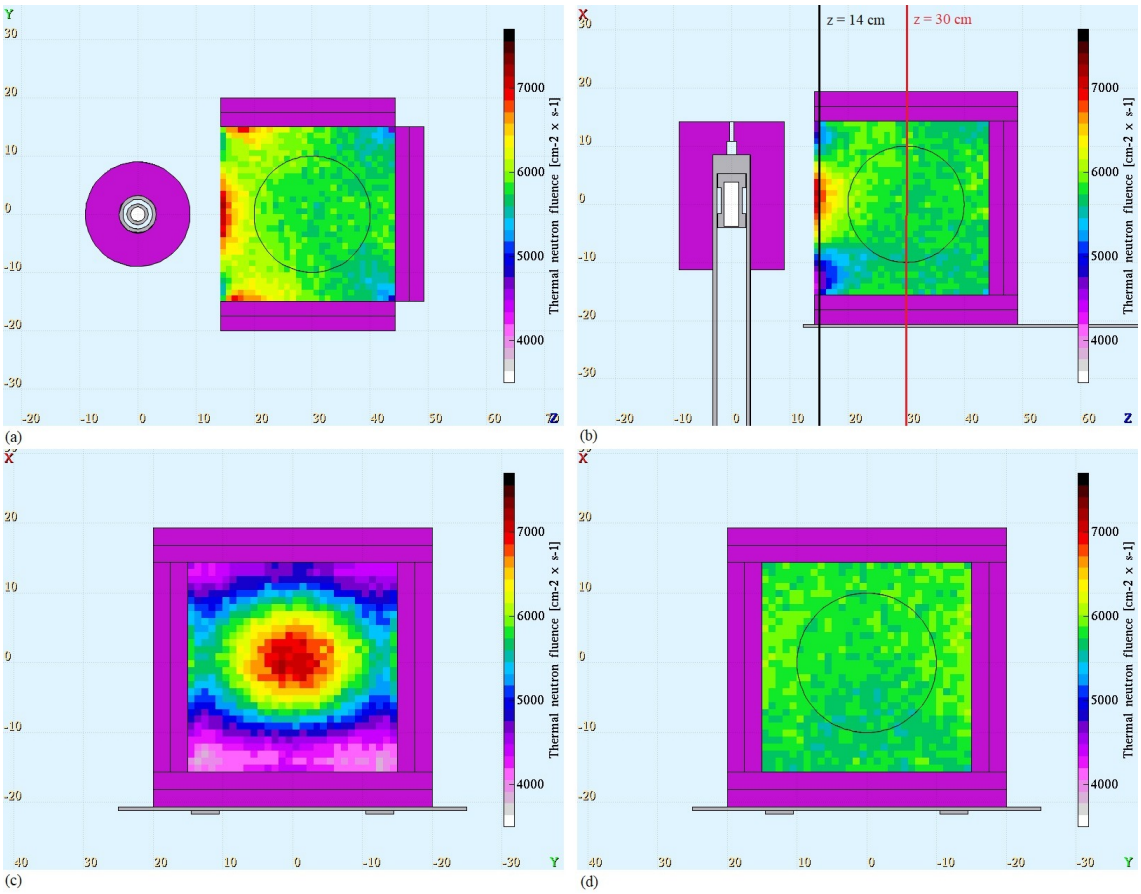

Figure A.12: 2D maps of the thermal neutron fluence calculated with FLUKA for the 888 GBq Am-Be source inside the PE box. (a) 2D maps on x = 0 cm; (b) 2D maps on y = 0 cm; (c) 2D map on z = 14 cm; (d) 2D map on z = 30 cm.

proximity of the source, specifically in the first 10 cm from the surface of the cylinder (which corresponds to 9 cm source-to-detector distance). A few centimetres from the cylinder, the thermal neutron fluence is around 4-5 $\times$ 10^3 $cm^{-2}s^{-1}$, similar to the value calculated for the "cylinder + box" configuration. Without the box, the detector under test can then be placed closer than 30 cm, where the thermal neutron fluence is more intense. Obviously, the achievable source-to-detector distance also depends on the size of the detector under test. The lateral view in figure A.13 (right plot) shows the effect of the moderator geometry on the thermal neutron distribution. The distribution of the thermal fluence is not perfectly isotropic. Nevertheless, this effect is not relevant especially for small detectors when placed at the source height, and vanishes beyond 10 cm distance from the moderator surface.

A.6.3 Neutron fluence calculation using the difference method

The thermal neutron flunece can be experimentally accessed by a difference method, as defined in [132], i.e. by performing measurements with and without a cadmium layer placed in between the source and the detector, and by subtracting the former to the latter. The cadmium is in fact a commonly used thermal neutron absorber, thank to its high absorption cross section at 0.5 eV. The detector with the cadmium layer is therefore sensitive only to the fast and epithermal components, while it is sensitive to all the field component without the cadmium. For this reason FLUKA simulation were performed to test this method. Essentially, we the previously described FLUKA simulations were repeated for

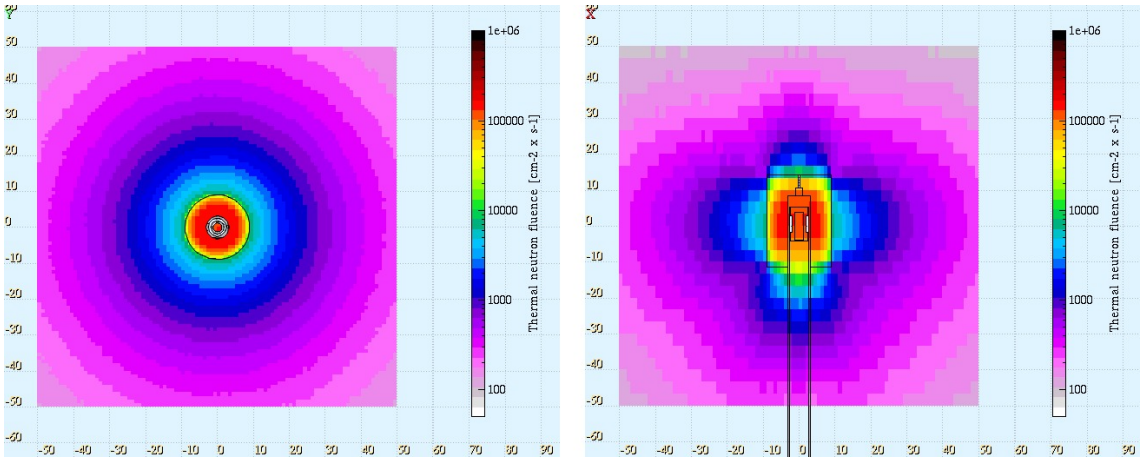

Figure A.13: 2D maps of the thermal neutron fluence along the planes x= 0 (on the left) and y = 0 (on the right), calculated with FLUKA for the 888 GBq Am-Be source for the "cylinder configuration".

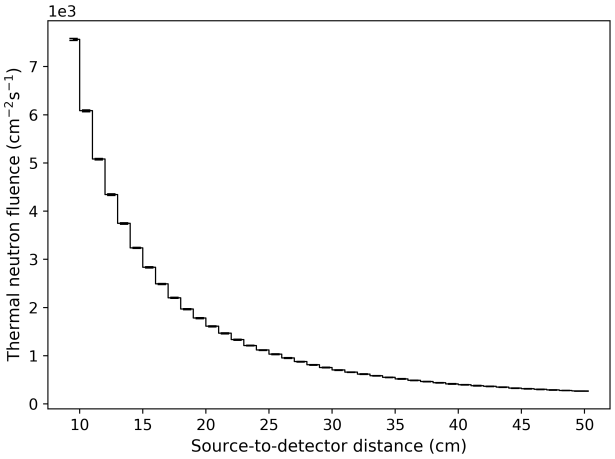

Figure A.14: 2D maps of the thermal neutron fluence along the planes x= 0 (on the left) and y = 0 (on the right), calculated with FLUKA for the 888 GBq Am-Be source for the "cylinder configuration".

both configurations by adding a thin cadmium shell around the scoring region. Figure A.15 compares the neutron fluence per Am-Be source neutron with and without the cadmium shell, for the "cylinder" and the "cylinder + box" configurations. The cadmium layer cuts the neutron component below 500 meV in both configurations, and the simulation confirms that the thermal neutron fluence can also be measured by subtracting the neutron fluence measured with the cadmium in place to the neutron fluence measured without the cadmium. In fact, the difference between the neutron fluence calculated with and without the cadmium (from two different and independent simulations) is 7.23×10^{2} cm^{-2}s^{-1} and 5.71×10^{3} cm^{-2}s^{-1} for the "cylinder" and "cylinder + box" configuration respectively, in good agreement with the values reported in Table A.4.

A.7 Comparison with different thermal neutron facilities

In order to compare different thermal neutron facilities, Bedogni et al. [129] define a q factor as follows:

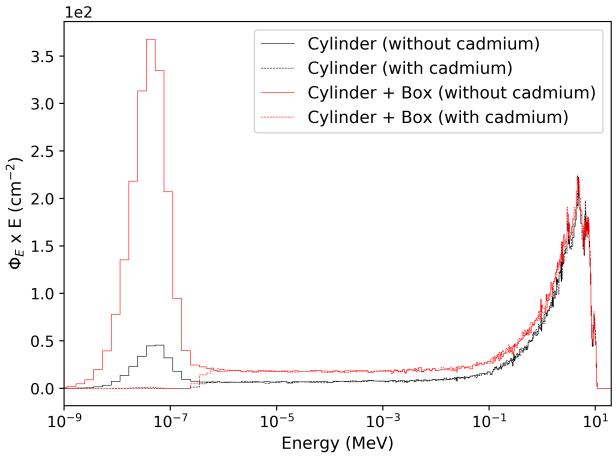

Figure A.15: Neutron fluence spectra per Am-Be source neutron for the "cylinder" and the "cylinder + box" configurations, at 30 cm from the source, with and without the cadmium shell around the scoring volume.

$$q = \frac{B}{\Theta_{th}} \tag{A.1}$$

where B is the total emission rate of the neutron source (in s^{-1}) and Θ_{th} is the neutron fluence rate below 500 meV in cm^{-2} s^{-1}. The q factor expresses the efficiency of the moderator assembly to thermalise neutrons, since it is calculated by taking into account the activity of the primary source. A smaller q value indicates a higher thermalisation efficiency. Table A.5 reports the q values of the thermal neutron facilities considered before, the moderator material and the volume occupied by each source.

Table A.5: Comparison of the thermalisation efficiency (q) and volume of six thermal neutron facilities with the thermal neutron source proposed in this work.

Facility	Moderator material	Volume	Thermal neutron fluence rate ($E_n < 0.5$ eV)	q
SIGMA	graphite	3.4×10^6 cm^3	1,500 cm^{-2} s^{-1}	1.3×10^5 cm^2[129]
PTB	graphite	4.1×10^6 cm^3	80 cm^{-2} s^{-1}	7×10^5 cm^2[129]
ETHERNES	polyethylene	1.3×10^5 cm^3	from 550 to 800 cm^{-2} s^{-1}	from 6×10^3 to 9×10^3 cm^2[129]
HOTNES	polyethylene	4.5×10^4 cm^3	from 700 to 1,000 cm^{-2} s^{-1}	from 3.5×10^3 to 5×10^3 cm^2[130]
This work	polyethylene	6.5×10^3 cm^3 (cylinder)	740 cm^{-2} s^{-1}	7×10^4 cm^2 (cylinder)
		4.3×10^4 cm^3 (cylinder + box)	5,700 cm^{-2} s^{-1}	9×10^3 cm^2 (cylinder + box)

The facilities employing graphite as moderator material are usually bigger in volume, because of the less efficiency in the neutron moderation on carbon ions (i.e. with graphite)

rather than on hydrogen (i.e. with polyethylene) [5]. For the same reason the corresponding q value is higher. The assembly proposed in this work has the smallest volume among the facilities reported in Table A.5 and its q value is comparable with the one of ETHERNES, but worst than HOTNES. Table A.5 shows that the present setup consists of a very light assembly with an efficient moderating capability, comparable with similar facilities (i.e. employing polyethylene as moderating material).

A.8 Conclusions

A lightweight and easy-to-make moderating assembly was designed, built and characterised, providing a thermal neutron field from the Am-Be neutron sources of CERN Cal Lab. The assembly consists of a PE cylinder placed around the source and a PE box providing a 30 cm $\times$ 30 cm $\times$ 30 cm irradiation volume. The FLUKA MC code was used to define the optimum geometry and dimensions and to calculate the thermal neutron fluence at the irradiation positions. The MC predictions were confirmed by measurements performed with a bare ^{3}He proportional counter.

For the highest activity source (888 GBq), the thermal neutron fluence at 30 cm distance from the source is 7.43 $\times$ 10^2 cm^{-2}s^{-1} with the cylindrical PE moderator only, and 5.75 $\times$ 10^3 cm^{-2}s^{-1} at the centre of the PE box, slightly higher than the fluence at ETHERNES [129] and HOTNES [130]. Inside the box, the fluence is almost uniform (4% variation throughout the irradiation volume) except in the region closest to the source, where the fluence is higher by 25% with a maximum around 7$\times$ 10^3 cm^{-2}s^{-1}. The q value is 7$\times$ 10^4 cm^2 with the cylindrical moderator, and 9$\times$ 10^3 cm^2 with the entire assembly, comparable with ETHERNES [129].

References

[1] *IAEA Safety glossary*. 2016. URL: https://www-ns.iaea.org/downloads/standards/glossary/iaea-safety-glossary-draft-2016.pdf (visited on 11/24/2021).

[2] S. Roesler and M. Silari. "Radiation protection principles". In: *Handbook of Accelerator Physics and Engineering*. Ed. by A. Wu Chao, K. H. Mess, and M. Tigner. Second edition. World Scientific Publishing, 2013. Chap. 8, pp. 767–768.

[3] P. H. Burgess. *Guidance on the Choice, Use and Maintenance of Hand-held Radiation Monitoring Equipment*. Tech. rep. NRPB-R326. National Radiological Protection Board, now part of Public Health England, 2001.

[4] U.S. Department of Homeland Security. *Radiation survey meters*. Tech. rep. 2006. URL: https://www.dhs.gov/sites/default/files/publications/SurveyMeters-TN_0406-508.pdf.

[5] G. F. Knoll. *Radiation Detection and Measurement*. Fourth edition. Wiley, 2010.

[6] S. Usman and A. Patil. "Radiation detector deadtime and pile up: A review of the status of science". In: *Nuclear Engineering and Technology* 50.7 (2018), pp. 1006–1016. ISSN: 2234358X. DOI: 10.1016/j.net.2018.06.014. URL: https://doi.org/10.1016/j.net.2018.06.014.

[7] C. Birattari, A. Esposito, A. Ferrari, M. Pelliccioni, T. Rancati, and M. Silari. "The extended neutron rem counter LINUS: overview and latest developments". In: *Radiation Protection Dosimetry* 76.3 (1998), pp. 135–148. URL: https://academic.oup.com/rpd/article/76/3/135/1631673.

[8] D. Celeste, A. Curioni, A. Fazzi, M. Silari, and V. Varoli. "B-RAD: A radiation survey meter for operation in intense magnetic fields". In: *Journal of Instrumentation* 14.5 (2019). ISSN: 17480221. DOI: 10.1088/1748-0221/14/05/T05007.

[9] M. Silari A. Fazzi. *Portable Radiation Detection Device for Operation in Intense Magnetic Fields*. CERN/ Polytechnic of Milan joint patent. Patent Grant number 9977134 (13 July 2017).

[10] *Experiments — CERN*. URL: https://home.cern/science/experiments (visited on 11/24/2021).

[11] *ATLAS Experiment at CERN — ATLAS Experiment at CERN*. URL: https://atlas.cern/ (visited on 11/11/2021).

[12] D. Celeste, A. Curioni, A. Fazzi, D.Perrin, and M. Silari. *Status report on the radiation survey meter operating in strong magnetic field - KT funded project*. Tech. rep. EDMS n°1504386. CERN-RP, 2015.

[13] *Products for nuclear safety, radiation detection and measurement - ELSE Nuclear*. URL: http://www.elsenuclear.com/en/ (visited on 11/24/2021).

[14] U.S. Department of Homeland Security. *Personal Radiation Detectors (PRDs) and Spectroscopic PRDs Market Survey Report*. Tech. rep. 2017. URL: https://www.dhs.gov/sites/default/files/NUSTL-SAVER_PRD-SPRD-MSR_1707-508.pdf (visited on 11/24/2021).

[15] *B-RAD - ELSE Nuclear*. URL: http://www.elsenuclear.com/it/b-rad (visited on 11/24/2021).

[16] *identiFINDER® R300 High-Res Spectroscopic Personal Radiation Detector — Teledyne FLIR*. URL: https://www.flir.com/products/identifinder-r300/ (visited on 11/24/2021).

[17] *GammaRAE II R User's Guide*. URL: https://safety.honeywell.com/content/dam/his-sandbox/products/gas-and-flame-detection/documents/Manual_GammaRAE-II-R_047-4505-000_RevD.pdf (visited on 11/24/2021).

[18] *NetS^2 SmartShield G300 Radiation Detector*. URL: https://passportsystems.com/wp-content/uploads/2020/05/1405946923smartshield_g300_product-sheet.pdf (visited on 11/24/2021).

[19] *Personal Radiation Detector — RadPavise — X-Z LAB*. URL: https://www.x-zlab.com/product/radpavise-personal-radiation-detector/ (visited on 11/24/2021).

[20] *Radiation Isotope Identifier, Handheld Radiation Detection System*. URL: https://www.berkeleynucleonics.com/sam-950-riid (visited on 11/24/2021).

[21] *LaBr$_3$(Ce) Scintillation detector*. URL: https://mirion.s3.amazonaws.com/cms4_mirion/files/pdf/spec-sheets/c39490_labr_super_spec_1.pdf?1557861183 (visited on 11/24/2021).

[22] *Spectrum survey meter TS215*. URL: http://www.techno-ap.com/img/TS215_e.pdf (visited on 11/24/2021).

[23] *RADEAGLE Next Generation Radioisotope Identification Device Detection and Identification: Fast, Accurate and Easy*. URL: https://www.nmas.no/files/nmas/Documents/Helsefysikk\%20og\%20str\%C3\%A5ling/CBRN/Radeagle_brosjyre.pdf (visited on 11/24/2021).

[24] A. Curioni and M. Silari. *Flattening of the energy response of the B-RAD survey meter*. Tech. rep. EDMS n°1556328. CERN-RP, 2015.

[25] F. Ferrulli, L. G. Manzano, M. Lorenzoli, and M. Silari. *Test of the B-RAD survey meter in a calibrated dipole up to 1.5 T*. Tech. rep. EDMS n°2259859. CERN-RP, 2019.

[26] URL: https://www.datadelay.com/_files/ugd/8d75f4_497e72504f254034813519b5382d9ddd.pdf (visited on 05/12/2022).

[27] *ISOLDE*. URL: http://isolde.web.cern.ch/ (visited on 11/24/2021).

[28] F. Ferrulli, J. Konki, and M. Silari. *Test of the B-Rad survey meter at ISOLDE facility inside a magnetic field up to 2.5 T*. Tech. rep. EDMS n°2314235. CERN-RP, 2020.

[29] private comunication.

[30] F. Pozzi. "CERN Radiation Protection (RP) calibration facilities". PhD thesis. Technische Universität München, 2015. URL: https://cds.cern.ch/record/2256137.

[31] M. Brugger, P. Carbonez, F. Pozzi, M. Silari, and H. Vincke. "New radiation protection calibration facility at CERN". In: *Radiation Protection Dosimetry* 161.1-4 (2014), pp. 181–184. ISSN: 17423406. DOI: 10.1093/rpd/nct318. URL: https://pubmed.ncbi.nlm.nih.gov/24327753/.

[32] D. Celeste, A. Curioni, and M. Silari. *The B-RAD radiation survey meter: temperature compensation, magnetic field measurements and characterization of SensL SiPM arrays and LaBr3 crystals*. Tech. rep. EDMS n°1555024. CERN-RP, 2015.

[33] G. Hull, F. Camera, G. Colombi, M. Josselin, and B. Million. "Detection properties and internal activity of newly developed La-containing scintillator crystals". In: *Nuclear Instruments and methods in Physics Research* A.925 (2019), pp. 70–75.

[34] A. Camp, A. Vegas, and J. M. Fernandéz-Varea. "Determination of $LaBr_3$(Ce) internal background using a HPGe detector and Monte Carlo simulations". In: *Applied Radiation and Isotope* 109 (2016), pp. 512–517.

[35] *Automess 6150AD6*. URL: https://www.automess.de/en/products/productfamily-6150ad/dose-rate-meter-6150ad (visited on 11/24/2021).

[36] *Scintillator probe 6150AD-b*. URL: https://www.automess.de/assets/documents/en/Prospekt_ADb_E.pdf (visited on 11/24/2021).

[37] B. D. Milbrath, J. I. Mcintyre, R. C. Runkle, and L. E. Smith. "Contamination studies of $LaCl_3$:Ce scintillators". In: *IEEE Transactions on Nuclear Science* 53 (2006), pp. 3031–3034.

[38] The LEP Injector Study Group. *LEP Design report. Vol. I: The LEP Injector Chain*. Tech. rep. LEP/TH/83-29. CERN, 1983.

[39] LEP 2 Team. *LEP Design report. Vol. II: The LEP Main Ring*. Tech. rep. LEP/84-01. CERN, 1984.

[40] LEP 2 Team. *LEP Design report. Vol. III: LEP2*. Tech. rep. AC/96-01 (LEP2). CERN, 1996.

[41] N. Dinar, M. Magistris, M. Silari, L. Vitkova, and B. Zaffora. *Project AMAL (Autres Matériaux LEP)-Radiological clearance of residual LEP materials*. Tech. rep. EDMS n°2266849. CERN-RP, 2019.

[42] F. Ferrulli, N. Dinar, and M. Silari. *Operational tests of the ELSE NUCLEAR B-RAD radiation survey meter*. Tech. rep. EDMS n°2314235. CERN-RP, 2020.

[43] U. Bravar, P. J. Bruillard, E. O. Flückiger, J. R. Macri, M. L. McConnell, M. R. Moser, J. M. Ryan, and R. S. Woolf. "Design and testing of a position-sensitive plastic scintillator detector for fast neutron imaging". In: *IEEE Transactions on Nuclear Science* 53.6 (2006), pp. 3894–3903. ISSN: 00189499. DOI: 10.1109/TNS.2006.886046.

[44] E. Brubaker and J. Steele. "Neutron imaging using the anisotropic response of crystalline organic scintillators". In: *IEEE Nuclear Science Symposium Conference Record* (2010), pp. 1647–1652. ISSN: 10957863. DOI: 10.1109/NSSMIC.2010.5874055.

[45] Yu A. Kaschuck, B. Esposito, L. A. Trykov, and V. P. Semenov. "Fast neutron spectrometry with organic scintillators applied to magnetic fusion experiments". In: *Nuclear Instruments and Methods in Physics Research, Section A: Accelerators, Spectrometers, Detectors and Associated Equipment* 476.1-2 (2002), pp. 511–515. ISSN: 01689002. DOI: 10.1016/S0168-9002(01)01499-1.

[46] M. M. Bourne, S. D. Clarke, N. Adamowicz, S. A. Pozzi, N. Zaitseva, and L. Carman. "Neutron detection in a high-gamma field using solution-grown stilbene". In: *Nuclear Instruments and Methods in Physics Research, Section A: Accelerators, Spectrometers, Detectors and Associated Equipment* 806 (2016), pp. 348–355. ISSN: 01689002. DOI: 10.1016/j.nima.2015.10.025. URL: http://dx.doi.org/10.1016/j.nima.2015.10.025.

[47] M. M. Bourne, S. D. Clarke, M. Paff, A. DiFulvio, M. Norsworthy, and S. A. Pozzi. "Digital pile-up rejection for plutonium experiments with solution-grown stilbene". In: *Nuclear Instruments and Methods in Physics Research, Section A: Accelerators, Spectrometers, Detectors and Associated Equipment* 842.July 2016 (2017), pp. 1–6. DOI: 10.1016/j.nima.2016.10.023.

[48] G. Dietze and H. Klein. "Gamma-calibration of NE 213 scintillation counters". In: *Nuclear Instruments and Methods* 193.3 (1982), pp. 549–556. DOI: 10.1016/0029-554X(82)90249-X.

[49] G. Dietze. "Energy calibration of NE-213 scintillation counters by x-rays". In: *IEEE Transactions on Nuclear Science* 26.1 (1979), pp. 398–402. ISSN: 15581578. DOI: 10.1109/TNS.1979.4329665.

[50] H. H. Knox and T. G. Miller. "A technique for determining bias settings for organic scintillators". In: *Nuclear Instruments and Methods* 101.3 (1972), pp. 519–525. ISSN: 0029554X. DOI: 10.1016/0029-554X(72)90040-7.

[51] J.B. Birks. "The scintillation process in organic materials." In: *The Theory and Practice of Scintillation Counting*. Ed. by J.B. Birks. Pergamon, 1964. Chap. 3, pp. 39–67.

[52] *Scintinel™ Stilbene*. URL: https://www.inradoptics.com/scintinel-stilbene (visited on 05/08/2021).

[53] *EJ-276 - Pulse Shape Discrimination Plastic Scintillator - Eljen Technology*. URL: https://eljentechnology.com/products/plastic-scintillators/ej-276 (visited on 05/08/2021).

[54] N. Zaitseva, A. Glenn, L. Carman, H. Paul Martinez, R. Hatarik, H. Klapper, and S. Payne. "Scintillation properties of solution-grown trans-stilbene single crystals". In: *Nuclear Instruments and Methods in Physics Research, Section A: Accelerators, Spectrometers, Detectors and Associated Equipment* 789.October (2015), pp. 8–15. DOI: 10.1016/j.nima.2015.03.090.

[55] Y. Shimizu, M. Minowa, H. Sekiya, and Y. Inoue. "Directional scintillation detector for the detection of the wind of WIMPs". In: *Nuclear Instruments and Methods in Physics Research, Section A: Accelerators, Spectrometers, Detectors and Associated Equipment* 496.2-3 (2003), pp. 347–352. ISSN: 01689002. DOI: 10.1016/S0168-9002(02)01661-3. arXiv: 0207529 [astro-ph].

[56] T. A. Laplace, B. L. Goldblum, J. E. Bevins, D. L. Bleuel, E. Bourret, J. A. Brown, E. J. Callaghan, J. S. Carlson, P. L. Feng, G. Gabella, K. P. Harrig, J. J. Manfredi, C. Moore, F. Moretti, M. Shinner, A. Sweet, and Z. W. Sweger. "Comparative scintillation performance of EJ-309, EJ-276, and a novel organic glass". In: *Journal of Instrumentation* 15.11 (2020). ISSN: 17480221. DOI: 10.1088/1748-0221/15/11/P11020. arXiv: 2011.01907.

[57] *J-Series High PDE and Timing Resolution, TSV Package*. URL: https://sensl.com/downloads/ds/DS-MicroJseries.pdf (visited on 05/07/2021).

[58] *Silitech AG*. URL: https://www.silitech.ch (visited on 11/06/2021).

[59] N. Dinar. "Development of neutron detectors for use in radiation protection". PhD thesis. University of Paris-Saclay, 2019.

[60] *A7585DU - Nuclear Instruments*. URL: https://www.nuclearinstruments.eu/product/a7585du/ (visited on 07/08/2021).

[61] G. Van Rossum. *Python 3 Reference Manual*. Ed. by F. L. Drake Jr. Scotts Valley, CA: CreateSpace, 2009. ISBN: 1441412697.

[62] L. E. Beghian, S. Wilensky, and W. R. Burrus. "A fast neutron spectrometer capable of nanosecond time gating". In: *Nuclear Instruments and Methods* 35.1 (1965), pp. 34–44. DOI: 10.1016/0029-554X(65)90004-2.

[63] R. Honecker and H. Grässler. "Detection efficiency of a plastic scintillator for neutrons between 0.2 and 3 MeV". In: *Nuclear Instruments and Methods* 46.2 (1967), pp. 282–288. DOI: 10.1016/0029-554X(67)90084-5.

[64] E. V. Pagano, M. B. Chatterjee, E. De Filippo, P. Russotto, L. Auditore, G. Cardella, E. Geraci, B. Gnoffo, C. Guazzoni, G. Lanzalone, S. De Luca, C. Maiolino, N. S. Martorana, A. Pagano, M. Papa, T. Parsani, S. Pirrone, G. Politi, F. Porto, L. Quattrocchi, F. Rizzo, A. Trifirò, and M. Trimarchi. "Pulse shape discrimination of plastic scintillator EJ 299-33 with radioactive sources". In: *Nuclear Instruments and Methods in Physics Research, Section A: Accelerators, Spectrometers, Detectors and Associated Equipment* 889.January (2018), pp. 83–88. DOI: 10.1016/j.nima.2018.02.010. URL: https://doi.org/10.1016/j.nima.2018.02.010.

[65] M. Sénoville, F. Delaunay, M. Pârlog, N. L. Achouri, and N. A. Orr. "Neutron-γ discrimination with organic scintillators: Intrinsic pulse shape and light yield contributions". In: *Nuclear Instruments and Methods in Physics Research, Section A: Accelerators, Spectrometers, Detectors and Associated Equipment* 971.April (2020), p. 164080. ISSN: 01689002. DOI: 10.1016/j.nima.2020.164080. arXiv: 2005.06025. URL: https://doi.org/10.1016/j.nima.2020.164080.

[66] G. Battistoni, T. Boehlen, F. Cerutti, P. W. Chin, L. S. Esposito, A. Fassò, A. Ferrari, A. Lechner, A. Empl, A. Mairani, A. Mereghetti, P. G. Ortega, J. Ranft, S. Roesler, P. R. Sala, V. Vlachoudis, and G. Smirnov. "Overview of the FLUKA code". In: *Annals of Nuclear Energy* 82 (2015), pp. 10–18. DOI: 10.1016/j.anucene.2014.11.007. URL: http://dx.doi.org/10.1016/j.anucene.2014.11.007.

[67] T. T. Böhlen, F. Cerutti, M. P.W. Chin, A. Fassò, A. Ferrari, P. G. Ortega, A. Mairani, P. R. Sala, G. Smirnov, and V. Vlachoudis. "The FLUKA Code: Developments and challenges for high energy and medical applications". In: *Nuclear Data Sheets* 120 (2014), pp. 211–214. DOI: 10.1016/j.nds.2014.07.049.

[68] *Home — The official CERN FLUKA website*. URL: https://fluka.cern/ (visited on 05/08/2021).

[69] M. Flaska, M. Faisal, D. D. Wentzloff, and S. A. Pozzi. "Influence of sampling properties of fast-waveform digitizers on neutron-gamma-ray, pulse-shape discrimination for organic scintillation detectors". In: *Nuclear Instruments and Methods in Physics Research Section A: Accelerators, Spectrometers, Detectors and Associated Equipment* 729 (2013), pp. 456–462. ISSN: 0168-9002. DOI: 10.1016/J.NIMA.2013.07.008.

[70] D. Cester, M. Lunardon, G. Nebbia, L. Stevanato, G. Viesti, S. Petrucci, and C. Tintori. "Pulse shape discrimination with fast digitizers". In: *Nuclear Instruments and Methods in Physics Research Section A: Accelerators, Spectrometers, Detectors and Associated Equipment* 748 (2014), pp. 33–38. ISSN: 0168-9002. DOI: 10.1016/J.NIMA.2014.02.032.

[71] C. Guerrero, D. Cano-Ott, M. Fernández-Ordóñez, E. González-Romero, T. Martínez, and D. Villamarín. "Analysis of the BC501A neutron detector signals using the true pulse shape". In: *Nuclear Instruments and Methods in Physics Research, Section A: Accelerators, Spectrometers, Detectors and Associated Equipment* 597.2-3 (2008), pp. 212–218. ISSN: 01689002. DOI: 10.1016/j.nima.2008.09.017.

[72] W. Steinberger, M. L. Ruch, and S. A. Pozzi. "Performance of Stilbene Bars Coupled to Silicon Photomultipliers Using Different Reflectors". In: *2017 IEEE Nuclear Science Symposium and Medical Imaging Conference, NSS/MIC 2017 - Conference Proceedings* (2018), pp. 12–14. DOI: 10.1109/NSSMIC.2017.8532739.

[73] M. P. Taggart and P. J. Sellin. "Comparison of the pulse shape discrimination performance of plastic scintillators coupled to a SiPM". In: *Nuclear Instruments and Methods in Physics Research, Section A: Accelerators, Spectrometers, Detectors and Associated Equipment* 908.May (2018), pp. 148–154. ISSN: 01689002. DOI: 10.1016/j.nima.2018.08.054. URL: https://doi.org/10.1016/j.nima.2018.08.054.

[74] M. Grodzicka-Kobylka, T. Szczesniak, M. Moszyński, K. Brylew, L. Swiderski, J. J. Valiente-Dobón, P. Schotanus, K. Grodzicki, and H. Trzaskowska. "Fast neutron and gamma ray pulse shape discrimination in EJ-276 and EJ-276G plastic scintillators". In: *Journal of Instrumentation* 15.3 (2020). ISSN: 17480221. DOI: 10.1088/1748-0221/15/03/P03030.

[75] J. Valentin. "Relative biological effectiveness (RBE), quality factor (Q), and radiation weighting factor (w_R): ICRP Publication 92". In: *Annals of the ICRP* 33.4 (2003), pp. 1–121. ISSN: 0146-6453. DOI: https://doi.org/10.1016/S0146-6453(03)00024-1. URL: https://www.sciencedirect.com/science/article/pii/S0146645303000241.

[76] D. S. McGregor and J. Kenneth Shultis. "Reporting detection efficiency for semiconductor neutron detectors: a need for a standard". In: *Nuclear Instruments and Methods in Physics Research, Section A: Accelerators, Spectrometers, Detectors and Associated Equipment* 632.1 (2011), pp. 167–174. DOI: 10.1016/j.nima.2010.12.084.

[77] *ISO 8529-1:2001, Reference neutron radiations — Part 1: Characteristics and methods of production.* URL: https://www.iso.org/standard/25666.html (visited on 05/27/2021).

[78] A. S. Sedra and K.C. Smith. *Microelectronic circuits.* Fifth edition. Oxford University Press, 2004.

[79] Tektronix inc. *2450 SourceMeter® SMU Instrument Datasheet.* 2021. URL: https://www.tek.com/keithley-source-measure-units/keithley-smu-2400-series-sourcemeter.

[80] E. Mullin, K. Mesick, S. Nowicki, D. Coupland, Natalia. Zaitseva, and K. Ianakiev. *Performance characterization of organic Pulse Shape Discrimination scintillators at Los Alamos National Laboratory.* Poster presented at: Nuclear Science Symposium and Medical Imaging Conference; November 2018; Sydney.

[81] J. H. Baker, N. Z. Galunov, and O. A. Tarasenko. "Variation of Scintillation Light Yield of Organic Crystalline Solids for Different Temperatures". In: *IEEE Transactions on Nuclear Science* 55.5 (2008), pp. 2736–2738. DOI: 10.1109/TNS.2008.2002146.

[82] P. Schuster and E. Brubaker. "Investigating the anisotropic scintillation response in anthracene through neutron, gamma-ray, and muon measurements". In: *IEEE Transactions on Nuclear Science* 63.3 (2016), pp. 1942–1954. DOI: 10.1109/TNS.2016.2542589.

[83] A S Beddar, T R Mackie, and F H Attix. "Water-equivalent plastic scintillation detectors for high-energy beam dosimetry: I. Physical characteristics and theoretical considerations". In: *Physics in Medicine and Biology* 37.10 (1992), pp. 1883–1900. DOI: 10.1088/0031-9155/37/10/006. URL: https://doi.org/10.1088/0031-9155/37/10/006.

[84] L. Wootton and S. Beddar. "Temperature dependence of BCF plastic scintillation detectors". In: *Physics in Medicine and Biology* 58.9 (2013), pp. 2955–2967. ISSN: 00319155. DOI: 10.1088/0031-9155/58/9/2955.

[85] L. Peralta. "Temperature dependence of plastic scintillators". In: *Nuclear Instruments and Methods in Physics Research, Section A: Accelerators, Spectrometers, Detectors and Associated Equipment* 883.November 2017 (2018), pp. 20–23. DOI: 10.1016/j.nima.2017.11.041. URL: https://doi.org/10.1016/j.nima.2017.11.041.

[86] J. Glodo, W. M. Higgins, E. V.D. Van Loef, and K. S. Shah. "Scintillation properties of 1 inch Cs_2LiYCl_6:Ce crystals". In: *IEEE Transactions on Nuclear Science* 55.3 (2008), pp. 1206–1209. ISSN: 00189499. DOI: 10.1109/TNS.2007.913467.

[87] N. D'Olympia, P. Chowdhury, C. J. Lister, J. Glodo, R. Hawrami, K. Shah, and U. Shirwadkar. "Pulse-shape analysis of CLYC for thermal neutrons, fast neutrons, and gamma-rays". In: *Nuclear Instruments and Methods in Physics Research, Section A: Accelerators, Spectrometers, Detectors and Associated Equipment* 714 (2013), pp. 121–127. ISSN: 01689002. DOI: 10.1016/j.nima.2013.02.043.

[88] A. Giaz, L. Pellegri, F. Camera, N. Blasi, S. Brambilla, S. Ceruti, B. Million, S. Riboldi, C. Cazzaniga, G. Gorini, M. Nocente, A. Pietropaolo, M. Pillon, M. Rebai, and M. Tardocchi. "The CLYC-6 and CLYC-7 response to γ-rays, fast and thermal neutrons". In: *Nuclear Instruments and Methods in Physics Research, Section A: Accelerators, Spectrometers, Detectors and Associated Equipment* 810 (2016), pp. 132–139. ISSN: 01689002. DOI: 10.1016/j.nima.2015.11.119.

[89] N. Dolympia, P. Chowdhury, E. G. Jackson, and C. J. Lister. "Fast neutron response of ^{6}Li-depleted CLYC detectors up to 20 MeV". In: *Nuclear Instruments and Methods in Physics Research, Section A: Accelerators, Spectrometers, Detectors and Associated Equipment* 763 (2014), pp. 433–441. ISSN: 01689002. DOI: 10.1016/j.nima.2014.06.074. URL: http://dx.doi.org/10.1016/j.nima.2014.06.074.

[90] N. Dinar, D. Celeste, M. Silari, V. Varoli, and A. Fazzi. "Pulse shape discrimination of CLYC scintillator coupled with a large SiPM array". In: *Nuclear Instruments and Methods in Physics Research, Section A: Accelerators, Spectrometers, Detectors and Associated Equipment* 935.April (2019), pp. 35–39. DOI: 10.1016/j.nima.2019.04.099. URL: https://doi.org/10.1016/j.nima.2019.04.099.

[91] M. B. Smith, T. Achtzehn, H. R. Andrews, E. T.H. Clifford, H. Ing, and V. D. Kovaltchouk. "Fast neutron spectroscopy using Cs2LiYCl6:Ce (CLYC) scintillator". In: *IEEE Transactions on Nuclear Science* 60.2 (2013), pp. 855–859. ISSN: 00189499. DOI: 10.1109/TNS.2012.2219068.

[92] N. Dolympia, P. Chowdhury, C. J. Guess, T. Harrington, E. G. Jackson, S. Lakshmi, C. J. Lister, J. Glodo, R. Hawrami, K. Shah, and U. Shirwadkar. "Optimizing Cs_2LiYCl_6 for fast neutron spectroscopy". In: *Nuclear Instruments and Methods in Physics Research, Section A: Accelerators, Spectrometers, Detectors and Associated Equipment* 694 (2012), pp. 140–146. ISSN: 01689002. DOI: 10.1016/j.nima.2012.07.021.

[93] A. Giaz, N. Blasi, C. Boiano, S. Brambilla, F. Camera, C. Cattadori, S. Ceruti, F. Gramegna, T. Marchi, I. Mattei, A. Mentana, B. Million, L. Pellegri, M. Rebai, S. Riboldi, F. Salamida, and M. Tardocchi. "Fast neutron measurements with ^{7}Li and ^{6}Li enriched CLYC scintillators". In: *Nuclear Instruments and Methods in Physics Research, Section A: Accelerators, Spectrometers, Detectors and Associated Equipment* 825 (2016), pp. 51–61. DOI: 10.1016/j.nima.2016.03.090. URL: http://dx.doi.org/10.1016/j.nima.2016.03.090.

[94] *ENDF: Evaluated Nuclear Data File*. URL: https://www-nds.iaea.org/exfor/endf.htm (visited on 11/09/2021).

[95] *CLYC Gamma-Neutron Scintillator for SPRDs and RIIDs — RMD, Dynasil*. URL: https://www.dynasil.com/product-category/scintillators/clyc-gamma-neutron-scintillators/ (visited on 05/17/2021).

[96] Ultra Bialkali and Super Bialkali. *Photomultiplier Tube Series "43% QE" !* URL: www.hamamatsu.com.

[97] *Générateurs de neutrons MP 320*. URL: https://www.thermofisher.com/order/catalog/product/1517021A (visited on 11/09/2021).

[98] A. Mentana, F. Camera, A. Giaz, N. Blasi, S. Brambilla, S. Ceruti, L. Gini, F. Groppi, S. Manenti, B. Million, and S. Riboldi. "Measurement of fast neutron detection efficiency with ^{6}Li and ^{7}Li enriched CLYC scintillators". In: *Journal of Physics: Conference Series* 763.1 (2016). ISSN: 17426596. DOI: 10.1088/1742-6596/763/1/012006.

[99] N. Blasi, S. Brambilla, F. Camera, S. Ceruti, A. Giaz, L. Gini, F. Groppi, S. Manenti, A. Mentana, B. Million, and S. Riboldi. "Fast neutron detection efficiency of ^{6}Li and ^{7}Li enriched CLYC scintillators using an Am-Be source". In: *Journal of Instrumentation* 13.11 (2018). DOI: 10.1088/1748-0221/13/11/P11010. arXiv: 1807.10759.

[100] D. Pérez-Loureiro, O. Kamaev, G. Bentoumi, L. Li, C. Jewett, and M. Thompson. "Evaluation of CLYC-6 and CLYC-7 scintillators for detection of nuclear materials". In: *Nuclear Instruments and Methods in Physics Research, Section A: Accelerators, Spectrometers, Detectors and Associated Equipment* 1012.April (2021), p. 165622. ISSN: 01689002. DOI: 10.1016/j.nima.2021.165622. URL: https://doi.org/10.1016/j.nima.2021.165622.

[101] J. Glodo, A. Gueorguiev, U. Shirwadkar, R. Hawrami, J. Tower, P. O'Dougherty, and K. S. Shah. "Integrated neutron detector for handheld systems". In: *IEEE Transactions on Nuclear Science* 60.2 (2013), pp. 903–907. ISSN: 00189499. DOI: 10.1109/TNS.2013.2252020.

[102] R. S. Woolf, A. L. Hutcheson, B. F. Phlips, and E. A. Wulf. "Response of the Li-7-enriched Cs_2LiYCl_6:Ce (CLYC-7) scintillator to 6-60 MeV neutrons". In: *Nuclear Instruments and Methods in Physics Research, Section A: Accelerators, Spectrometers, Detectors and Associated Equipment* 803 (2015), pp. 47–54. ISSN: 01689002. DOI: 10.1016/j.nima.2015.08.080.

[103] D. Henzlova, R. Kouzes, R. McElroy, P. Peerani, M. Aspinall, K. Baird, A. Bakel, M. Borella, M. Bourne, L. Bourva, F. Cave, R. Chandra, D. Chernikova, S. Croft, G. Dermody, A. Dougan, J. Ely, E. Fanchini, P. Finocchiaro, V. Gavron, M. Kureta, K. D. Ianakiev, K. Ishiyama, T. Lee, Ch. Martin, K. McKinny, Howard Olsen Menlove, Ch. Orton, A. Pappalardo, B. Pedersen, D. Peranteau, R. Plenteda, S. Pozzi, M. Schear, M. Seya, E. Siciliano, S. Stave, L. Sun, Martyn Thomas Swinhoe, H. Tagziria, S. Vaccaro, J. Takamine, A. L. Weber, T. Yamaguchi, and H. Zhu.

"Current status of helium-3 alternative technologies for nuclear safeguards". In: 01 (2015), LA–UR–15–21201. URL: http://inis.iaea.org/Search/search.aspx?orig_q=RN:47006525\%0Ahttp://www.osti.gov/servlets/purl/1227248/.

[104] G. Zorloni, F. Cova, M. Caresana, M. Di Benedetto, J. Hostaša, M. Fasoli, I. Villa, I. Veronese, A. Fazzi, and A. Vedda. "Neutron/γ discrimination by an emission-based phoswich approach". In: *Radiation Measurements* 129.October (2019), pp. 1–6. ISSN: 13504487. DOI: 10.1016/j.radmeas.2019.106203.

[105] S. Gundacker, E. Auffray, K. Pauwels, and P. Lecoq. "Measurement of intrinsic rise times for various L(Y)SO and LuAG scintillators with a general study of prompt photons to achieve 10 ps in TOF-PET". In: *Physics in Medicine and Biology* 61.7 (2016), pp. 2802–2837. ISSN: 13616560. DOI: 10.1088/0031-9155/61/7/2802.

[106] S. Gundacker, R. M. Turtos, E. Auffray, and P. Lecoq. "Precise rise and decay time measurements of inorganic scintillators by means of X-ray and 511 keV excitation". In: *Nuclear Instruments and Methods in Physics Research, Section A: Accelerators, Spectrometers, Detectors and Associated Equipment* 891.November 2017 (2018), pp. 42–52. ISSN: 01689002. DOI: 10.1016/j.nima.2018.02.074. URL: https://doi.org/10.1016/j.nima.2018.02.074.

[107] E. V.D. Van Loef, P. Dorenbos, C. W.E. Van Eijk, K. W. Krämer, and H. U. Güdel. "Scintillation and spectroscopy of the pure and Ce^{3+}-doped elpasolites: Cs_2LiYX_6 (X = Cl, Br)". In: *Journal of Physics Condensed Matter* 14.36 (2002), pp. 8481–8496. ISSN: 09538984. DOI: 10.1088/0953-8984/14/36/307.

[108] P. Dorenbos. "Scintillation mechanisms in Ce^{3+} doped halide scintillators". In: *Physica Status Solidi (A) Applications and Materials Science* 202.2 (2005), pp. 195–200. ISSN: 18626300. DOI: 10.1002/pssa.200460106.

[109] R. H. Pots, E. Auffray, and S. Gundacker. "Exploiting Cross-Luminescence in BaF_2 for Ultrafast Timing Applications Using Deep-Ultraviolet Sensitive HPK Silicon Photomultipliers". In: *Frontiers in Physics* 8 (2020), p. 482. ISSN: 2296424X. DOI: 10.3389/fphy.2020.592875. URL: https://www.hamamatsu.com/jp/en/product/.

[110] Z. W. Bell, D. E. Hornback, M. Z. Hu, and J. S. Neal. "Wavelength-based neutron/gamma ray discrimination in CLYC". In: *2014 IEEE Nuclear Science Symposium and Medical Imaging Conference, NSS/MIC 2014* (2016). DOI: 10.1109/NSSMIC.2014.7431197.

[111] B. S. Budden, L. C. Stonehill, J. R. Terry, A. V. Klimenko, and J. O. Perry. "Characterization and investigation of the thermal dependence of Cs_2LiYCl_6: Ce^{3+} (CLYC) waveforms". In: *IEEE Transactions on Nuclear Science* 60.2 (2013), pp. 946–951. ISSN: 00189499. DOI: 10.1109/TNS.2012.2215884.

[112] P. Lecoq, A. Gektin, and M. Korzhik. *Inorganic Scintillators for Detector Systems.* Second edition. Springer-Verlag, 2006. DOI: 10.1007/3-540-27768-4.

[113] F. Cova. "Study of Radiation-Induced Defects in Rare-Earth doped Silica Preforms and Optical Fibers for High Energy Physics Detectors". MA thesis. Università degli Studi di Milano-Bicocca, 2016.

[114] *Prime™ X.* URL: https://www.snowhouse.ca/pdf/BWTek\%20-\%20280001178-D\%20PrimeX\%20Data\%20Sheet.pdf (visited on 11/24/2021).

[115] *ISO 4037-1:2019, Radiological protection — X and gamma reference radiation for calibrating dosemeters and doserate meters and for determining their response as a function of photon energy.* URL: https://www.iso.org/standard/66872.html (visited on 05/08/2021).

[116] *Optical Filters and Instruments — Asahi Spectra USA Inc.* URL: https://www.asahi-spectra.com/ (visited on 05/17/2021).

[117] S. Lam, J. Fiala, M. Hackett, and S. Motakef. "A High-Performance CLYC(Ce)-PVT Composite for Neutron and Gamma Detection". In: *IEEE Transactions on Nuclear Science* 65.1 (2018), pp. 609–615. ISSN: 00189499. DOI: 10.1109/TNS.2017.2779783.

[118] *PerkinElmer — For The Better.* URL: https://www.perkinelmer.com/it (visited on 11/06/2021).

[119] *PHOTOMULTIPLIER TUBE ASSEMBLIES H6533/H6610.* URL: http://web-docs.gsi.de/~nkuzminc/Images/H6533+H6610_TPMH1199E01.pdf (visited on 11/24/2021).

[120] X. Wen and A. Enqvist. "Measuring the scintillation decay time for different energy deposited by γ-rays and neutrons in a Cs_2LiYCl_6:Ce^{3+} detector". In: *Nuclear Instruments and Methods in Physics Research, Section A: Accelerators, Spectrometers, Detectors and Associated Equipment* 853.February (2017), pp. 9–15. ISSN: 01689002. DOI: 10.1016/j.nima.2017.02.019. URL: http://dx.doi.org/10.1016/j.nima.2017.02.019.

[121] F. Anghinolfi, P. Jarron, F. Krummenacher, E. Usenko, and M. C.S. Williams. "NINO, an ultra-fast, low-power, front-end amplifier discriminator for the Time-Of-Flight detector in ALICE experiment". In: *IEEE Nuclear Science Symposium Conference Record*. Vol. 1. Institute of Electrical and Electronics Engineers Inc., 2003, pp. 375–379. DOI: 10.1109/nssmic.2003.1352067.

[122] A. Gola, F. Acerbi, M. Capasso, M. Marcante, A. Mazzi, G. Paternoster, C. Piemonte, V. Regazzoni, and N. Zorzi. "NUV-sensitive silicon photomultiplier technologies developed at fondazione Bruno Kessler". In: *Sensors (Switzerland)* 19.2 (2019). ISSN: 14248220. DOI: 10.3390/s19020308.

[123] SensL. *Introduction to SiPM.* Tech. rep. 2011. URL: https://www.sensl.com/downloads/ds/TN\%20-\%20Intro\%20to\%20SPM\%20Tech.pdf (visited on 11/24/2021).

[124] S. Gundacker, R. H. Pots, A. Nepomnyashchikh, E. Radzhabov, R. Shendrik, S. Omelkov, M. Kirm, F. Acerbi, M. Capasso, G. Paternoster, A. Mazzi, A. Gola, J. Chen, and E. Auffray. "Vacuum ultraviolet silicon photomultipliers applied to BaF_2cross-luminescence detection for high-rate ultrafast timing applications". In: *Physics in Medicine and Biology* 66.11 (2021). ISSN: 13616560. DOI: 10.1088/1361-6560/abf476.

[125] C. M. Combes, P. Dorenbos, C. W.E. Van Eijk, K. W. Krämer, and H. U. Güdel. "Optical and scintillation properties of pure and Ce^{3+}-doped Cs_2LiYCl_6 and Li_3YCl_6 : Ce^{3+} crystals". In: *Journal of Luminescence* 82.4 (1999), pp. 299–305. ISSN: 00222313. DOI: 10.1016/S0022-2313(99)00047-2.

[126] M. Kirm, A. Lushchik, C. Lushchik, A. I. Nepomnyashikh, and F. Savikhin. "Dependence of the efficiency of various emissions on excitation density in BaF_2 crystals". In: *Radiation Measurements* 33.5 (2001), pp. 515–519. ISSN: 1350-4487. DOI: 10.1016/S1350-4487(01)00044-0.

[127] K. Kimura. "LET-, ionic species- and temperature-dependence on Auger-free and self-trapped exciton luminescence of ion-irradiated BaF_2 and CsCl single crystals". In: *Nuclear Instruments and Methods in Physics Research Section B: Beam Interactions with Materials and Atoms* 116.1 (1996), pp. 57–60. ISSN: 0168-583X. DOI: https://doi.org/10.1016/0168-583X(96)00011-0. URL: https://www.sciencedirect.com/science/article/pii/0168583X96000110.

[128] Fabio Pozzi, Ruben Garcia Alia, Markus Brugger, Pierre Carbonez, Salvatore Danzeca, Blerina Gkotse, Martin Richard Jaekel, Federico Ravotti, Marco Silari, and Maris Tali. "CERN irradiation facilities". In: *Radiation Protection Dosimetry* 180.1-4 (2018), pp. 120–124. ISSN: 17423406. DOI: 10.1093/RPD/NCX187.

[129] R. Bedogni, D. Sacco, J.M. Gómez-Ros, M. Lorenzoli, A. Gentile, B. Buonomo, A. Pola, M.V. Introini, D. Bortot, and C. Domingo. "ETHERNES: A new design of radionuclide source-based thermal neutron facility with large homogeneity area". In: *Applied Radiation and Isotopes* 107 (2016), pp. 171–176. ISSN: 09698043. DOI: 10.1016/j.apradiso.2015.10.016. URL: https://linkinghub.elsevier.com/retrieve/pii/S0969804315302104.

[130] R. Bedogni, A. Pietropaolo, and J. M. Gomez-Ros. "The thermal neutron facility HOTNES: theoretical design". In: *Applied Radiation and Isotopes* 127 (2017), pp. 68–72. ISSN: 18729800. DOI: 10.1016/j.apradiso.2017.05.003. URL: https://pubmed.ncbi.nlm.nih.gov/28527348/.

[131] V. Lacoste, V. Gressier, H. Muller, and L. Lebreton. "Characterisation of the IRSN graphite moderated Americium–Beryllium neutron field". In: *Radiation Protection Dosimetry* 110.1-4 (2004), pp. 135–139. ISSN: 0144-8420. DOI: 10.1093/RPD/NCH188. URL: https://academic.oup.com/rpd/article/110/1-4/135/1598299.

[132] M. Luszik-Bhadra, M. Reginatto, H. Wershofen, B. Wiegel, and A. Zimbal. "New PTB thermal neutron calibration facility: First results". In: *Radiation Protection Dosimetry* 161.1-4 (2014), pp. 352–356. ISSN: 17423406. DOI: 10.1093/rpd/nct354.

[133] L. E. Cevallos-Robalino, G. F. García-Fernández, A. Lorente, E. Gallego, S. Ibañez-Fernández, H. R. Vega-Carrillo, and K. A. Guzmán-Garcia. "Monte Carlo design and experimental characterization of a moderator device to produce a thermal neutron source from a ^{241}Am/^{9}Be source". In: *Radiation Physics and Chemistry* 168.July 2019 (2020), p. 108599. ISSN: 18790895. DOI: 10.1016/j.radphyschem.2019.108599. URL: https://doi.org/10.1016/j.radphyschem.2019.108599.

[134] C. Birattari, E. Dimovasili, A. Mitaroff, and M. Silari. "A Bonner Sphere Spectrometer with extended response matrix". In: *Nuclear Instruments and Methods in Physics Research, Section A: Accelerators, Spectrometers, Detectors and Associated Equipment* 620.2-3 (2010), pp. 260–269. ISSN: 01689002. DOI: 10.1016/j.nima.2010.04.033.

Caractérisation du radiamètre B-RAD et développement de nouvelles sondes

Résumé : Le B-RAD est un détecteur commercial pour la mesure du débit de dose et la spectrométrie des rayons γ, capable de fonctionner dans les champs magnétiques intenses. Il est constitué d'une sonde et d'une unité centrale : la sonde est équipée d'un cristal de $LaBr_3$ couplée à une matrice de photomultiplicateurs au silicium (SiPM), l'unité centrale abrite le circuit électronique principal et la batterie. Sa réponse est faiblement affectée par le champ magnétique lorsque l'unité centrale est à l'intérieur du champ (variation <10% jusqu'à 1.5 T). Sa réponse est linéaire entre 1 μSv/h et 2 mSv/h. Le B-RAD possède une bonne résolution en énergie (< 5% à 662 keV) et une large gamme d'énergie (30 keV–1.5 MeV).

Deux scintillateurs organiques, stilbène et EJ-276, ont été sélectionnés pour développer une sonde destinée aux mesures de débit de dose des neutrons rapides. Le stilbène a une figure de mérite (FOM) plus élevée pour la discrimination des neutrons/rayons γ (n/γ) via la *Pulse Shape Discrimination* (PSD) (1.54 contre 0.90) et une meilleure efficacité de détection (12% contre 9%). Les deux détecteurs montrent une bonne linéarité du taux de comptage jusqu'à 1 mSv/h avec une source de ^{137}Cs et 1.5 mSv/h avec une source Am-Be. Entre -10°C et 40°C, les deux détecteurs montrent une variation du taux de comptage des neutrons de 10%. Une sonde basée sur le stilbène est actuellement en développement.

Deux autres sondes ont été étudiées sur la base de scintillateurs $Cs_2LiYCl_6:Ce^{3+}$ (CLYC). La première utilise un CLYC-6 (enrichi en ^{6}Li) pour la détection des neutrons thermiques. Le CLYC-6 présente une excellente capacité de discrimination n/γ (FOM > 2) et une grande efficacité de détection des neutrons par unité de volume. La deuxième sonde utilise un CLYC-7 (enrichi en ^{7}Li) adapté à la spectrométrie des neutrons rapides. Une discrimination proton/particule α a été proposée et testée, ce qui améliore la capacité de spectrométrie du CLYC jusqu'à 6 MeV. Une nouvelle méthode de discrimination passive n/γ pour le CLYC a été développée, basée sur la sélection de la lumière de scintillation *Core-to-Valence* (CVL) par filtrage optique. D'après la littérature, la CVL est excitée seulement par les rayons γ et apparaît dans une gamme de longueurs d'onde différente de celle des autres mécanismes de scintillation. Nous avons montré que l'intensité de la CVL sous irradiation aux rayons X et γ est constante dans la gamme 17–662 keV et que la CVL est efficacement réduite par les neutrons. Cependant, un résidu de la CVL a été détecté également sous irradiation neutronique.

Une nouvelle source de neutrons thermiques pour le laboratoire d'étalonnage du CERN a été conçue, construite et caractérisée. La source se compose d'un modérateur cylindrique et d'un réflecteur en polyéthylène. Les dimensions optimales de la source ont été déterminées par des simulations Monte Carlo. La nouvelle source fournit une fluence de neutrons thermiques de 6000 $cm^{-2}s^{-1}$.

Mots clés : Radioprotection, Développement de détecteurs, CERN, Scintillateurs, SiPM.

Characterisation of the B-RAD radiation survey meter and development of new probes

Abstract: The B-RAD is a commercial device for dose rate monitoring and γ-ray spectrometry in high intensity magnetic fields. It consists of an active probe and a central unit: the probe is equipped with a $LaBr_3$ crystal coupled with a Silicon Photomultiplier (SiPM) array, the central unit houses the main electronic circuit and the battery. Its response is only slightly affected by the magnetic field when the central unit is inside the field (variation <10% up to 1.5 T). It is linear between 1 μSv/h and 2 mSv/h and it has a good energy resolution (<5% at 662 keV) and a wide operational energy range (30 keV–1.5 MeV).

A stilbene and an EJ-276 plastic scintillator were selected for dose rate measurements of fast neutrons. The stilbene shows a higher Figure of Merit (FOM) for the Pulse Shape Discrimination (PSD) (1.54 vs 0.90) and a higher detection efficiency (12% vs 9%). Both detectors show a good linearity of the count rate up to 1 mSv/h with a ^{137}Cs source and 1.5 mSv/h with an Am-Be source. In the -10°C to 40°C temperature range, both detectors show a variation of the neutron count rate of 10%.

Other two probes were investigated based on $Cs_2LiYCl_6:Ce^{3+}$ (CLYC). The first employs CLYC-6 (enriched in ^{6}Li) for thermal neutron detection. CLYC-6 shows an excellent n/γ discrimination capability (FOM > 2) and a high neutron detection efficiency per unit volume. The second probe employs a CLYC-7 (enriched in ^{7}Li) suitable for fast neutron spectrometry. A proton/α-particle discrimination method is here proposed and tested, which improves the CLYC spectrometry capability up to around 6 MeV.

A new passive n/γ discrimination method for CLYC was studied, based on the selection of the Core-to-Valence (CVL) scintillation light by optical filtering. According to the literature, CVL is only excited by γ-rays and emits in a different wavelength range than the other scintillation mechanisms. We verifyed that the intensity of the CVL under X and γ-ray irradiation is constant in the 17–662 keV range and the CVL is effectively quenched by neutrons. However, a residual signal of the CVL was detected also under neutron irradiation.

A new thermal neutron source for the CERN Calibration Laboratory was designed, built and characterised. The source consists of a polyethylene cylindrical moderator and a polyethylene reflector. The optimum dimensions of the source were provided by Monte Carlo simulations. The new source provides a thermal neutron fluence of around 6000 $cm^{-2}s^{-1}$.

Keywords: Radiation protection, Detector development, CERN, Scintillators, SiPM.